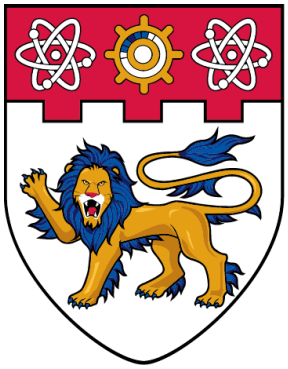

NANYANG TECHNOLOGICAL UNIVERSITY
SINGAPORE

DEVELOPMENT OF AN OIL-FREE SWING VANE COMPRESSOR WITH LIQUID REFRIGERANT INJECTION

HENG KIM RUI

SCHOOL OF MECHANICAL AND AEROSPACE ENGINEERING

2020

DEVELOPMENT OF AN OIL-FREE SWING VANE COMPRESSOR WITH LIQUID REFRIGERANT INJECTION

Heng Kim Rui

School of Mechanical and Aerospace Engineering

A thesis submitted to the Nanyang Technological University
in partial fulfilment of the requirements for the degree of
Doctor of Philosophy

August 2020

Heng Kim Rui

Development of An Oil-Free Swing Vane Compressor With Liquid Refrigerant Injection

Nanyang Technological University

School of Mechanical and Aerospace Engineering

Energy Systems Laboratory

65 Nanyang Drive

N3.1A-B4-01/02

Singapore 637460

Statement of Originality

I hereby certify that the work embodied in this thesis is the result of original research, is free of plagiarised materials, and has not been submitted for a higher degree to any other University or Institution.

24/08/20

. . . . . .

Date

. . . . . .

Heng Kim Rui

Supervisor Declaration Statement

I have reviewed the content and presentation style of this thesis and declare it is free of plagiarism and of sufficient grammatical clarity to be examined. To the best of my knowledge, the research and writing are those of the candidate except as acknowledged in the Author Attribution Statement. I confirm that the investigations were conducted in accord with the ethics policies and integrity standards of Nanyang Technological University and that the research data are presented honestly and without prejudice.

24/08/20

. . . . . .

Date

. . . . . .

Assoc. Prof. Chan Weng Kong

Supervisor Declaration Statement

I have reviewed the content and presentation style of this thesis and declare it is free of plagiarism and of sufficient grammatical clarity to be examined. To the best of my knowledge, the research and writing are those of the candidate except as acknowledged in the Author Attribution Statement. I confirm that the investigations were conducted in accord with the ethics policies and integrity standards of Nanyang Technological University and that the research data are presented honestly and without prejudice.

24/08/20

. . . . . .
Date

. . . . . .
Prof. Ooi Kim Tiow

Authorship Attribution Statement

This thesis contains material from 1 paper presented at the 25th IIR International Congress of Refrigeration conference in which I am listed as an author.

Section 2.1.4 of Chapter 2 contains material from: K. R. Heng, K. T. Ooi, and W. K. Chan, ‘‘Performance of a non-uniform width rotating discharge valve in the revolving vane (RV) compressor,’’ *IIR International Congress of Refrigeration*. Montréal, Québec, Canada, August 24-30, 2019. Manuscript 347, (2019). DOI: 10.18462/iir.icr.2019.347

The contributions of the co-authors are as follows:

- I formulated the mathematical models, developed the numerical simulation codes and investigated the performance of a non-uniform width rotating discharge valve in the revolving vane (RV) compressor under the supervision of Assoc. Prof. Chan Weng Kong and Prof. Ooi Kim Tiow.
- I prepared the manuscript drafts. The manuscript was revised by Assoc. Prof. Chan Weng Kong and Prof. Ooi Kim Tiow.

24/08/20

. . . . . .
Date

. . . . . .
Heng Kim Rui

Abstract

A conventional compressor in a vapour-compression refrigeration system often requires the extensive use of active oil lubrication to ensure reliable operations. The use of active oil lubrication, however, has resulted in the low portability and poor compactness of current compressors because the lubrication system often requires components such as the oil filter, oil pump, oil cooler and oil sump. In addition, these compressors must always be operated in the upright orientation to ensure that the oil sump is always located at the lowest position to allow the lubricant to flow back to the oil sump by gravity. This is required to maintain a functional lubrication system that provides a continuous re-circulation of lubrication flow. As a result, the conventional vapour-compression refrigeration system has limited cooling and heating applications since the orientation of the compressor is fixed.

The current refrigeration system that relies on oil-lubricated compressor is not feasible for applications such as wearable cryogenic cooling bags for the ease of vaccine transportation or compact cryogenic coolers for space applications. With the successful development of an oil-free compressor, the vapour-compression refrigeration system would be able to operate freely under any orientation and become an alternative for small-scale portable cooling and heating applications.

This work aims to develop a simple positive-displacement vane type compressor for oil-free operation. Potential key failure modes and the performance characteristics of an oil-free compressor were determined theoretically and experimentally. Without oil lubrication, an oil-free compressor would easily get overheated and seizure may occur. To resolve this issue, liquid refrigerant injection cooling was used in the new compressor design to improve its reliability.

In this study, an oil-free swing vane compressor prototype was designed and its performance was evaluated through experimental testing with air and R134a as the working fluid. Theoretical models were formulated to predict its operational characteristics. The models developed include the mathematical descriptions of the geometry and kinematics of the swing vane mechanism, the thermodynamics analysis of the working cycle, the dynamic analysis of the moving parts and valve vibrations, the leakage flow analysis and the heat transfer

study. In the theoretical analysis of the liquid refrigerant injection cooling, a two-phase orifice flow model was also used to predict the injected mass flow of the refrigerant and the injected liquid refrigerant was assumed to evaporate instantaneously after absorbing heat from the compression chamber.

Experimental studies of the oil-free prototype were conducted at operating speeds ranging from 1080 to 1800 rev min^{-1} with air as the working fluid. Compression ratios between 2.11 and 4.08 with mechanical efficiency ranging from 19.3% to 30.3% and volumetric efficiency ranging from 30.9% to 67.5% were achieved. The overall isentropic efficiency achieved from these experiments varies from 0.52 to 0.71. Predicted results from the theoretical models were compared with measured data and the maximum discrepancy of each measured output was found to be less than 15%. Experimental tests of the prototype in a vapour-compression cycle with R134a were conducted at an operating speed of 1620 rev min^{-1} and the prototype achieved a mechanical efficiency of 35.6% and a volumetric efficiency of 55.5%. The coefficients of performance (COPs) measured and predicted were 1.25 and 1.28, respectively. The low COPs values were largely due to substantial internal leakages in the prototype in the absence of oil lubrication. Liquid refrigerant was also injected into the compression chamber of the prototype for durations of 0.005s and 0.01s to cool the compressor mechanism and the performance of the prototype was analysed. It was found that the injected liquid refrigerant was able to cool the compressor significantly without increasing the compression power and decreasing the compressor efficiency. No significant improvement to the COP for operations under effects of liquid injection cooling was observed. However, the surface temperature of the compressor was cooled by 6.5 to 8.1°C while only a small additional 2.4% increment in the average power input was measured. With a liquid refrigerant injection duration of 0.01s, the isentropic efficiency was predicted to improve from 0.70 to 0.90 due to lesser compression work required.

Overall, the conceptual prototype of an oil-free swing vane compressor was successfully tested experimentally. As compared to other existing oil-free refrigeration compressors, the COPs achieved in the experiments were low. Higher COPs can be achieved with better fabrication accuracy to reduce internal leakages and with better self-lubricating materials with higher wear resistance and lower friction coefficient.

Acknowledgements

Firstly, the author would like to express his deepest gratitude to his supervisor, Assoc Prof Chan Weng Kong and his co-supervisor Prof Ooi Kim Tiow for their patient guidance, support and constructive advice on this research. Their encouragements have motivated the author in taking on greater challenges and to strive for continuous improvements.

Next, the author would like to thank Nanyang Technological University (NTU), Singapore for giving him the opportunity to pursue his Ph.D. with the Nanyang President's Graduate Scholarship (NPGS). The author had presented a paper at the 25^{th} IIR International Congress of Refrigeration which was funded by the NPGS's conference allowance. He was also given the opportunity to attend the Lean LaunchPad entrepreneurship course by NTUitive and NUS Enterprise which was funded by his co-supervisor's NTUitive Gap Fund and has gained precious experience.

Thirdly, the author would like to thank Mr. Koh Chin Boon, the director of Time Engineering Industries Sdn, for his expertise in the fabrication of the prototype developed in this work. Without his practical knowledge and patience in repairing worn out parts of the prototype, the prototype would not be able to function satisfactorily.

Next, the author would like to thank the helpful technical staff of MAE, Mr Edward Yeo Boon Chuan, Mr Lawrence Ang Koon Teck, Mr Koh Tian Guan, Mr Roger Lee from Energy Systems Laboratory, Ms Chia Hwee Lang from Aerospace Structures Laboratory, Mr Chia Yak Khoong from Heat Transfer Laboratory, Mr Ricky Lim Lye Hock, Mr Koh Wing Leong, Mr Elson Ng Moo Kheo, Mr Yew Ying Yeow, Ms Tan How Jee from Manufacturing Processes Laboratory, Mdm Nge Tak Heng from Clean Energy Research Centre. Their kind assistance in aiding the author in the setup of the experiment was very much appreciated. The author has also gained valuable technical knowledge and skills from the technical staff which have serve the author well. The author's sincerest thanks would also go to the administrative staff of MAE, Mr Roger Tan, Ms Yeo Lay Foon, Mr Mohammad Nazri Bin Khairuddin, Mr Lee Boon Kiang, Ms Christina Toh Meow Hwee from the Administration and Chair's office

for their help in the administrative work.

In addition, the author would like to appreciate and thank his supervisor's FYP student, his seniors and fellow colleagues, Ms Lim Li Ying, Dr Yap Ken Shaun and Dr Aw Kuan Thai for their help given. Ms Lim's work in the CFD simulation of leakage flow was cited and used in the validation of the theoretical leakage flow model. Dr Yap has shared his valuable expertise on measurement instrumentation and Dr Aw has helped tremendously in the project with his advice on certain numerical models. The author is also extremely thankful to his fellow Ph.D. batch-mates, Dr Cheng Kai Xian, Dr Lim Yeu De, Dr Pradeep Shakya and Mr Poh Wai Chang for their camaraderie. Their unwavering friendship and companionship have definitely made the author's Ph.D. journey an enjoyable and memorable one.

Last but not least, the author would like to thank his family for their continued support and encouragement throughout the Ph.D. journey.

Contents

List of Figures

List of Tables

Nomenclature

Greek Symbols

α	angular acceleration, heat distribution coefficient	[rad s^{-2}, -]
δ	clearance	[m]
ϵ	surface emissivity	[-]
η	efficiency	[-]
γ	heat capacity ratio	[-]
λ	natural frequency of vibration mode	[Hz]
μ	friction coefficient	[-]
ω	angular speed	[rad s^{-1}]
ϕ	rotational angle of split bush, vector of interpolation functions, tangential friction per unit of circumference	[rad, -, N m^{-1}]
ρ	density	[kg m^{-3}]
σ	Stefan-Boltzmann constant	[W $m^{-2}K^{-4}$]
τ	time-dependent mode participation factor	[m]
Θ	dimensionless angular displacement	[-]
θ	rotational angle	[rad, °]
ε	angle	[rad]
ξ	dimensionless displacement interval	[-]

Roman Symbols

A	area	[m^2]
a	vector of nodal displacements	[-]
B	spatial peiodicity between asperities	[m]
C	centre of axis, coefficient, arbitrary constant	[-, -, -]
c	damping coefficient, arbitrary constant	[-, -]
c_p	specific heat	[J kg^{-1} K^{-1}]
D	diameter	[m]
E	energy, Young's modulus	[J, Pa]
F	force	[N]
f	force per unit area	[N m^{-2}]
g	gravitational acceleration	[m s^{-2}]
H	thermal conductance coefficient, asperity height	[W K^{-1}, m]
h	specific enthalpy	[J kg^{-1}]
I	second moment of area, rotational inertia	[m^4, kg m^2]
K	element stiffness matrix	[-]
k	thermal conductivity	[W $m^{-1}K^{-1}$]
L	length of valve reed	[m]
l	length	[m]
M	moment, mass matrix, Mach number	[N.m, -, -]
m	mass	[kg]
N	normal force	[N]
P	power	[W]

p	pressure	[Pa]
Q	thermal energy	[J]
q	vapour quality of saturated mixture	[-]
$\dot{Q}$	rate of heat transfer	[W]
R	thermal contact resistance	[m^2 K W^{-1}]
r	radial distance, critical pressure ratio	[m, -]
S	internal heat generation	[W]
T	kinetic energy, torque, temperature	[J, N.m, K]
t	time, thickness	[s, m]
U	potential energy	[J]
u	specific internal energy	[J kg^{-1}]
V	volume, shear force	[m^3, N]
v	velocity	[ms^{-1}]
W	work, weight	[J, N]
w	width	[m]
$\dot{W}$	work done per unit time	[W]
x	x-coordinate	[m]
Y	mode shape, dimensionless displacement	[-, -]
y	y-coordinate	[m]
z	z-coordinate	[m]

Subscripts

avg	average
br	ball bearing

c	compression, cylinder
$circumf$	circumferential
com	compression
$correc$	correction
cr	critical
cv	control volume
d	discharge
$disc$	discharge
dp	discharge port, discharge pipe
e	outlet, eccentricity, exit
ec	eccentric
ef	endface
f	friction, liquid state
g	gaseous state
i	inlet, inner
inj	injection
liq	liquid refrigerant
lk	leakage
m	motor
mid	middle
o	outer
r	rotor
rad	radial

rr	rolling
s	suction, isentropic, shaft
sb	split bush
sc	solenoid valve chamber
sl	sliding
so	spray orifice
ss	sonic speed
suc	suction
sur	surrounding environment
t	throat
v	vane
vo	solenoid valve orifice
x	x-directional
y	y-directional
z	z-directional

Chapter 1

Introduction

1.1 Motivation of Work

A vapour-compression refrigeration system plays an indispensable role in industrial and household cooling and heating due to its high coefficient of performance (COP) values and its capability to operate in wide operating temperature range while achieving adequate degrees of targeted cooling and heating. At the heart of the vapour-compression refrigeration system, the compressor is the core element that drives refrigerant through the condensation, throttling and evaporation processes.

In current compressor designs used in vapour-compression refrigeration system, the compressors are heavily reliant on active oil lubrication systems to ensure reliable and lasting operations with high mechanical and volumetric efficiencies. This is because lubrication reduces friction, promotes heat dissipation and improves sealing of clearances between moving parts. The use of oil lubricant requires compressors to be always operated in a specified upright orientation to ensure that the oil sump is located at the lowest position for the collection of oil lubricant back to the oil sump by gravity. Any change in the orientation of an oil-lubricated compressor during operations would essentially restrict the re-circulation of oil lubricant and its flow to the moving interfaces. This would eventually cause severe thermal decomposition of the oil lubricant due to high temperature exposure and the seizure of the compressor due to oil starvation [1]. This means that vapour-compression refrigeration system which runs on an oil-lubricated compressor is bulky and has restrictive operating orientation, hence limiting its application where portability and orientation-free of the system are required.

In addition, the use of oil lubricant often requires a complex and extensive lubrication flow network and centralised reservoir to distribute clean lubricant to all moving components and to extract heat from the compressor's mechanism [2, 3]. The main components of such lubrication system require an oil filter to remove the solid contaminants together with any atmospheric dust, a heat exchanger for cooling the heated oil, an oil sump, an oil pump as an external driver and/or complex oil channels on the driving mechanism for reliable oil feeding and hydrodynamic lubrication [1, 4]. This reliance on oil lubrication would also indicate that the current systems using oil-lubricated compressors are sizeable and poor in compactness.

The use of oil lubrication in current compressor also has the impending problem of oil logging in the evaporator and condenser of the refrigeration system. During operation, a portion of oil is usually circulated with the refrigerant flow through the heat exchange components while most of the oil stays in the compressor. When oil retention or "oil fouling" occurs inside the heat exchange components, a significant decrease in heat transfer rate and an increase in pressure drop along the refrigeration cycle will result [5]. Over time, the COP of vapour-compression refrigeration will decline and the compressor might seize due to insufficient oil lubrication. For this reason, there are also growing interests in the use of oil-free compressor for refrigeration purposes due to its non-degrading compressor performance over time without the consequences of oil fouling [6–8]. Furthermore, the use of oil limits both the choice of refrigerants and their operating temperature range.

A direct solution to these aforementioned problems would be the elimination of the need of oil lubrication in the operation of a compressor. This would require a successful development of an oil-free compressor. With such development, the vapour-compression refrigeration system would be an alternative for small-scale portable and wearable cooling and heating applications. Since an oil-free compressor can operate freely under any orientation, the practicability of a portable vapour-compression cooling system will also be extended to potential applications that require high cooling capacity and portability. The current refrigeration system that relies on oil-lubricated compressor is not feasible for applications such as wearable cryogenic cooling bags for the ease of vaccine transportation or compact cryogenic coolers for space applications. In addition, the refrigeration system will be more compact and scalable for portable usage without the use of oil lubrication system. The long-term cooling efficiency of the

refrigeration system will also be improved due to a better heat exchange across the condenser and the evaporator without the effect of oil fouling.

Current oil-free refrigeration compressors, however, are mainly centrifugal compressors which rely on active magnetic levitation bearing systems to mitigate friction and overheating at moving interfaces [9]. Magnetic bearings are typically used in specialised applications in aerospace and large industrial machineries, limited to high-end applications where cost is not the major consideration [10]. The bearing system usually uses permanent magnets for primary levitation of the driving shaft while on-board digitally controlled electro-magnets and feedback controls are needed to actively rectify shaft misalignment due to dynamic vibration during operations [11, 12]. Additionally, portability of centrifugal compressors is also limited, mainly because they operate on multi-stage compression at high revolution per minute (RPM) with intercooling between each stage in order to achieve high compression ratio and these stages occupy large footprints.

Although there are existing small-scale portable and relatively cheaper thermoelectric cooling/heating systems on the market, their working principle is usually based on Peltier and Thomson effects [13] which can only achieve low COP ranging from 0.3 to 0.5 for cold side temperature of -7.4 to 5°C and an ambient temperature of 25 to 30°C [14–18]. Such systems are usually used for low cooling demand applications like cooler for personal comfort or cold storage of vaccine and are unsuitable for high demand applications for food and beverages storage freezing.

Positive-displacement vane type compressors are mainly used in small-to-medium scale vapour compression refrigeration system and heating applications. Namely, the well-established rotary compressors like rolling piston [19], swing vane [20], revolving vane [21] and rotary sliding vane [22] compressors are used in commercial air-conditioning and refrigerators. In comparison to other compressor types used in vapour-compression refrigeration cycle such as centrifugal compressor [9], screw compressor [23], reciprocating piston compressor [3] and scroll compressor [24], positive-displacement vane compressors offer a better reasonable balance between simplicity in design, initial cost, efficiency, size and capacity [25]. While it is simple in design with low production cost, there is currently no commercialised oil-free positive-displacement rotary vane type compressor for refrigeration purposes in the market.

In this study, a new oil-free positive-displacement vane type rotary compressor will be designed based on the swing vane mechanism due to its simplicity in

design and its high efficiency. Modifications to existing swing vane design will be made to allow the mechanism to run without oil lubrication system. Since the operating temperature of the compressor will be much higher than that of conventional oil-lubricated compressors due to the high frictional heat generated and the lack of heat removal by the oil re-circulation, failure may occur during operation. Liquid refrigerant injection cooling technique will be used in the new compressor design to address this problem. The effects and the efficiency of liquid refrigerant injection cooling on the performance of the oil-free swing vane compressor will also be investigated in this study.

1.2 Objective and Scope

The main objective of this study is to develop a swing vane compressor for operation under oil-free condition. Potential key failure modes will be identified and the performance characteristics of an oil-free swing vane compressor will be determined both theoretically and experimentally. This study also aims to test the effectiveness of liquid refrigerant injection in cooling an oil-free compressor that is operating in a vapour-compression refrigeration system. This includes the mathematical model, design, fabrication and testing of a working prototype. To achieve this, the scope of work includes:

- Conceptual design of an oil-free swing vane compressor.
- Development of mathematical model for an oil-free swing vane compressor with liquid refrigerant injection cooling.
- Design, fabrication and instrumentation of a working oil-free swing vane compressor prototype.
- Measurement and evaluation of the working prototype.
- Verification of mathematical model with measured data.

1.3 Organisation

This thesis consists of 9 chapters and 6 appendices. Chapter 1 explains the motivation, the scope and objectives of developing an oil-free compressor. This is followed by Chapter 2 which reviews relevant literature of current compressor

mechanisms used in vapour compression refrigeration systems, existing oil-free compressors, liquid refrigerant injection cooling, self-lubricating material coatings for engineering applications and some modelling studies. Chapter 3 presents the conceptual design of the oil-free swing vane compressor with elaboration on the critical design features which are designed to improve its reliability.

The theoretical models are presented in Chapters 4 to 6. Chapter 4 first presents the geometrical model which describes the volumetric variation of the compressor's working chamber throughout the working cycle which is used in the thermodynamics analysis of the state of the working fluid. This is followed by the kinematic modelling of the motions of swing vane mechanism that is needed in dynamic analysis of the compressor. Modelling of two-phase flow of injected refrigerant and liquid refrigerant injection cooling will also be explained in Chapter 4. The valve dynamic response which influences the gas discharge performance of the compressor will be presented in Chapter 5 together with the formulation of comprehensive equations describing the dynamic motion of the compressor. As internal gas leakages and heat generation in an oil-free compressor would be significant, Chapter 6 presents the analysis of internal gas leakages and the heat transfer within the compressor.

The detailed fabrication process of the entire prototype and the experimental setups will be shown in Chapter 7 with detailed explanations of the experimental apparatus and test method used for the performance evaluation of the working prototype. Chapter 8 will present the experimental findings and validation of the mathematical models. Finally, Chapter 9 summarises the findings in this study along with recommendations for future works.

Chapter 2

Literature Review

In this chapter, literature relevant to current compressor mechanisms used in vapour-compression refrigeration systems, design of existing oil-free compressors, liquid refrigerant injection cooling technique and material coatings for bearing applications will be reviewed and discussed. Theoretical studies on different compressor's mechanisms, liquid refrigerant injection cooling modelling and wear behaviour of different bearing materials under high friction rubbing will be the focus of this review.

2.1 Positive-Displacement Vane Compressors

The oil-free compressor prototype developed in this study has to undergo vigorous testing and measurement in order to determine its performance characteristics and failure modes. Seizure of compressor due to extreme wear is foreseeable, so the compressor developed has to be simple in design, easy to be reproduced and repaired. The simplicity in the design of a positive-displacement vane type compressor is most suitable for such experiments. A selected number of commercialised positive-displacement vane compressors will be reviewed in this section with attention to their mechanism designs, dynamic characteristics and potential failure modes.

2.1.1 Rolling Piston Compressor

The rolling piston compressor is made up of a piston, a vane, an eccentric which forms part of the driving shaft and a cylinder, as shown in Figure 2.1. The vane divides the working chamber into the suction and compression chambers by maintaining a constant contact with the piston under the downward force

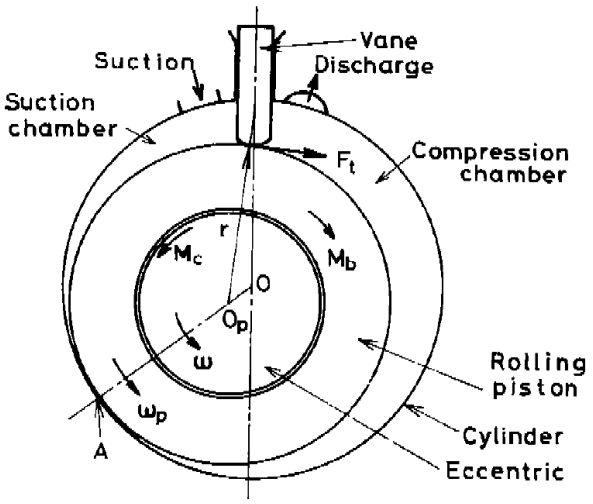

Figure 2.1: Schematic view of a rolling piston compressor [19].

provided by a spring and the vane is allowed to slide freely within the vane slot in the cylinder. The piston is mounted eccentrically on the driving shaft and the shaft is supported concentrically on the cylinder journal bearing. During operation, the driving shaft rotates the piston while the vane-piston and cylinder-piston interfaces maintained contact to separate the suction chamber from the compression chamber. This rotational motion causes the volumes bounded by the vane, the cylinder wall and piston to vary; resulting in suction, compression and discharge of the working fluid every two revolutions.

The rolling piston compressor is a matured compressor design which is widely used in small and medium scale air-conditioning applications. As seen from its schematic design, it has advantages of being compact and lightweight with low manufacturing cost and high performance as compared to reciprocating or other dynamic compressors. However, rolling piston compressor suffers from shortcomings such as high contact friction at the vane tip and rolling piston interfaces which leads to wear and tear. The severe wear between the vane and roller sliding pair has been a persistent failure cause such that many studies have been carried out to understand how vane design affects the frictional losses of a rolling piston compressor [26–29]. Tribology analysis has been conducted to understand how vane tip wears off [30, 31]. Various lubrications and surface coatings have also been tested on vane surfaces in order to improve the tribological characteristics and the compressor's mechanical efficiency [32–34]. Ooi et al. [29] have studied the effect of vane spring stiffness on rolling piston compressor and found that low vane tip-piston contact force may lead to higher piston-cylinder

and piston-eccentric frictional losses due to an increase in the angular speed of the piston. Adequate vane tip contact force is generally needed to reduce vane chattering and vane tip leakage. Liu and Kosco [28], on the other hand, studied the effect of tilted vane design on rolling piston compressor and found that the tilted vane structure has no significant effect in reducing frictional loss and in improving the mechanical efficiency. Sung [32] has studied the tribological performance of ceramic coated vane tip. It was found that coatings are required to have optimal hardness and good adhesion between coating and vane to prevent extensive break-off of the coating layer and easily shearable tribofilm-forming capability.

In general, the consensus drawn from the literature was that the vane tip-piston frictional loss is inevitable and wear rate can only be mitigated. In scenario where the rolling piston compressor operates without oil lubricant, vane tip and piston will be dry rubbing and the severity of the frictional effects will be more severe. If rolling piston mechanism is adopted in the development of an oil-free compressor, the vane tip wear and potential failure like interfacial heat fusion of rubbing surfaces have to be resolved. Coating of vane tip to prevent wear may pose difficulties in the prototype development as complex manufacturing processes such as plasma nitriding, ion plating or ion beam sputtering are needed and the cost of manufacturing will be high.

2.1.2 Rotary Vane Compressor

The rotary vane or sliding vane compressor consists of an external housing or cylinder and an internal rotor with radially or non-radially positioned vane slots, in which vanes reside (Figure 2.2). The rotor is supported eccentrically offset from the centre of the cylinder. The space enclosed by two adjacent vanes, the rotor and the cylinder wall forms the working chamber. When the rotor spins, the vanes are thrown out by the centrifugal force and maintain constant contact with the cylinder housing wall. If the compressor is oil-lubricated, a thin film of oil will seal and lubricate the vane tip-cylinder moving interface. As the rotor continues to rotate, the working chambers between adjacent vanes vary in volume; chambers beyond discharge port expands to draw in gas and chambers after intake port gradually reduce in volume, compressing the gas through the rotation until discharge of gas occurs.

Generally, sliding vane compressor with more than two compression chambers

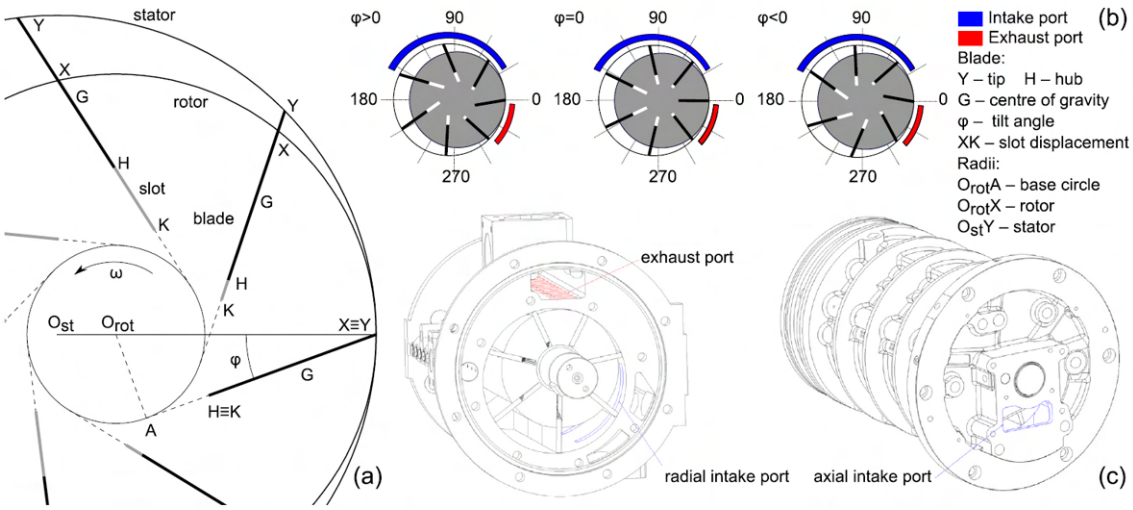

Figure 2.2: Design variations of rotary vane compressors — (a) Geometrical view (b) Schematic views of rotary vane compressor with forward tilted vanes, radial vanes and backward tilted vanes (c) Isometric view of rotary vane compressor with axial and radial intake ports designs. [35].

can achieve near-continuous suction and discharge of gas throughout the cycle with reduced noise and vibration from smaller gas pulsation. Furthermore, the rotary vane compressor does not require a discharge valve to operate. The discharge pressure is predetermined by the built-in volume ratio based on the suction process and the volume of the working chambers. This means that a rotary vane compressor will not suffer from valve losses where excess energy is not required for the overcompression of gas needed to open the valve during discharge process. This also removes the valve-fatigue issue which decreases the reliability of the compressor and also minimises the pulsating noise and vibration arising from the opening and closing of the valve.

The rotary vane compressor, however, experiences inherent vibration and vane chattering during start-up and at low rotational speed situation [36, 37]. In an ideal operation of a rotary vane compressor, the vanes are in constant contact with the cylinder inner wall and sliding on the wall at all times regardless of the rotational speed. In an experimental study conducted by Tojo et al. [37], it was found that the vane can get detached from the cylinder surface before completing a revolution during a start-up with a low back-pressure in the vane-slot and the vanes might be pulled down into the vane-slot before coming to an abrupt stop under an impact with the rotor. The vane will then slide back out again when exposed to the low-pressure gas intake side of the cylinder, impacting the cylinder surface abruptly. This detachment from and spring-back onto the

cylinder wall are the main causes to the chattering and the impact fatigue on the vanes. Furthermore, gas will leak from high pressure chamber to adjacent lower pressure chamber through the clearance between the vane tip and the cylinder wall when vanes detachment happens. This will result in lower volumetric efficiency of the compressor during the start-up. In a theoretical study of a sliding vane compressor with leakage, Al-Hawaj [38] has identified that the highest leakage losses occurred through the clearance between the vane tip and cylinder. To resolve this leakage issue caused by vane chattering, Shu et al. [36] proposed the use of appropriate constant back pressure in the vane slot to assist in pushing the vane out and ensure the constant contact of vane with the cylinder wall while minimum friction loss is achieved.

In rotary vane compressor, frictional wear occurs due to rubbing at vane sides with vane slot, vane tip with stator/cylinder and the endfaces of the rotor and vanes with the cylinder cover. Bianchi and Cipollone [35] have studied the mechanical losses in a mid-size industrial multi-vane compressor and have concluded that the rubbing of the vane tip against the cylinder wall contributes to the highest power loss since vane-tip and cylinder interface has the highest slip velocity. In their parametric studies for performance optimisation [35, 39], it was found that a lighter vane mass can help to reduce the contact force between the vane tip and the cylinder wall due to the lower centrifugal force pushing the vane onto the wall.

Similar to the rolling piston compressor, the dynamic behaviour and tribological characteristic of the sliding vane motion in a rotary vane compressor directly impact the durability and efficiency of the compressor. To adopt sliding vane mechanism in the design of an oil-free compressor, the mass, the tip profile and the material of the vane have to be assessed and designed appropriately.

2.1.3 Swing Vane Compressor

The swing vane compressor, a variant of the rolling piston compressor, was first introduced by Daikin in 1996 [40] to improve the mechanical efficiency of the rolling piston compressor. Similar to a rolling piston compressor, a swing vane compressor is also made up of a piston, a vane, an eccentric shaft and a cylinder. The vane, however, was fixed onto the rotor and allowed to slide in the vane slot in the cylinder, as shown in Figure 2.3a. In the other configuration, one side of the vane was connected to the cylinder wall via a hinge joint and the

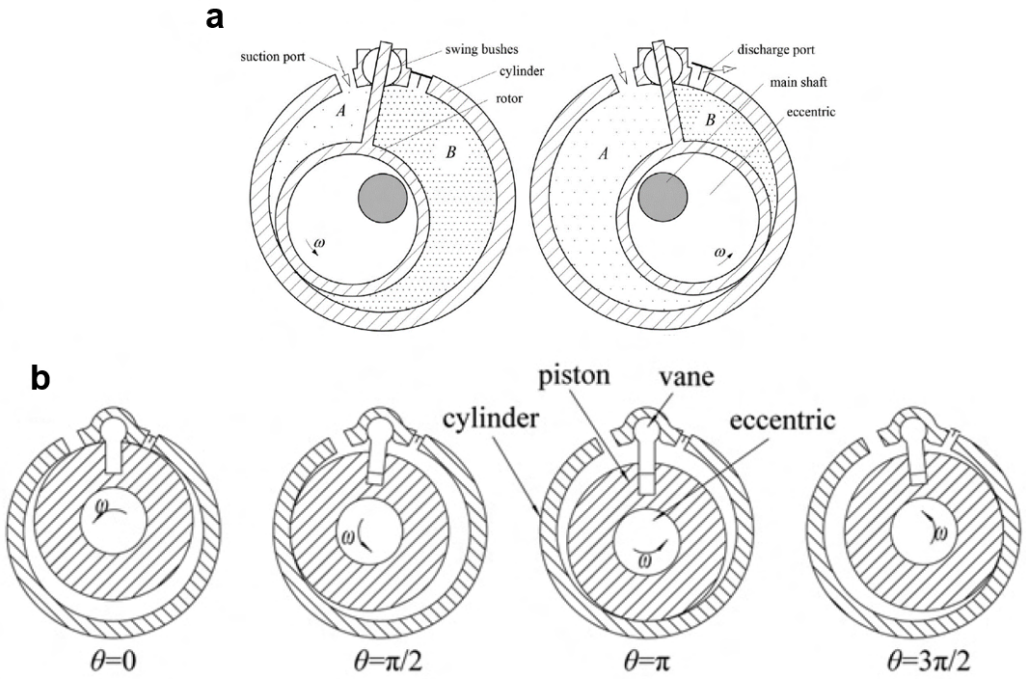

Figure 2.3: Illustration of swing vane compressors with different configurations — (a) Schematic view of the working principle of a swing vane compressor with the vane fixed on the rotor [20] (b) Schematic view of swing vane compressor with the vane connected to the cylinder via a hinge joint [41].

other end was inserted into the vane slot in the rotor, as shown in Figure 2.3b. In both designs, the new configurations eliminate the contact point between the vane tip and the piston, thereby, eliminating the frictional loss at the vane tip and improving the volumetric efficiency with no leakage at vane tip and piston interface [20, 40, 41]. In addition, the vane which divides the suction and compression chambers has a greater load bearing capacity since it is now simply-supported on both ends as compared to the cantilever-supported vane in a rolling piston compressor. The piston is also mounted eccentrically on the eccentric of the driving shaft, but it now swings about the swing bushes or the vane's hinge during operation instead of rotating about the eccentric.

Experimental studies by Masuda et al. [40] showed that the overall efficiency of the swing vane compressor was 5 to 9% higher than that for a rolling piston compressor at low to middle range speed due to reduced internal leakage and 2% higher in the high-speed range due to reduced mechanical loss. The overall and volumetric efficiencies of each compressor, swing and rolling piston, are shown in Figure 2.4.

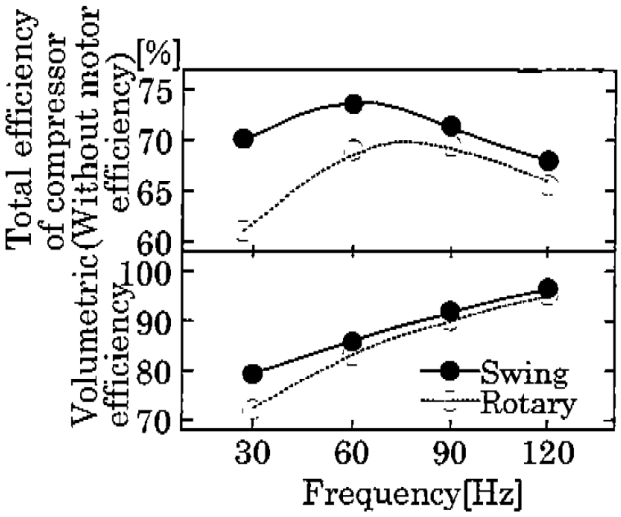

Figure 2.4: Efficiencies of swing vane and rolling piston compressors [40].

Although the overall mechanical loss in a swing vane compressor has been reduced by 3% to 4% as compared to a rolling piston compressor based on simulation, Masuda et al. [40] have found that the mechanical loss at the roller and crankshaft moving interface was generally greater in the swing vane compressor (34.5%) than that in the rolling piston compressor (31.7%), as shown in Table 2.1. This is because the roller/piston in a rolling piston compressor is pressed hard against the eccentric by the downward force from the spring and this restricts the roller's rotation relative to the eccentric. Angular speed of roller is less than 10% of the shaft speed in rolling piston compressor. In absence of oil lubrication, the swing vane mechanism is a more viable design for an oil-less compressor prototype as compared to rolling piston mechanism for its improved volumetric and mechanical efficiencies. The rotor-eccentric moving interface, however, has to be re-designed due to the relatively higher sliding velocity between the swinging rotor and rotating eccentric.

Table 2.1: Comparison of mechanical loss in swing and rotary compressors using R22 refrigerant [40].

Lubrication parts	Swing vane compressor	Rolling piston compressor
Main/sub bearing	24.1%	24.0%
Crank-pin bearing	34.5%	31.7%
Vane and roller	-	12.5%
Vane side	24.0%	26.5%
Outside of swing bush	6.6%	-
Crank thrust	6.0%	5.3%
Total losses	95.3%	100%
Comparison of the same design and same class of compressor (3/4 horsepower or 0.559kW)		

In comparison with the sliding vane compressor, Hu et al. [41] reported that the total theoretical frictional loss in the swing vane compressor (using vane configuration shown in Figure 2.3b) was only 35.87% of that in sliding vane compressor when the rotational speed was at a low range of 1000 rpm under same working condition, and it increased to 68.96% when the rotational speed was increased from 1000 to 3000 rpm. Frictional loss at vane side is the main contribution to the overall frictional loss for a swing vane compressor at low rotational speed and endface losses become the largest part of the frictional loss as rotational speed increases. For an oil-less compressor, high rotational speed is crucial for reducing internal leakage. If the swing vane compressor is used as an oil-free compressor prototype for high speed operation, special self-lubricating materials or coatings have to be employed to reduce the endface frictional loss.

2.1.4 Revolving Vane Compressor

The revolving vane compressor design was first developed by Teh and Ooi [21] in 2006 as a more mechanically efficient compressor alternative to other rotary compressors. In its basic form, the revolving vane compressor appears to be similar to that of a rolling piston compressor or a swing vane compressor; it is also made up of a rotor, a vane and a cylinder, as shown in Figure 2.5a. The rotor and cylinder are both supported on two journal bearings individually, where they rotate about their respective axis while keeping a virtual line of contact at the radial interface. The vane is attached to the cylinder wall via a pin-joint and is allowed to slide within the vane slot in the rotor while keeping the suction and compression chambers separated. During the operation, the rotor which is connected to the driveshaft rotates the vane which in turn rotates the cylinder. This rotational motion causes the volumes bounded by the vane, cylinder wall and rotor to vary; resulting in suction, compression and discharge of the working fluid. As seen from Figure 2.5b, the working principle differs from that of a rolling piston or a swing vane compressor, in which, the cylinder is now made to rotate together with the rotor instead of being fixed. This simple modification reduces all relative motion between rubbing endfaces in the compressor mechanism, thus effectively reducing the frictional loss therein.

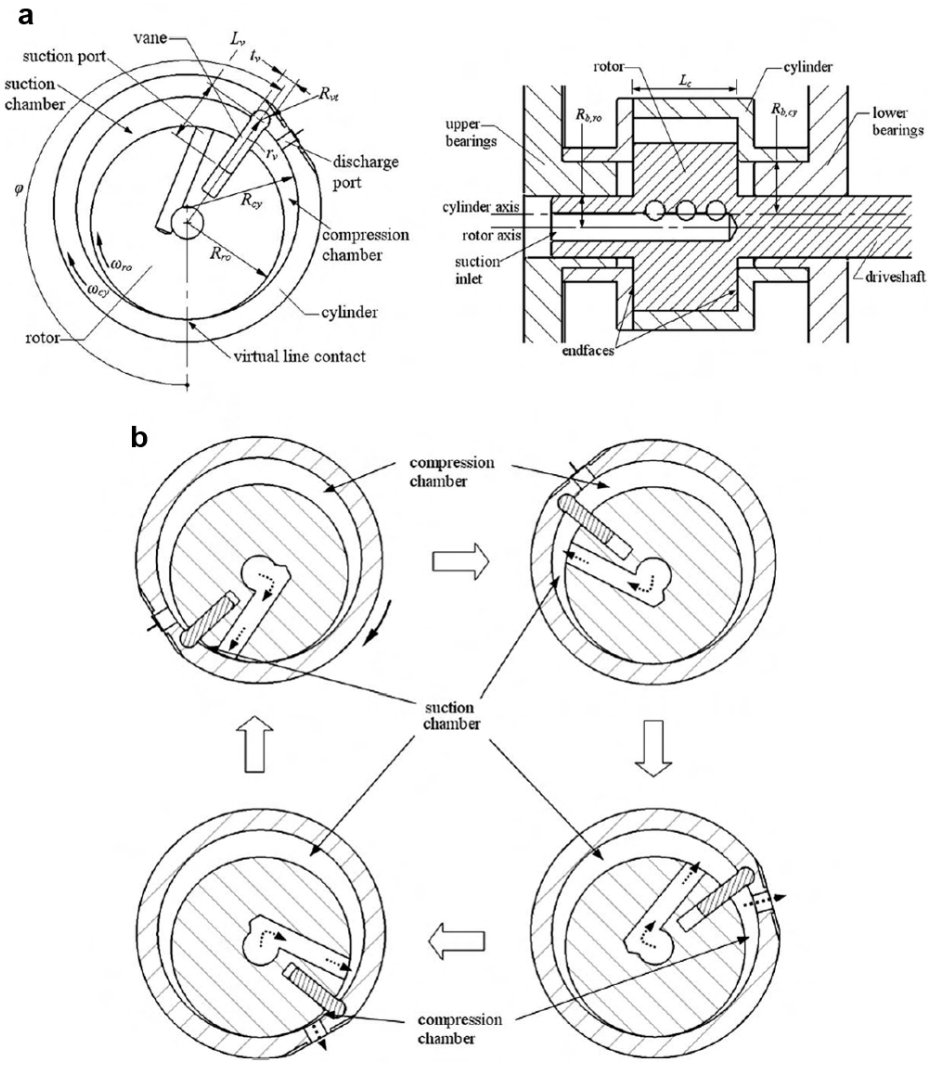

Figure 2.5: Illustration of revolving vane compressor — (a) Schematic and section views (b) Working principle [42].

An analytical study of frictional losses in a revolving vane compressor by Teh and Ooi [42] predicted that the overall frictional loss of a revolving vane mechanism was 20% less than that of a rolling piston mechanism and a 94.1% mechanical efficiency is theoretically achievable, which is above the mechanical efficiency of a rolling piston and scroll type rotary compressors (as seen in Table 2.2). The vane tip frictional loss (2.1%) is negligible as compared to that of rolling piston vane tip (16.7%) due to elimination of vane tip and rotor interface. The endface loss in a revolving vane mechanism (3%) is reduced due to smaller sliding velocities between cylinder and rotor while the roller rotates against a static cylinder endface in a rolling piston design which results in greater friction rubbing (5.8%). The shaft frictional loss in a revolving vane mechanism

Table 2.2: Comparison of frictional losses in revolving vane and rolling piston compressors.[42]

S/n	Frictional loss	Rolling piston compressor (%)	Revolving vane (%)
1.	Vane sides	32.6	39.1
2.	Shaft bearing	15.1	10.8
3.	Cylinder bearing	-	26.3
4.	Piston bearing	29.8	-
5.	Vane tip	16.7	2.1
6.	Endfaces	5.8	3.0
7.	Total	100	81.3

(10.8%) is also smaller than that in rolling piston (15.1%) due to absence of vane tip normal force. However, due to the co-rotating cylinder, a revolving vane mechanism requires an additional cylinder bearing which contributes to an additional 26.3% of frictional loss. The cylinder bearing loss in revolving vane compressor is substantially larger than that of shaft bearing because the cylinder has a large radius and, hence, larger frictional torque. This cylinder bearing loss can be effectively minimised by proper sizing of cylinder dimensions and through the use of hydrodynamic lubrication. If revolving vane mechanism is to be operated without such oil lubrication, the high frictional loss at cylinder bearing will pose a challenge to the durability of the dry compressor.

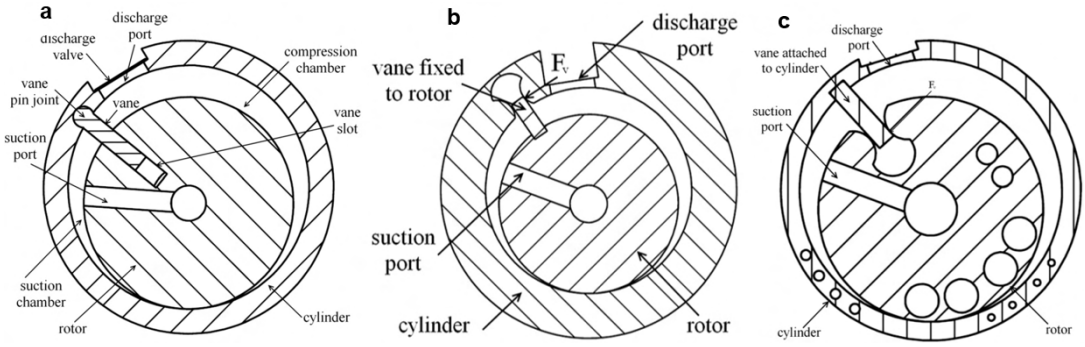

Figure 2.6: Schematic comparisons of revolving vane variants — (a) Rotor-driven with swivelling vane, b) Rotor-driven with fixed vane on driver and c) Cylinder-driven with fixed vane on driver. [43].

To further improve the mechanical efficiency of the revolving vane compressor, two variants of revolving vane compressor, namely the fixed-vane revolving vane compressor (as shown in Figure 2.6), were developed by Tan and Ooi [43] in 2011. In the first design as shown in Figure 2.5, the hinge-joint design of the vane allows swivelling and tilting motions of the vane which in turn allow high gas pressure differential force across the vane to push and tilt it in the vane slot, causing high vane-side and slot contact force. In the theoretical dynamic

analysis of fixed-vane revolving vane compressor variants by Tan and Ooi [43], the vane side frictional loss has been reduced 30% by rigidly fixing the vane to the driver-rotor (Figure 2.6b)and the mechanical efficiency has increased by 1.2%. A further 1.6% improvement in mechanical efficiency was achieved by the second variant design, as shown in Figure 2.6c, by making the cylinder that has a larger rotational inertia as the driver. Since the heavier cylinder which rotates at constant speed is being used to rotate the lighter rotor, the inertia torque and hence, the contact force to rotate the lighter rotor and the vane side friction loss are smaller (Figure 2.7).

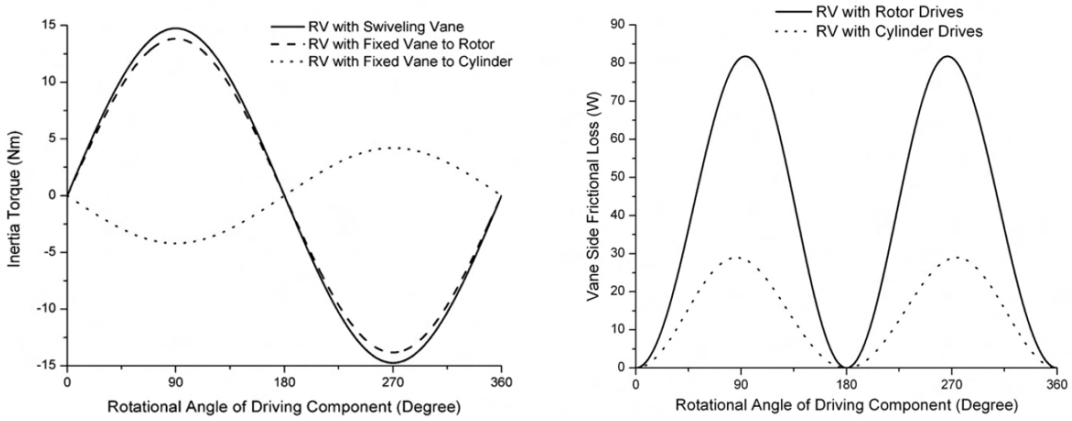

Figure 2.7: Comparisons of inertia torque and vane side frictional loss of different revolving vane compressor variants [43].

Due to the rotation of the entire cylinder in a revolving vane compressor, the discharge valve employed to regulate the discharge process also rotates together with the cylinder [44]. As a result, the rotating discharge valve is subjected not only to the net pressure of gas from compression chamber and discharge tank but also centrifugal and Coriolis forces. The dynamic behaviour of the rotating discharge valve was studied by Teh et al. using Euler-Bernoulli beam theory [44] and by Heng et al. using finite element modelling [45]. Teh et al. [44] found that the centrifugal force from the rotational motion has a 'dampening' effect of reducing valve fluttering and has helped reduce over-compression. The revolving vane compressor can be designed with stiffer valves for better reliability without over-compression issue. According to Heng et al.[45], however, it was noted that the rotating valve may experience possible overloading of centrifugal dampening when the rotational speed exceeds a designated range such that a delay in valve closure of the discharge port may result. This incomplete valve closure at the end of the discharge process will result in reversed flow from the discharge plenum

back to the compression chamber, resulting in lower volumetric efficiency of the compressor.

A revolving vane mechanism can be a viable design for an oil-free compressor with its high mechanical efficiency nature. However, its high efficiency and smooth operation are achieved due to proper lubrication of its multiple journal bearings and moving components. In an oil-free operation, more moving components means higher risk of wear and early seizure. Furthermore, the valve placement has to be re-designed to prevent backflow of discharged gas.

2.2 Oil-Free Compressors

In this section, the works on the developments of different oil-free compressors will be reviewed and presented.

2.2.1 Centrifugal Compressor

Due to the increasing global push for solutions of renewable energy, many carmakers are introducing eco-friendly hybrids and battery electric vehicles. Fuel cell electric vehicle, which is one of the highly sustainable and viable green automobile alternatives to petrol powered vehicles, is powered by the electricity generated from the fuel cells' electrochemical reaction between oxygen from surrounding air and hydrogen from the fuel tank with water vapour as the only by-product of the reaction. A compressor is a key component of this system as the intake air for the reaction has to be pressurised to increase the fuel cells efficiency. In an attempt to produce uncontaminated compressed air efficiently for a better chemically-stable reaction of the fuel cells, Ha et al. [46] from Hyundai Motor Company developed and tested a 10 kW class single stage compression lightweight centrifugal compressor with an oil-free Air Foil Bearing (AFB) system for fuel cell electric vehicle usage. The centrifugal compressor was made up of impeller shaft, a vaneless type diffuser, a volute, two airfoil journal bearings and a pair of thrust bearings. The shaft has a thrust collar designed with an Inconel sleeve to form rubbing surfaces with airfoil journal bearings during startup/shutdown phase of operation. With a single stage compression, the compressor only achieves a pressure ratio of about 1.0 – 1.4 even when operated at a speed of 100,000 rpm. Ha et al.'s measurements showed that the centrifugal compressor needs to operate beyond 7000 rpm to achieve full lift-off and contactless rotation from the AFBs. The air film thickness between the thrust top foil and collar of the

shaft was also measured and it was estimated that the minimum roughness of the thrust collar and the top foil should be designed to not more than 5 μm to ensure the hydrodynamic lubrication of the air film. From the pressure ratio achieved by the centrifugal compressor with AFB bearings, it seems that a single stage centrifugal compressor is not suitable for the development of this work since it is targeted for vapour-compression refrigeration cycle that requires high compression ratio more than 3.0. Furthermore, a typical speed of more than 7000 rpm is required for the air film hydrodynamic lubrication of AFB to work in this oil less centrifugal compressor. During startup or shutdown where rotation speed is low, contact rubbing of the shaft and bearings will demand the use of expensive, high-strength and durable material like Inconel.

For the application of mid-range cooling capacity vapour-compression refrigeration usage, Conry et al. [9] from Turbocor Incorporation has developed a 211 — 316 kW two-stage centrifugal oil-free R-134A refrigerant compressor utilising magnetic bearings and on-board digital controls, as shown in Figure 2.8. Magnetic bearing technology has been proven to be highly reliable for its applications in aerospace, precision engineering and turbo-machinery where conventional lubrications are unsuitable and where cost is not the major consideration. Conry et al. [9] has designed the compressor with only a single main moving part which was the impeller shaft that was levitated during rotation by a digitally controlled magnetic bearing system. The impeller shaft was primarily levitated by permanent magnets and digitally-controlled active magnets are used to trim shaft's vibration and movement during operation by responding to inbuilt proximity sensors that are sensitive to shaft movement of less than 1.27 μm. Overall, the compressor has measured improvement in energy efficiency through the elimination of friction losses inherent in oil-lubricated mechanical contact bearings used in conventional refrigerant compressors and improved reliability due to reduction of wear and tear. However, such compressor system (as seen in Figure 2.8) is only suitable for mid-range refrigeration tonnage such as rooftop air-conditioning, refrigeration and chillers due to its large footprint (120.2 kg, 1.022 m by 0.65 m by 0.49 m [9]).

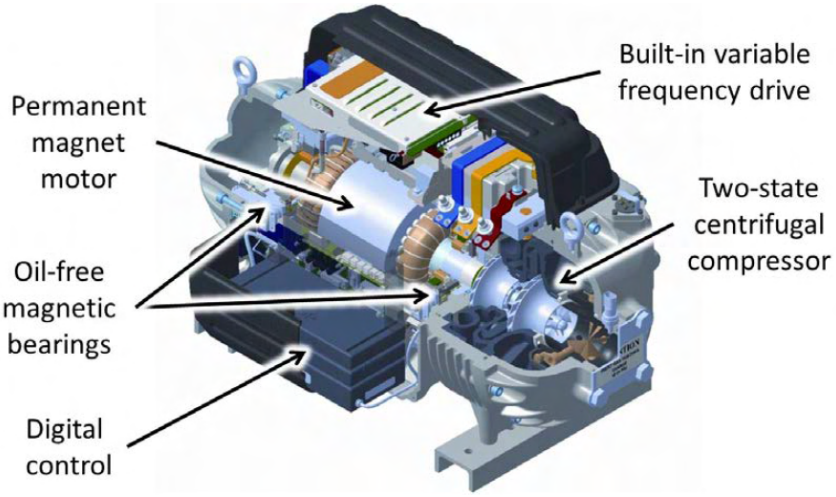

Figure 2.8: Cut-away view of the Turbocor compressor [47].

2.2.2 Scroll Compressor

Ni and Cai [48] studied the loadings imposed on the moving parts of a conventional scroll compressor and conceptualised the design of a 'floating scroll' oil-free compressor. The floating scroll mechanism was made of dual orbiting scrolls, a front and back scroll, which orbit in opposing but synchronous motion due to connecting synchroniser bearings between the scrolls that balance all pressure and centrifugal forces within orbiting scrolls. As a result, the reactional contact forces and moments are balanced and minimised, such that sealing of compression pockets was achieved with low wear rate. The volumetric efficiency of the compressor (ratio of actual flow rate to theoretical flow rate) was found to exceed 90% even when there was a lack of oil lubrication sealing [49]. Interestingly, the isentropic energy efficiency (ratio of isentropic compression work to actual shaft work) of the 'floating scroll' compressor was more than 50% and was almost constant for pressure ratios ranging from 1.6 to 2.8. This suggests that the compressor can operate under varying discharge pressure fluctuations. This concept of opposing but synchronised motion of components can be incorporated in the development of lubricant-free compressor to alleviate frictional wear issue.

2.2.3 Screw Compressor

In the oxygen supply circuit of a fuel cell system, the compressed air supplied to the fuel cell stack must be oil-free to avoid contamination of the expensive cathode with rare metal. To resolve this issue, He et al. [50] developed an

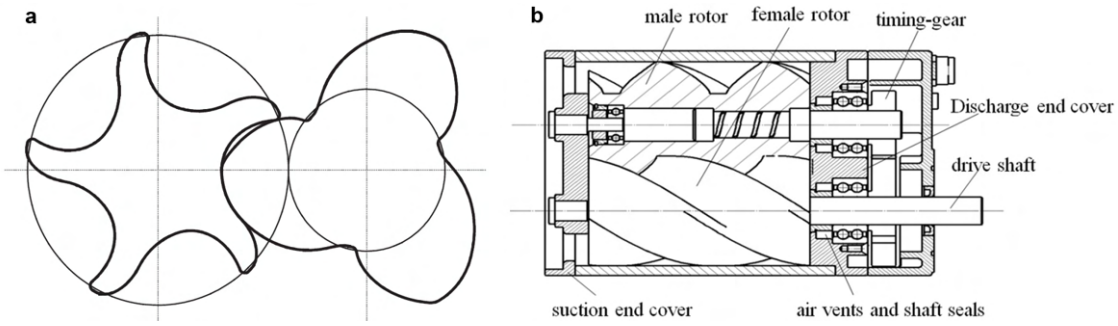

Figure 2.9: Illustrations of air-cooled dry oil-free twin-screw — (a) Profile of rotors (b) Schematic view of prototype [50].

air-cooled dry oil-free twin-screw compressor that was tested on a truck with fuel cell system. The structure of the oil-free twin-screw compressor consists of a 3 lobes male and 5 lobes female rotors with a clearance of 90 μm between them. The male and the female rotors of the compressor do not contact each other during rotation and were separated by the use of timing-gears system that coordinates the rotation of both male and female rotors. The timing-gears system is grease-lubricated and supported by oil-lubricated ball bearings which are separated from the rotors' compartment, as shown in Figure 2.9.

This allows no contamination of intake air during compression while rotors do not suffer from contact friction wear. Screw compressors generally also require high rotation speed to reduce internal leakage of gas during compression. For the oil-free twin-screw compressor, a typical high rotation speed of more than 5000 rpm is required for 140 to 220 kPa discharge pressure within 0.02 to 0.03 m^3s^{-1} volumetric flow rate. The mechanical efficiencies are also averaging between 75% to 85% for discharge pressure between 140 to 220 kPa which is considerably high and similar to that of an oil-lubricated rotary compressor.

Similarly, the design of the oil-free screw compressor for helium compression by Kitagawa et al. [51] also uses timing-gears to maintain non-contact operation between the rotors. In addition, Kitagawa et al. applied high rotational cylindrical roller bearings for radial support of the timing-gears because of its high accuracy of positioning to maintain an infinitesimal rotor-lobe clearance during operation. These bearings also require oil lubrications to work and therefore, two stage seals consisting of an oil and a gas seals were utilised in Kitagawa et al.'s design to prevent lubricant oil of the bearings from penetrating into the rotors' chamber. With the use of better roller bearing and better rotor-lobe clearance, Kitagawa et al. demonstrated that the oil-free screw compressor can

attain an isothermal efficiency of 50% for a flow rate of 125 gs^{-1} with a discharge pressure of 800 kPa and a suction pressure of 100 kPa and a suction temperature of -23.15°C via two-stage helium gas compression at 11,000 rpm and 19,000 rpm respectively with a compression ratio of 2.9 for both stages.

However, both designs are still heavily dependent on the oil lubrication of the timing-gear which maintains the rotors clearance and allow oil-free compression. Such design can only operate in the upright orientation to ensure continuous oil re-circulation and are not orientation-free and portable.

2.2.4 Linear Compressor

In a conventional reciprocating compressor commonly used for refrigeration applications, the piston is driven by an induction motor through a crank mechanism to provide reciprocating motion to compress the gas. As a result, the mechanism of the conventional reciprocating compressor has four friction contact points (crankshaft–crank, crank–connecting rod, connecting rod–piston pin and piston–cylinder) that require oil lubrication to mitigate the frictional losses and wear during the conversion of the rotary motion into an oscillatory motion. Furthermore, these oil-lubricated crank-driven reciprocating compressors have limited choice of refrigerants and operating temperature range since thermal stability and miscibility of oil-refrigerant mixture are crucial for the reliability of an oil-lubricated compressor [52]. To overcome these problems, oil-free positive displacement linear type compressor that utilises a linear motor to drive the linear motion of a piston for the compression of the working fluid has been developed and studied in recent years [53–57].

In this linear type compressor, as shown in Figure 2.10, the mechanism has only one friction point at the piston-cylinder interface due to the absence of crank and linkages and has a significantly improved mechanical efficiency as compared to that of a reciprocating compressor. According to the report by Lee et al. [59], the operation life, reliability, and efficiency of the linear compressor are at least 25% higher than reciprocating compressor. This is why this mechanism has been widely used for oil-free positive displacement type compressor. The COPs achieved by the oil-free linear compressor usually ranges from 1.4 to 3.7 for cooling load from 75 W to 458 W and pressure ratios from 2.0 to 10.0. An oil-free refrigeration linear compressor based on solenoid was built by Liang et al. [54] and the compressor had achieved a COP of 3.2 at a cooling capacity of

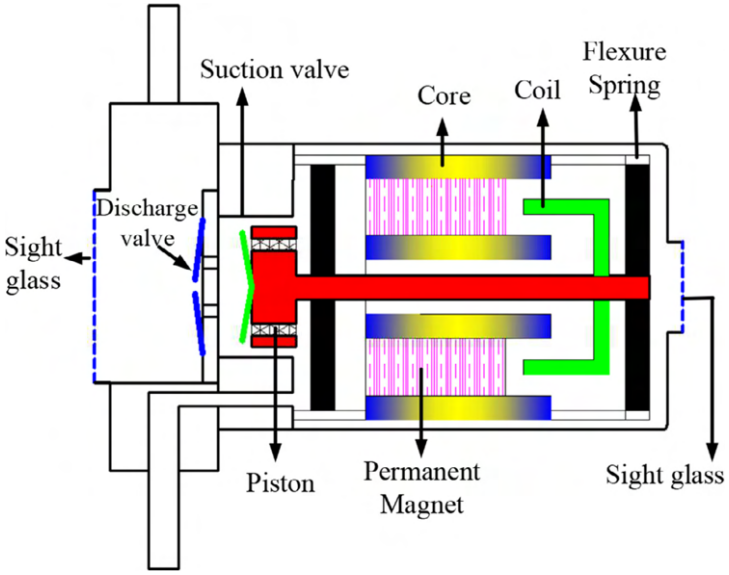

Figure 2.10: Schematic diagram of an oil-free linear compressor [58].

384 W with a pressure ratio of 2.5 and a condenser temperature of 54°C and an evaporator temperature of 20°C using R134a. Jomde et al. [55], on the other hand, reported a COP of 1.4 at a condenser temperature of 54°C, an evaporator temperature of -20°C and a pressure ratio of 10.0 with a low cooling capacity of 134 W. The maximum COP achieved at a condenser temperature of 54°C and an evaporator temperature of 2°C and a pressure ratio of 4.0, was 2.13 with a cooling capacity of 325 W.

These linear compressors, however, are more commonly designed for refrigerator usage with low cooling capacity and not for air-conditioning (typically 1 to 6 kW cooling capacity). For larger cooling capacity, the number of coil springs needed for resonant operation in order to minimise the drive current and ohmic losses of the linear motor will increase and the size of the solenoid will be much larger [52]. Efficiency of the linear compressor with such higher power output and greater fabrication cost and larger dimension makes it less attractive for large scale refrigeration applications [52, 60]. Another main limitation of a linear compressor is the cost since linear motor requires more rare earth materials and tighter tolerance for the fabrication of piston-cylinder clearance [52]. In addition, linear compressors typically has lower volumetric efficiency than the reciprocating crank-driven compressor as a result of larger clearance volume to avoid collision between the cylinder head [54].

2.3 Liquid Refrigerant Injection Cooling

Liquid refrigerant injection has been a cooling technique used in vapour-compression cycle to lower extreme high discharge refrigerant temperature and the overall temperature of the compressor system unit in order to prevent chemical degradation of oil-refrigerant mixture and thermally-induced mechanical failure [61–63]. This method seems viable in the development of an oil-free compressor where overheating and thermal expansion of moving parts are foreseeable problems. In this cooling technique, a small quantity of liquid refrigerant is channelled from the outlet of the condenser and injected into the compressor at the early stage of the compression process when the pressure of the injected refrigerant is still higher than that of the vapour in the compression chamber. The chamber temperature is then lowered after the liquid refrigerant undergoes vaporisation with the heat absorbed from existing chamber gas, as illustrated in Figure 2.11.

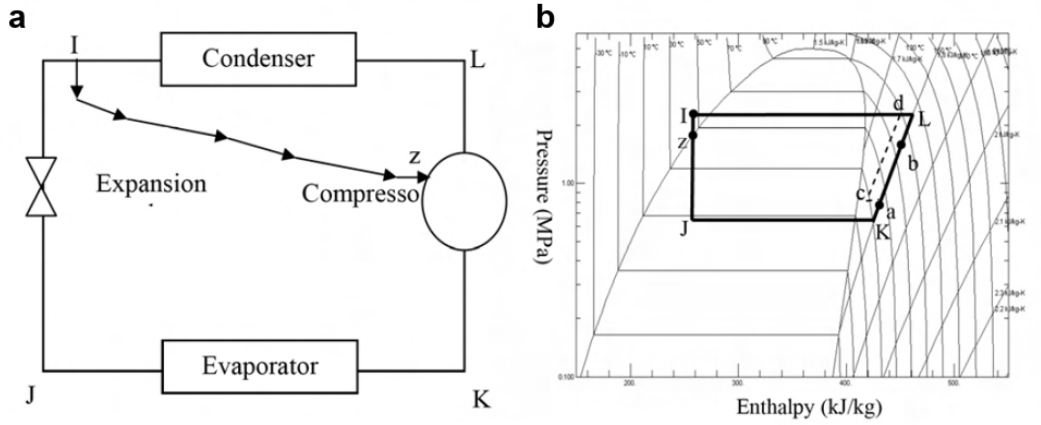

Figure 2.11: Illustration of liquid refrigerant injection method — (a) Schematic of a vapour compression cycle with liquid injection (b) p-h diagram of vapour compression cycle with liquid injection [61].

Ooi [61] has simulated the effects of liquid injection on the performance of a rolling piston compressor using R22 refrigerant under varying injector orifice diameters and injection positions conditions at evaporating and condensing conditions of 7°C, 635 kPa and 55°C, 2170 kPa, respectively. In his vaporisation model of the injected liquid refrigerant, Ooi assumed instant vaporisation of the liquid and the resultant thermodynamic state of the chamber vapour was numerically iterated with the enthalpy of the instantaneous amount injected. The mass flow rate of the liquid refrigerant injected was modelled as flow through an orifice with the assumption that no vaporisation occurs across the orifice

and the refrigerant flow remains as subcooled or saturated liquid state until vaporisation occurs when the liquid is exposed to the chamber gas. However, Ooi [61]'s assumption might not be appropriate because in real operations, drastic pressure drop of the injected refrigerant would occur during its flow from the condenser to the injector and across the injector's orifice. These subcooled or saturated liquid refrigerant would have expanded into saturated mixture in reality and two-phase flow will result even before injection and vaporisation process in the chamber. It would be more practical to simulate the flow from the condenser to the injector as a two-phase refrigerant mixture since the liquid refrigerant would have undergone flashing in practice due to the drastic pressure drop across the injector.

Ooi [61] has found that, apart from lowering the overall discharge temperature, liquid refrigerant injection of up to 27% of the compression chamber mass does not seem to affect the chamber pressure and does not increase the required power input to the compressor. A 30 to 60 degree reduction in discharge temperature without significant pressure change is achievable ideally. The theoretical results also showed that earlier liquid injection reduces discharge temperature and hence, overall temperature of compressor system more significantly than injection at later stage of compression, as greater mass of liquid refrigerant can be injected.

Dutta et al. [62] have theoretically analysed the effect of liquid refrigerant on the performance of a scroll compressor. In their analytical modelling of the heat transfer and vaporisation process of the atomised liquid refrigerant in the chamber, the vaporisation duration of the liquid injected was not modelled to be instantaneous and the amount of vaporised refrigerant was obtained by solving the energy equations for both the chamber vapour and the liquid refrigerant in each time step with consideration of heat transfer from high temperature chamber vapour to the liquid refrigerant droplets. Furthermore, heat transfer effect between the cylinder wall and the injected flow during injection process was also taken into consideration and the heat transfer coefficient was obtained from the Dittus-Boelter correlation for heating of turbulent pipe flow [64].

Yamazaki et al. [63] from Mitsubishi Corporation, Japan have also applied the use of liquid refrigeration injection in a R134a scroll compressor to lower the discharge gas temperature in order to prevent oil degradation. Instead of the complex vaporisation analysis method by Dutta et al. [62], as shown in Figure 2.12a, Yamazaki et al. predicted the compressor's performance under liquid refrigerant injection using a simpler vaporisation model similar to Ooi

[61] where the liquid refrigerant was assumed to evaporate immediately after injection and to be mixed uniformly with the chamber vapour (Figure 2.12b). The resultant thermodynamic state of the chamber vapour takes the enthalpy of the entire injected mass into consideration. Using this simple vaporisation modelling, Yamzaki et al. compared the decrease in discharge gas temperature and power consumption at different injected mass ratio (injected mass flow rate normalised by suction mass flow rate) between simulation and experimentally measured results. The results were found to be in close agreement with the accuracy of the power consumption within a discrepancy of approximately 3%. The simple vaporisation modelling seems to be able to predict the compressor's performance under the effect of liquid injection accurately with a shorter calculation time.

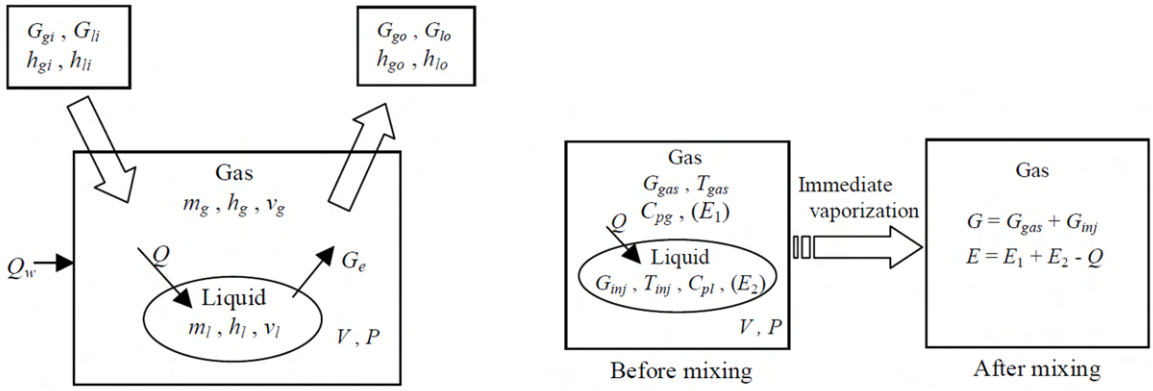

Figure 2.12: Analysis model of the liquid refrigerant injection — (a) Dutta et al. [62] (b) Yamazaki et al. [63].

If liquid refrigerant injection is utilised in the cooling of the oil-free compressor prototype, an injector mechanism has to be designed for precise timing of the opening and closing of injection orifice for accurate liquid injection at suitable chamber condition. The injector orifice, position and duration of injection also have to be optimised.

2.4 Material Coatings for Bearing Applications

To reduce friction and wear in an oil-free compressor, special material coatings may have to be employed in the design of journal bearings or even applied on bearing surfaces of moving parts. This section will review some self-lubricating materials with good tribological properties that are commonly used for mechanical bushing applications and are commercially available.

2.4.1 Polytetrafluoroethylene (PTFE)/Teflon and Composites

Polytetrafluoroethylene (PTFE) or Teflon is a useful self-lubricating material with low coefficient of friction (typically μ — 0.075 to 0.3 [65]) when rubbed against metallic bearing surfaces, and it exhibits excellent chemical resistance against corrosion and has high thermal stability [66–68]. Furthermore, PTFE is widely available and is not expensive. The low friction coefficient of PTFE has been attributed to its wear mechanism. In dry sliding conditions, it was observed that thin films and fibres are drawn out from the bearing surface of the PTFE to form lubricating transfer layers for contacting surfaces to slide on [69]. However, this wear mechanism which has contributed to the low friction coefficient of PTFE, also results in its low wear resistance [70]. Pure PTFE is usually used in low-speed and low load applications; it is usually used as a thermal or electrical insulation sheath or low-pressure gasket as this excessively high wear rates of pure PTFE often lead to early failure in high-load bearings and leakage in seals for high pressure connectors.

To improve the wear resistance of pure PTFE, filler materials are added to the PTFE polymer matrix to reduce the wear rate. The additions of inorganic and some organic fillers have been found to reduce wear rate by a factor of 100 or more [71, 72]. Some fillers commonly added are carbon in form of graphite, copper monosulfide, molybdenum disulfide, trilead tetroxide or aluminium oxide. Although filler materials improve wear rate of PTFE composites, they are also found to increase the friction coefficient of the composite. For example, graphite as a filler reduced the wear rate of PTFE by about a factor of 100 while the coefficient of friction is increased to 0.44 from unfilled coefficient of 0.35 at a testing condition of 39N normal load and sliding speed of 4.9 ms^{-1} [71]. In contrast, some fillers such as CuS can provide an equally large reduction in wear rate without an increase in the coefficient of friction.

However, the ease of forming wear particles and fragments from the PTFE might be a cause for concern if it is used as a bearing inside a compressor. These fragments might get lodged in the compressor or heat exchange components of the vapour-compression cycle overtime and may cause jamming, choked flow or reduction in heat exchange efficiency.

2.4.2 Polyetheretherketone (PEEK)

Because of its excellent mechanical strength, high stiffness and high wear resistance with reasonably low friction coefficient (typically μ — 0.3 to 0.5 [73]), polyetheretherketone (PEEK) is often an alternative material to various metallic components such as seal rings, transmission gears, bushings, sliders and bearings where PEEK is rubbed against a metal counterface. Compared with PTFE which has a general melting point of 327°C [74] and a tensile strength of 26.89 MPa [75], PEEK has a melting point of 343°C [76] and a tensile strength of 96.53 MPa [77]. PEEK, in general, has the same thermal stability as PTFE but it has a much higher wear resistance than PTFE.

Addition of fillers are also done to further improve its wear resistance. Voss and Friedrich [78] have studied the wear behaviour of short-fibre-reinforced PEEK composite and found that the addition of carbon fibres generally enhances the sliding wear resistance of PEEK better than glass fibres where wear mainly occurs in carbon fibre reinforced PEEK by thinning and breakage of fibres with reduced fibre pulverisation and formation of large wear particles. Schelling et al. [73] has investigated the friction behaviour of PEEK composite under dry reciprocating movement to assess its performance for use in a dry compressor and have found varying friction coefficients at different reciprocating speed and contact pressures. It was found that friction coefficient of pure PEEK drastically increases with interface temperature between pure PEEK and stainless steel with friction coefficient went as high as 0.55 at 120°C even at low speed of 0.6 ms^{-1}. This increase in friction coefficient is due to 'scuffing' or the transfer of irregular and thick polymer on counter sliding surface which leads to rubbing of similar material [79]. PEEK with graphite fillers, PTFE additives or short carbon fibres were concluded to be more suitable for high sliding velocities as friction coefficient and interface temperature of the composite are always lower than that of the pure PEEK.

To this end, PEEK composites do show promise as a suitable bearing material for oil-free compressor. However, in most tribology literature for PEEK, the testing conditions are not exactly similar to the normal operating condition of a compressor. The highest tested sliding velocity is often in the range of 0.1 to 2.5 ms^{-1} [73] whereas a generic household compressor can easily experience a sliding speed of more than 9 ms^{-1} at the endface of radius 30mm and under 3000 rpm.

2.4.3 Polyamide and Composites

Polyamide or nylon polymers is also widely used as surface coatings for its low friction coefficient and high strength-to-weight ratio. It also offers the ease of manufacturing with its thermoplasticity for polymer shape casting. However, pure polyamide polymer such as polyamide 66 generally has lower thermal stability and glass transition temperature as compared to PEEK; polyamide 66 gets softer and deflects easily under a load of 1.8 MPa at 85°C as compared to that of PEEK at 152.22°C based on ISO 75-1/-2 test method [77, 80]. Fillers like glass fibre [81], ultra-high molecular weight polyethylene (UHMWPE) and PTFE additives have been known to provide substantial improvements in mechanical and thermal properties of polyamide at a relatively low cost [82].

Byett and Allen [82] has tested the dry sliding wear behaviour of polyamide 66 under normal loading of 0.22 MPa and 1.09 MPa at 0.33 to 0.4 ms^{-1} sliding speed using pin-on-plate tester and found that polyamide 66-PTFE composite has shown to have the best overall wear performance with friction coefficient ranging from 0.1 to 0.2. Tensile strength has also shown improvement with increasing glass fibre composition.

Generally, polyamide polymers are commercially available and much cheaper than high performance engineering plastics such as PEEK. One disadvantage of polyamide polymer, however, is that it is sensitive to water moisture in the working environment (0.6% water absorption, 24 hour immersion ISO 62 test [80]). Moisture absorption is an undesirable trait for a bearing material as moisture will cause swelling and warping of material. This makes polyamide less attractive as a lubricating material in an oil-free compressor design especially dimensioning and clearances are important in ensuring no mechanical interference during operations.

2.4.4 Aluminium Bronze Alloy

Copper-aluminium-iron alloy or aluminium bronze alloy has been widely used in heavy industrial and marine applications as bearings and bushings due to its high strength, corrosion and wear resistance properties [83]. The friction coefficient of aluminium bronze under normal loading and sliding against mild steel is generally within 0.01 to 0.25 under greased or oiled conditions [83, 84]. Aluminium bronze alloy is usually strengthened with nanoparticles of aluminium oxide, titanium dioxide [85] or higher composition of iron and nickel [86] as it

was found that these oxide dispersions strengthened alloys or iron-nickel enriched copper alloys tend to have higher elevated thermal stability, increased hardness and improved creep resistance which are properties more suitable for dry sliding applications [87, 88].

Ajeel et al. [85] have investigated the wear resistance of aluminium bronze alloy (Cu — 7.7wt%Al) reinforced by Al_2O_3 and TiO_2 nanoparticles under dry sliding condition on ball-on-disc tribometer and found that microhardness of aluminium bronze alloy (Cu — 7.7wt%Al) increases from microhardness value of 166.1HV to 227.6HV with the presence of 3 wt% each of Al_2O_3 and TiO_2 nanoparticles in the alloy matrix with respect to copper composition. In addition, the wear rate of aluminium bronze alloy has decreased from high wear rate of $6.79 \times 10^{-7}\,\mathrm{gcm}^{-1}$ to $1.17 \times 10^{-7}\,\mathrm{gcm}^{-1}$ with the addition of 3 wt% each of Al_2O_3 and TiO_2 nanoparticles under the wear testing conditions of 20 N normal force, sliding speed of 0.16 ms^{-1}, sliding distance of 100 m and 20 min test duration. Under Scanning Electron Microscope of surface morphologies, it was found that the harder nanoparticles help form grooves on rubbing surface which prevent the delamination of the aluminium bronze matrix and the occurrence of abrasion wear. However, adhesive wear, which is a type of wear due to localised bonding between contacting solid surfaces [89], was observed in both aluminium bronze alloy and reinforced alloy even at low rubbing speed of 300 rpm with dissimilar material 100 Cr6 martensitic bearing steel and material transfer between two surfaces or loss from either surfaces was observed. This suggests that friction coefficient might increase over time under prolonged duration of dry rubbing as material transferred to the counterface might lead to adhesion between similar materials. If aluminium bronze alloy is used in dry compressor testing, seizure occurrence might increase overtime with adhesive wear between the alloy and the steel moving parts.

Dry sliding wear behaviour of aluminium bronze alloy enriched with iron and nickel was also studied by Simsek et al. [86]. Wear tests were performed using a block-on-ring wear testing device with 0.2 ms^{-1} sliding velocity, four different sliding distances (400 – 1600 m) and three different loads (10 N, 20 N and 30 N) and it was found that increasing the iron content increases the hardness of aluminium bronze with the highest hardness value of 55.74 HV observed. Generally, iron and nickel enriched aluminium bronze has lower hardness as compared to aluminium bronze strengthened with nanoparticles, comparing with results from Ajeel et al. [85]. However, iron and nickel enriched aluminium

bronze has a much lower friction coefficient of 0.02 to 0.04 under approximately similar testing conditions.

A summary table of the characteristic properties of each self-lubricating material reviewed in Section 2.4 is presented in Table 2.3.

Table 2.3: Summary of the characteristic properties of various commercially available self-lubricating materials.

Material	Friction coefficient	Melting point, °C	Characteristics
PTFE	0.075 — 0.3	335	Very low friction coefficient. Exhibits excellent chemical resistance against corrosion and has high thermal stability. Very low wear resistance with ease of forming wear fragments.
PEEK	0.3 — 0.5	340	Excellent mechanical strength, thermal stability, chemical resistance. Has high stiffness and high wear resistance with reasonably low friction coefficient.
Polyamide	0.1 — 0.2	214	Has reasonably low friction coefficient with high thermoplasticity for ease of polymer shape casting. Generally cheaper than PEEK and PTFE. Low thermal stability and glass transition temperature as compared to PTFE. Prone to swelling and warping due to moisture.
Aluminium bronze alloy	0.02 — 0.7	1038	Widely used in heavy industrial and marine applications as bearings and bushings due to its high strength, corrosion and wear resistance properties. Prone to adhesive wear which causes localised bonding between contacting solid surfaces.

2.5 Theoretical Modelling and Simulation Studies

In this section, various experimentally verified theoretical models and simulation studies that are relevant for a comprehensive theoretical analysis of an oil-free compressor, including two-phase orifice flow model, leakage model for rotary compressor and heat transfer model will be presented. Limitations and assumptions of each model will be discussed.

2.5.1 Two-Phase Orifice Flow Model

As pressure drops along the flow of liquid refrigerant from the condenser to the injector and across the injector nozzle during liquid refrigerant injection, flashing of the subcooled or saturated liquid flow may result and two-phase saturated mixture should have been injected in the compression chamber in reality. Modelling of the two-phase refrigerant flow is critical to the analysis of liquid refrigerant cooling as the extent of cooling is dependent on the mass flow rate of the two-phase saturated mixture and the quality of liquid refrigerant injected.

The flash vaporisation behaviour and the formation of two-phase refrigerant flow through the injector orifice due to pressure drop is very similar to the transient development of two-phase flashing propellant flow inside a pressurized metered dose inhalers (pMDI), including the heat transfer mechanism and the thermo-fluid dynamics of momentum and mass transfer between the liquid and vapour phase. Furthermore, the inhalers normally use non-ozone depleting hydrofluorocarbon and haloalkane or refrigerant as drug propellant. This means that two-phase flow models that are validated for pMDI's propellant flow during drug dispersion can be used to model the flow during liquid refrigerant injection. Generally, two-phase flow across orifice is a transient process and its flow characteristic is affected by metastability of the fluid, fluid properties, orifice structure and complex aerodynamic atomisation mechanism. However, simple conceptual models of two-phase flow have shown to give satisfactory predictions of mass flow and spray velocity in some works [90–92]. In general, there are three extreme scenarios of two-phase flow interphase phenomena through orifice (Figure 2.13), namely, Homogeneous Frozen Model (HFM), Homogeneous Equilibrium Model (HEM) and Slip Equilibrium Model (SEM) [90].

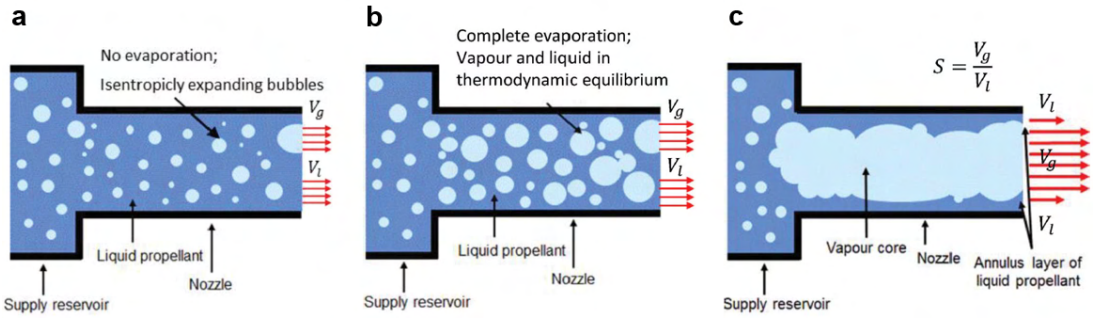

Figure 2.13: Schematics of two-phase flow through orifice — (a) HFM (b) HEM (c) SEM [90].

For HFM and HEM models, as shown in Figure 2.13a and b, the vapour and liquid phases formed during flashing flow are assumed to be interpenetrating continua and the phases flow with the same velocity through the orifice. However, in the HFM model, there is no phase change across the orifice and hence, vapour quality of the two-phase mixture remains constant even when pressure changes. For HEM model, the liquid refrigerant/propellant is assumed to evaporate and reach thermodynamic equilibrium as the flow expands across the orifice. In SEM model (Figure 2.13c), the flow is modelled as an annular liquid film along the walls of the nozzle surrounding a vapour core. Similar to HEM, the flow is assumed to be at thermodynamic equilibrium at orifice exit. However,

the phases are travelling with different velocities characterised by velocity slip ratio (ratio of vapour velocity to liquid velocity). Predicted flow velocity in the near-orifice region was directly related to the amount of evaporation. To verify the prediction of each model, results calculated were compared with Phase Dopple Anemometry (PDA) flow velocity measurements of Myatt et al. [93, 94] using propellant/refrigerant HFA134a/R134a and HFA227. It was found that the prediction by HFM model was generally closer to the PDA data and this agreement of HFM with data suggests that the two-phase flow across orifice is generally non-equilibrium in nature and thus, the vapour quality of the flow should be 'frozen' at that instant. The flow will be emerging from the orifice as metastable fluid. HFM model should be viable to predict the transient spraying process in the compression chamber.

2.5.2 Leakage Models

Generally, all compressor types suffer from varying degrees of internal leakages that reduce the volumetric efficiency of a compressor. There are three methodologies commonly used in the modelling of internal leakage of compressor's working fluid, namely, modelling leakage points in a compressor as an isentropic orifice flow [95], hybrid models using correlations obtained from regression analysis of experimental datasets and compressible flow model assuming adiabatic and frictional flow [96, 97]. Depending on the design of each compressor and the nature of each leakage path, leakage flow characteristics may differ at different leakage paths and require different modelling methods.

Leakage of pressure-driven fluid between suction and compression chambers of a compressor through converging points such as the radial clearance at the rotor-cylinder interface in a rolling piston or swing vane compressor can be modelled by assuming isentropic steady state flow of compressible fluid through a nozzle. Such a method requires the calculation of an effective cross-sectional flow area of the theoretical nozzle. The effective flow area is usually dependent on machining tolerance of the compressor or operating conditions like pressure ratio of discharge and suction that causes dynamic movement of leakage clearances. In Chen et al.'s [95] mathematical modelling of a scroll compressor, the effective flow area for radial leakage was formulated to be varying with pressure ratio between adjacent chambers and constants based on machined surface finish, whereas Cho et al. [98] uses a constant effective flow area based on the dimension

measurement of the machined clearance in their theoretical calculations of radial leakage in scroll compressor. In addition, this method also requires the use of the flow coefficient to account for losses due to irreversibility and non-ideal conditions of the actual flow. Flow coefficient, in general, is empirically determined based on experimental results and/or computational simulations and is usually limited in its use to predict leakage flow for other compressors with different dimensions, machined surfaces or operating conditions. Cho et al. [98] obtained the flow coefficient for a radial leakage based on experimental results with assumptions of negligible axial leakage and suction heating effect and determined the coefficient to be 0.11 for radial clearance of 10 μm and 60 μm. However, no further verification with experimental values at different clearances and other operating conditions were done. Also, overall experimental values are affected by other leakages and various effects of operating conditions and so flow coefficient derived based on one leakage point might be inaccurate. Kim et al. [99, 100], on the other hand, developed a functional formula of flow coefficient based on experiments and CFD simulation with various flow area, pressure ratio and temperature conditions considered. The flow coefficient calculated from the functional formula showed good agreement with Yanagisawa and Shimizu's [97] experimental values with 3 to 9% error.

To include the effects of compressibility of gas, some works has modelled the flow as compressible flow. Pandeya and Soedel [96] modelled the leakage flow through radial clearance and vane tip clearance of a rolling piston compressor as an ideal and adiabatic compressible flow through a convergent-divergence nozzle. Modelling the exiting flow into the suction chamber as a diverging guided flow, however, might be inaccurate as the flow might expand and decelerate abruptly when the flow passes the converging point. To model an unguided exiting flow with the effect of fluid viscosity, Yanagisawa and Shimizu [97] has modelled the radial clearance leakage flow in a rolling piston compressor as an ideal and adiabatic compressible flow through a convergent nozzle and as a Fanno flow as the flow exits through a straight channel where viscous drag was accounted for. In addition, Yanagisawa and Shimizu [97] included the effects of dynamic change of clearance. Their model was able to predict the experimental leakage values at subcritical and choked flow conditions with close agreement and has proven consideration of viscous drag in leakage prediction indispensable.

These studies on internal leakage of compressors, however, were verified against experimental values that are obtained from the testing of oil-lubricated

compressors. This means that the flow characteristics, flow coefficient and effective flow areas derived in these modelling are implicitly influenced by the sealing effect of oil lubrication or the incompressibility of the oil and working fluid mixture. Practicability and accuracy of using current verified leakage coefficients from rotary compressor for the prediction of the internal leakage in an oil-free compressor might be low. A similar theoretical model can still be used for analysis of oil-free compressor, but leakage flow coefficient has to be empirically determined after experiments. Furthermore, existing modellings on oil-lubricated compressor have assumed that the leakage flow is a continuum at equilibrium. However, given the small dimensions of these leakage clearances, a rarefied flow of working fluid can occur especially in an oil-free compressor where working fluid is purely in gaseous form unlike the liquid oil-gas mixture in an oil-lubricated compressor [101]. When the length scale of a flow approaches the mean free path of the working fluid, the gas flow starts to deviate from the equilibrium continuum regime and non-equilibrium phenomena such as viscous slip between the fluid and solid boundaries will occur, and they cannot be predicted by the classical fluid-mechanics continuum assumptions. Such flow characteristic is measured by Knudsen number $Kn = \frac{\lambda}{L}$, where λ is the mean free path between gas molecules and L is the characteristic length of the fluid flow. Continuum assumption-based models become invalid when describing flows at large Knudsen numbers, typically $Kn > 0.001$. In the slip flow regime, $0.001 < Kn < 0.1$, which is the most frequently encountered condition in current microchannel applications like leakage flow in clearances of compressor, the velocity slip and temperature jump at the gas–solid boundaries need to be taken into account [102, 103]. Silva et al. [101] has conducted an experimental study on the viscous slip flows of refrigerant R134a and R600a through microtubes of dimensions (diameter = 438.6 μm, length = 92.22 μm and diameter = 444.17 μm, length = 92.44 μm) in the order of micrometres typical to clearance gaps found in compressor. The Knudsen numbers measured for both R134a and R600a flow through microtubes due to pressure difference are found to be in the order of 10^{-2}, ranging from 0.04 to 0.05, under pressure ratio of 1.1 to 6.5. This shows that rarefaction effects can occur even in such gases of complex polyatomic refrigerant molecules. Guo et al. [102] conducted numerical and experimental studies of air flow in microchannel (hydraulic diameter = 151.7 μm and length = 127 μm) under pressure ratio of 1.76 to 20.0 and found that the Knudsen numbers are in a range between 0.022 to 0.064. This suggests that

leakage flow simulated using the existing isentropic nozzle or compressible flow might even be lower than experimental measurements of an oil-free compressor since rarefied flow is possible in an oil-free clearance.

In general, the literature shows that there are various methods to model different leakage flow depending on the design of the compressor and nature of the leakage clearance. Most models are limited by the isentropic assumption based on continuum models. Applications of such models may require the use of corrected leakage coefficient based on test results of oil-free compressor in order to account for greater leakage due to slip flow and rarefaction effects.

2.5.3 Heat Transfer Model

High-temperature thermal expansion and failure have significant influence on compressor reliability, particularly that of an oil-free compressor. The understanding of heat transfer and temperature distribution of components in a compressor helps improve compressor's performance in determining high heat transfer region susceptible to thermal failure and in determining better material selection [104]. Analysing how the heat transfer between working chambers also helps in better designing the geometry of compressor components in preventing overheating of fluid which requires higher power compression. A comprehensive analysis of heat transfer in a compressor involves the compressor dynamics, mechanical losses, thermodynamic analysis of gas compression and determination of the heat transfer coefficient for various interfaces of the compressor.

To determine heat transfer coefficients at different parts of the compressor, empirical correlations based on dimensionless characteristic parameters that describe fluid behaviour in the compressor have been formulated and are corrected with empirical coefficients that are derived from experimental results. Adair et al. [105] studied the instantaneous heat transfer rates between the working fluid and the cylinder wall of a reciprocating refrigerating compressor and developed a correlation for the Nusselt number that describes the average conductive heat transfer at the fluid-surface boundary of the cylinder wall, as shown in Equation (2.1). Their model was based on other correlations developed by Woschni [106], Annand [107] and Lefeuvre et al. [108] for the internal combustion reciprocating engine. The Reynolds number used in equation (2.1) was based on the characteristic swirl-velocity of chamber gas due to piston and crankshaft

motion.

$$Nu = 0.053(Re)^{0.8}(Pr)^{0.6} \tag{2.1}$$

As correlations and heat transfer coefficients are usually experimentally fitted using regression analysis, different correlation constants were formulated in various works based on their testing conditions. Liu and Zhou [109] presented a different experimentally-derived correlation for heat transfer between cylinder wall and working fluid in a reciprocating compressor, as shown in Equation (2.2), using a different swirl-velocity expression to describe in-cylinder gas motion. The temperature distribution on the cylinder wall was first measured at different pressure ratios, different suction conditions, operating speeds and lubricating oil temperatures. The correlations were then obtained using the least square method.

$$Nu = 0.75(Re)^{0.8}(Pr)^{0.6} \tag{2.2}$$

Tan and Ooi [110] studied the effect of heat transfer on the pressure variations in the compression chamber of a revolving vane compressor using correlations presented by Adair et al. [105], Annand [107] and Liu and Zhou [109] found that the correlation presented by Liu and Zhou [109] gives the best compression chamber pressure prediction, with discrepancies between predicted and measured results ranging from 1.3% to 1.6% for all tested operating conditions.

As heat transfer coefficients and correlations for compressors are not widely verified due to the need for complicated experimental setup, Fagotti et al. [111] have assessed the accuracy of various heat transfer correlations [105, 107, 109, 112–114] by comparing the predicted results of isentropic efficiency, cooling capacity and overall power consumption for gas compression with experimentally measured data. It was found that there was no best-fit correlation model for predicting all aspects of compressor performance. Annand's correlation [107] was observed to show the least overall discrepancies with the measured data even though best results for temperature evaluation of compressor parts were presented by Liu and Zhou's [109] model. Liu and Zhou's [109] expression of in-cylinder gas swirl-velocity has resulted in inconsistent results for some working conditions, such as predicting illogical negative heat transfer coefficient of cylinder to gas. Furthermore, Tuhovcak et al. [115] have studied the influence of various heat transfer models [105–107, 116, 117] on the volumetric and isentropic efficiencies of a reciprocating compressor and found that the predictions of a particular performance aspect of a compressor may vary substantially

among different empirical correlations; for example, the maximum difference for isentropic efficiency of R134a between the models can range from 9.6% to 30.4%, depending on operating conditions.

Most available correlations did not consider the turbulent flow characteristic of the gas during the suction and discharge processes which is dependent on the suction port design, valve design and valve dynamics. As turbulent flow is too complex to be theoretically-modelled through the use of CFD simulation, Pereira et al. [118] numerically investigated the turbulent heat transfer process inside the cylinder of a small reciprocating compressor and have simulated the flow through valves using RNG k-ϵ turbulence model and Launder and Spalding's [119] wall functions. Predictions of heat transfer revealed a significant influence of the flow through valves on the in-cylinder heat transfer. Disconzi et al. [116] employed RNG k-ϵ turbulence model and eddy viscosity concept to simulate a two-dimensional in-cylinder compressible turbulent flow of a reciprocating compressor that takes into account the effect of fluid flow through the valves during the suction and discharge processes. Using the results of the numerical simulation, they proposed four new heat transfer correlations, as shown in Equation (2.3), for each process of the compression cycle, namely, compression, discharge, expansion and suction process, each with a characteristic velocity expression for the Reynolds number; characteristic velocity during compression and expansion processes defined as the piston mean velocity and characteristic velocity during suction and discharge processes defined as average velocity at valve orifice. The heat flux predictions using the new correlation was found to be in reasonable agreement with the numerical predictions of other works [105–107, 109] for different refrigerants and operating conditions.

$$\begin{aligned} Nu &= 0.08(Re)^{0.8}(Pr)^{0.6} \quad \text{Compression} \quad (a) \\ Nu &= 0.08(Re)^{0.8}(Pr)^{0.6} \quad \text{Discharge} \quad (b) \\ Nu &= 0.12(Re)^{0.8}(Pr)^{0.6} \quad \text{Expansion} \quad (c) \\ Nu &= 0.08(Re)^{0.9}(Pr)^{0.6} \quad \text{Suction} \quad (d) \end{aligned} \tag{2.3}$$

Another simplified theoretical modelling on heat transfer that helps predict temperature of each compressor part, is the lumped conductance approach. In this approach, all the components of the compressor are divided into individual discrete elements each modelled as a relatively simpler geometric block. For example, a precisely machined eccentric shaft can be modelled as a cylinder

block. Each element is assumed to be at a uniform temperature while heat transfer between each element in this system of elements are balanced according to conservation of energy and mass. The thermal properties of each element's material, heat transfer coefficient derived from correlations and the geometry of each element are lumped together as a thermal conductance coefficient. Heat transfer rate between two elements is then calculated as the product of lumped conductance coefficient and the temperature difference between the elements. Padhy and Dwivedi [120] have used the lumped conductance approach to predict the temperature of the compressor at various locations and found that the biggest temperature prediction difference between theoretical and measured results was only 5.5°C. Similarly, Ooi [121] has used the same approach in the heat transfer study of a hermetic reciprocating compressor and found that the prediction was in reasonably good agreement with the measured results; average discrepancies were mostly less than 10% with the highest discrepancy at 20%.

To conclude, there are no correlations and heat transfer models that are most accurate in predictions and versatile for all compressor types. Most correlations are also derived from the experimental results of an oil-lubricated compressor that experiences oil lubrication cooling during operation. Using these correlations for the analysis of an oil-free compressor may underpredict the effect of heat transfer.

2.6 Research Gap

From the literature reviewed, positive-displacement rotary vane type compressors appear to be the simplest in design and cheapest to fabricate with the standard geometrically shaped rotor and shaft as compared to other compressor types such as centrifugal, scroll, screw or linear types which are often used in the development of oil-free compressors. However, there are not much research works done on designing oil-free positive-displacement rotary vane type compressors. In this study, a conceptual prototype based on positive-displacement rotary vane type mechanism will be designed and tested under oil-free conditions to analyse its performance characteristics. This study will also explore different modifications to existing positive-displacement rotary vane type mechanisms that help mitigate the intrinsic problem of high wear rate at the vane sides.

From all the tribology literature reviewed for different commercially available self-lubricating materials, it was observed that most wear test conditions for

polymer-based self-lubricating materials are not similar to the normal operating conditions (e.g. contact force and sliding speed) of a compressor. In this study, different commercially available self-lubricating materials, namely PTFE, PEEK, Polyamide composites and Aluminium Bronze, will be tested in the prototype for wear resistance and durability at normal operating conditions of a generic compressor. The wear test results are shown in Chapter 7 Section 7.3.

In most liquid refrigerant injection cooling simulation work conducted, subcooled or saturated liquid state refrigerant is assumed to be injected into the chamber with no vaporisation occurring along the flow from the condenser to the injector and across the injector's orifice. In practice, flashing will occur throughout the flow from the condenser to the injector and two-phase mixture will form even before injection process due to drastic pressure drop along the pipe and across the injector's orifice. To better predict the quality and the mass flow rate of injected refrigerant, modelling of the flashing phenomenon of the subcooled or saturated liquid refrigerant into two-phase mixture during the flow from the condenser to the injector is required. Among all three two-phase flow models reviewed, the HFM model gives the best prediction of the mass flow rate of two-phase flashing refrigerant flow through an orifice and will be used in the modelling of the liquid refrigerant injection cooling process of the oil-free prototype. This model is presented in Chapter 4 Section 4.7.

While most studies on leakage flow modellings have shown predictions that are in good agreement with experimental results, the accuracies are verified against experimental values that are obtained from the testing of oil-lubricated compressors. This means that the flow coefficients and flow characteristics modelled are implicitly influenced by the sealing effects of oil-lubrication. Using such models and flow coefficients may lead to underprediction of internal leakage inside an oil-free compressor since oil-free clearances allow greater leakage due to slip flow and rarefaction effects. Accuracy in using these models for the leakage flow prediction of an oil-free compressor have not been verified yet.

In addition, although reviewed studies on heat transfer correlations and theoretical modellings are experimentally validated to be accurate in the predictions of heat flux and temperature of the compressor components, such validations are done using the experimental results of an oil-lubricated compressor that experiences oil-lubrication cooling during operation. The accuracies in the thermal predictions of an oil-free compressor using these heat transfer correlations and theoretical models have yet to be investigated.

2.7 Summary

This chapter presents an overview of the positive displacement vane compressors, theoretical modelling and experimental analysis on performance of compressors. The key points are summarised as follows:

- The existing positive displacement vane type compressor designs such as rolling piston compressor, rotary/sliding vane compressor, swing vane compressor and revolving compressor are simple in design and have varying degree of efficiency. In terms of mechanical efficiency, rolling piston and rotary vane compressors in particular suffer from severe vane-rotor interface and vane sides frictional rubbing and wear. Almost 30—40% of overall frictional loss in a rolling piston or a rotary vane compressor is mainly contributed from these rubbing interfaces. Leakage and vane chattering at the vane-rotor clearance are also causes for concern.

- Swing vane and revolving compressor are mechanically more efficient than other existing positive displacement vane type compressor designs. The key advantage of swing vane compressor is the elimination of vane-rotor interface with improved vane motion and vane side frictional loss since the vane is simple-supported on both ends instead of being cantilever-supported in rolling piston compressor. Revolving compressor has improved mechanical efficiency due to its simpler geometry, less rubbing interfaces and lower relative velocities at endfaces between the rotor and cylinder.

- A selection of materials with low friction coefficient that can be potentially used to mitigate large friction losses has also been reviewed.

- Simplified theoretical modellings for liquid injection refrigerant cooling, two-phase flow, leakage and heat transfer analysis are reviewed with assumptions presented. It is noted that most models and correlations developed are usually verified with conventional oil-lubricated compressors. The practicability and accuracy of these modellings have to be validated through experimentation on practical oil-free compressor.

Chapter 3

Oil-free Swing Vane Compressor with Liquid Refrigerant Injection Cooling

In this chapter, the design challenges of an oil-free compressor and the development of an oil-free swing vane compressor will be presented. The first section of this chapter will explain the limitations in the design of each existing positive displacement vane type compressors for use in oil-free operation and ultimately the rationale of choosing the swing vane mechanism in this research study. In the second section, the detailed design and overall working principle of the oil-free swing vane compressor prototype with liquid refrigerant injection will be presented.

3.1 Selection of Mechanism for Oil-Free Compressor Prototype

The working mechanism of the oil-free compressor prototype developed in this study is based on the swing vane compressor due to its simplicity in design and ease of modifying its existing parts with minimum compromise to its reliability and performance. The selection rationale is explained in this section. Based on the reviews of existing positive displacement vane type compressor in Section 2.1, the advantages and disadvantages of each compressor type are presented in Table 3.1 with focus on the mechanical losses, leakage points, complexity in fabrication and the reliability of the working mechanism:

Table 3.1: Summary of advantages and disadvantages of various positive displacement vane compressors.

Rolling piston compressor	
Advantages	Disadvantages
• Simpler and compact design with a cylinder, an eccentric shaft, a roller, and a vane with spring.	• Multiple leakage paths: through vane-tip and rotor clearance, vane side clearance, radial clearance between rotor and cylinder and clearance at the endface. Most leakages occur through vane-tip and rotor clearance and radial clearance between rotor and cylinder since these points are the shortest connecting path between suction and compression chamber. • High contact friction at vane tip and rotor moving interface. • Vane chattering might occur. • The vane is cantilever-supported and experiences greater contact force when the vane length is long. Designs with larger eccentricity suffers higher risk of vane failure due to the need for longer vane. • Failure mode usually involves vane wearing out and mechanical binding of moving parts due to adhesive wear.
Rotary vane compressor	
Advantages	Disadvantages
• Able to achieve near-continuous suction and discharge flow. • Does not require a discharge valve to operate, thereby avoiding risk of valve failure due to material fatigue. • Low noise operation due to reduced pulsation of near-continuous gas flow and no noise from opening and closing of valve.	• Multiple sources of frictional loss due to greater number of vanes rubbing against the vane slot and inner cylinder wall. • Vane chattering during start-up under low back-pressure in vane slot and low operating speed. • Severe leakage at low speed due to low centrifugal force required to maintain constant contact between vane tips and inner cylinder wall. It needs to operate above a minimum designated speed. • Increased precision and complexity in manufacturing due to multiple vane slot and vane to be machined.

Swing vane compressor	
Advantages	Disadvantages
• Simpler and compact design with a cylinder, an eccentric shaft, a rotor fixed with vane and split bushes/swing bushes. • Improved volumetric efficiency as compared to rolling piston compressor due to the elimination of leakage at vane-tip and rotor clearance. • Frictional loss at the vane sides is drastically reduced as compared to rolling piston compressor because the vane is now simply-supported instead of being cantilever-supported.	• Sliding speed between rotor and eccentric shaft increases as compared to rolling piston compressor. • Retains similar leakage paths as rolling piston compressor but with the elimination of leakage at vane tip and rotor clearance.
Revolving vane compressor	
Advantages	Disadvantages
• Improved endface frictional loss as compared to rolling piston and swing vane compressor because of the lower relative sliding speed between the endfaces of cylinder, rotor and vane.	• Additional journal bearings are required to support rotating cylinder and rotor individually which increase the risk of bearing misalignments and the complexity of machining due to the need for high precision in multiple bearing surfaces. • Mechanical efficiency and failure rate might be higher without the use of oil lubrication especially in oil-free operations. Current revolving vane compressor is able to achieve low frictional losses even with the usage of multiple journal bearings because well-designed hydrodynamic oil lubrication is employed to mitigate the frictional torque at multiple bearing surfaces.

From the summary of advantages and disadvantages, it seems that rotary vane compressor is the least viable design among the positive displacement vane type compressor for oil-free operation due to its higher risk of seizure with multiple vane tips wearing out and mechanically binding onto the cylinder wall. Multiple vanes design would also lead to a higher fabrication cost and complexity in manufacturing the prototype. Since parts are worn out quickly in vigorous experimental tests and are needed to be replaced frequently, the prototype mechanisms have to be simple and cheap to be manufactured.

3.1.1 Identifications of Components that undergo Dry Friction Rubbing

In the absence of oil lubrication to separate two bearing surfaces in contact, microscopic peaks at the interface will touch and interlocking will occur [2]. For the oil-free compressor prototype to operate efficiently, it is important to ensure that dissimilar materials of low friction coefficient are used as bearing surfaces to avoid excessive frictional wear and friction-induced temperature rise at the sliding interface. This is because the accumulations of wear and heat will eventually lead to the seizure of the prototype. In the worst case, friction welding of similar surfaces due to the heat generated [122] may occur. Among the positive displacement vane type compressors, the rolling piston is the hardest to be modified with self-lubricating materials incorporated into the working mechanism due to the cantilever-supported vane design.

Figure 3.1 shows the working mechanism of a rolling piston compressor in which each moving interface is highlighted in blue or red. In a rolling piston compressor, the contacting surfaces (blue colour) between the vane sides and vane slot and between the vane tip and rotor experience high frictional losses [40, 42]. To bond self-lubricating material to the vane surfaces, coating or mechanical fastening or adhesive bonding of self-lubricating material layers onto the vane

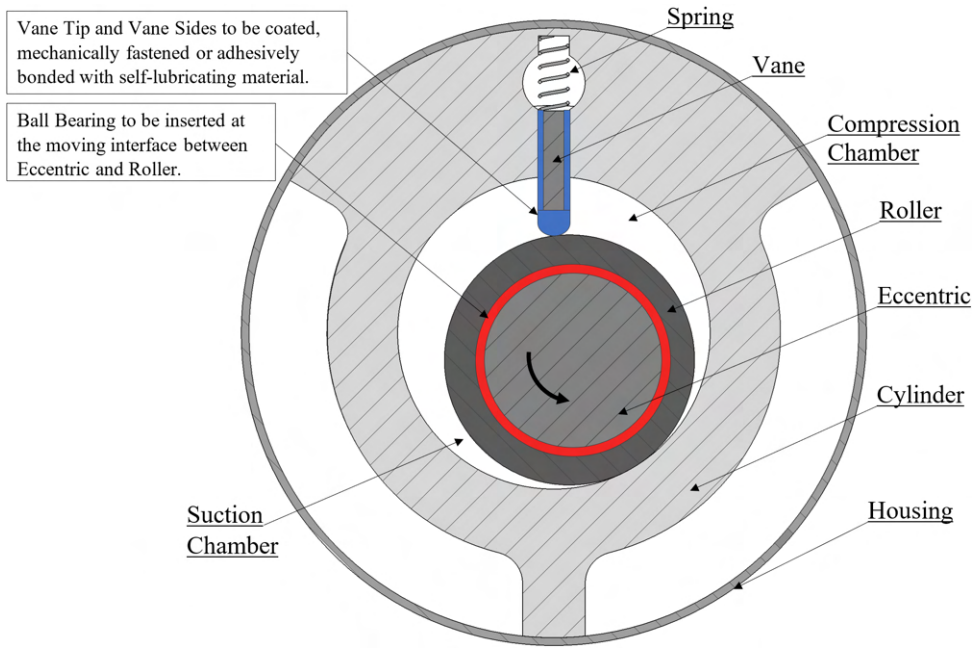

Figure 3.1: Front view of rolling piston compressor — Bearing surfaces of rolling piston mechanism to be modified.

sides and vane tip are the only viable methods in reducing friction at all the metal-to-metal bearing surfaces of the vane. However, there are shortcomings in these methods. Bonding between dissimilar material surfaces, especially metal-to-polymer joints, are generally weak; metal-to-polymer coatings such as PEEK coatings on stainless steel by Electrophoretic Deposition [123] usually result in fragile deposits with micro-cracks and the surface finishings are imprecise without additional surface treatments. Mechanical fastening of self-lubricating material onto a metal vane will lead to a bulky vane design which reduces the working volume of the compressor. Furthermore, self-loosening and fatigue failure of mechanical fasteners can occur [124, 125], especially under dynamic loadings of a vane. In addition, the adhesive also becomes weak and ductile in high temperature environment [126]. Delamination of metal-polymer laminate might even occur due to bending [127] especially a vane-polymer laminate will be subjected to lateral load from high gas pressure force. It will be easier to make the entire vane out of self-lubricating polymers or alloys, but these materials usually have low yield and tensile strength as compared to steel; such vane design will ultimately fail under high gas pressure loadings.

To reduce friction at the two endface surfaces (yellow colour) between the roller, vane and cylinder covers (as shown in Figure 3.2), bushing plates made of self-lubricating material can be easily fastened onto both the static top and

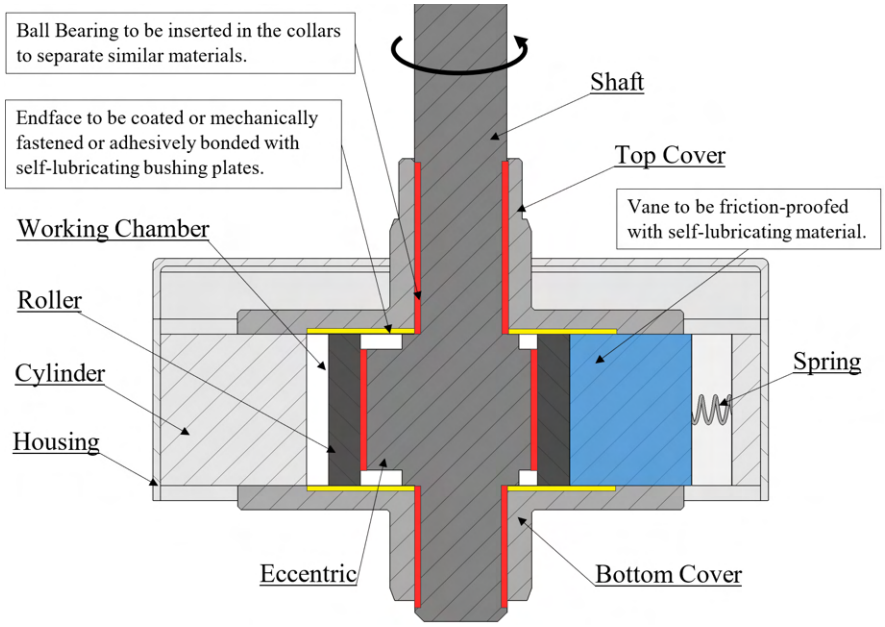

Figure 3.2: Sectional view of rolling piston compressor — Bearing surfaces of rolling piston mechanism to be modified.

bottom covers using screws or rivets without much alteration to the overall design. On the other hand, friction at the three bearing surfaces (red colour) namely, the eccentric-roller and cover-shaft interfaces, can be reduced by inserting bushings into the covers' collar and roller's inner wall. However, frictional losses at eccentric-roller and shaft bearing surfaces are known to contribute the highest friction losses (∼29 to 34% of overall frictional losses) in a rolling piston compressor [40] even when these surfaces are constantly lubricated by full-film hydrodynamic oil lubrication of the journal bearings during operations [26, 27]. Bushing made of self-lubricating material will lose its surface tolerance easily due to its low wear resistance under such high friction loading and will easily cause shaft misalignment. Grease-lubricated and sealed ball bearing should be used in place of bushings at these high load bearing surfaces in order to avoid the increase of vibrations and acceleration of wear over time.

The revolving vane compressor with fixed vane to cylinder has the lowest average vane side frictional losses among all revolving vane configurations [43] and is chosen to be reviewed. Unlike the cantilever-supported vane in the rolling piston mechanism, the split bush in the revolving vane mechanism is not subjected to lateral loading of high gas pressure force and mainly rotates under point loading (as shown in enlarged detailed view of Figure 3.3) so it does not undergo bending and deflection. The entire split bush (blue colour) can

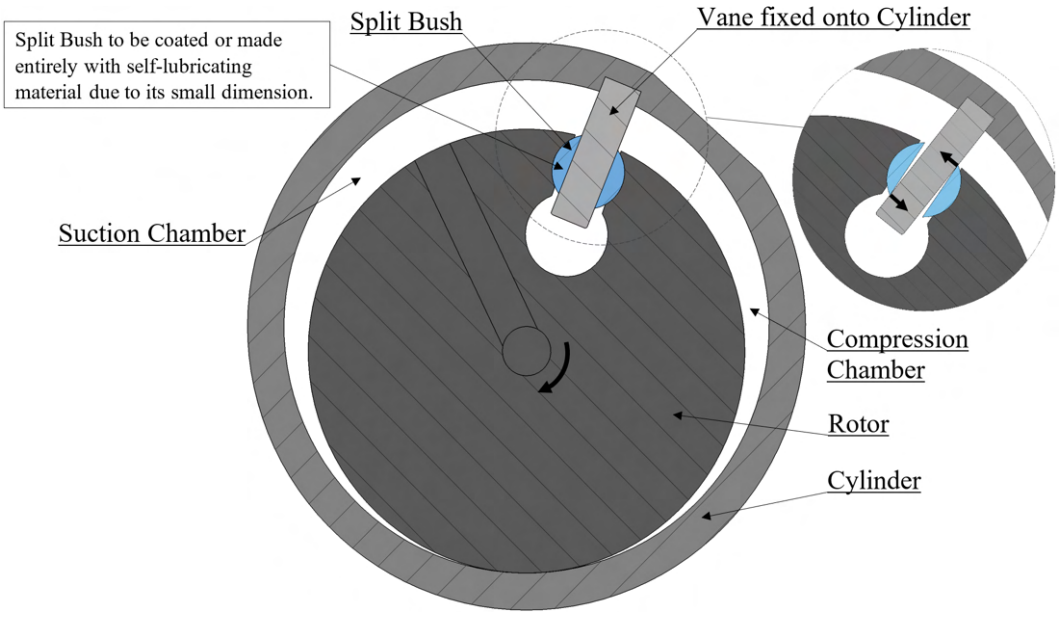

Figure 3.3: Front view of revolving vane compressor — Bearing surfaces of revolving vane mechanism to be modified with enlarged detailed view of split bush and vane contact points.

be coated or made of self-lubricating material to minimise the friction at both the bearing surfaces of rotor and vane without much structural deformation, as shown in Figure 3.3. The main concern is the durability of split bush to withstand frictional wear from prolonged vane sliding during prototype testing. Materials will be tested out for their durability in Chapter 7 in the split bush and endface bushing material selection process.

The revolving vane mechanism generally has more endfaces than rolling piston and swing vane mechanisms. As seen in Figure 3.4, there are four endface bearing surfaces (yellow colour) to be coated or shielded by bushing plates to reduce friction. More dry contacting bearing surfaces would mean higher chances of mechanical surface binding and seizure during compression cycle. Similarly, bushing plates can be fastened to these endfaces to separate metal-to-metal contact. However, in current revolving vane compressor, one housing has to accommodate the rotations of both the cylinder and rotor. This results in a larger housing design with larger bearing surfaces that usually needs full-film oil lubrication to ensure low frictional losses. In oil-free operations, these endface bushing plates are expected to wear out fast. Moreover, degradation of dimensional tolerance at multiple dry bearing surfaces will easily lead to vibration, misalignment of rotation axis between the cylinder and rotor and

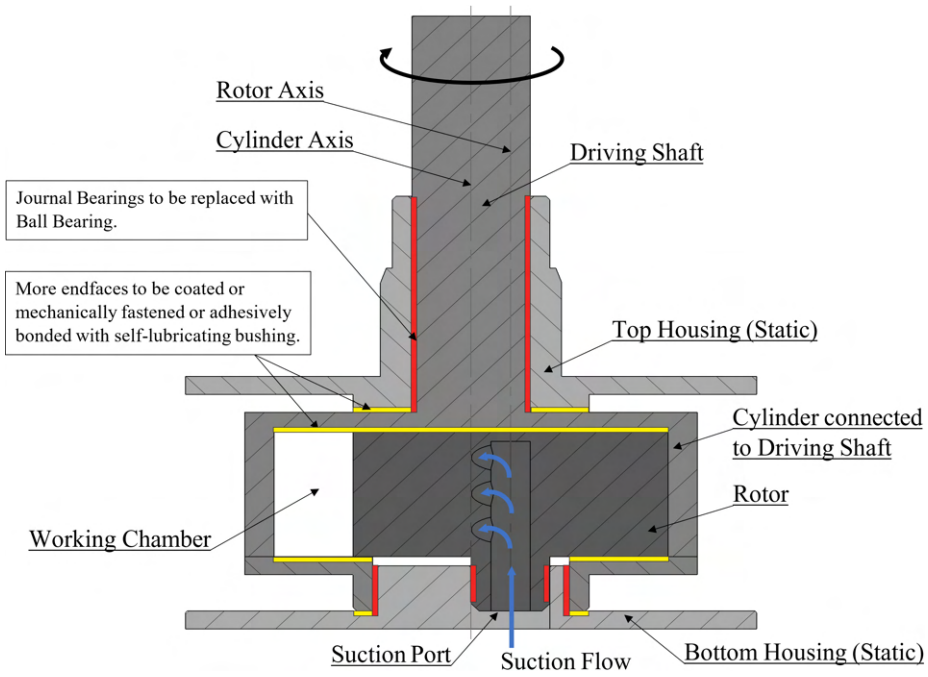

Figure 3.4: Sectional view of revolving vane compressor — Bearing surfaces of revolving vane mechanism to be modified.

seizure of the compressor. It is not advisable to use wear bushing that has low wear resistance for the friction-reduction of the three bearing surfaces (red colour) at rotor-housing, cylinder-housing and shaft-housing interfaces when hole tolerance and alignment of the rotational axis are critical for the revolving vane mechanism. For durability and avoidance of misalignment between multiple rotating components, grease-lubricated and sealed ball bearing should also be used in these high loading points instead, especially at the bottom cylinder bearing where frictional loss is substantially larger than that at shaft bearing due to a larger radius [42].

In the swing vane compressor, the vane is fixed onto the rotor on one end and simple-supported on the other by the split bush, as shown in Figure 3.5. Therefore, the reaction forces acting on the sides of the vane and split bush are drastically reduced. In addition, the split bush only rotates and bears the sliding friction. The entire split bush (blue colour) can also be coated or made of self-lubricating material to prevent metal-to-metal rubbing. For the friction-reduction of the endfaces (yellow colour), the swing vane mechanism only has two endfaces to be modified by coating of the covers or with the insertion of bushing plates. Since the rotor is now constrained by the split bush in swing vane mechanism, the rotor swings about the split bush with increased sliding speed

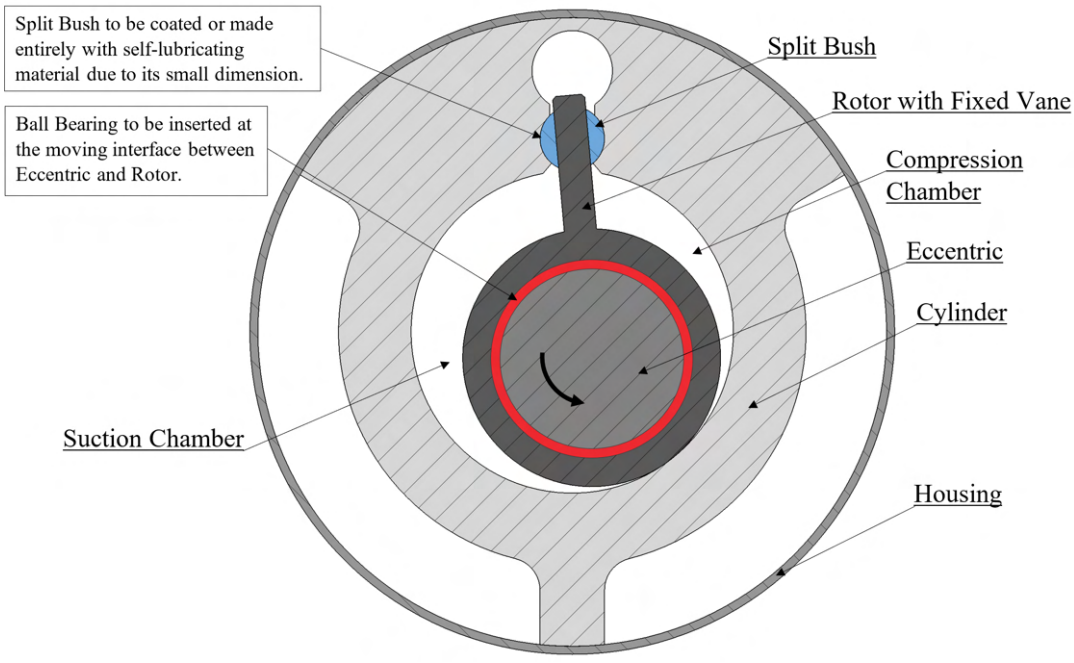

Figure 3.5: Front view of swing vane compressor — Bearing surfaces of swing vane mechanism to be modified.

between the rotor and eccentric bearing surfaces. Therefore, grease-lubricated and sealed ball bearing should also be used in place of wear bushing in the eccentric-rotor interface and also shaft-housing interface which requires good alignment in rotation.

As compared to rolling piston mechanism, the swing vane mechanism does not require any re-designing or friction-reducing of the vane with the elimination of vane tip and rotor interface. Friction-reduction of the split bush is also much easier and reliable than to attach bushing layers onto the vane surface in the rolling piston mechanism. Comparing with the revolving vane compressor, the top and bottom housings/covers of the swing vane compressor only bear the loading of the shaft which is of a smaller radius (red colour) as compared to that of the larger housing and cylinder bearing of the revolving vane compressor, as shown in Figure 3.6. Furthermore, it is easier to fix an injection nozzle onto the static cylinder walls of a swing vane compressor for liquid refrigerant injection cooling of the compression chamber as compared to a revolving vane compressor where multiple components are moving (as shown in Figure 3.7). There is no direct entry path for the injection of liquid refrigerant to reach the rotating compression chamber except through the axial port in the rotor which is occupied by the suction port.

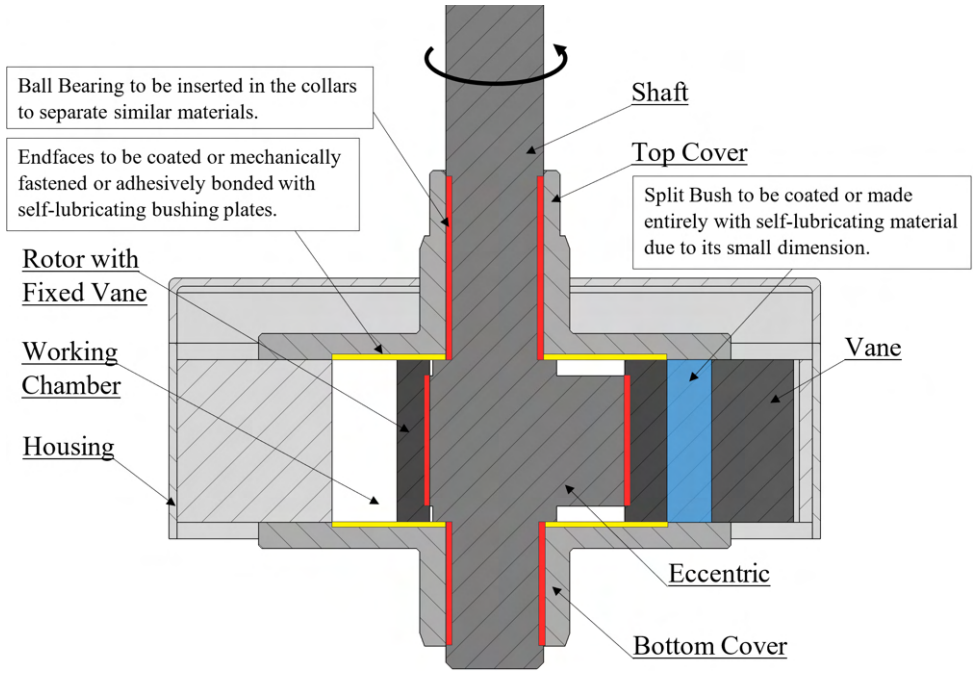

Figure 3.6: Sectional view of swing vane compressor — Bearing surfaces of swing vane mechanism to be modified.

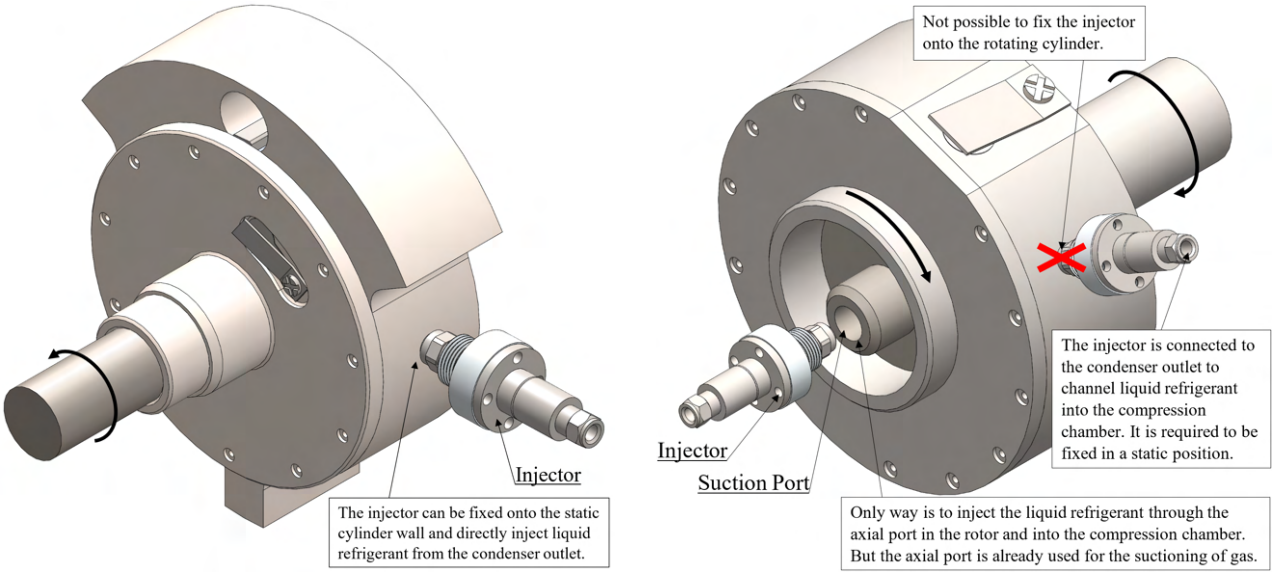

Figure 3.7: Position of Injector for liquid refrigerant injection — (a) Swing Vane Compressor (b) Revolving Vane Compressor.

With the consideration of all design limitations and difficulties of friction-reducing the dry bearing surfaces in the rolling piston and revolving vane mechanism, the swing vane mechanism is reviewed to be the most durable design out of all positive displacement vane type compressor mechanism for dry compression operations. The following experimental study of an oil-free compressor with liquid refrigerant injection in Chapter 8 was conducted based on a dry swing vane compressor.

3.2 Prototype Design

In this section, the working principle of the oil-free swing vane compressor prototype with liquid refrigerant injection cooling will be explained. The design features of the oil-free swing vane mechanism to minimise frictional losses will be discussed.

3.2.1 Detailed Design of Oil-Free Swing Vane Compressor with Liquid Refrigeration Injection Cooling

With the identification of key components that undergo dry friction rubbing in the compressor and possible ways of reducing friction at these interfaces with self-lubricating materials in Subsection 3.1.1, this section will now go into the design details of the prototype.

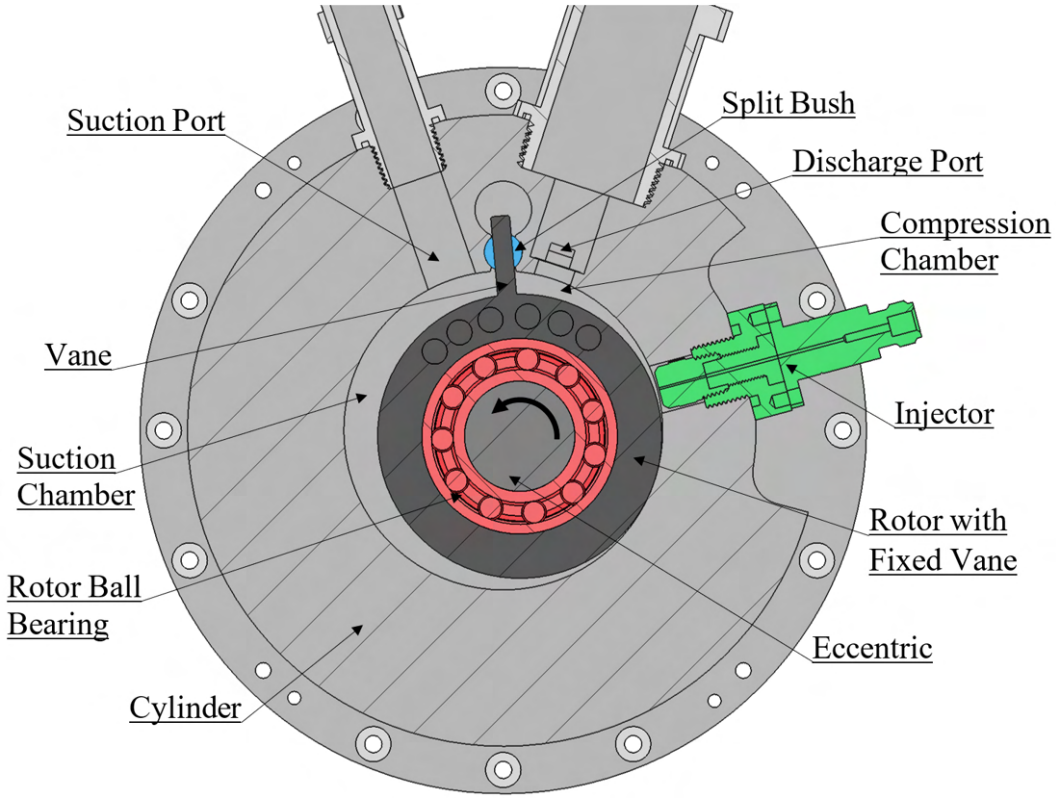

Figure 3.8: Front view of oil-free swing vane compressor prototype.

Figure 3.8 shows the main components of the oil-free swing vane compressor prototype which are, namely, the rotor with fixed vane, the cylinder, the eccentric shaft and the split bush made entirely of self-lubricating material. The split-bush (blue colour) rotates in the bushing slot to guide the sliding motion of the vane

and undergoes dry rubbing with the vane and the cylinder. As the split bush will wear out after prolonged dry rubbing, the clearance between the vane and the split bush will be enlarged and vibration of the vane within the clearance will intensify. The durability of the material selected for the construction of the split bush is critical for ensuring that the oil-free swing vane mechanism can run smoothly for prolonged experimental testing without severe wear and so bushings made of different self-lubricating materials were tested in the prototype before proceeding with experimental studies. The detailed durability testing of each material as wear bushing will be explained in Chapter 7. As the shaft and eccentric bearing surfaces experience the highest frictional losses, ball bearings are used in place of low wear-resistance bushings to ensure minimum changes to the hole tolerance so as to avoid misalignments of the shaft and the rotor which may lead to vibration and prototype seizure. The injector (green colour) that controls the timing and duration of liquid refrigerant injection is screwed onto the cylinder inner wall near the compression side to allow direct injection of liquid refrigerant into the compression chamber and cooling of the compressed gas.

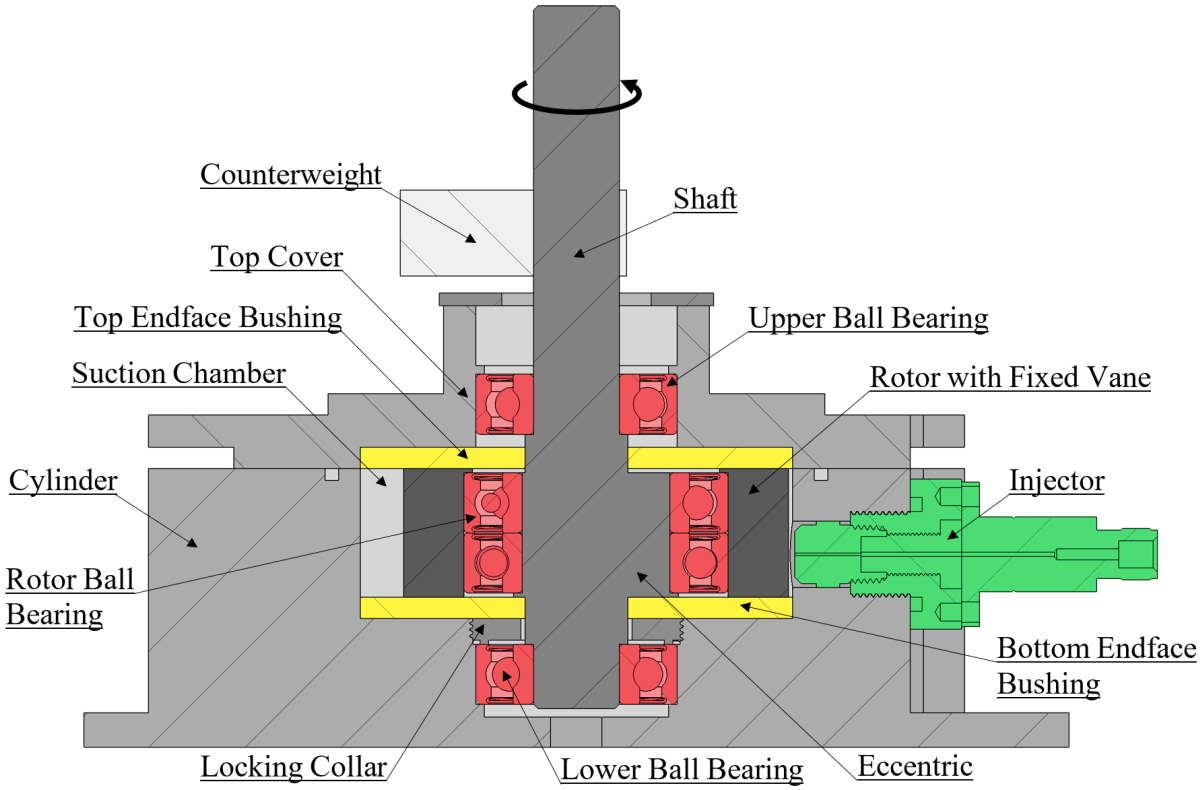

Figure 3.9: Sectional view of oil-free swing vane compressor prototype.

3.2.2 Working Principle of Oil-Free Swing Vane Compressor with Liquid Refrigeration Injection Cooling

The working cycle of the prototype begins at step (a) as shown in Figure 3.10, where the suction process of the working fluid has ended and the compression process has just begun. As the shaft rotates in the anti-clockwise direction, the rotor swings about the split bush, causing the volumes bounded by the vane, cylinder wall and rotor to vary; the volume of suction chamber increases while the compression chamber decreases in volume. The increase in the volume of the suction chamber leads to the inflow of working fluid via the suction port throughout the cycle from step (a) to (e) in Figure 3.10. Meanwhile, the decrease

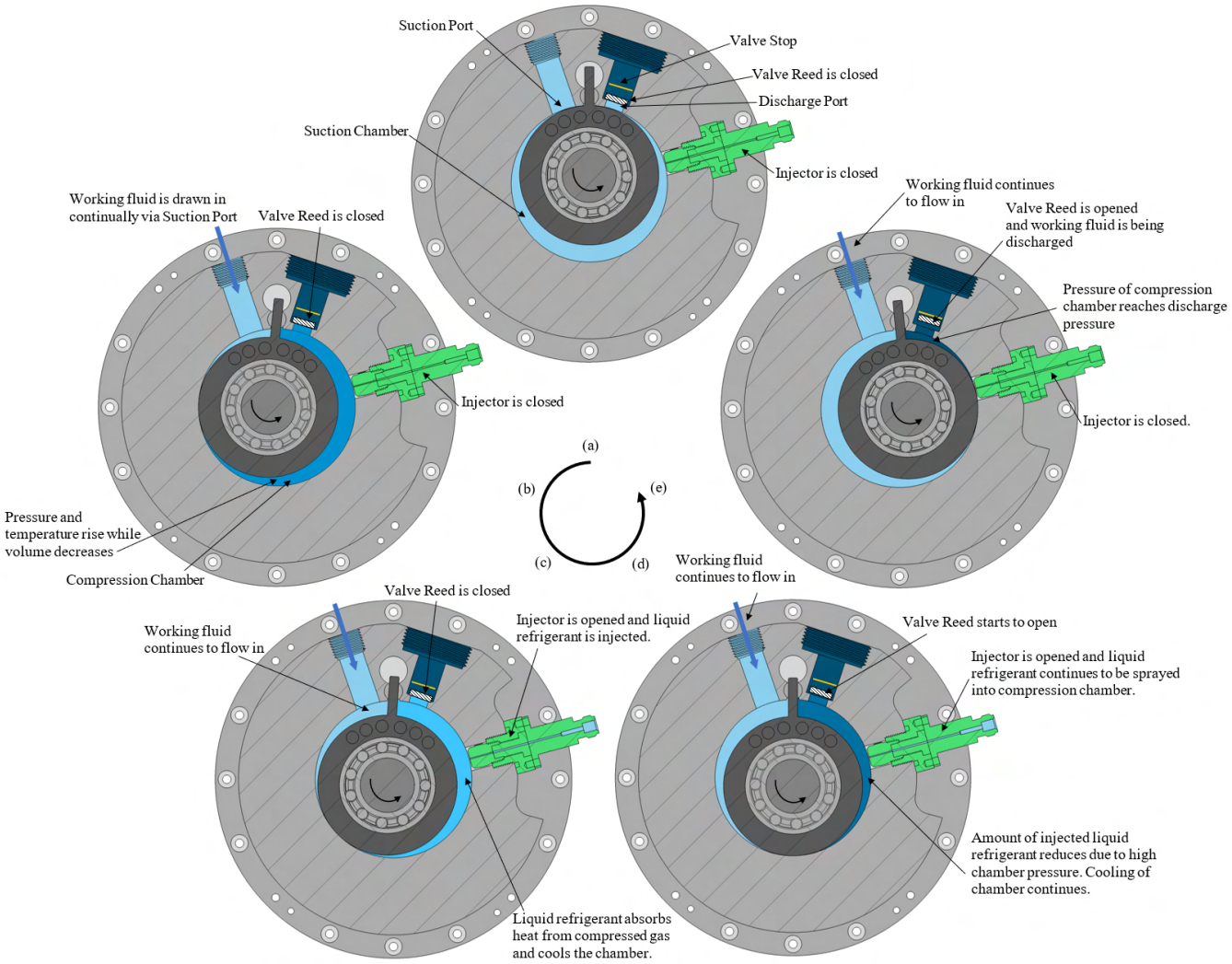

Figure 3.10: Working principle of oil-free swing vane compression with liquid injection cooling during compression cycle.

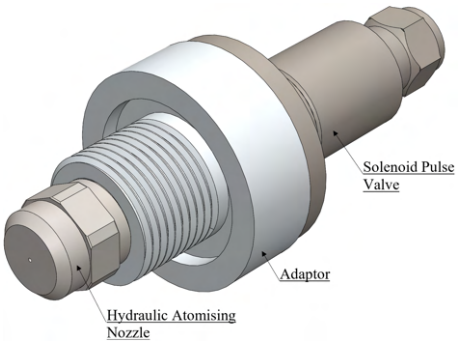

(a)

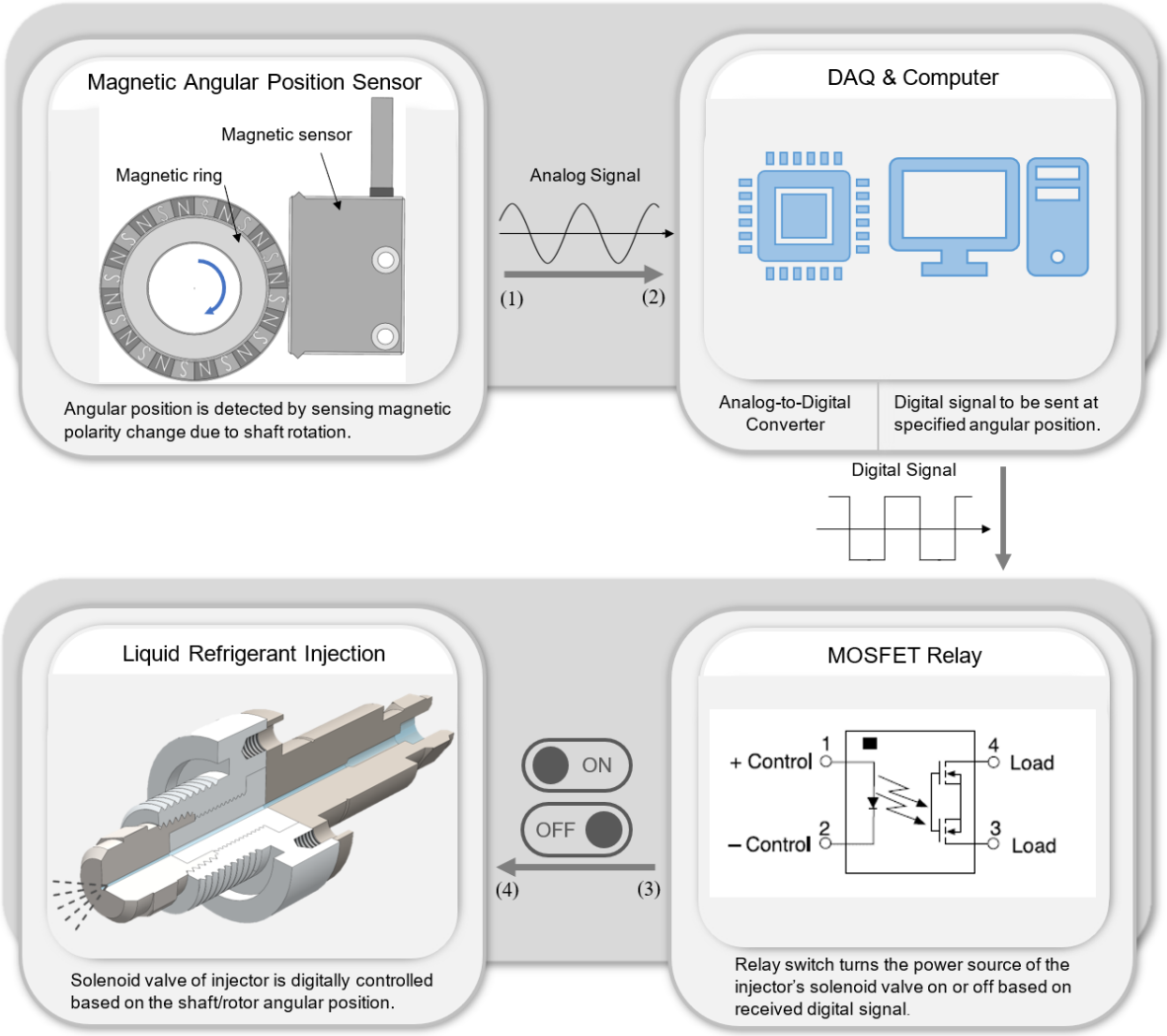

(b)

Figure 3.11: Working principle of liquid refrigerant injection.

in the volume of compression chamber results in the temperature and pressure rise of the existing working fluid in the chamber. To cool the compression chamber and the compressor components, liquid refrigerant is injected during the compression process by activating the injector (shown in steps (c) and (d) in

Figure 3.10). The injector is made up of an electronically-controlled (normally closed) solenoid valve, an adaptor to secure the whole injector onto the wall and a hydraulic atomising nozzle (as shown in Figure 3.11(a)). When the rotor swings to a specified angular position where the temperature of the compressed vapour is greater than that of liquid refrigerant for heat exchange while the vapour pressure is still much lower than that of the liquid refrigerant, the position is detected by a magnetic angular position sensor which sends an analogue signal to the data-acquisition system. The data-acquisition system in turn converts the analogue signal to a digital signal and sends it to the relay switch, as illustrated in step (1) to (3) in Figure 3.11(b). The relay switch then activates the power source of the solenoid valve, opening the valve for inflow of liquid refrigerant into the injector. Under high pressure and swirling flow through the nozzle, the liquid refrigerant is atomised and sprayed into the compression chamber. The optimised effect of cooling is dependent on the conditions of liquid refrigerant and in-chamber vapour and the position of rotor which will be discussed in later chapters.

As compression proceeds, the liquid refrigerant continues to be injected into the compression chamber until the rotor reaches the specified ending angular position for solenoid valve closure where the power source to the valve is cut (in step (d) in Figure 3.10). The discharge valve reed remains closed during the compression process until the fluid pressure in the compression chamber exceeds the discharge pressure on the other side of the valve. Once the differential pressure across the discharge valve reed becomes sufficiently large to overcome the valve stiffness, the compressed fluid pushes the valve open and is discharged out of the compression chamber via the discharge port, as shown in step (e) in Figure 3.10. The discharge and suction processes are completed once the rotor swings back to the original position in step (a) in Figure 3.10 and the cycle repeats.

3.3 Summary

In this chapter, the detailed design and the working principle of the oil-free swing vane compressor prototype with liquid refrigerant injection functionality were presented and explained. The design features of incorporating self-lubricating bearing materials into the swing vane mechanism were also discussed. With the finalisation of the prototype design, the detailed dimensioning of the prototype and the durability evaluation process of different self-lubricating materials will be presented in Chapter 7. In the following chapters, theoretical models of the oil-free swing vane compressor will be presented.

Chapter 4

Theoretical Model: Geometry, Kinematics and Thermodynamics

In this chapter, mathematical models that describe and predict the operational characteristics of the compressor prototype will be presented. The mathematical models formulated include the geometrical descriptions of the swing vane mechanism and the volume of the working chambers. The models also include the mathematical derivations of kinematics which focuses on the velocity and acceleration of each moving part and also the thermodynamics of the working fluid which predicts the variation of thermodynamics properties of the working fluid due to the varying volume of working chambers, mass flow and heat transfer.

4.1 Assumptions for Theoretical Modelling

The theoretical models were formulated based on the following assumptions:

1. Deformations and structural deflections of the moving components are assumed to be negligible.
2. Reactional translations and rotations of the mechanism due to input torque from the motor acting on the shaft is assumed to be instantaneous.
3. Volume of the clearances are assumed to be negligible as compared to that of the working chambers.
4. Effects of vibrational motions of the moving parts within the clearances are neglected.
5. Rotational speeds of the motor and the shaft are constant throughout the working cycle although in reality, the speed may vary due to dynamic loadings on the shaft and motor slippage.

6. The working fluid properties are homogeneous and the working fluid is uncontaminated by other substances.
7. Changes to fluid properties are propagated instantaneously due to fast molecular speed and small mean free path between molecules and hence, the suction and compression processes in the working chambers are assumed to be quasi-static processes. Resultant properties of working fluid are uniform throughout the working chambers.
8. Suction, discharge and leakage flow through the respective suction, discharge ports and clearances are unidirectional flows.

4.2 Geometry

In this section, only the main geometrical relationships that are required for the derivations of the chambers' volumes, thermodynamics and dynamics analysis will be mentioned. Auxiliary geometrical relationships and detailed derivations are shown in the Section A.1 and Section A.2. Figure 4.1 illustrates the geometrical parameters that are used for the formulation of the working chamber volumes of the compressor.

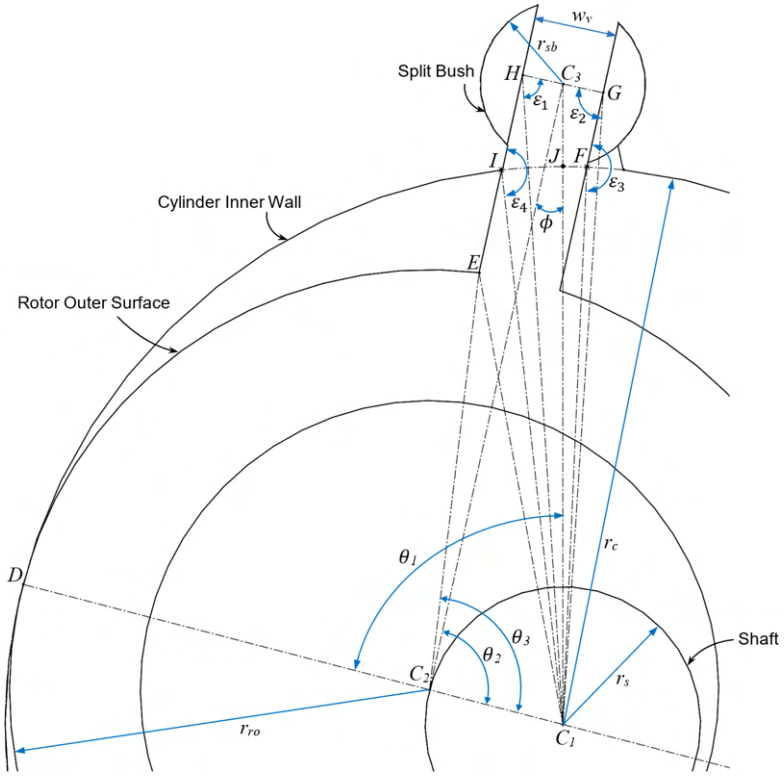

Figure 4.1: Front view of swing vane mechanism showing different basic geometrical parameters.

As described in Subsection 3.2.1, the swing vane mechanism consists of a cylinder with an internal radius r_c, a shaft with radius r_s, a rotor with radius r_{ro}, a split bush with radius r_{sb} and a vane with width w_v. The shaft is supported concentrically to the cylinder and it rotates about the centre of the cylinder C_1 while the rotor is centred at the origin of the eccentric C_2 and it swings about the centre of the split bush C_3. The rotational angle θ_1 of the shaft is measured with respect to the vertical central line $l_{C_1C_3}$ and virtual contact line l_{C_1D} in anti-clockwise direction while the relative rotational angle θ_2 between the rotor and shaft is taken with respect to line $l_{C_2C_3}$. The rotational angle of the vane or the split bush ϕ is measured with respect to the vertical central line $l_{C_1C_3}$ and line $l_{C_2C_3}$. Based on Figure 4.1, the expressions for the basic geometric relations are presented in Equations (4.1) to (4.8).

$$l_{C_2C_3} = \sqrt{(r_c - r_{ro})^2 + (r_c + r_{sb})^2 - 2(r_c - r_{ro})(r_c + r_{sb})\cos\theta_1} \tag{4.1}$$

$$\theta_2 = \begin{cases} \cos^{-1}\left(\dfrac{(r_c + r_{sb})^2 - l_{C_2C_3}^2 - (r_c - r_{ro})^2}{-2(r_c - r_{ro})l_{C_2C_3}}\right) & , \theta_1 < \pi \\ 2\pi - \cos^{-1}\left(\dfrac{(r_c + r_{sb})^2 - l_{C_2C_3}^2 - (r_c - r_{ro})^2}{-2(r_c - r_{ro})l_{C_2C_3}}\right) & , \theta_1 \geq \pi \end{cases} \tag{4.2}$$

$$\phi = \begin{cases} \pi - \theta_1 - \theta_2 & , \theta_1 < \pi \\ \theta_1 + \theta_2 - 540^\circ & , \theta_1 \geq \pi \end{cases} \tag{4.3}$$

$$l_{C_1H} = \begin{cases} \sqrt{\left(\dfrac{w_v}{2}\right)^2 + (r_c + r_{sb})^2 - 2(r_c + r_{sb})\dfrac{w_v}{2}\cos(\dfrac{\pi}{2} - |\phi|)} & , \phi < 0 \\ \sqrt{\left(\dfrac{w_v}{2}\right)^2 + (r_c + r_{sb})^2 - 2(r_c + r_{sb})\dfrac{w_v}{2}\cos(\dfrac{\pi}{2} + |\phi|)} & , \phi \geq 0 \end{cases} \tag{4.4}$$

$$\varepsilon_1 = \cos^{-1}\left(\frac{(r_c + r_{sb})^2 - \left(\dfrac{w_v}{2}\right)^2 - {l_{C_1H}}^2}{-l_{C_1H}w_v}\right) \tag{4.5}$$

$$l_{EH} = (r_c + r_{sb}) + \left(r_{ro} - \sqrt{{r_{ro}}^2 - \left(\frac{w_v}{2}\right)^2} \right) \tag{4.6}$$

$$l_{C_1E} = \sqrt{{l_{EH}}^2 + {l_{C_1H}}^2 - 2 l_{EH} l_{C_1H} \cos(\varepsilon_1)} \tag{4.7}$$

$$\theta_3 = \cos^{-1}\left(\frac{l_{C_1E}^2 - {r_{ro}}^2 - (r_c - r_{ro})^2}{-2 r_{ro}(r_c - r_{ro})} \right) \tag{4.8}$$

4.3 Volumes of working chambers

Figure 4.2 illustrates the suction and compression chamber volumes which are the spaces bounded by the inner wall of the cylinder, the outer circumference of the rotor and the exposed vane length. The volumes of the working chambers varies with respect to the rotational angle of the shaft and are expressed in Equations (4.9) and (4.10).

$$V_{suc} = \begin{cases} \frac{1}{2} l_{com}[{r_c}^2\theta_1 - {r_{ro}}^2(\pi - \theta_3) - l_{EH} l_{C_1H} \sin(|\frac{\pi}{2} - \varepsilon_1|) - \frac{w_v}{2} l_{C_1H} \sin(\varepsilon_1) \\ - r_{ro}(r_c - r_{ro}) \sin(\theta_3) + V_{correc1}] & , \theta_1 < \pi \\ \begin{cases} \frac{1}{2} l_{com}[{r_c}^2\theta_1 - {r_{ro}}^2(\pi - \theta_3) - l_{EH} l_{C_1H} \sin(|\frac{\pi}{2} - \varepsilon_1|) - \frac{w_v}{2} l_{C_1H} \sin(\varepsilon_1) \\ - r_{ro}(r_c - r_{ro}) \sin(\theta_3) + V_{correc1}] & , \phi > 0 \; or \; \phi < 0 \; \& \; (\frac{\pi}{2} - \varepsilon_1) > 0 \\ \frac{1}{2} l_{com}[{r_c}^2\theta_1 - {r_{ro}}^2(\pi - \theta_3) - l_{EH} l_{C_1H} \sin(|\frac{\pi}{2} - \varepsilon_1|) - \frac{w_v}{2} l_{C_1H} \sin(\varepsilon_1) \\ - r_{ro}(r_c - r_{ro}) \sin(\theta_3) + V_{correc1}] & , \phi \leq 0 \; or \; \phi \geq 0 \; \& \; (\frac{\pi}{2} - \varepsilon_1) \leq 0 \end{cases} & , \theta_1 \geq \pi \end{cases} \tag{4.9}$$

$$V_{com} = l_{com}\pi({r_c}^2 - {r_{ro}}^2) - V_{suc} + V_{correc2} - V_{correc3} \tag{4.10}$$

where,

V_{suc} is the volume of the suction chamber (m^3).

V_{com} is the volume of the compression chamber (m^3).

l_{com} is the axial length of the compressor (m).

$V_{correc1}$ is the blue-coloured correctional volume (m^3).

$V_{correc2}$ is the green-coloured correctional volume (m^3).

$V_{correc3}$ is the red-coloured correctional volume (m^3).

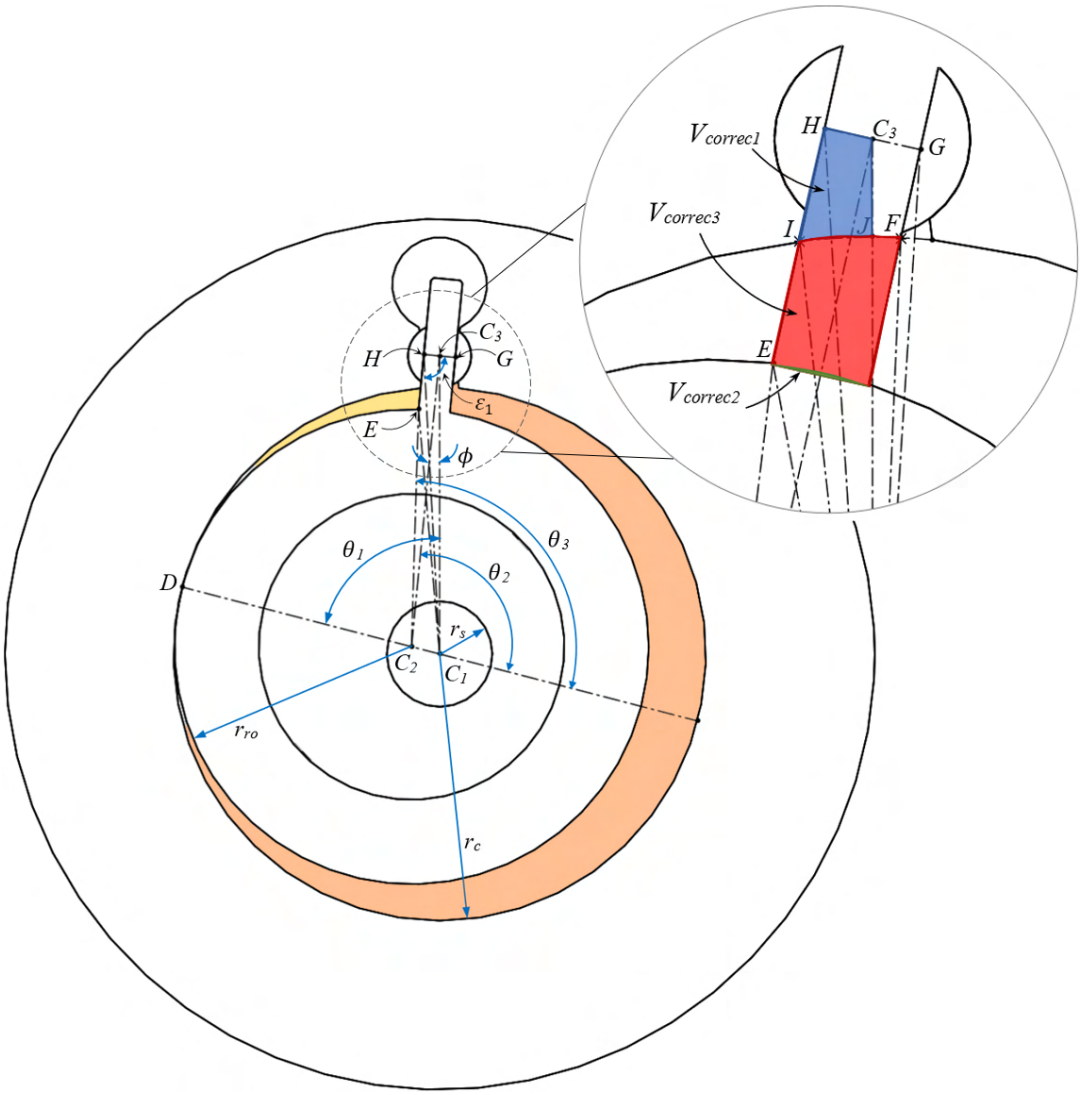

Figure 4.2: Illustration of suction and compression volumes with correctional volumes shown in detailed view.

As the vane occupies part of the working capacity of the compressor, correctional volumes $V_{correc1}, V_{correc2}, V_{correc3}$ (shown in the detailed view of Figure 4.2) are added to the derived expressions of suction and compression chamber volumes in Equations (4.9) and (4.10) to account for the reduction in the working volumes. Due to the rotational motion of the vane and bushing in the slot, the correctional volumes are changing with respect to the shaft's rotational angle and the derivations are complex. The detailed derivations of the correctional volumes $V_{correc1}, V_{correc2}, V_{correc3}$ and additional required geometrical relations are shown in the Section A.1 and Section A.2.

4.4 Kinematics

In this section, kinematics of the moving components in swing vane mechanism are presented. These relations will be used in the dynamic model in Chapter 5 to evaluate the forces and torques acting on the compressor components. This includes the rate of change of the exposed vane length, the rate of change of angular position of the split bush about the bushing slot and the relative angular velocity and acceleration of the rotor with respect to the eccentric. Only kinematics of the moving components under constant rotational speed of the shaft and motor (steady operation) are considered and formulated.

4.4.1 Sliding Velocity and Acceleration of Vane

The rate of change of vane exposure length in the working chamber with respect to time, which is also the sliding velocity of vane against the split bush, is given by Equation (4.11).

$$\begin{aligned}\frac{dl_{C_2C_3}}{dt} &= \frac{dl_{C_2C_3}}{d\theta_1} \times \frac{d\theta_1}{dt} \\ &= \frac{(r_c + r_{sb})(r_c - r_{ro}) \sin\theta_1}{\sqrt{(r_c - r_{ro})^2 + (r_c + r_{sb})^2 - 2(r_c - r_{ro})(r_c + r_{sb}) \cos\theta_1}} \omega_1\end{aligned} \tag{4.11}$$

The sliding acceleration of the vane is derived as Equation (4.12).

$$\begin{aligned}\frac{d^2 l_{C_2C_3}}{dt^2} = \Bigg[&\frac{(r_c + r_{sb})(r_c - r_{ro}) \sin^2\theta_1}{[(r_c - r_{ro})^2 + (r_c + r_{sb})^2 - 2(r_c - r_{ro})(r_c + r_{sb}) \cos\theta_1]^{1.5}} \\ &+ \frac{\cos\theta_1}{\sqrt{(r_c - r_{ro})^2 + (r_c + r_{sb})^2 - 2(r_c - r_{ro})(r_c + r_{sb}) \cos\theta_1}} \Bigg] {\omega_1}^2\end{aligned} \tag{4.12}$$

where

$\frac{dl_{C_2C_3}}{dt}$ is the rate of change of the vane exposure length or sliding velocity of the vane (m s^{-1}),

$\frac{d^2 l_{C_2C_3}}{dt^2}$ is the sliding acceleration of the vane (m s^{-2}), and

ω_1 is rotational speed or angular velocity of the shaft about centre C_1 (rad s^{-1}).

4.4.2 Kinematics of Eccentric-Rotor

As the rotor with fixed vane in a swing vane mechanism is restrained by the split bush from rotating about the centre of eccentric C_2, there is a relative sliding motion between the rotor and eccentric and a relative angular velocity between the eccentric-rotor bearing surfaces. The relative angular velocity and acceleration are given by Equations (4.13) and (4.14).

$$\frac{d\theta_2}{dt} = \omega_2 = \begin{cases} -\left(\dfrac{{l_{C_2C_3}}^2 + (r_c + r_{sb})^2 - (r_c - r_{ro})^2}{2(r_c - r_{ro}){l_{C_2C_3}}^2 \sin\theta_2}\right)\dfrac{dl_{C_2C_3}}{dt} & ,\theta_1 < \pi \\ \left(\dfrac{{l_{C_2C_3}}^2 + (r_c + r_{sb})^2 - (r_c - r_{ro})^2}{2(r_c - r_{ro}){l_{C_2C_3}}^2 \sin(2\pi - \theta_2}\right)\dfrac{dl_{C_2C_3}}{dt} & ,\theta_1 \geq \pi \end{cases} \tag{4.13}$$

$$\frac{d^2\theta_2}{dt^2} = \alpha_2 = \begin{cases} \left(\dfrac{{l_{C_2C_3}}^2 + (r_c + r_{sb})^2 - (r_c - r_{ro})^2}{2(r_c - r_{ro}){l_{C_2C_3}}^2 \sin\theta_2}\right)\left(\dfrac{-1}{\sin\theta_2}\dfrac{d^2l_{C_2C_3}}{dt^2} + \dfrac{\cos\theta_2}{\sin^2\theta_2}\dfrac{dl_{C_2C_3}}{dt}\omega_2\right) \\ + \dfrac{(r_c + r_{sb})^2 - (r_c - r_{ro})^2}{(r_c - r_{ro}){l_{C_2C_3}}^3 \sin\theta_2}\left(\dfrac{dl_{C_2C_3}}{dt}\right)^2 & ,\theta_1 < \pi \\ \left(\dfrac{{l_{C_2C_3}}^2 + (r_c + r_{sb})^2 - (r_c - r_{ro})^2}{2(r_c - r_{ro}){l_{C_2C_3}}^2 \sin(2\pi - \theta_2)}\right)\left(\dfrac{1}{\sin(2\pi - \theta_2)}\dfrac{d^2l_{C_2C_3}}{dt^2}\right. \\ \left. + \dfrac{\cos\theta_2}{\sin^2(2\pi - \theta_2)}\dfrac{dl_{C_2C_3}}{dt}\omega_2\right) \\ + \dfrac{-(r_c + r_{sb})^2 + (r_c - r_{ro})^2}{(r_c - r_{ro}){l_{C_2C_3}}^3 \sin(2\pi - \theta_2)}\left(\dfrac{dl_{C_2C_3}}{dt}\right)^2 & ,\theta_1 \geq \pi \end{cases} \tag{4.14}$$

where

ω_2 is the relative angular velocity of bearing surfaces between the rotor and eccentric (rad s^{-1}), and

α_2 is the relative angular acceleration of bearing surfaces between the rotor and eccentric (rad s^{-2}).

4.4.3 Kinematics of Split Bush

The angular velocity and acceleration of split bush about the centre C_3 are shown in Equations (4.15) and (4.16). These expressions are needed for the calculation of the frictional loss due to split bush's rotation in later chapters.

$$\frac{d\phi}{dt} = \begin{cases} -\omega_1 - \omega_2 & , \theta_1 < \pi \\ \omega_1 + \omega_2 & , \theta_1 \geq \pi \end{cases} \tag{4.15}$$

$$\frac{d^2\phi}{dt^2} = \begin{cases} -\alpha_2 & , \theta_1 < \pi \\ \alpha_2 & , \theta_1 \geq \pi \end{cases} \tag{4.16}$$

where

$\frac{d\phi}{dt}$ is the angular velocity of the split bush about centre C_3 (rad s^{-1}), and

$\frac{d^2\phi}{dt^2}$ is the angular acceleration of the split bush about centre C_3 (rad s^{-2}).

4.5 Thermodynamics

The thermodynamics modelling helps to predict the thermodynamics properties of the working fluid throughout a working cycle. The geometrical relations and the volume derivations developed in Section 4.2 and Section 4.3 will be used in the thermodynamics numerical iterations and formulations that describe these fluid properties change. A complete working cycle for a compressor involves three processes, namely, the suction, compression and discharge process. The modelling of each process is based on the mass and energy analysis of a control volume [128–132] using First Law of Thermodynamics and Conservation of Mass, as illustrated in Figure 4.3.

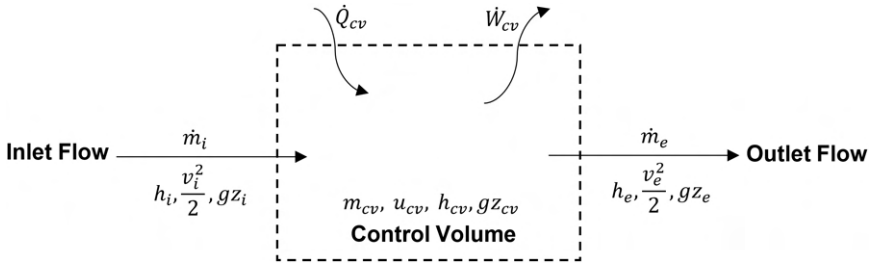

Figure 4.3: Energy balance of a generic control volume using First Law of Thermodynamics.

During each process, the suction and compression chambers can be modelled as a control volume with mass transfer due to inflow and outflow of working fluid through the ports and leakages via the clearances with moving boundary work and heat exchange interactions with the surroundings, as described in Equation (4.17). Any changes to the working fluid properties are assumed

to occur instantaneously and properties are uniform with no spatial variation throughout the working chamber [133], as mentioned in Section 4.1.

$$\frac{dE_{cv}}{dt} = \dot{Q}_{cv} - \dot{W}_{cv} + \sum_i \dot{m}_i \left(h_i + \frac{{v_i}^2}{2} + g z_i \right) - \sum_e \dot{m}_e \left(h_e + \frac{{v_e}^2}{2} + g z_e \right) \quad (4.17)$$

where

E_{cv} is the total energy of the control volume (J).
$\dot{Q}_{cv}$ is the net heat transfer rate into the control volume (W).
$\dot{W}_{cv}$ is the net work done per unit time by the control volume (W).
$\dot{m}_i$ is the mass flow rate of the inflow working fluid (kg s^{-1}).
$\dot{m}_e$ is the mass flow rate of the outflow working fluid (kg s^{-1}).
h_i is the specific enthalpy of the inflow working fluid (J kg^{-1}).
h_e is the specific enthalpy of the outflow working fluid (J kg^{-1}).
v_i is the velocity of the inflow working fluid (m s^{-1}).
v_e is the velocity of the outflow working fluid (m s^{-1}).
z_i is the vertical height of the inflow working fluid (m).
z_e is the vertical height of the outflow working fluid (m).
g is the gravitational acceleration (m s^{-2}).

Since the total energy of the control volume consists of mainly the internal energy, kinetic energy and gravitational potential energy (as shown in Equation (4.18))

$$E_{cv} = m_{cv} \left(u_{cv} + \frac{{v_{cv}}^2}{2} + g z_{cv} \right) \quad (4.18)$$

and the net work done by the control volume W_{cv} is due to moving boundary work done (as shown in Equation (4.19)),

$$\dot{W}_{cv} = p_{cv} \frac{dV_{cv}}{dt} \quad (4.19)$$

where

p_{cv} is the pressure of control volume (Pa), and

V_{cv} is the volume of the control volume (m^3).

Equation (4.17) can be rewritten as (4.20) with (4.18) and (4.19).

$$\begin{aligned}&\frac{d\left[m_{cv}\left(u_{cv}+\frac{{v_{cv}}^2}{2}+gz_{cv}\right)\right]}{dt}\\&=\dot{Q}_{cv}-p_{cv}\frac{dV_{cv}}{dt}+\sum_i \dot{m}_i\left(h_i+\frac{{v_i}^2}{2}+gz_i\right)-\sum_e \dot{m}_e\left(h_e+\frac{{v_e}^2}{2}+gz_e\right)\end{aligned} \tag{4.20}$$

As kinetic energy of the working fluid is relatively small compared to its enthalpy and the gravitational potential energy of the fluid does not change much throughout the working cycle, both terms can be neglected. Hence, by applying the product rule in Equation (4.20), the equation can be simplified as Equation (4.21).

$$\frac{du_{cv}}{dt}=\frac{1}{m_{cv}}\left(\dot{Q}_{cv}-p_{cv}\frac{dV_{cv}}{dt}+\sum_i \dot{m}_i h_i-\sum_e \dot{m}_e h_e-u_{cv}\frac{dm_{cv}}{dt}\right) \tag{4.21}$$

By Law of Conservation of Mass, the net rate of change of the mass in the control volume $\frac{dm_{cv}}{dt}$ can be expressed as:

$$\begin{aligned}\frac{dm_{cv}}{dt}&=\frac{d\rho_{cv}V_{cv}}{dt}\\&=\rho_{cv}\frac{dV_{cv}}{dt}+V_{cv}\frac{d\rho_{cv}}{dt}\\&=\sum_i \dot{m}_i-\sum_e \dot{m}_e\end{aligned} \tag{4.22}$$

where

ρ_{cv} is the density of the working fluid in the control volume (kg m^{-3}).

Furthermore, the net rate of change of mass in control volume in (4.22) can be reformulated as:

$$\frac{d\rho_{cv}}{dt}=\frac{1}{V_{cv}}\frac{dm_{cv}}{dt}-\frac{m_{cv}}{{V_{cv}}^2}\frac{dV_{cv}}{dt} \tag{4.23}$$

With the time derivative of density and specific internal energy of the control volume, $\frac{d\rho_{cv}}{dt}$, $\frac{du_{cv}}{dt}$ from Equations (4.23) and (4.21), the two independent and intensive properties ρ_{cv}, u_{cv} of the working fluid can be found via numerical iteration using Runge-Kutta method of 4^{th} order [134] with the help of real gas equation programme such as REFPROP [135]. With two independent and intensive properties, the other thermodynamic properties of the working fluid

can also be found according to state postulate [136].

The mass and energy analysis for the suction chamber are illustrated in Figure 4.4. For the suction process, there is only an inflow of working fluid from the suction port when no backflow occurs at the suction port. Backflow occurs when fluid from the dead volume of the compressor undergoes re-expansion and pressure in the suction chamber becomes greater than that of the fluid at the suction inlet. Throughout the suction process, leakages via the clearances also contribute to mass and internal energy increase in the suction chamber. The net rates of change of the mass and internal energy in the suction chamber are described by Equations (4.24) and (4.25).

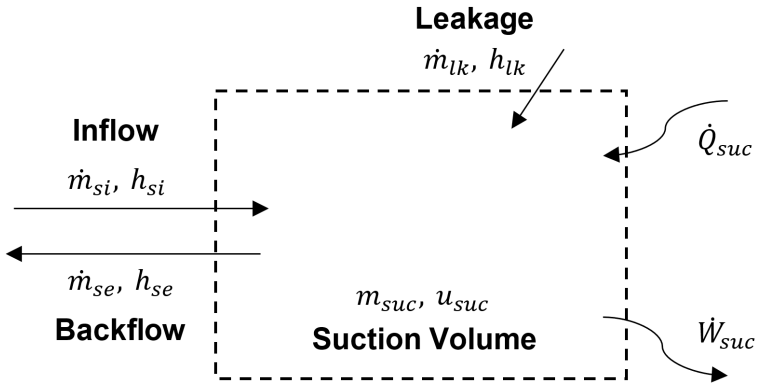

Figure 4.4: Mass and energy analysis of the suction control volume.

$$\frac{du_{suc}}{dt} = \begin{cases} \dfrac{1}{m_{suc}}\left(\dot{Q}_{suc} - p_{suc}\dfrac{dV_{suc}}{dt} + \dot{m}_{lk}h_{lk} + \dot{m}_{si}h_{si} - u_{suc}\left(\dot{m}_{lk} + \dot{m}_{si}\right)\right) & \textit{Normal suction} \\ \dfrac{1}{m_{suc}}\left(\dot{Q}_{suc} - p_{suc}\dfrac{dV_{suc}}{dt} + \dot{m}_{lk}h_{lk} - \dot{m}_{se}h_{se} - u_{suc}\left(\dot{m}_{lk} - \dot{m}_{se}\right)\right) & \textit{backflow occurs} \end{cases} \tag{4.24}$$

$$\frac{d\rho_{suc}}{dt} = \begin{cases} \dfrac{\left(\dot{m}_{lk} + \dot{m}_{si}\right)}{V_{suc}} - \dfrac{m_{suc}}{{V_{suc}}^2}\dfrac{dV_{suc}}{dt} & \textit{Normal suction} \\ \dfrac{\left(\dot{m}_{lk} - \dot{m}_{se}\right)}{V_{suc}} - \dfrac{m_{suc}}{{V_{suc}}^2}\dfrac{dV_{suc}}{dt} & \textit{backflow occurs} \end{cases} \tag{4.25}$$

Throughout the compression process, mass outflow due to leakages from the compression chamber to the suction side through the clearances will occur. During the discharge process, mass flows out of the compression chamber via the discharge port. Also, during the compression process, liquid refrigerant will be injected into the compression chamber when the injector was activated and there will be inflow of injected refrigerant into the control volume with the addition of the enthalpy of the injected refrigerant to the total energy content of the

compression volume. Instant vaporisation of the injected refrigerant and uniform mixing is assumed with the entire enthalpy of injected refrigerant taken into consideration in energy balance [63]. Similarly, there may be inflow of working fluid from the discharge pipe back into the compression chamber when backflow occurs. The process is illustrated in Figure 4.5 with the net rate of change of the mass and internal energy for the compression chamber described in equations (4.26) and (4.27).

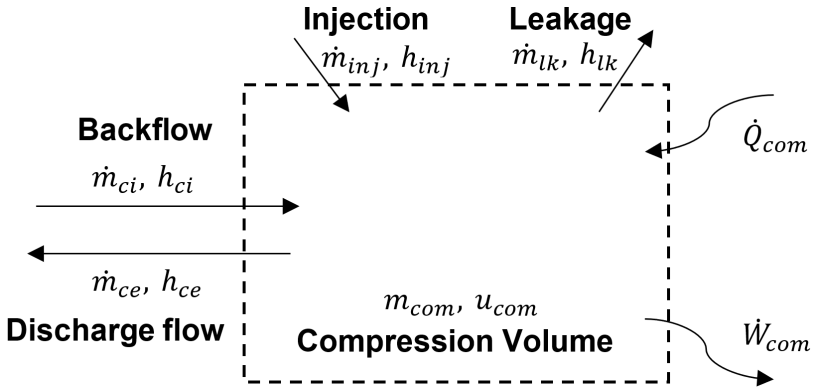

Figure 4.5: Mass and energy analysis of the compression control volume.

$$\frac{du_{com}}{dt} = \begin{cases} \frac{1}{m_{com}}\left(\dot{Q}_{com} - p_{com}\frac{dV_{com}}{dt} - \dot{m}_{lk}h_{lk} - u_{com}\dot{m}_{cl}\right) & \textit{compression} \\ \frac{1}{m_{com}}\left(\dot{Q}_{com} - p_{com}\frac{dV_{com}}{dt} - \dot{m}_{lk}h_{lk} + \dot{m}_{inj}h_{inj} - u_{com}\left(\dot{m}_{lk} + \dot{m}_{inj}\right)\right) & \textit{compression with injection} \\ \frac{1}{m_{com}}\left(\dot{Q}_{com} - p_{com}\frac{dV_{com}}{dt} - \dot{m}_{lk}h_{lk} + \dot{m}_{ci}h_{ci} - u_{com}\left(\dot{m}_{lk} + \dot{m}_{ci}\right)\right) & \textit{Discharge with backflow} \\ \frac{1}{m_{com}}\left(\dot{Q}_{com} - p_{com}\frac{dV_{com}}{dt} - \dot{m}_{lk}h_{lk} - \dot{m}_{ce}h_{ce} - u_{com}\left(\dot{m}_{lk} - \dot{m}_{ce}\right)\right) & \textit{Normal discharge} \end{cases} \tag{4.26}$$

$$\frac{d\rho_{com}}{dt} = \begin{cases} \frac{\dot{m}_{lk}}{V_{com}} - \frac{m_{com}}{{V_{com}}^2}\frac{dV_{com}}{dt} & \textit{compression} \\ \frac{\left(\dot{m}_{lk} + \dot{m}_{inj}\right)}{V_{com}} - \frac{m_{com}}{{V_{com}}^2}\frac{dV_{com}}{dt} & \textit{compression with injection} \\ \frac{\left(\dot{m}_{lk} + \dot{m}_{ci}\right)}{V_{com}} - \frac{m_{com}}{{V_{com}}^2}\frac{dV_{com}}{dt} & \textit{Discharge with backflow} \\ \frac{\left(\dot{m}_{lk} - \dot{m}_{ce}\right)}{V_{com}} - \frac{m_{com}}{{V_{com}}^2}\frac{dV_{com}}{dt} & \textit{Normal discharge} \end{cases} \tag{4.27}$$

The leakage flow $\dot{m}_{lk}h_{lk}$ that affects the mass and energy balance equations of both the suction and compression control volumes will be explained in detail

in Section 6.1. The computation of the heat transfer interaction $\dot{Q}_{cv}$ between the working fluid in the control volumes and the compressor's components that is required in Equation (4.21) for the thermodynamics iteration, will also be presented in Section 6.2.

4.6 Suction and Discharge Flows

The mass flow rates through the suction and discharge ports can be modelled as a unidirectional flow through an orifice [137] as shown in Figure 4.6. With the assumption of one dimensional, adiabatic and isentropic steady flow through a simple orifice with negligible initial upstream velocity and change in potential energy, the energy equation describing the orifice flow can be written as Equation (4.28). The ideal mass flow rate through the orifice is formulated as shown in (4.29).

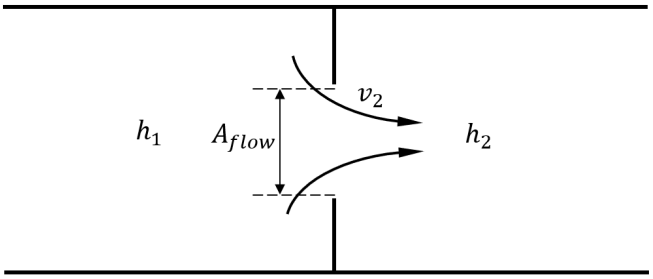

Figure 4.6: Orifice Flow Model.

$$v_2 = \sqrt{2(h_1 - h_{2s})} \tag{4.28}$$

$$\begin{aligned} \dot{m}_{orifice} &= \rho_1 A_{flow} v_2 \\ &= \rho_1 A_{flow} \sqrt{2(h_1 - h_{2s})} \end{aligned} \tag{4.29}$$

where,
v_2 is the velocity of the downstream flow (m s^{-1}).
h_1 is the specific enthalpy of the upstream flow (J kg^{-1}).
h_{2s} is the specific enthalpy of the downstream isentropic flow (J kg^{-1}).
ρ_1 is the density of the upstream flow (kg m^{-3}).
A_{flow} is the cross sectional area of orifice hole (m^2).
$\dot{m}_{orifice}$ is the mass flow rate through the orifice (kg s^{-1}).

The mass flow rate computed using Equation (4.29) would yield the maximum theoretical flow rate since the flow is ideal. In reality, reduced mass flow will

occur due to viscous dissipation and flow resistance that results in pressure loss. To account for the reduction in mass flow, a constant discharge coefficient C_d is introduced and the actual reduced mass flow is shown in Equation (4.30). The flow coefficients for the suction inlet and discharge port of the oil-free swing vane prototype are either empirically derived based on results from previous experimental studies or verified by computational modelling as the coefficients are dependent on the dimensioning of the orifice design and will be presented in Appendix B.

$$\dot{m}_{orifice} = C_d \rho_1 A_{flow} \sqrt{2(h_1 - h_{2s})} \tag{4.30}$$

As the discharge process in a positive-displacement type compressor is regulated by the dynamic motion of the discharge valve reed, the effective discharge flow area A_{flow} at the discharge port varies during discharge process. Detailed analysis of the valve dynamics and the variation of the effective flow area at the discharge port will be presented in Chapter 5.

4.7 Mass Discharge During Liquid Refrigerant Injection

As discussed in the literature review of Section 2.3 and Subsection 2.5.1, pressure drop and flashing of the subcooled or saturated liquid refrigerant would have occurred along the flow from the condenser to the injector and across the atomising nozzle in real operations. Two-phase saturated mixture should have been injected into the compression chamber for cooling. The modelling of this transient development of two-phase flashing refrigerant flow in the injector plays a significant role in determining the mass flow and liquid quality of the two-phase mixture injected which affects the amount of cooling achievable. In this section, conceptual modelling of the development of two-phase refrigerant R134a flow based on Homogeneous Frozen Model (HFM) [90–92] will be shown .

4.7.1 Mass Discharge Through Valve Orifice Of Solenoid Valve

The flow from the condenser to the injector's solenoid valve inlet (as shown in Figure 4.7) is to be considered as subcooled or saturated liquid phase because the length and size of pipe between the condenser and solenoid valve inlet can be carefully selected to ensure only single liquid phase is present in the pipe. In addition, the discharge flow through the solenoid valve orifice can also be

considered as liquid phase only due to metastability characteristic of refrigerant flow in short-tube orifice. Nilpueng et al. [138, 139] had experimentally found that metastable liquid R134a flows remains in liquid state in an orifice with length-to-diameter $\left(\frac{L_{orifice}}{D_{orifice}}\right)$ ratio of less than 2.91. With reference to the solenoid valve orifice dimension shown in Section F.8, it can be seen that this criterion is not exceeded and discharge flow at solenoid valve can be assumed to be in liquid phase.

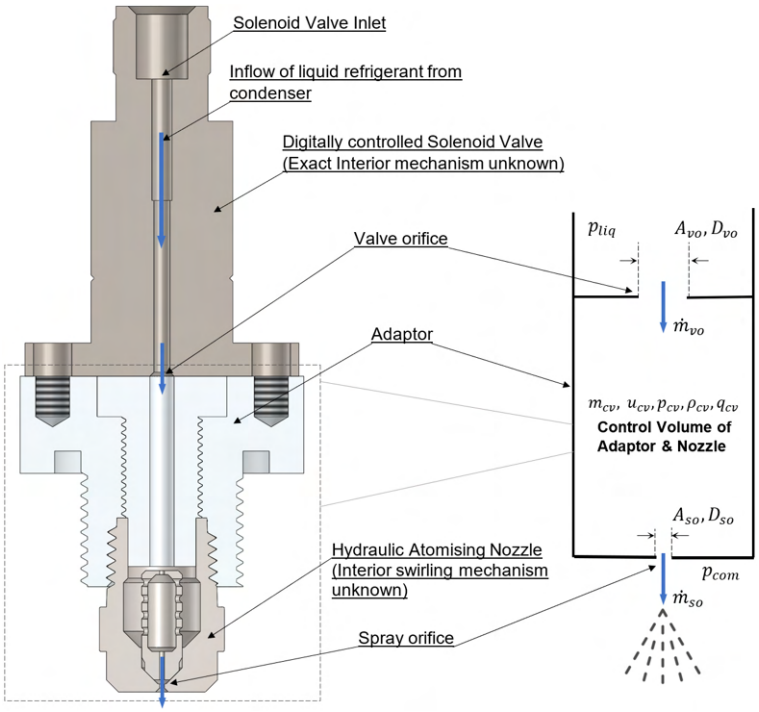

Figure 4.7: Illustration of injector — (a) Sectional view of injector (interior mechanisms of solenoid valve and nozzle are unknown) (b) Conceptual diagram of injector based on control volume analysis.

Since the flow through valve orifice of solenoid valve is single-phase liquid state, the standard equation for single-phase incompressible fluid is used to model the mass flow through the valve orifice, as shown in Equation (4.31).

$$\begin{aligned} \dot{m}_{vo} &= C_d \frac{\pi}{4} {D_{vo}}^2 \sqrt{\frac{2\rho_{liq}(p_{liq} - p_{cv})}{\left(1 - \frac{{D_{vo}}^2}{{D_{sc}}^2}\right)}} \\ &\approx C_d \frac{\pi}{4} {D_{vo}}^2 \sqrt{2\rho_{liq}(p_{liq} - p_{cv})} \end{aligned} \tag{4.31}$$

where

$\dot{m}_{vo}$ is the mass flow rate discharged through the valve orifice (kg s^{-1}).

C_d is the discharge coefficient for the valve orifice (-).
D_{vo} is the diameter of the valve orifice (m).
D_{sc} is the diameter of the solenoid valve inlet (m).
ρ_{liq} is the density of liquid refrigerant from the condenser (kg m^{-3}).
p_{cv} is the pressure of the control volume of the adaptor and nozzle cavity (Pa).
p_{liq} is the pressure of liquid refrigerant from the condenser (Pa).

The inlet of the solenoid valve is much larger than the diameter of its orifice so the denominator of Equation (4.31) can be neglected without much loss in accuracy.

4.7.2 Mass Discharge Through Spray Orifice of Hydraulic Atomising Nozzle

As the single-phase refrigerant flows into the larger adaptor cavity and the nozzle core via the valve orifice, flashing of liquid refrigerant would have occurred and the resultant refrigerant injected into the downstream compression chamber via the spray orifice of the hydraulic atomising nozzle will eventually be in two-phase state. There are two possible two-phase discharge flow conditions that may occur in the spray orifice. The first is sub-critical flow and the second is sonic or critical flow where the orifice is choked with mass limiting flow. Equations to describe these two discharge spray conditions will be shown.

Sub-critical Discharge

Based on HFM analysis mentioned in Subsection 2.5.1, the two-phase flow through the spray orifice is assumed to be one-dimensional and ideal with homogeneous mixture of saturated liquid and vapour. As injection is a short pulse, usually less than a third of the duration of a working cycle, heat transfer effect assumed negligible and flow is considered to be adiabatic. Also, the quality of the mixture does not change during the flow through the orifice and hence, the quality is 'frozen'.The discharge velocity of the two-phase fluid may be found using the one-dimensional flow energy balance equation as present in Equation (4.32).

$$\frac{{v_{so}}^2}{2} = -\int_{p_{com}}^{p_{cv}} \frac{dp}{\rho_{cv}} \tag{4.32}$$

where ρ_{cv} is the density of the two-phase mixture shown in Equation (4.33)

$$\frac{1}{\rho_{cv}} = \frac{q}{\rho_g} + \frac{1-q}{\rho_f} \tag{4.33}$$

and therefore, (4.32) is further formulated as (4.34) with quality q as constant:

$$\frac{{v_{so}}^2}{2} = \frac{1-q}{\rho_f}(p_{cv} - p_{com}) - q\int_{p_{com}}^{p_{cv}} \frac{dp}{\rho_g} \tag{4.34}$$

In addition, the vapour in the mixture is assumed to satisfy the isentropic gas equation with ideal gas behaviour.

$$\frac{p}{{\rho_g}^\gamma} = \frac{p_{cv}}{{\rho_g}^\gamma} = Constant \tag{4.35}$$

Substitution of Equation (4.35) into (4.34) yields:

$$\frac{{v_{so}}^2}{2} = \frac{1-q}{\rho_f}(p_{cv} - p_{com}) + \frac{q{p_{cv}}^{\frac{1}{\gamma}}}{\rho_g\left(1-\frac{1}{\gamma}\right)}({p_{cv}}^{1-\frac{1}{\gamma}} - {p_{com}}^{1-\frac{1}{\gamma}}) \tag{4.36}$$

The mass discharge rate for sub-critical flow is as shown:

$$\begin{aligned}\dot{m}_{so} &= C_d\frac{\pi}{4}{D_{so}}^2\rho_{cv}v_{so} \\ &= \frac{C_d\frac{\pi}{4}{D_{so}}^2}{\left(\frac{q}{\rho_g} + \frac{(1-q)}{\rho_f}\right)}\left[2\left(\frac{1-q}{\rho_f}(p_{cv} - p_{com}) + \frac{q{p_{cv}}^{\frac{1}{\gamma}}}{\rho_g\left(1-\frac{1}{\gamma}\right)}({p_{cv}}^{1-\frac{1}{\gamma}} - {p_{com}}^{1-\frac{1}{\gamma}})\right)\right]^{0.5}\end{aligned} \tag{4.37}$$

where
$\dot{m}_{so}$ is the mass flow rate discharged through the spray orifice (kg s^{-1}).
C_d is the discharge coefficient for the spray orifice (-).
D_{so} is the diameter of the spray orifice (m).
q is the vapour quality of the saturated mixture in adaptor and nozzle cavity.
ρ_g is the vapour density of the saturated mixture in adaptor and nozzle cavity (kg m^{-3}).
ρ_f is the liquid density of the saturated mixture in adaptor and nozzle cavity (kg m^{-3}).
ρ_{cv} is the overall density of the saturated mixture in adaptor and nozzle cavity (kg m^{-3}).
p_{cv} is the upstream pressure of the control volume of the adaptor and nozzle cavity (Pa).
p_{com} is the downstream pressure of compression chamber (Pa).
γ is the heat capacity ratio of the saturated mixture in adaptor and nozzle cavity (-).

Critical Discharge

The mass discharge under critical conditions can be obtained from Equation (4.37) by substituting the sonic velocity (4.39) in the two-phase fluid for the discharge velocity. Since the flow is choked, the critical mass flow is dependent on the critical downstream properties.

$$\dot{m}_{so} = C_d \frac{\pi}{4} {D_{so}}^2 \rho_{cr} v_{ss} \tag{4.38}$$

The detailed derivation of the sonic velocity v_{ss} and Equation (4.40) is given in Section A.3.

$$v_{ss} = \sqrt{\left(\frac{q\gamma p_{cr}}{\rho_{g_{cr}}}\right)\left(1 + \left(\frac{1-q}{q}\right)\left(\frac{\rho_{g_{cr}}}{\rho_f}\right)\right)^2} \tag{4.39}$$

$$\rho_{cr} v_{ss} = \sqrt{\frac{\gamma p_{cr} \rho_{g_{cr}}}{q}} \tag{4.40}$$

In terms of downstream critical pressure and gas density p_{cr}, $\rho_{g_{cr}}$ the mass discharge at critical condition is given by:

$$\dot{m}_{so} = C_d \frac{\pi}{4} {D_{so}}^2 \sqrt{\frac{\gamma p_{cr} \rho_{g_{cr}}}{q}} \tag{4.41}$$

However, downstream critical pressure p_{cr} can be further simplified to be in terms of critical pressure ratio r_{cr} and pressure of control volume p_{cv}:

$$r_{cr} = \frac{p_{cr}}{p_{cv}} \tag{4.42}$$

Using isentropic gas law, downstream critical gas density $\rho_{g_{cr}}$ can be written in terms of critical pressure ratio r_{cr} and gas density of control volume ρ_g:

$$\rho_{g_{cr}} = \rho_g {r_{cr}}^{\frac{1}{\gamma}} \tag{4.43}$$

and the critical pressure ratio r_{cr} can be defined in terms of properties of the control volumes as shown (4.44) which is a transcendent equation that can be solved computationally using bisection method. The detail derivation of (4.44) is shown in Section A.3.

$$\left(\frac{1}{r_{cr}} - 1\right) + X_{cr} \left(\frac{\gamma}{\gamma - 1}\right) \left({r_{cr}}^{\frac{1-\gamma}{\gamma}} - 1\right) = \frac{\gamma X_{cr}}{2} \left(\frac{1}{X_{cr}} + 1\right)^2 \tag{4.44}$$

$$X_{cr} = \left(\frac{q}{1-q}\right) \left(\frac{\rho_f}{\rho_g}\right) {r_{cr}}^{-\frac{1}{\gamma}} \tag{4.45}$$

The mass discharge at critical condition in (4.41) can be re-written as:

$$\dot{m}_{so} = C_d \frac{\pi}{4} {D_{so}}^2 \sqrt{\frac{\gamma \rho_g p_{cv} {r_{cr}}^{\frac{\gamma+1}{\gamma}}}{q}} \tag{4.46}$$

Since the quality and the mass discharge through the spray orifice are dependent on the conditions of the expanded refrigerant in the adaptor cavity and the nozzle core, mass and energy analysis of control volume shown in Section 4.5 is also applied here to determine the thermodynamic properties of the expanded refrigerant in the control volume of the adaptor cavity and the

nozzle core (as shown in Figure 4.8). Since the heat transfer surface of the adaptor cavity is small and residing time of the mixture in the control volume is a fraction of the injection duration, heat transfer to the control volume is neglected. In addition, there is no work interaction of the mixture with the surrounding. The mass discharge $\dot{m}_{vo}$ via the valve orifice and mass discharge $\dot{m}_{so}$ out of the injector via spray orifice will help solve for the density change $\frac{d\rho_{cv}}{dt}$ in the control volume and the enthalpy of both flow will help solve for the energy change $\frac{du_{cv}}{dt}$ in the control volume. The enthalpy of the injected refrigerant, which is also the enthalpy of the spray orifice discharge flow from the control volume, will be used in Equation (4.27) in Section 4.5 for thermodynamic analysis of liquid refrigerant injection cooling due to the vaporisation of liquid refrigerant in the injected mixture.

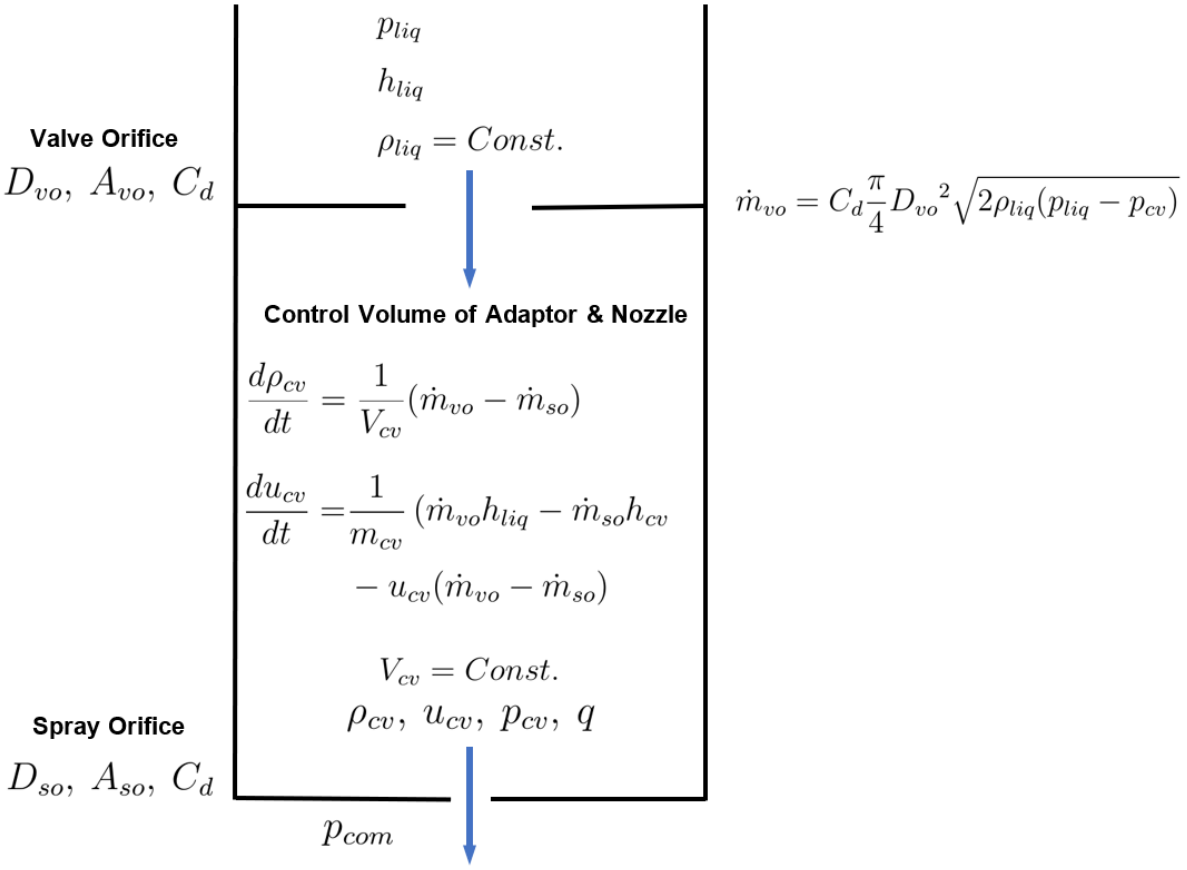

$$\frac{p_{com}}{p_{cv}} > r_{cr} \qquad \dot{m}_{so} = \frac{C_d}{\left(\frac{q}{\rho_g} + \frac{(1-q)}{\rho_f}\right)} \frac{\pi}{4} {D_{so}}^2 \left[2 \left(\frac{1-q}{\rho_f}(p_{cv} - p_{com}) + \frac{q p_{cv}^{\frac{1}{\gamma}}}{\rho_g \left(1 - \frac{1}{\gamma}\right)} (p_{cv}^{1-\frac{1}{\gamma}} - p_{com}^{1-\frac{1}{\gamma}}) \right) \right]^{0.5}$$

$$\frac{p_{com}}{p_{cv}} \leq r_{cr} \qquad \dot{m}_{so} = C_d \frac{\pi}{4} {D_{so}}^2 \sqrt{\frac{\gamma \rho_g p_{cv} {r_{cr}}^{\frac{\gamma+1}{\gamma}}}{q}}$$

Figure 4.8: Overall relationships governing the two-phase orifice flow through the solenoid valve and spray nozzle based on HFM model.

4.8 Summary

In this chapter, the basic geometrical relations, kinematics and the thermodynamics analysis of the swing vane mechanism are presented. The summary of this chapter can be presented as follows:

- The mathematical models for the geometric relations of the swing vane mechanism and the volume of the working chambers (suction and compression chambers) were developed.
- The mathematical models for the kinematics of the rotor with fixed vane and the split bush were developed.
- Mass and energy balance analysis of control volumes based on First Law of Thermodynamics and Conservation of Mass are applied to the thermodynamic analysis of the working cycle which involves suction of working fluid, compression and discharge of compressed working fluid.
- Suction and discharge flows are modelled as one-dimensional orifice flow with coefficient of discharge to account for flow reduction.
- Two-phase flow of injected refrigerant is modelled using Homogeneous Frozen Model (HFM).

In the next chapter, the modelling of the vibrational dynamics of the valve reed which affects the discharge mass flow and the dynamics analysis of the swing vane mechanism under dry rubbing condition will be presented and discussed.

Chapter 5

Theoretical Model - Valve Dynamics and Dynamics of Oil-Free Swing Vane Compressor

In this chapter, the theoretical modelling of the valve vibration and the dynamics of an oil-free swing vane mechanism will be presented. The vibrational dynamics of a non-uniform width reed-type discharge valve will first be modelled based on force balance analysis and Finite Element Method (FEM) in order to determine the valve displacement which affects the effective discharge flow area and discharge mass flow as previously discussed in Section 4.6. This is followed by the dynamics model where kinematics relations derived in Section 4.4 will be used in the dynamics analysis of the swing vane mechanism under dry rubbing condition to predict relevant frictional forces and losses at various bearing surfaces.

5.1 Valve Dynamics

In general, the valve system used in a postive-displacement type compressor consists of a valve reed and a valve stop plate, as shown in Figure 5.1. At any given instance, the free end of the valve reed is under constant pre-set discharge pressure that forces the reed to close off the discharge port. During the discharge process, the valve reed opens when the pressure of the working fluid in the compression chamber exceeds the pre-set discharge pressure and is sufficient to overcome the stiffness of the valve reed. The valve stop, on the other hand, is installed on top of the reed to limit the maximum valve deflection to prevent any premature valve reed failure due to overbending.

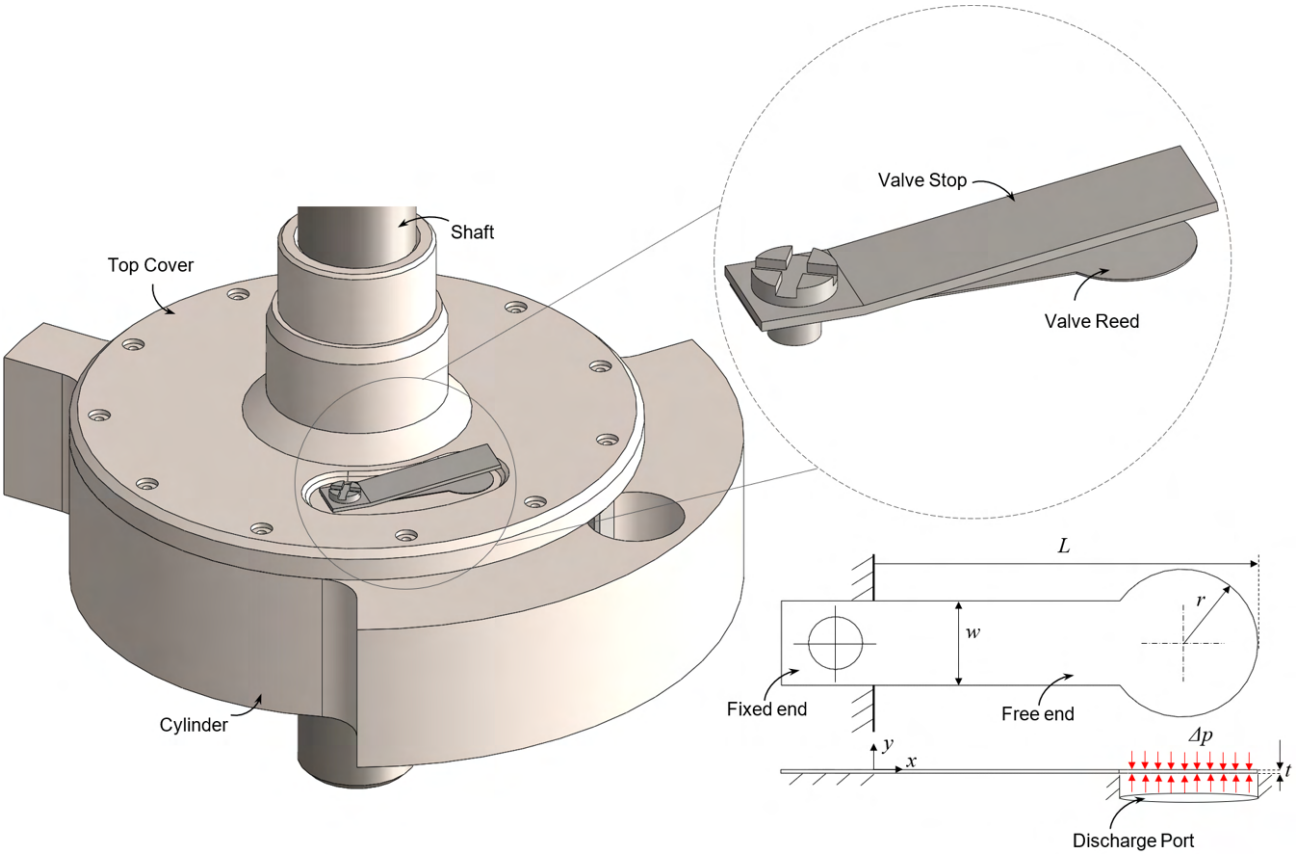

Figure 5.1: Illustration of discharge valve system in a conventional positive-displacement compressor.

Valve dynamics is a critical aspect of the discharge process as it affects the effective flow area for the discharged fluid. To study the dynamics of the valve response, the valve reed is modelled as a clamped-free cantilever beam. The free body diagram of a valve element of an arbitrarily shaped valve plate is presented in Figure 5.2. The element experiences non-linear bending moment M due to lateral loading from differential pressure Δp, internal shear force V and damping force $c\frac{dy}{dt}\delta x$ due to air-cushioning effect and material deformation, where $\Delta p = (p_{com} - p_{disc})$ is the pressure difference between the pressure of compression chamber and the pre-set discharge pressure and c is the damping coefficient.

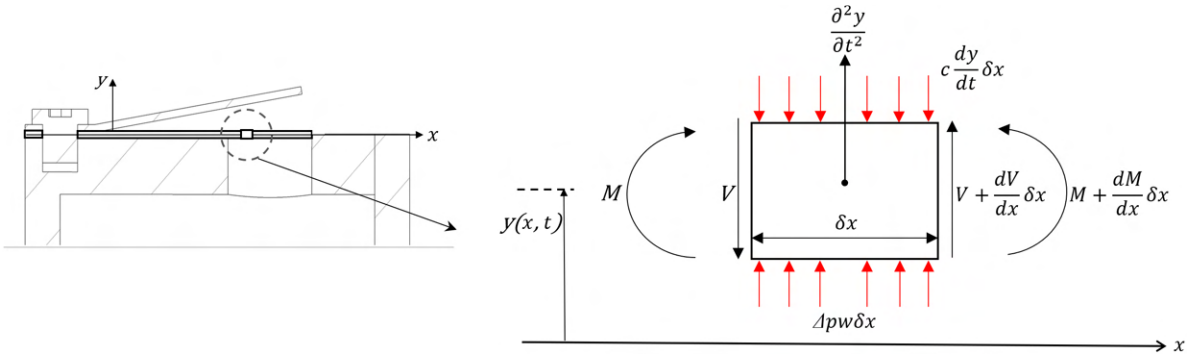

Figure 5.2: Free body diagram of infinitesimal element along the valve.

The overall force and moment balance analysis of the element are shown in Equations (5.1) and (5.2), respectively.

$$-V+\left(V+\frac{\partial V}{\partial x}\delta x\right)+\Delta p(x,t)\delta x-c\frac{\partial y}{\partial t}\delta x=\rho A(x)\frac{\partial^2 y}{\partial t^2} \tag{5.1}$$

$$\left(V+\frac{\partial V}{\partial x}\delta x\right)\delta x+\left(M+\frac{\partial M}{\partial x}\delta x\right)-M=0 \tag{5.2}$$

Ignoring the second and higher order δx terms in Equation (5.2), Equation (5.3) can be obtained.

$$V=-\frac{\partial M}{\partial x} \tag{5.3}$$

Based on the flexural theory, the relationship between bending moment and beam deflection can be expressed in Equation (5.4).

$$M=EI(x)\frac{\partial^2 y}{\partial x^2} \tag{5.4}$$

where
E is the Young's Modulus of valve reed material (Pa), and
I is the second moment of the valve reed's cross section about its neutral axis (m^4).

Combining Equation (5.1) with Equations (5.3) and (5.4), the general governing force balanced equation of transverse vibration of an arbitrarily shaped valve [140] is given as:

$$-\frac{\partial^2}{\partial x^2}\left(EI(x)\frac{\partial^2 y}{\partial x^2}\right)-c\frac{\partial y}{\partial t}+\Delta p(x,t)w=\rho A(x)\frac{\partial^2 y}{\partial t^2} \tag{5.5}$$

where
ρ is the density of valve reed material (kg m^{-3}),
$A(x)$ is the cross-sectional area of an arbitrarily shaped valve reed (m^2), and
c is the damping coefficient from gas and internal material damping (-).

Considering principle of superposition for transverse vibration, the valve deflection is assumed to take on the form of a series of separable variable shape functions [140]:

$$y(x,t) = \sum_{n=1}^{\infty} Y_n(x)\tau_n(t) \tag{5.6}$$

which is the product of mode shape $Y(x)$ and time-dependent mode participation factor $\tau(t)$. Hence, the overall governing equation of valve deflection in terms of separable variable shape functions is given by Equation (5.7).

$$\tau_n(t)\frac{d^2}{dx^2}\left(EI(x)\frac{d^2Y_n(x)}{dx^2}\right) + cY_n(x)\frac{d\tau_n(t)}{dt} + \rho A(x)Y_n(x)\frac{d^2\tau_n(t)}{dt^2} = \Delta p(x,t)w \tag{5.7}$$

The valve displacement $y(x,t)$ is obtained by individually solving for the mode shape Y_n and mode participation factor τ_n.

5.1.1 Mode Shapes of Valve Reed

As the mode shapes are invariant under free or forced vibrations, the homogeneous part of Equation (5.7) can be addressed to solve for the mode shapes function $Y_n(x)$ which yields Equation (5.8) by the method of separation of variables as follows:

$$\begin{aligned}
&\tau_n(t)\frac{d^2}{dx^2}\left(EI(x)\frac{d^2Y_n(x)}{dx^2}\right) + cY_n(x)\frac{d\tau_n(t)}{dt} + \rho A(x)Y_n(x)\frac{d^2\tau_n(t)}{dt^2} = 0 \\
&\frac{1}{\rho A(x)Y_n(x)}\frac{d^2}{dx^2}\left(EI(x)\frac{d^2Y_n(x)}{dx^2}\right) = -\frac{c}{\rho A(x)\tau_n(x)}\frac{d\tau_n(t)}{dt} - \frac{1}{\tau_n(x)}\frac{d^2\tau_n(t)}{dt^2} = {\lambda_n}^2
\end{aligned} \tag{5.8}$$

By re-arranging the left-hand side of Equation (5.8), Equation (5.9) is obtained as:

$$\frac{d^2}{dx^2}\left(EI(x)\frac{d^2Y_n(x)}{dx^2}\right) = \rho A(x)Y_n(x){\lambda_n}^2 \tag{5.9}$$

where
λ_n is the natural frequency of vibration mode n (Hz).

with the boundary conditions of the valve vibration during discharge process:

$$
\begin{aligned}
&\text{During valve lift-off (clamped-free)} && \text{at } x = 0,\ Y_n = 0,\ \frac{dY_n}{dx} = 0 && \text{(a)}\\
& && \text{at } x = L,\ \frac{d^2Y_n}{dx^2} = 0,\ \frac{d^3Y_n}{dx^3} = 0 && \text{(b)}\\
&\text{Hitting valve stop (clamped-pinned,} \\
&y = 0 \text{ relative to the height of valve stop)} && \text{at } x = 0,\ Y_n = 0,\ \frac{dY_n}{dx} = 0 && \text{(c)}\\
& && \text{at } x = L,\ Y_n = 0,\ \frac{d^2Y_n}{dx^2} = 0 && \text{(d)}
\end{aligned}
\tag{5.10}
$$

It can be observed that the mode shapes Y_n, are orthogonal in nature, considering the boundary conditions of Equation (5.10)(a) to (d):

$$
\int_0^L \rho A(x) Y_n Y_m dx = \begin{cases} 0, \ if\ m \neq n \\ 1, \ if\ m = n \end{cases} \tag{5.11}
$$

Equation (5.9), however, is a non-linear fourth order partial differential equation since both the cross sectional area and second moment of area of an arbitrarily-shaped valve reed can be non-uniform lengthwise and are functions of x, making closed-formed exact solution to Equation (5.9) impossible. The mode shapes Y_n and natural frequencies λ_n are approximated using Finite Element Method (FEM) which is shown in Appendix A Section A.4. The approximated mode shapes Y_n are in forms of linear polynomial functions as given in Equation (A.35) and can be easily used in the numerical iteration of mode participation factor τ_n which will be shown in the next Subsection 5.1.2. In most cases, the valve only exhibits first vibration mode during discharge and only mode 1 modal shape Y_1 is used in computation of valve displacement $y(x, t)$.

5.1.2 Numerical Iteration of Mode Participation Factor

The time-variant factor or mode participation factor $\tau_n(t)$ has to be solved using fourth-order Runge-Kutta numerical iterative method (RK4) since it is dependent on external excitations such as differential pressure $\Delta p(x, t)$ which varies with the pressure of the compression chamber. By multiplying Y_n throughout (5.7), integrating the equation over the length of valve L and applying orthogonality of Y_n based on (5.11), Equation (A.19) is obtained as follows:

$$\int_0^L \Delta P(x,t) w dx =$$
$$\int_0^L \left(\tau_n(t) \frac{d^2}{dx^2} \rho A(x) Y_n(x) {\lambda_n}^2 + c Y_n(x) \frac{d\tau_n(t)}{dt} + \rho A(x) Y_n(x) \frac{d^2\tau_n(t)}{dt^2} \right) dx$$

$$\frac{d^2\tau_n(t)}{dt^2} = \int_0^L \left(p_{com} - p_{disc}\right) w Y_n dx - c \frac{d\tau_n(t)}{dt} \int_0^L {Y_n}^2(x) dx - {\lambda_n}^2 \tau_n \tag{5.12}$$

In addition, Equation (5.12) can be separated into two first order differential equations by letting $\frac{d\tau}{dt} = h$:

$$\frac{dh}{dt} = \int_0^L \left(p_{com} - p_{disc}\right) w Y_n dx - c \frac{d\tau_n(t)}{dt} \int_0^L {Y_n}^2(x) dx - {\lambda_n}^2 \tau_n \tag{5.13}$$

$$\frac{d\tau}{dt} = h \tag{5.14}$$

By solving Equations (5.13) and (5.14) numerically using RK4 integration method together with the pressure of the compression chamber from the thermodynamics model, the mode participation factor $\tau_1(t)$ can be obtained. Subsequently, the valve deflection $y(x,t)$ can be found by multiplying it $\tau_1(t)$ with the mode shape $Y_1(x)$.

5.1.3 Effective Discharge Flow Area

The effective discharge flow area is found by comparing the circumferential flow area and the discharge port cross-sectional area, as illustrated in Figure 5.3 and shown in Equation (5.16). The smallest area will be the effective discharge area as it is the limiting flow area.

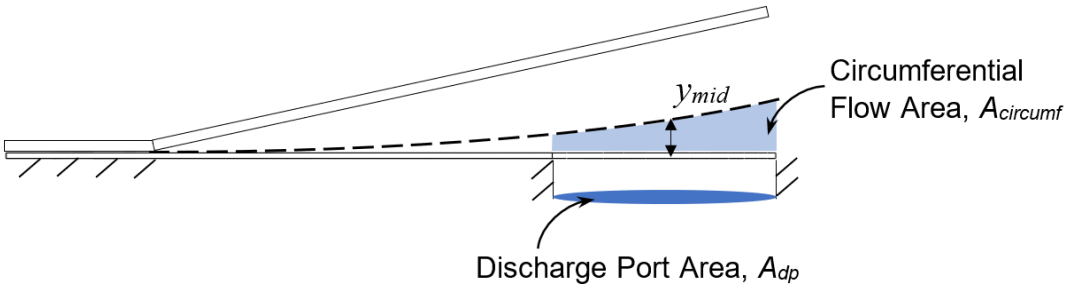

Figure 5.3: Schematic diagram of valve system showing different flow area for discharge.

$$A_{circumf} = 2\pi r_{dp} y_{mid} \tag{5.15}$$

$$A_{disc_{effective}} = \begin{cases} A_{circumf}, & for\ A_{circumf} < A_{dp} \\ A_{dp}, & for\ A_{circumf} > A_{dp} \end{cases} \tag{5.16}$$

5.2 Dynamics Of Oil-Free Swing Vane Mechanism

In this section, the dynamic analysis which focuses on the modelling of forces and torques acting on the moving components will be presented. The forces and torques calculated will be used for further computation of motor power input, the frictional losses and the mechanical efficiency. Since most of the bearing surfaces of the oil-free swing vane mechanism are dry rubbing (except eccentric-rotor and shaft bearing surfaces where sealed grease-lubricated ball bearings are used), Coulomb's law of friction model given in Equation (5.17) is used to model the dry contact frictional forces and torques. In this model, N is the normal load and μ, which represents the coefficient of friction, is assumed to be a constant and is only dependent on the surface nature.

$$F_f = \mu N \tag{5.17}$$

However, as discussed in the literature review of Section 2.4, friction coefficients of self-lubricating bearing surfaces are found to change with respect to sliding velocity. For example in the case of PEEK, it was found that friction coefficient between pure PEEK and stainless steel can drastically increase from 0.3 to 0.55 [73] at high interface temperature due to wear and transfer of irregular PEEK on counter sliding surface which leads to rubbing of similar material [79]. This means that surface nature of the self-lubricating bearing surfaces will change over the dry operation of the prototype and friction coefficient μ may vary. For simplicity of modelling and dynamic analysis of swing vane mechanism under worst case of dry rubbing, the highest value of friction coefficient for each pair of bearing surfaces will be used in the modelling and is assumed to be constant throughout the working cycle. In addition, the analysis of the model does not take into consideration the vibration of the moving parts within the clearances.

5.2.1 Dynamic Analysis Of Eccentric Shaft

Figure 5.4 illustrates the dry contact forces and torques acting on the eccentric shaft. As the ball bearings are tight-fitted onto the eccentric and shaft, the inner races of the ball bearings and the eccentric shaft together with the counterweight are considered as one free body.

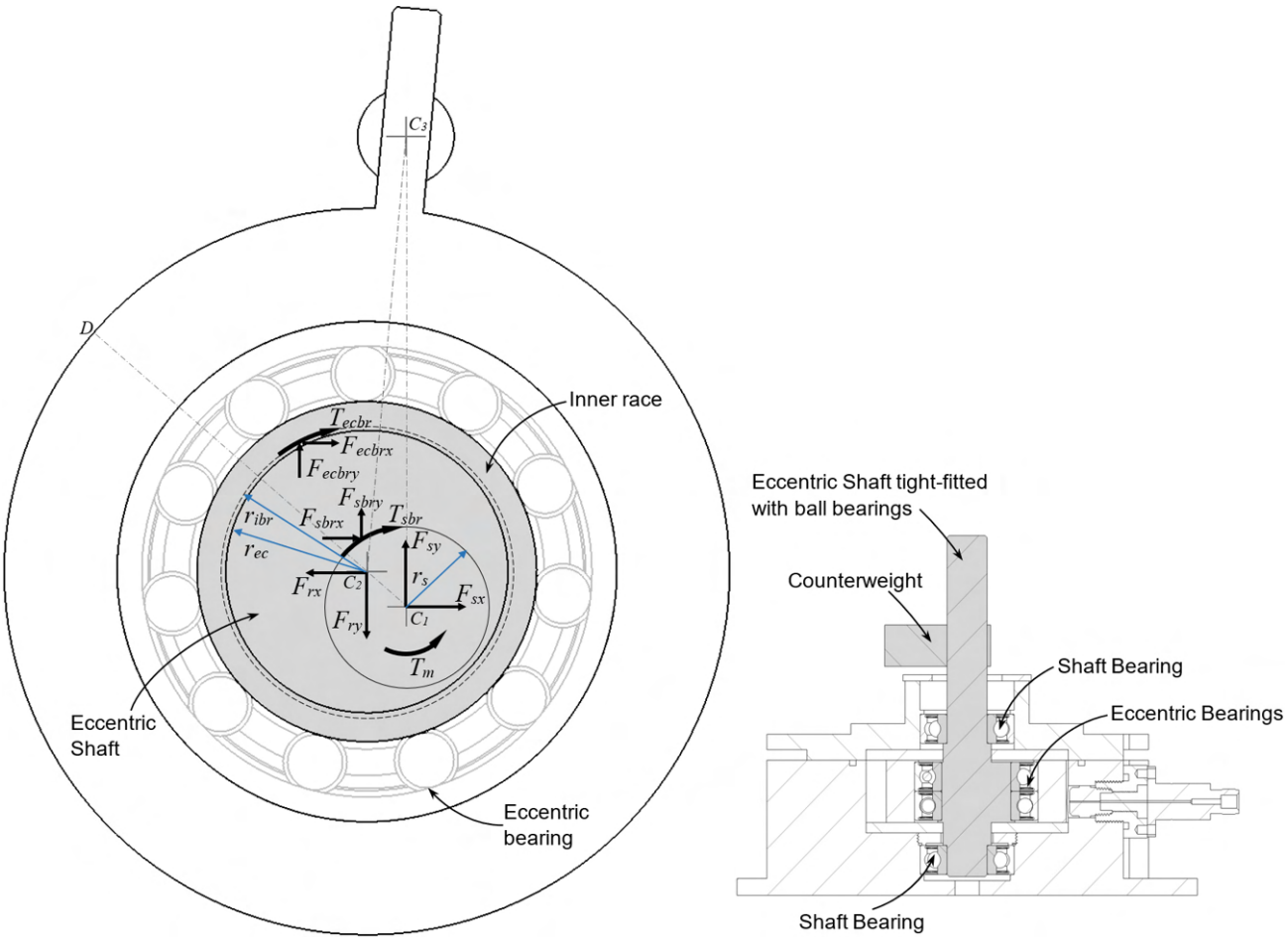

Figure 5.4: Illustration of all forces and torques acting on eccentric shaft.

$$\rightarrow_{+ve} \sum F_x = 0,$$

$$F_{sx} - F_{rx} + F_{sbrx} + F_{ecbrx} - m_s c_m {\omega_1}^2 \sin\theta_1 = 0 \qquad (5.18)$$

$$\uparrow_{+ve} \sum F_y = 0,$$

$$F_{sy} - F_{ry} - F_{sbry} - F_{ecbry} + m_s c_m {\omega_1}^2 \cos\theta_1 = 0 \qquad (5.19)$$

$$
\begin{aligned}
&\circlearrowleft_{+ve} \sum M_{C_1} = 0, \\
&T_m - F_{ecbrx} e \cos\theta_1 + F_{ecbry} e \sin\theta_1 - T_{ecbr} - T_{sbr} = 0 \quad \text{for } F_{rx} > 0 \ \& \ F_{ry} > 0 \\
&T_m + F_{ecbrx} e \cos\theta_1 - F_{ecbry} e \sin\theta_1 - T_{ecbr} - T_{sbr} = 0 \quad \text{for } F_{rx} < 0 \ \& \ F_{ry} < 0 \\
&T_m - F_{ecbrx} e \cos\theta_1 - F_{ecbry} e \sin\theta_1 - T_{ecbr} - T_{sbr} = 0 \quad \text{for } F_{rx} < 0 \ \& \ F_{ry} > 0 \\
&T_m + F_{ecbrx} e \cos\theta_1 + F_{ecbry} e \sin\theta_1 - T_{ecbr} - T_{sbr} = 0 \quad \text{for } F_{rx} > 0 \ \& \ F_{ry} < 0
\end{aligned}
\tag{5.20}
$$

where
F_s is the radial contact force exerted on the shaft by the shaft bearings (N).
F_r is the radial contact force exerted on the eccentric by the rotor (N).
F_{sbr} is the tangential contact force exerted on the shaft by the shaft bearings (N).
F_{ecbr} is the tangential contact force exerted on the eccentric by the eccentric bearings (N).
T_{sbr} is the frictional moment of the shaft bearings (N.m).
T_{ecbr} is the frictional moment of the eccentric bearings (N.m).
T_m is the motor input torque to drive the compressor (N.m).
r_{ec} is the radius of the eccentric (m).
r_{ibr} is the radius of the deep-grooved inner race of eccentric bearing and is approximated to be radius of eccentric $r_{ibr} \approx r_{ec}$ (m).
e is the eccentricity of the eccentric shaft $(r_c - r_{ro})$ (m).
c_m is the centre of gravity of the eccentric shaft with counterweight about centre C_1 (m).
m_s is the mass of the eccentric shaft with counterweight (kg).

Bearing Friction

The bearing friction is not constant throughout the working cycle and depends on the bearing loads (e.g. F_s, F_r) and the tribological conditions in the bearing. SKF self-lubricated sealed ball bearings are used in the operation of the oil-free swing vane prototype and the frictional moments of the bearings T_{sbr},T_{ecbr}, are calculated based on SKF empirical model with reference to Appendix F, Section F.14.

$$T_{sbr} = (M_{rr} + M_{sl} + M_{seal})_{sbr} \tag{5.21}$$

$$T_{ecbr} = (M_{rr} + M_{sl} + M_{seal})_{ecbr} \tag{5.22}$$

where
M_{rr} is the rolling frictional moment due to the viscous shear force from the grease (N.m),
M_{sl} is the sliding frictional moment which is dependent on the axial and radial contact loadings (N.m), and
M_{seal} is the constant frictional moment which is dependent on the seal and bearing types (N.m).

The directions of the tangential contact forces F_{sbr} and F_{ecbr} are varying throughout the working cycle and are dependent on the position of the radial contact forces F_s and F_r. An illustration of the directions of the tangential contact force F_{ecbr} is given in Figure 5.5. The forces can be determined based on the bearing frictional moments M_{rr}, M_{sl} that are dependent on contact loading and are shown in equations (5.23) and (5.24).

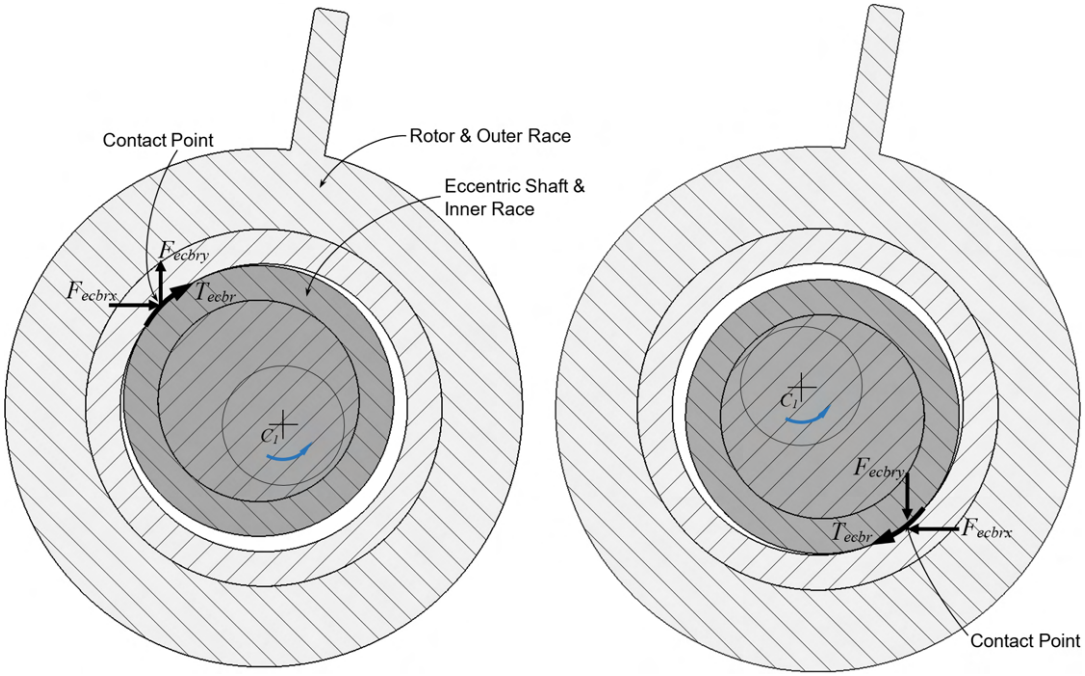

Figure 5.5: Exaggerated illustration of tangential contact force F_{ecbr} acting on eccentric.

$$
\begin{aligned}
F_{sbrx} &= -\frac{(M_{sl}+M_{rr})_{sbr}}{r_s}\left(\frac{F_{sx}}{|F_{sx}|}\right)\sin\left(\tan^{-1}\left|\frac{F_{sy}}{F_{sx}}\right|\right) && \text{for } (F_{sx}>0 \;\&\; F_{sy}>0) \text{ or } (F_{sx}<0 \;\&\; F_{sy}<0)\\
F_{sbrx} &= \frac{(M_{sl}+M_{rr})_{sbr}}{r_s}\left(\frac{F_{sx}}{|F_{sx}|}\right)\sin\left(\tan^{-1}\left|\frac{F_{sy}}{F_{sx}}\right|\right) && \text{for } (F_{sx}>0 \;\&\; F_{sy}<0) \text{ or } (F_{sx}<0 \;\&\; F_{sy}>0)
\end{aligned}
\tag{5.23}
$$

$$F_{sbry} = \frac{(M_{sl} + M_{rr})_{sbr}}{r_s} \left(\frac{F_{sy}}{|F_{sy}|} \right) \cos \left(\tan^{-1} \left| \frac{F_{sy}}{F_{sx}} \right| \right) \quad \begin{matrix} \text{for } (F_{sx} > 0 \ \& \ F_{sy} > 0) \\ \text{or } (F_{sx} < 0 \ \& \ F_{sy} < 0) \end{matrix}$$

$$F_{sbry} = -\frac{(M_{sl} + M_{rr})_{sbr}}{r_s} \left(\frac{F_{sy}}{|F_{sy}|} \right) \cos \left(\tan^{-1} \left| \frac{F_{sy}}{F_{sx}} \right| \right) \quad \begin{matrix} \text{for } (F_{sx} > 0 \ \& \ F_{sy} < 0) \\ \text{or } (F_{sx} < 0 \ \& \ F_{sy} > 0) \end{matrix} \tag{5.24}$$

$$F_{ecbrx} = \frac{(M_{sl} + M_{rr})_{ecbr}}{r_{ec}} \left(\frac{F_{rx}}{|F_{rx}|} \right) \sin \left(\tan^{-1} \left| \frac{F_{ry}}{F_{rx}} \right| \right) \quad \begin{matrix} \text{for } (F_{rx} > 0 \ \& \ F_{ry} > 0) \\ \text{or } (F_{rx} < 0 \ \& \ F_{ry} < 0) \end{matrix}$$

$$F_{ecbrx} = -\frac{(M_{sl} + M_{rr})_{ecbr}}{r_{ec}} \left(\frac{F_{rx}}{|F_{rx}|} \right) \sin \left(\tan^{-1} \left| \frac{F_{ry}}{F_{rx}} \right| \right) \quad \begin{matrix} \text{for } (F_{rx} > 0 \ \& \ F_{ry} < 0) \\ \text{or } (F_{rx} < 0 \ \& \ F_{ry} > 0) \end{matrix} \tag{5.25}$$

$$F_{ecbry} = -\frac{(M_{sl} + M_{rr})_{ecbr}}{r_{ec}} \left(\frac{F_{ry}}{|F_{ry}|} \right) \cos \left(\tan^{-1} \left| \frac{F_{ry}}{F_{rx}} \right| \right) \quad \begin{matrix} \text{for } (F_{rx} > 0 \ \& \ F_{ry} > 0) \\ \text{or } (F_{rx} < 0 \ \& \ F_{ry} < 0) \end{matrix}$$

$$F_{ecbry} = \frac{(M_{sl} + M_{rr})_{ecbr}}{r_{ec}} \left(\frac{F_{ry}}{|F_{ry}|} \right) \cos \left(\tan^{-1} \left| \frac{F_{ry}}{F_{rx}} \right| \right) \quad \begin{matrix} \text{for } (F_{rx} > 0 \ \& \ F_{ry} < 0) \\ \text{or } (F_{ry} < 0 \ \& \ F_{ry} > 0) \end{matrix} \tag{5.26}$$

5.2.2 Dynamic Analysis Of Rotor

As the rotor's swing motion about the split bush creates the intake and compression of gas in the suction and compression chambers respectively, the exposed surfaces of the rotor body and vane experience pressure forces $F_{r\,gas}$, $F_{v\,gas}$ from the working fluid, as illustrated in Figure 5.6. The swing motion of the rotor also results in swivelling motion of the vane; sliding and tilting within the split bush's slot which lead to dry contact normal forces F_{vb1}, F_{vb2} and sliding frictions μF_{vb1}, μF_{vb2} acting on the vane. The overall force and moment balance analysis of the rotor is shown in Equations (5.27), (5.28) and (5.29).

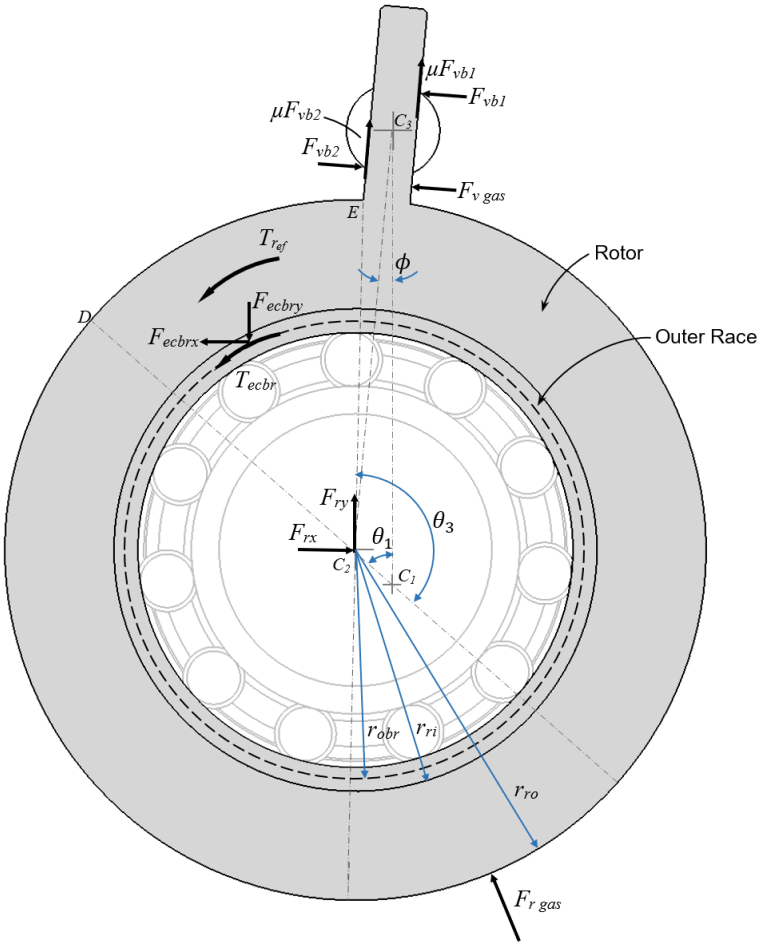

Figure 5.6: Illustration of all forces and torques acting on rotor.

$$
\begin{aligned}
&\rightarrow_{+ve} \sum F_x = 0, \\
&F_{rx} + (-\cos|\phi| + \mu \sin|\phi|)F_{vb1} + (\cos|\phi| + \mu \sin|\phi|)F_{vb2} \\
&- m_r e {\omega_1}^2 \sin\theta_1 - F_{r\,gas_x} - F_{v\,gas_x} - F_{ecbrx} = 0
\end{aligned} \tag{5.27}
$$

$$\uparrow_{+ve} \sum F_y = 0,$$
$$F_{ry} + (\sin|\phi| + \mu\cos|\phi|)F_{vb1} + (-\sin|\phi| + \mu\cos|\phi|)F_{vb2} + m_r e{\omega_1}^2\cos\theta_1 + F_{r\,gas_y} + F_{v\,gas_y} - F_{ecbry} = 0 \tag{5.28}$$

$$\circlearrowleft_{+ve} \sum M_{C_2} = 0, \tag{5.29}$$
$$\left[\sqrt{{r_{ro}}^2 - \left(\frac{w_v}{2}\right)^2} + l_{EH} + r_{sb} + \mu\left(\frac{w_v}{2}\right)\right] F_{vb1} + \left(-l_{EH} - r_{sb} - \mu\left(\frac{w_v}{2}\right)\right) F_{vb2} - I_r\frac{d^2\theta_3}{dt^2} + T_{ecbr} + T_{r_{ef}} + l_{com}(p_{com} - p_{suc})(l_{C_2C_3} - r_{sb} - r_{ro})\left(\frac{l_{C_2C_3} - r_{sb} - r_{ro}}{2} + r_{ro}\right) = 0 \ , \frac{d\theta_3}{dt} < 0$$

$$\left[\sqrt{{r_{ro}}^2 - \left(\frac{w_v}{2}\right)^2} + l_{EH} + r_{sb} + \mu\left(\frac{w_v}{2}\right)\right] F_{vb1} + \left(-l_{EH} - r_{sb} - \mu\left(\frac{w_v}{2}\right)\right) F_{vb2} + I_r\frac{d^2\theta_3}{dt^2} + T_{ecbr} + T_{r_{ef}} + l_{com}(p_{com} - p_{suc})(l_{C_2C_3} - r_{sb} - r_{ro})\left(\frac{l_{C_2C_3} - r_{sb} - r_{ro}}{2} + r_{ro}\right) = 0 \ , \frac{d\theta_3}{dt} \geq 0$$

The resolved pressure force acting on the rotor in x and y-directions are shown in Equations (5.30) and (5.31):

$$F_{r\,gas_x} = \begin{cases} -l_{com}(p_{com} - p_{suc})\left[-r_{ro}\cos(\theta_3 - \pi + \theta_1) + r_{ro}\sin\left(\frac{\pi}{2} - \theta_1\right)\right] & , \frac{d\theta_3}{dt} < 0 \\ -l_{com}(p_{com} - p_{suc})\left[-r_{ro}\cos(\theta_3 + \pi - \theta_1) + r_{ro}\sin\left(\frac{\pi}{2} - \theta_1\right)\right] & , \frac{d\theta_3}{dt} \geq 0 \end{cases} \tag{5.30}$$

$$F_{r\,gas_y} = \begin{cases} l_{com}(p_{com} - p_{suc})\left[-r_{ro}\sin(\theta_3 - \pi + \theta_1) + r_{ro}\cos\left(\frac{\pi}{2} - \theta_1\right)\right] & , \frac{d\theta_3}{dt} < 0 \\ l_{com}(p_{com} - p_{suc})\left[r_{ro}\sin(\theta_3 + \pi - \theta_1) + r_{ro}\cos\left(\frac{\pi}{2} - \theta_1\right)\right] & , \frac{d\theta_3}{dt} \geq 0 \end{cases} \tag{5.31}$$

Furthermore, the resolved pressure force acting on the vane in x and y-directions are shown in Equations (5.32) and (5.33):

$$F_{v\,gas_x} = l_{com}(p_{com} - p_{suc})(l_{C_2C_3} - r_{ro} - r_{sb})\cos|\phi| \tag{5.32}$$

$$F_{v\,gas_y} = l_{com}(p_{com} - p_{suc})(l_{C_2C_3} - r_{ro} - r_{sb})\sin|\phi| \tag{5.33}$$

Endface Frictional Torque

As explained in Subsection 3.1.1, the rotor endface rubs against the bottom endface bushing plate which is designed to prevent metal-to-metal contact rubbing of similar material as shown in Figure 5.7b. The endface frictional torque acting on the rotor $T_{r_{ef}}$ is dependent on the absolute shear direction of rotor surface against the bottom endface bushing and can be solved using vector analysis as shown in Figure 5.7a. For an arbitrary point on the rotor

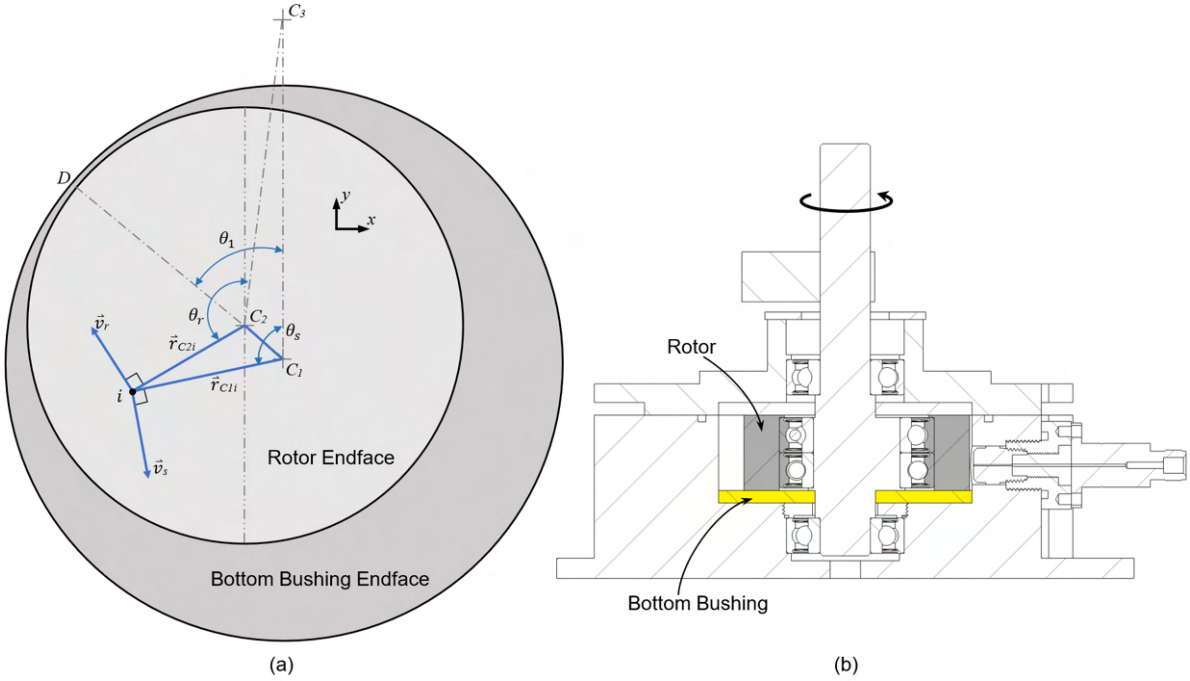

Figure 5.7: Endface frictional torque at bearing surface between rotor and bottom bushing.

endface, the relative tangential velocity $\vec{v_r}$ between rotor and eccentric shaft about C_2 and the entrained tangential velocity of the eccentric shaft $\vec{v_s}$ about centre C_1 are expressed as shown in Equations (5.34) and (5.35), respectively. The absolute velocity $\vec{v}$ is then calculated as shown in (5.36).

$$\vec{v_r} = \omega_3 \times \vec{r_{C_2 i}} = \begin{pmatrix} 0 \\ 0 \\ \dfrac{d\theta_3}{dt} \end{pmatrix} \times \begin{pmatrix} -|\vec{r_{C_2 i}}|\sin\theta_r \\ |\vec{r_{C_2 i}}|\cos\theta_r \\ 0 \end{pmatrix} \tag{5.34}$$

$$\vec{v_s} = \omega_1 \times \vec{r_{C_1 i}} = \begin{pmatrix} 0 \\ 0 \\ \dfrac{d\theta_1}{dt} \end{pmatrix} \times \begin{pmatrix} -|\vec{r_{C_1 i}}|\sin\theta_s \\ |\vec{r_{C_1 i}}|\cos\theta_s \\ 0 \end{pmatrix} \tag{5.35}$$

$$\begin{aligned}\vec{v} &= \vec{v_s} + \vec{v_r} \\ &= -|\vec{r_{C_1 i}}|\cos\theta_s\omega_1\hat{i} - |\vec{r_{C_1 i}}|\sin\theta_s\omega_1\hat{j} - |\vec{r_{C_2 i}}|\cos\theta_r\omega_3\hat{i} - |\vec{r_{C_2 i}}|\sin\theta_r\omega_3\hat{j} \\ &= [|\vec{r_{C_2 i}}|\cos\theta_r(-\omega_3-\omega_1) - e\cos\theta_1\omega_1]\hat{i} + [|\vec{r_{C_2 i}}|\sin\theta_r(-\omega_3-\omega_1) - e\sin\theta_1\omega_1]\hat{j}\end{aligned} \tag{5.36}$$

$$\begin{aligned}|\vec{v}| &= \sqrt{[-|\vec{r_{C_2 i}}|\cos\theta_r(-\omega_3-\omega_1) - e\cos\theta_1\omega_1]^2 + [-|\vec{r_{C_2 i}}|\sin\theta_r(-\omega_3-\omega_1) - e\sin\theta_1\omega_1]^2} \\ &= \sqrt{|r_{C_2 i}|^2(-\omega_3-\omega_1)^2 + e^2{\omega_1}^2 - 2e\omega_1|r_{C_2 i}|(-\omega_3-\omega_1)\cos(\theta_1-\theta_r)}\end{aligned} \tag{5.37}$$

The friction torque acting on the rotor endface $T_{r_{ef}}$ can be found by summing all the points on the rotor endface as shown in Equation (5.38) where the shear stress $\vec{f_r}$ shown in Equation (5.39) is in the direction of the absolute velocity vector $\vec{v}$ and is simply the product of the stress magnitude $|\vec{f_r}|$ and unit vector for the absolute velocity $\frac{\vec{v}}{|\vec{v}|}$. The magnitude of shear stress $|\vec{f_r}|$ is due to the normal loading from the gas pressure acting on the top rotor endface via the top clearance and the weight of the rotor W_r.

$$\begin{aligned}T_{r_{ef}} &= \int_{r_{ri}}^{r_{ro}}\int_0^{2\pi}(\vec{r_{C_2 i}}\times\vec{f_r})|\vec{r_{C_2 i}}|d\theta_r d\vec{r_{C_2 i}} \\ &= \int_{r_{ri}}^{r_{ro}}\int_0^{2\pi}(\vec{r_{C_2 i}}\times|\vec{f_r}|\frac{\vec{v}}{|\vec{v}|})|\vec{r_{C_2 i}}|d\theta_r d\vec{r_{C_2 i}} \\ &= \int_{r_{ri}}^{r_{ro}}\int_0^{2\pi}\begin{pmatrix}-|\vec{r_{C_2 i}}|\sin\theta_r \\ |\vec{r_{C_2 i}}|\cos\theta_r \\ 0\end{pmatrix}\times\begin{pmatrix}|\vec{r_{C_2 i}}|\cos\theta_r(-\omega_3-\omega_1) - e\cos\theta_1\omega_1 \\ |\vec{r_{C_2 i}}|\sin\theta_r(-\omega_3-\omega_1) - e\sin\theta_1\omega_1 \\ 0\end{pmatrix}\frac{|\vec{f_r}|}{|\vec{v}|}|\vec{r_{C_2 i}}|d\theta_r d\vec{r_{C_2 i}} \\ &= |\vec{f_r}|\int_{r_{ri}}^{r_{ro}}\int_0^{2\pi}\frac{-|r_{C_2 i}|^3(-\omega_3-\omega_1) + |r_{C_2 i}|^2 e\omega_1\cos(\theta_1-\theta_r)}{\sqrt{|r_{C_2 i}|^2(-\omega_3-\omega_1)^2 + e^2{\omega_1}^2 - 2e\omega_1|r_{C_2 i}|(-\omega_3-\omega_1)\cos(\theta_1-\theta_r)}}d\theta_r d\vec{r_{C_2 i}}\end{aligned} \tag{5.38}$$

$$|\vec{f_r}| = \begin{cases}\dfrac{\mu W_r}{\pi({r_{ro}}^2 - {r_{ri}}^2)} + \dfrac{(p_{suc}(\pi-\theta_3) + p_{com}(\pi+\theta_3)}{2\pi}, \dfrac{d\theta_3}{dt} < 0 \\ \dfrac{\mu W_r}{\pi({r_{ro}}^2 - {r_{ri}}^2)} + \dfrac{(p_{suc}(\pi+\theta_3) + p_{com}(\pi-\theta_3)}{2\pi}, \dfrac{d\theta_3}{dt} \geq 0\end{cases} \tag{5.39}$$

Due to the complex denominator $|\vec{v}|$, an exact analytical solution to the double integrations of Equation (5.38) will not be possible and Equation (5.38) has to be solved numerically. A numerical double integration programme based on Weddle's Rule was written in Fortran language and was used to solve Equation (5.38).

5.2.3 Dynamic Analysis Of Split Bush

From Figure 5.6, it is noted that, for the rotor to swing about the centre of split bush C_3, the split bush has to rotate about its centre C_3 in order to accommodate the swivelling motion of the vane. The vane and the split bush are assumed to be in contact at the extreme contact points 1 and 2 due to slight tilting and leaning of the vane within the sliding clearance between the vane and the split bush, as shown in the detailed view of Figure 5.8. The overall force and moment balance analysis of the split bush is shown in Equations (5.40) to (5.42).

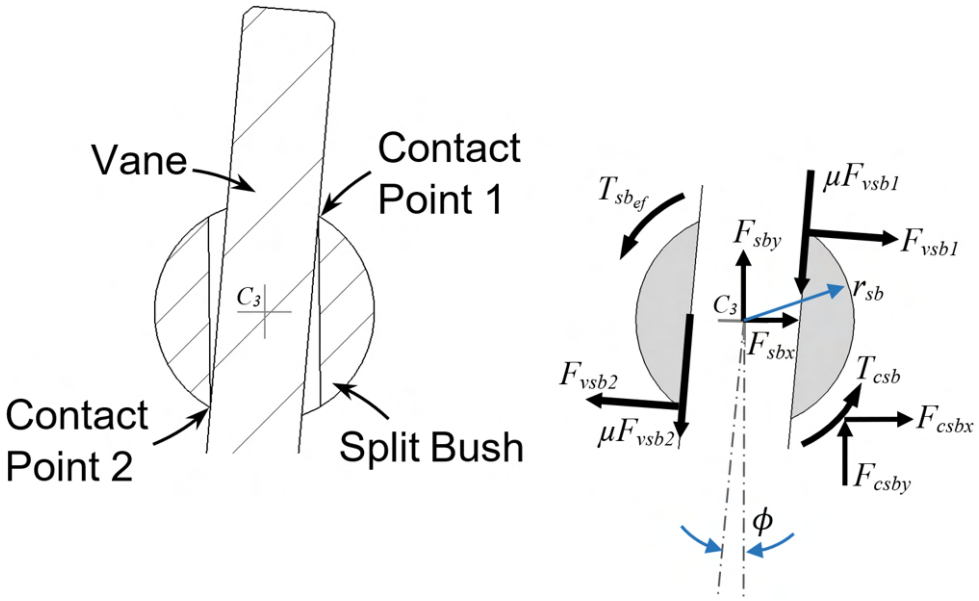

Figure 5.8: Illustration of all forces and torques acting on split bush.

$$\rightarrow_{+ve} \sum F_x = 0,$$
$$F_{sbx} + (\cos|\phi| - \mu \sin|\phi|)F_{vsb1} + (-\cos|\phi| - \mu \sin|\phi|)F_{vsb2} + F_{cbx} = 0 \tag{5.40}$$

$$\uparrow_{+ve} \sum F_y = 0,$$
$$F_{sby} + (-\sin|\phi| - \mu \cos|\phi|)F_{vsb1} + (\sin|\phi| - \mu \cos|\phi|)F_{vsb2} + F_{csby} = 0 \tag{5.41}$$

$$\circlearrowleft_{+ve} \sum M_{C_3} = 0,$$
$$I_{sb}\frac{d^2\phi}{dt^2} + T_{csb} + T_{sb_{ef}} + (-r_{sb} - \frac{\mu w_v}{2})F_{vsb1} + (-r_{sb} + \frac{\mu w_v}{2})F_{vsb2} = 0 \tag{5.42}$$

Contact Friction And Torque

As the split bush rotates about centre C_3 in the split bush slot in the cylinder, there will be dry rubbing between the split bush and slot wall. The magnitude

of the frictional torque acting on the split bush T_{csb} is dependent on the radial contact force F_{sb} acting on the split bush and the direction is dependent on the rotation of split bush $\frac{\frac{d\phi}{dt}}{\left|\frac{d\phi}{dt}\right|}$, as shown in Equation (5.43).

$$T_{csb} = \mu r_{sb} \sqrt{{F_{sbx}}^2 + {F_{sby}}^2} \frac{\frac{d\phi}{dt}}{\left|\frac{d\phi}{dt}\right|} \tag{5.43}$$

The split bush also experiences endface friction torque $T_{sb_{ef}}$ and the shear stress f_{sb} is dependent on the weight of the split bush W_{sb} and the pressure force from the gas within the clearance.

$$T_{sb_{ef}} = \int_0^{r_{sb}} \int_0^{2\pi} f_{sb} r d\theta dr = \frac{2}{3} f_{sb} {r_{sb}}^3 \frac{\frac{d\phi}{dt}}{\left|\frac{d\phi}{dt}\right|} \tag{5.44}$$

$$f_{sb} = \frac{\mu W_{sb}}{(\pi {r_{sb}}^2)} + \mu \left(\frac{p_{disc} + p_{suc}}{2} \right) \tag{5.45}$$

Similarly, the direction of the tangential contact force F_{csb} acting on the split bush due to radial contact with the split bush slot wall varies throughout the working cycle and is dependent on the position of the radial contact force F_{sb}, as shown in Figure 5.9. The tangential contact force F_{csb} is determined as shown in Equations (5.46) and (5.47).

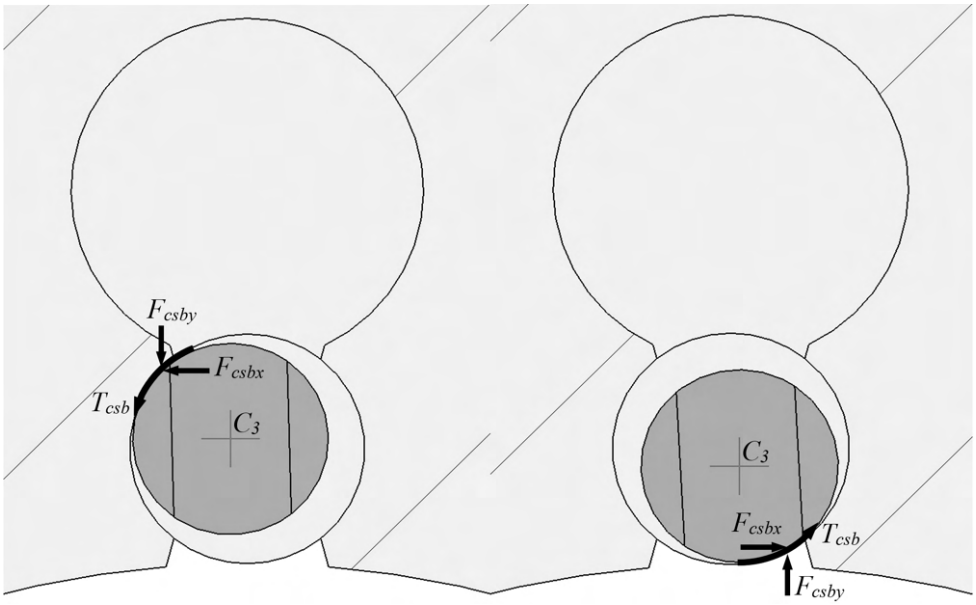

Figure 5.9: Exaggerated illustration example of tangential contact forces acting on split bush.

$$F_{csbx} = \frac{T_{csb}}{r_{sb}} \left(\frac{F_{sbx}}{|F_{sbx}|} \right) \sin \left(\tan^{-1} \left| \frac{F_{sby}}{F_{sbx}} \right| \right) \quad \text{for } (F_{sbx} > 0 \ \& \ F_{sby} > 0) \text{ or } (F_{sbx} < 0 \ \& \ F_{sby} < 0)$$

$$F_{csbx} = -\frac{T_{csb}}{r_{sb}} \left(\frac{F_{sbx}}{|F_{sbx}|} \right) \sin \left(\tan^{-1} \left| \frac{F_{sby}}{F_{sbx}} \right| \right) \quad \text{for } (F_{sbx} > 0 \ \& \ F_{sby} < 0) \text{ or } (F_{sbx} < 0 \ \& \ F_{sby} > 0) \tag{5.46}$$

$$F_{csby} = -\frac{T_{csb}}{r_{sb}} \left(\frac{F_{sby}}{|F_{sby}|} \right) \cos \left(\tan^{-1} \left| \frac{F_{sby}}{F_{sbx}} \right| \right) \quad \text{for } (F_{sbx} > 0 \ \& \ F_{sby} > 0) \text{ or } (F_{sbx} < 0 \ \& \ F_{sby} < 0)$$

$$F_{sbry} = \frac{T_{csb}}{r_{sb}} \left(\frac{F_{sby}}{|F_{sby}|} \right) \cos \left(\tan^{-1} \left| \frac{F_{sby}}{F_{sbx}} \right| \right) \quad \text{for } (F_{sbx} > 0 \ \& \ F_{sby} < 0) \text{ or } (F_{sbx} < 0 \ \& \ F_{sby} > 0) \tag{5.47}$$

5.3 Summary

In this chapter, the mathematical models to predict the valve response and the dynamic forces within the compressor are formulated. The summary of this chapter can be presented as follows:

- Valve dynamics modelling of non-uniform arbitrary discharge valve to determine the valve displacement and the effective discharge flow area has been developed.
- Dynamics model based on force and moment balance analysis of the swing vane mechanisms are presented.
- Evaluation of individual frictional forces and torques, namely the ball bearing's friction moment, the tangential frictional forces due to radial contacts, rotor endface friction and vane sliding friction has been carried out.

In the next chapter, theoretical modellings of the internal leakages and the heat transfer within the oil-free compressor will be presented and discussed in greater detail.

Chapter 6

Theoretical Model - Internal Leakages and Heat Transfer Within Oil-Free Swing Vane Compressor

In this chapter, leakage flow through internal clearances and heat transfer between each compressor component will be modelled. Internal leakages from the high pressure compression chamber to low pressure suction chamber often occur in compressors during operation due to the presence of clearance gaps designed for movement allowance between mating surfaces of moving components. Such a phenomenon is undesirable for the performance of the compressor, especially for an oil-free compressor where there is no sealing of these clearances in the absence of oil lubrication. To understand the effects of internal leakage on the performance of an oil-free swing vane compressor, the first section of this chapter will present a theoretical model to predict the internal leakage mass flow. As the prototype operates without oil lubrication, dry sliding between bearing surfaces would also generate excessive heat in the compressor which may cause mechanical interference due to over-expansion from excessive heat. In addition, the heat generated will also be transferred to the working fluid which affects its thermodynamic properties. The second half of this chapter will present the heat transfer model for estimating the steady-state operating temperatures of the oil-free swing vane compressor components and the heat transfer between each part.

6.1 Internal Leakages

Three main leakage paths are identified in the prototype design which are namely, the leakage through the radial clearance between the cylinder and the rotor and the leakages through the top endface clearances of both the vane and rotor. These leakage paths are illustrated in Figure 6.1.

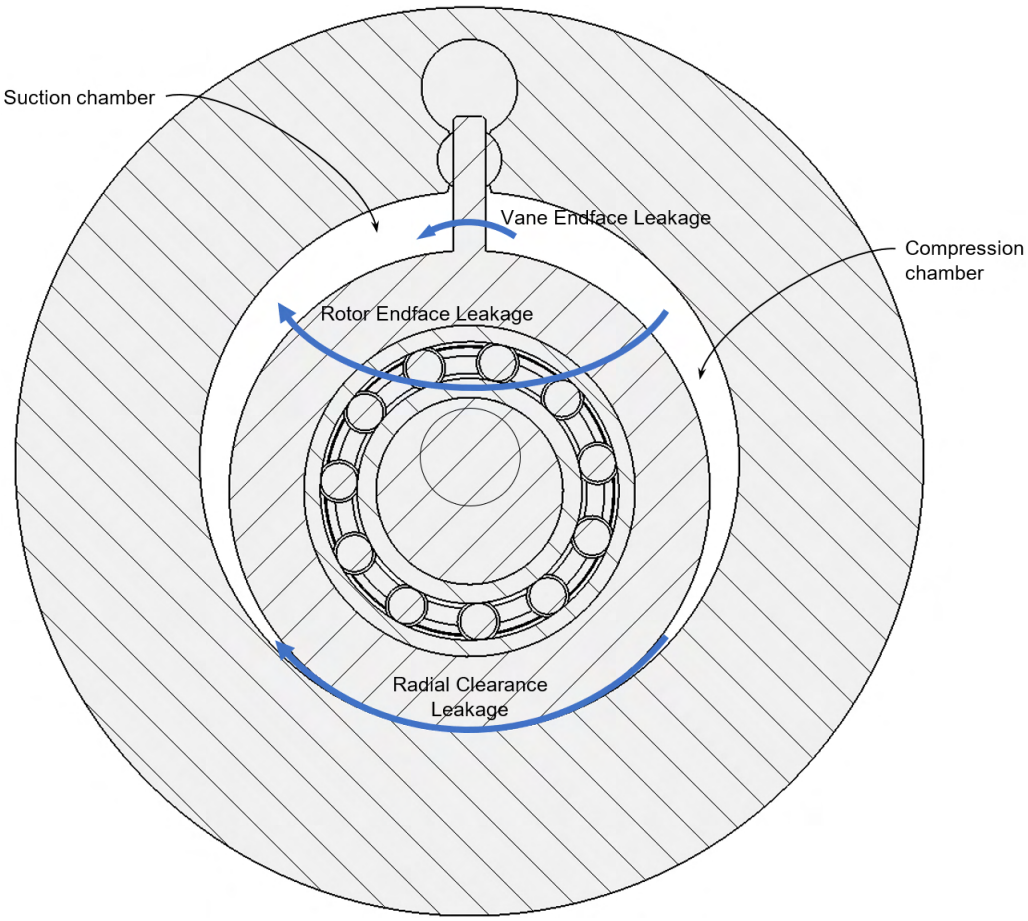

Figure 6.1: Internal leakage paths of oil-free swing vane compressor.

6.1.1 Radial Clearance Leakage

Since the swing vane mechanism has the same rotor and cylinder configuration as that of the rolling piston, the leakage flow through the radial clearance gap is modelled using the theoretical model proposed by Yanagisawa and Shimizu [97] for the study of radial leakage losses of rolling piston type rotary compressor. In the study, the proposed model was validated by experimental results and good agreements were shown for different fluids and different clearances.

The clearance gap between the cylinder and rotor is shown in Figure 6.2. This leakage path is narrow and long as compared to the axial length l_{com} of the chamber ($l_f >> l_{com}$) and as such, it is necessary to analyse the leakage with viscous effects taken into consideration. The leakage path developed along the rotor-cylinder surfaces is modelled by a conceptual flow channel, as shown in Figure 6.3 and Figure 6.4, which is made up of the compression chamber, a convergent nozzle, a straight channel with viscous drag and a suction chamber. This leakage channel has a constant rectangular flow area with an axial length/height l_{com} and width δ_{rad}. An adiabatic, ideal and compressible leakage flow is assumed for the modelling with the flow through the straight channel modelled as Fanno flow by taking viscous effect into consideration.

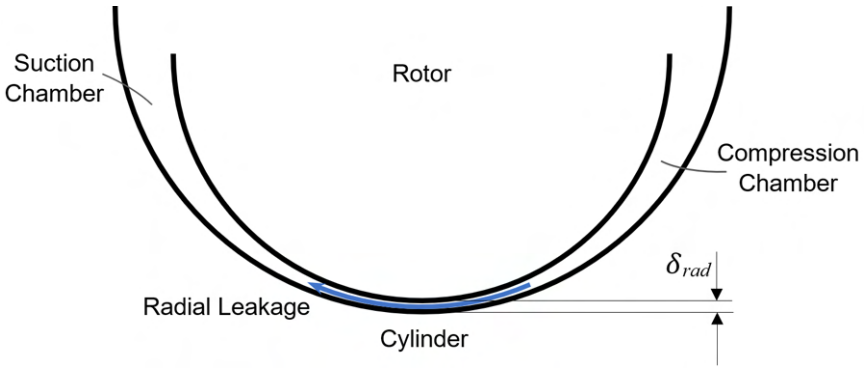

Figure 6.2: Close-up view of the radial clearance.

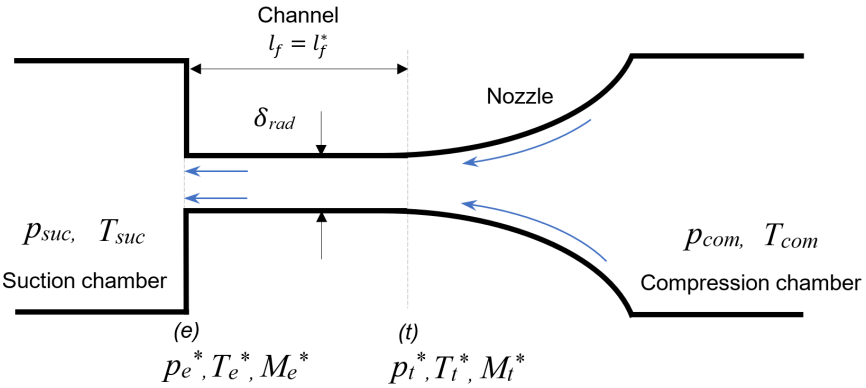

Figure 6.3: Fanno Flow model of leakage flow through radial clearance [97].

Critical Leakage Flow

To predict the radial leakage flow, the flow is first assumed to be choked at the exit of the straight channel where the exit Mach number M_e^* is assumed

to be unity and the equivalent actual channel length l_f is equal to the length for choked flow l_f^*. The length of the channel l_f, is determined based on the inner radius of the cylinder r_{ci}, the radial clearance gap δ_{rad} and the eccentricity $e = (r_{ci} - r_{ro})$, as shown in Equation (6.1).

$$l_f = \frac{2\pi\delta_{rad} r_{ci}}{e\sqrt{1 - \left(1 - \frac{\delta_{rad}}{e}^2\right)}} \tag{6.1}$$

With the fluid velocity at the channel exit equal to velocity of sound, the throat Mach number M_t^* at the inlet of the channel must satisfy Equation (6.1).

$$\lambda \frac{{l_f}^*}{2\delta_{rad}} = \frac{1 - M_t^{*2}}{\gamma M_t^{*2}} + \frac{\gamma + 1}{2\gamma} log \frac{(\gamma + 1)M_t^{*2}}{2 + (\gamma - 1)M_t^{*2}} \tag{6.2}$$

The friction factor λ of the viscous drag acting on the flow is based on laminar and turbulent flow for smooth pipes [141]:

$$\lambda = \begin{cases} \dfrac{96}{Re} & (Re \leq 3560) \\ \dfrac{0.3164}{Re^{0.25}} & (Re > 3560) \end{cases} \tag{6.3}$$

and the local Reynolds number of the leakage flow is given by Equation (6.4).

$$Re = \frac{2\dot{m}_{leak,rad}}{\mu l_{com}} \tag{6.4}$$

The pressure ratio between exit and inlet of Fanno flow $\frac{p_t^*}{p_e^*}$, pressure ratio at the converging nozzle $\frac{p_{com}}{p_t^*}$, temperature ratios and the leakage flow rate for critical/choked flow $\dot{m}_{leak}$ which is obtained iteratively are shown in equations (6.5) to (6.8).

$$\dot{m}_{leak,rad} = \delta_{rad} l_{com} \left(\frac{p_e^*}{RT_e^*}\right) \sqrt{\gamma R T_e^*} \tag{6.5}$$

$$T_e^* = T_{com} \left(1 + \frac{\gamma - 1}{2}\right)^{-1} \tag{6.6}$$

$$\frac{p_t^*}{p_e^*} = \frac{1}{M_t^*} \sqrt{\frac{\gamma + 1}{2 + (\gamma - 1)M_t^{*2}}} \tag{6.7}$$

$$\frac{p_{com}}{p_t^*} = \left(1 + \frac{\gamma - 1}{2} M_t^{*2}\right)^{\frac{\gamma}{\gamma - 1}} \tag{6.8}$$

If the total pressure ratio $\frac{p_{com}}{p_e^*} = \frac{p_{com}}{p_t^*}\frac{p_t^*}{p_e^*}$, is less than or equal to the given pressure ratio $\frac{p_{com}}{p_{suc}}$, between the suction and compression chambers, the flow chokes.

Sub-Critical Leakage Flow

However, when the flow does not choke, sub-critical leakage flow has to be modelled. The exit velocity of the channel is no longer sonic and the Mach number at both the inlet and outlet of the channel have to be iterated. A throat Mach number M_t is first assumed and the corresponding exit Mach number is calculated based on the longer imaginary critical channel length l_f^* and the actual length l_f, as illustrated in Figure 6.4, using Equations (6.2) and (6.9).

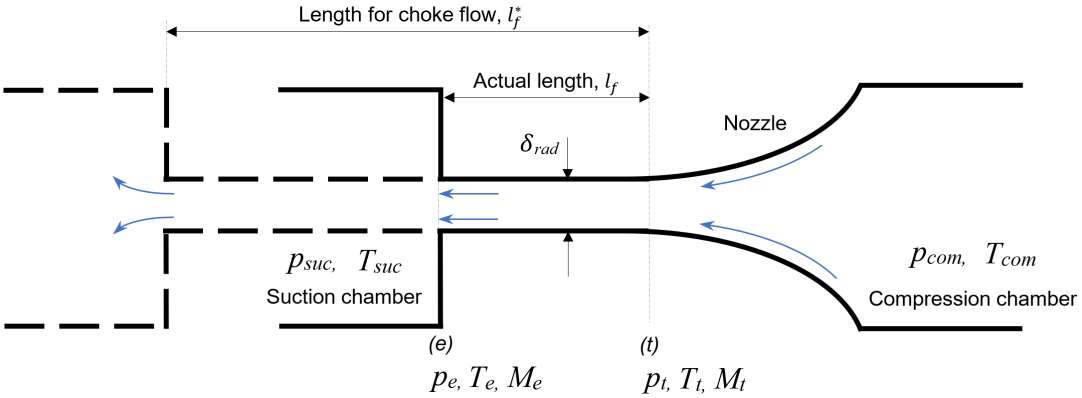

Figure 6.4: Modelling of sub-critical leakage flow through radial clearance.

$$\lambda\frac{{l_f}^* - l_f}{2\delta_{rad}} = \frac{1 - {M_e}^2}{\gamma {M_e}^2} + \frac{\gamma+1}{2\gamma} log \frac{(\gamma+1){M_e}^2}{2+(\gamma-1){M_e}^2} \tag{6.9}$$

With each assumed M_t, the critical pressure ratios $\frac{p_t}{p^*}$, $\frac{p_e}{p^*}$ and the nozzle pressure ratio $\frac{p_{com}}{p_t}$ can be calculated by equations (6.10) to (6.12).

$$\frac{p_t}{p^*} = \frac{1}{M_t}\sqrt{\frac{\gamma+1}{2+(\gamma-1){M_t}^2}} \tag{6.10}$$

$$\frac{p_e}{p^*} = \frac{1}{M_e}\sqrt{\frac{\gamma+1}{2+(\gamma-1){M_e}^2}} \tag{6.11}$$

$$\frac{p_{com}}{p_t} = \left(1 + \frac{\gamma-1}{2}{M_t}^2\right)^{\frac{\gamma}{\gamma-1}} \tag{6.12}$$

If the resultant assumed pressure ratio $\frac{p_{com}}{p_e} = \frac{p_{com}}{p_t}\frac{p_t}{p^*}/\frac{p_e}{p^*}$ is equal to the pressure ratio $\frac{p_{com}}{p_{suc}}$ between the compression and suction chambers, the assumed Mach

number M_t is valid and the sub-critical mass flow rate can be calculated from the above Equation (6.5).

6.1.2 Vane Endface Leakage

Figure 6.5 illustrates the close-up view of the endface clearance between the vane and top bushing and it can be observed that endface leakage path is similar to that of the radial leakage flow, albeit without the converging section. The leakage through the vane endface clearance can be conceptually modelled as a Fanno flow through a straight channel without the converging nozzle, as illustrated in Figure 6.6. The solution methods and equations (6.1) to (6.12) for the radial

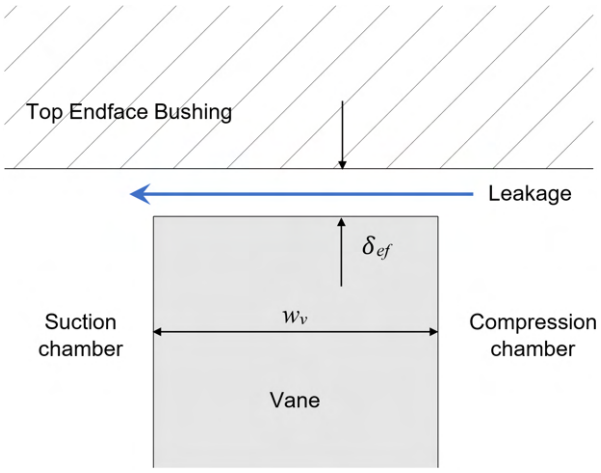

Figure 6.5: Top endface clearance between Vane and Top Bushing.

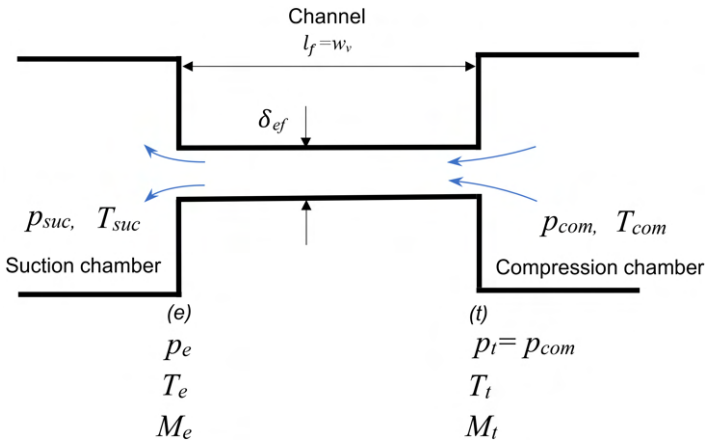

Figure 6.6: Fanno flow through straight channel with no converging section.

leakage are adapted for the calculation of the vane endface leakage with the equivalent channel length l_f equal to the width of the vane w_v,the clearance

gap to be the endface clearance δ_{ef} and the throat pressure to be approximately equal to the pressure of compression chamber $p_t \cong p_{com}$. As the vane length exposed to the working chambers l_v varies throughout the working cycle, the cross section of the leakage channel changes and hence, the vane endface leakage mass flow rate $\dot{m}_{leak,endf}$ is given as:

$$\dot{m}_{leak,endf} = \delta_{ef} l_v \left(\frac{p_e}{RT_e}\right) \sqrt{\gamma R T_e} \tag{6.13}$$

where, the exposed vane length is expressed as $l_v = l_{C_2C_3} - r_{sb}$ based on Equation (4.1) in Section 4.2.

To verify the adoption of the Fanno Flow model for the leakage through the vane endface clearance, the Computational Fluid Dynamics (CFD) numerical analysis approach is used to calculate the leakage flow for comparison. The assumptions used for the analysis are similar to those of the analytical model presented by Yanagisawa and Shimizu [97] where the flow is assumed to be adiabatic, steady and ideal with the surface walls and endfaces deemed to be stationary. The CFD analysis [142] was conducted using realisable k-ϵ model

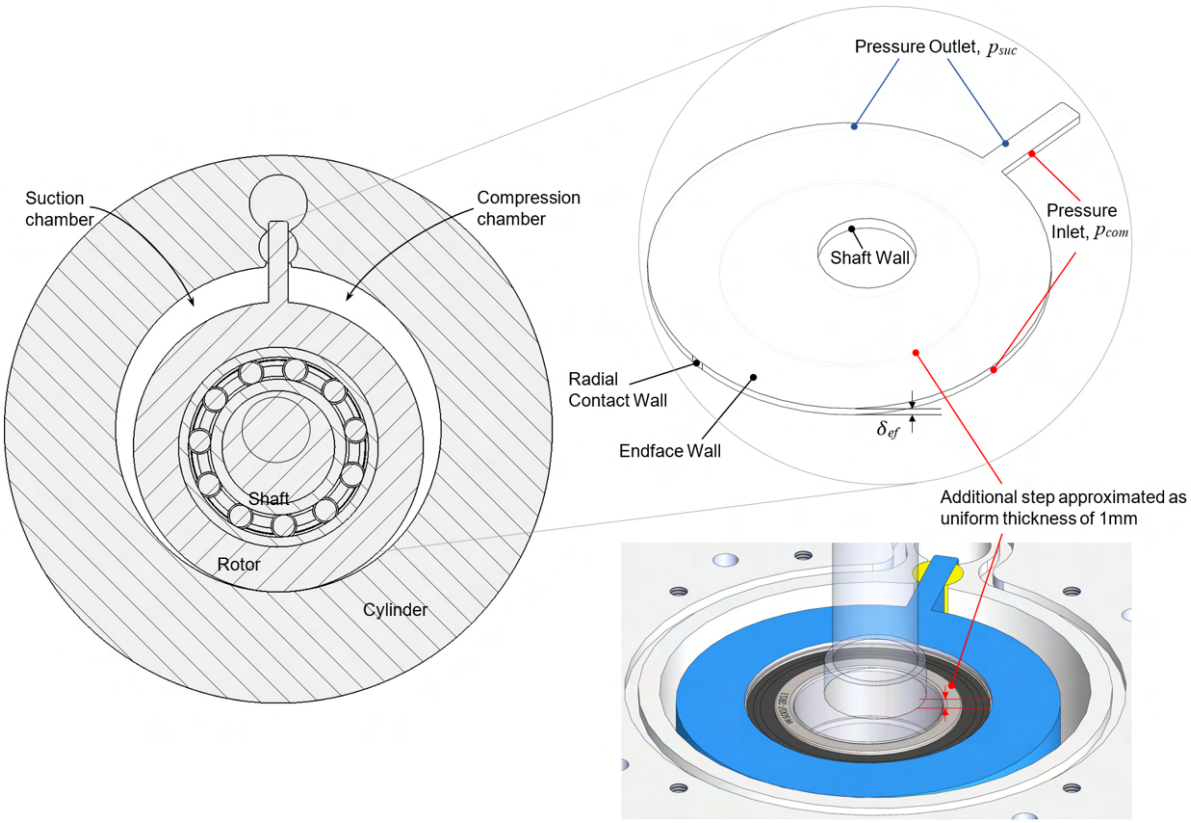

Figure 6.7: Flow domain of the endface leakage for both vane and rotor at 180°.

with mesh of 964,640 cells and 8 cell layers in the end face clearance thickness based on convergence criterion of residual value smaller than 10^{-6}. The fluid flow domain and boundary conditions at shaft rotation angle of 180° is shown in Figure 6.7. During the operation, the shaft rotates about the centre of the rotor with an offset eccentric distance, which causes the shaft wall boundary and the radial contact point between rotor and cylinder to vary. As a result, both the boundary condition, the geometry of the leakage flow path and hence, the resultant leakage flow velocity and mass flow at each rotation angle will change, as illustrated in Figure 6.8 and Figure 6.9.

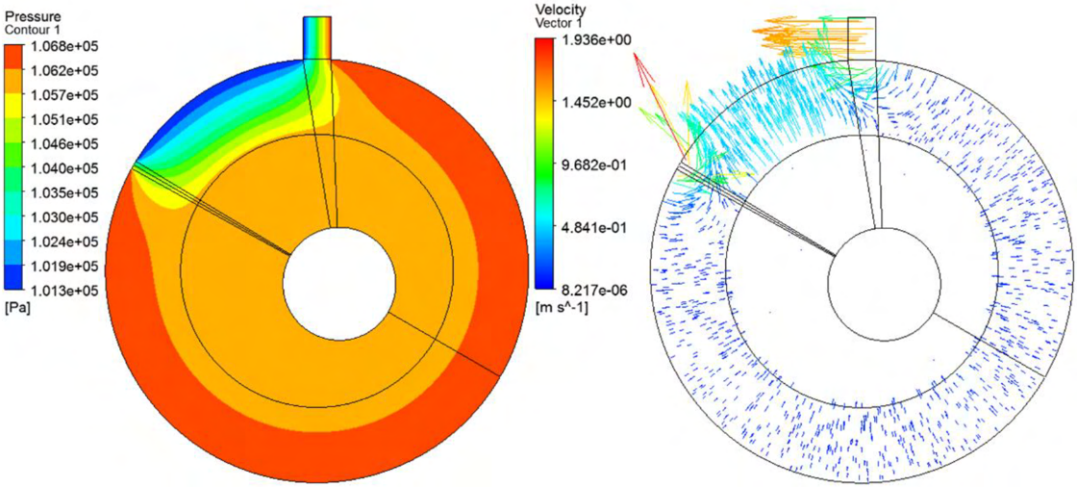

(a) 60° rotation angle.

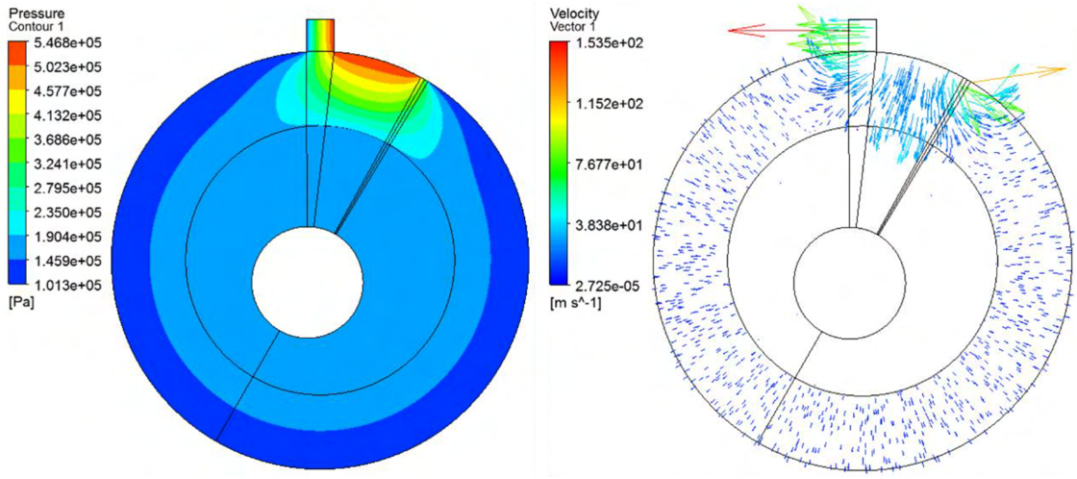

(b) 330° rotation angle.

Figure 6.8: Pressure contour and velocity vectors at different shaft rotation angle.

For each rotational angle, the pressure ratio between the working chambers p_{com}/p_{suc} is obtained from the overall theoretical simulation of the oil-free prototype. The CFD analysis was conducted using the following simulation

parameters as shown in Table 6.1 with air as the working fluid. Figure 6.9 shows the mass flow rate across the vane endface at each varying rotational angle.

Table 6.1: Simulation parameters for CFD analysis of the vane endface leakage.

Simulation parameters	Value
Outer radius of rotor, r_{ro}	45 mm
Inner radius of cylinder, r_{ci}	50.5 mm
Eccentricity, e	5.5 mm
Top endface clearance, δ_{ef}	16 μm
Suction pressure	101 kPa
Discharge pressure	550 kPa
Operating speed	1800 rpm

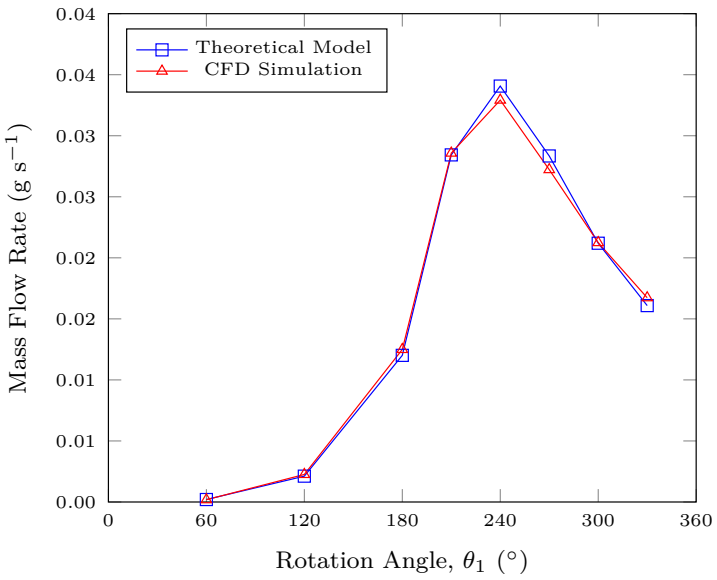

Figure 6.9: Comparison of vane endface leakage results between theoretical modelling and CFD simulation.

From Figure 6.9, it can be observed that there is a strong agreement between the results predicted by the theoretical model and the CFD simulations with an average error of 3.9%. This suggests that the experimentally verified leakage model proposed by Yanagisawa and Shimizu [97] is appropriate in modelling the leakage flow behaviour across the vane endface.

6.1.3 Rotor Endface Leakage

Previous analytical studies on leakages through rolling piston endfaces [143, 144] are found to be inapplicable for the analysis of oil-free endface leakage path as these studies often include the effect of oil flow in the endface clearances. Unlike the radial or vane endface leakage, it is difficult to ascertain the exact leakage path across the complex geometry of the rotor endface. To simplify the modelling of the rotor endface leakage, the leakage flow through the top endface clearance is also modelled as a Fanno flow through a conceptual straight channel with the fluid flowing along the average shortest straight line path between two points from the discharge side to the suction side, as shown in Figure 6.10 and Figure 6.11. The average shortest straight line path $l_{avg,min}$ is obtained by

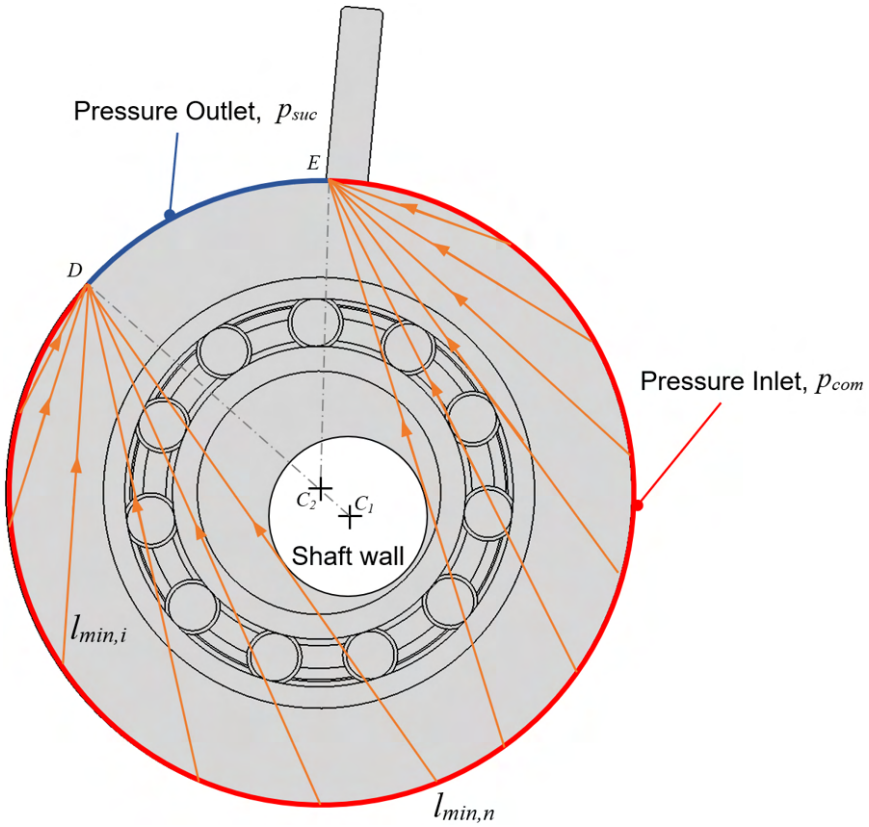

Figure 6.10: Shortest flow path between suction and discharge side.

averaging all the shortest paths l_{min} between low pressure point D and discharge side, as shown in Equation (6.14) and it is the equivalent channel length l_f for the Fanno flow.

$$l_{avg,min} = \frac{\sum_{i=1}^{n} l_{min,i}}{n} \tag{6.14}$$

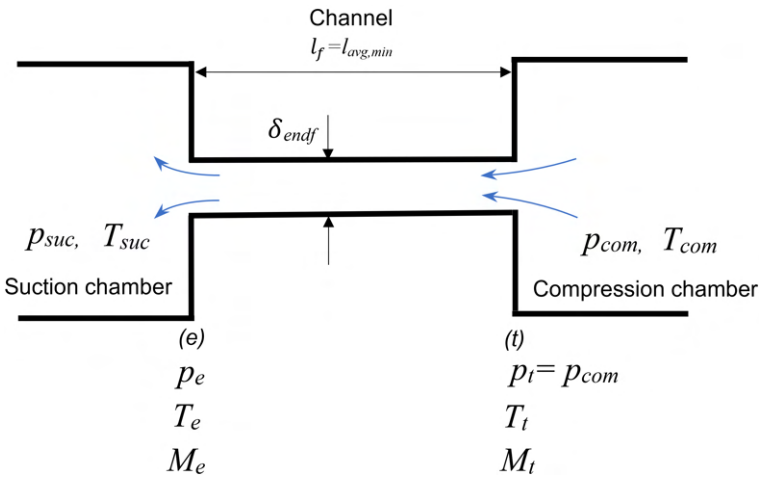

Figure 6.11: Fanno flow through straight channel with no converging section.

The adoption of the Fanno Flow model for the leakage through the rotor endface clearance is also verified by comparing the theoretically calculated leakage flow with results from CFD simulations. Similarly, the simulation is conducted with the same assumptions that the flow is adiabatic, steady and ideal and the surface walls to be stationary. For the same dimensions of oil-free swing vane compressor and working conditions as the CFD simulations for vane endface leakage in Subsection 6.1.2, Figure 6.12 shows the mass flow rate comparison between the theoretical model and CFD simulations.

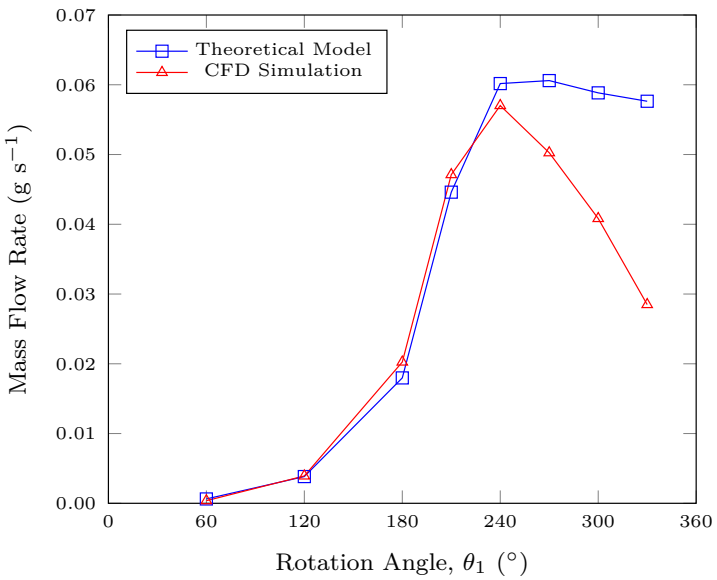

Figure 6.12: Comparison of rotor endface leakage results between theoretical modelling and CFD simulation.

From Figure 6.12, the same leakage variation trend is generally observed across the rotation angles for both the theoretical modelling and CFD simulations. However, there are considerable discrepancies between the leakage mass flow after rotational angle of 240°. This discrepancy could have been due to the differences in the assumption of fluid paths — in the theoretical modelling, the fluid is assumed to flow along the shortest straight line path from the high pressure discharge side to low pressure suction side, while in the CFD simulation, the flow vector is assumed to be normal to the pressure inlet and outlet boundaries (coloured in red and blue, respectively in Figure 6.10) and curved within the flow domain along the path of the least resistance. As a result, the assumed leakage path in the theoretical model is comparatively shorter than that in the CFD simulation for a given pressure ratio between discharge and suction side, resulting in higher flow velocity in the Fanno flow channel with the steeper pressure gradient and higher chances of choked flow. This effect is observed to be most dominant at extreme rotation angle beyond 240°, as shown in Figure 6.13, where bulk of the leakage flow occurs along the curved paths at the radial contact wall.

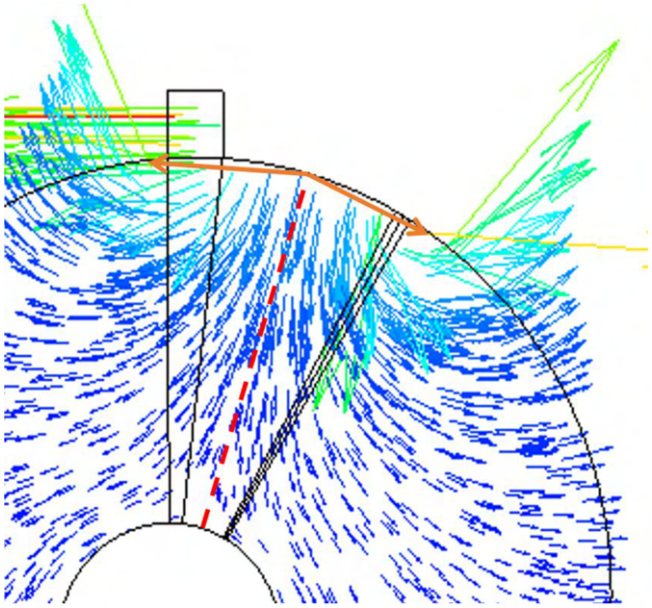

Figure 6.13: Velocity vectors along longer curved paths from high pressure side to low pressure side — theoretical straight line path assumption in orange arrow lines.

The assumption of a shortest straight line flow path in the theoretical model thus results in greater leakage flow as compared to the CFD model. In both theoretical and CFD simulations, non-slip boundary condition is assumed for the leakage flow in the clearance channel. However, with reference to literature

reviewed in Subsection 2.5.2, rarefaction effects for both air and refrigerant flow are observed in micro-channels of diameter under 400 μm under pressure ratio ranging from 1.1 to 6.5 and viscous slip flow is found to be possible. For movement allowance between the moving parts in compressor, the clearance is usually in the range of 10 to 30 μm. This suggests that rarefied flow can occur in compressor's clearances and the leakage flow simulated based on non-slip viscous flow condition might be under-predicted especially for the oil-free compressor where rarefied flow is more likely to occur in the dry clearance gap. Since both models predict similar flow behaviour in the leakage clearance and the CFD simulation is more conservative in the prediction of leakage mass flow as compared to the theoretical model, the theoretical model based on the shortest straight path is adopted in the overall leakage modelling to predict the maximum possible rotor endface leakage of an oil-free prototype. In addition, the theoretical modelling allows flexibility in modelling any arbitrary prototype dimensions and boundary conditions with minimal computational time.

6.2 Heat Transfer Within Oil-Free Swing Vane Compressor

The temperature profile and the heat transfer between the components of the compressor play a critical role in its reliability and efficiency, especially for an oil-free compressor where heat generation from dry sliding of bearing surfaces and suction heating of gas are more prominent. This section presents the theoretical model for the heat transfer and temperature distribution within an oil-free swing vane compressor using the lumped thermal conductance approach [120, 121].

6.2.1 Conceptual Modelling Of Components And General Assumptions

In this model, the oil-free prototype is divided into 38 discrete elements each with a relatively simple geometry as shown in Figure 6.14 and Figure 6.15, and each element is assumed to be isothermal and at a uniform temperature. This is because the majority of the components are made from aluminium which has high thermal conductivity and each component is discretised into multiple elements to ensure spatial temperature variation within these smaller elements can be considered insignificant. The prototype is divided into these lumped elements

such that most of them conformed to their natural geometric boundaries which include bearing surfaces where heat generation occurs, solid-to-solid contacts where heat conduction occurs and solid-to-fluid interfaces where convection occurs. For the cylinder body, however, it is not treated as one element and instead, it is divided into top and bottom layers in which each layer is further divided radially into another 9 elements as the cylinder body is too thick in radius. Multiple sub-division of the elements ensures higher accuracy in the temperature prediction of each element. In order to use verified convection correlations from existing literature, simplifications were also made on the intricate geometry of the prototype components with solid-fluid interfaces where they were reduced to standard geometrical shapes with simplified convection surfaces.

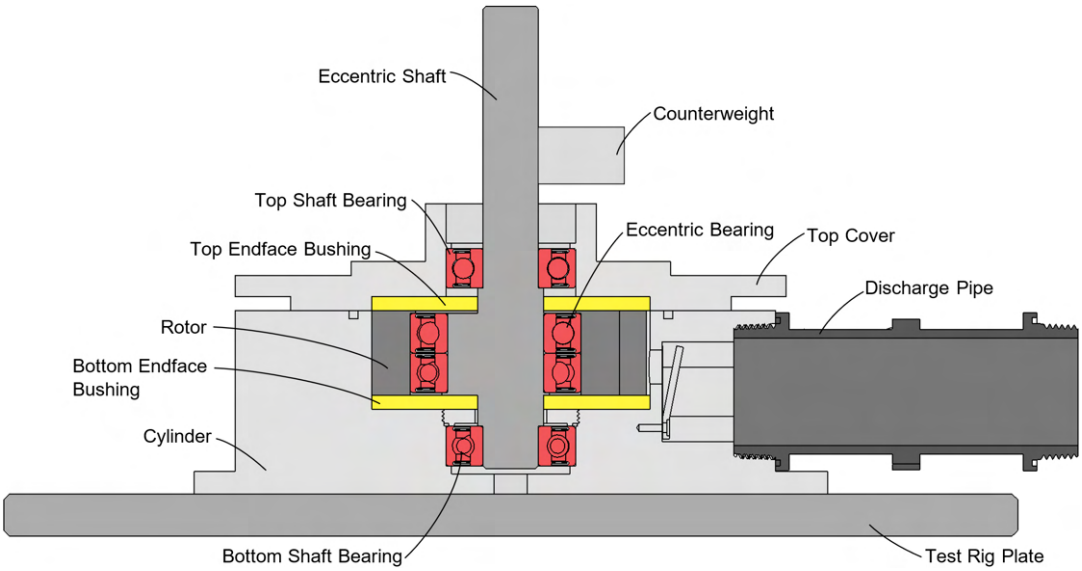

Figure 6.14: Prototype Cross-section.

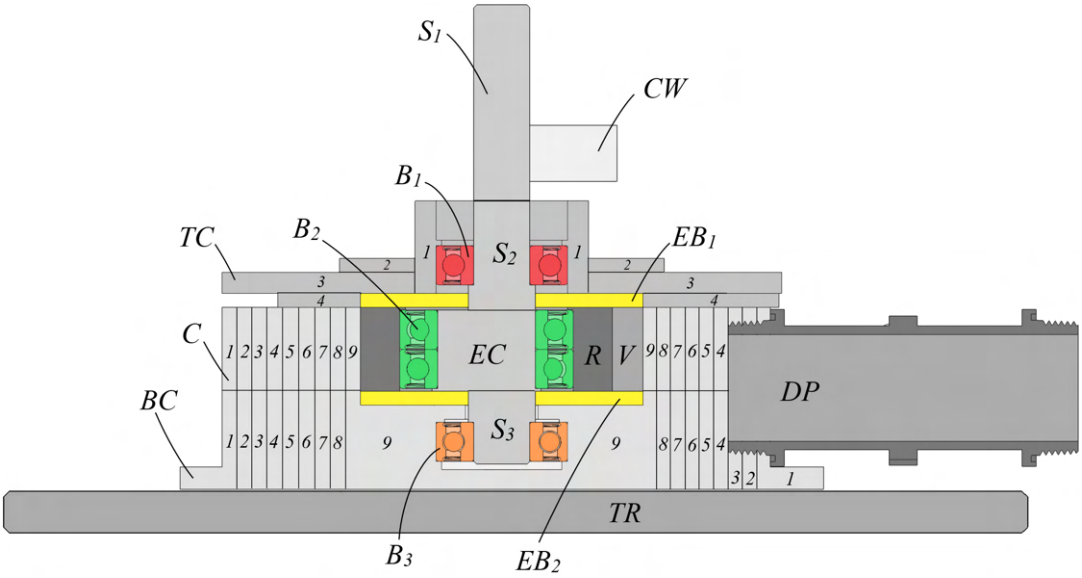

(a) Cross-section view of divided elements.

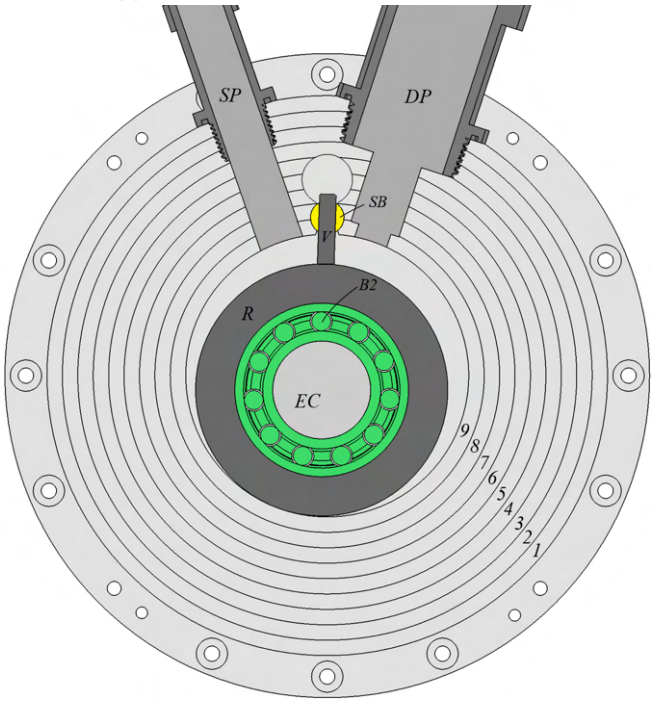

(b) Front view of divided elements.

Figure 6.15: Conceptual modelling of prototype into 38 simplified discrete elements.

6.2.2 Heat Transfer Governing Equations

The fundamental laws governing the system of 38 elements (see Figure 6.15) and the working fluid in the chambers are the conservation of mass and the first law of thermodynamics. For any element of the compressor system, the energy

balance within the element i can be expressed as Equation (6.15).

$$\dot{Q}_i + \sum_i \dot{m}_{in} h_{in} - \sum_j \dot{m}_{out} h_{out} - \dot{W}_i = \frac{d}{dt}\left[m_i(u_i + \frac{{v_i}^2}{2} + g z_i)\right] \tag{6.15}$$

As the elements are solids, there is no mass transfer across the solid boundaries. Furthermore, the change in kinetic and potential energies of the elements are negligible as compared to the heat transferred. For steady-state analysis of the system, Equation (6.15) can be further expressed as Equation (6.16).

$$\dot{Q}_i - \dot{W}_i = 0 \tag{6.16}$$

Since each lumped element is considered as a control volume by itself where volume change due to thermal expansion/contraction is negligible, work interaction $\dot{W}_i = 0$ and therefore, the energy balance for each element is given by Equation (6.17).

$$\dot{Q}_i = 0 \tag{6.17}$$

According to Equation (6.17), the total rate of heat transfer within an element i is the resultant sum of heat transferred to or from other elements or fluid via conduction, radiation or convection together with the heat generated within the element or at the surface boundary. The principle mode of heat transfer inside the compressor are primarily conduction for solid-to-solid contact and convection for solid-fluid interfaces at the working chamber. Radiative heat transfer is not considered within the compressor because of the relatively small temperature differences between elements inside the compressor. For heat transfer between the compressor parts exposed to the surrounding environment such as the top cover or the suction/discharge pipe, convection and radiation are considered. The general equation for heat transfer [120] is given as:

$$\dot{Q} = H\Delta T \tag{6.18}$$

and H is the thermal conductance coefficient that is calculated based on the actual geometry, the thermal properties of the component and the heat transfer coefficients from verified correlations. For heat conduction, the thermal conductance coefficient is given by

$$H = \frac{k_i A_i}{\Delta x} \tag{6.19}$$

where
k_i is the thermal conductivity of element i (W m^{-1}K^{-1}),
A_i is the heat transfer area (m^2), and
Δx is centre-to-centre distance between two lumped elements (m).

The thermal conductance coefficient for convective heat transfer is given by

$$H = \frac{k_{fluid} A_i Nu}{D} \tag{6.20}$$

where
k_{fluid} is the thermal conductivity of fluid medium at the solid-fluid interface i (W m^{-1}K^{-1}).
D is the characteristic length of convection (m).
Nu is the Nusselt number (-).

The thermal conductance coefficient for radiation heat transfer with ambient surroundings is shown in Equation (6.21) with the view factor as unity since the prototype is not a hermetic compressor and is entirely exposed to the surroundings.

$$H = A_i \epsilon \sigma (T_i + T_{sur})(T_i^2 + T_{sur}^2) \tag{6.21}$$

where
ϵ is the emissivity of the element surface i (-).
σ is the Stefan-Boltzmann constant (W m^{-2}K^{-4}).
T_{sur} is the absolute temperature of ambient surrounding (K).

As a result, the total rate of heat transfer to or from an element i together with rate of heat generation within the element $\dot{S}_i$, Equation (6.17) can also be written as

$$\dot{Q}_i = \sum_{j=1}^{n} H_{j,i}(T_i - T_j) - \dot{S}_i = 0 \tag{6.22}$$

In the above equations, heat transfer away from the element i is considered positive and internal or boundary heat generation due to compression processes or frictional losses are considered positive.

6.2.3 Heat Transfer Correlations And Assumptions

With the division of the prototype's components into lumped elements with standard geometrical shapes, as shown in Figure 6.15, the convective heat transfer at intricate surfaces of the prototype (as presented in Figure 6.14) are simplified

and can be modelled using existing convective heat transfer correlations for generic geometry and boundary configurations in literature. Therefore, relevant free and forced convective heat transfer correlations for convection over horizontal surfaces, vertical surfaces, cylindrical surfaces, rotating cylinder and disk can be applied to these simplified solid-fluid interfaces. Some of these crucial convective heat transfer correlations are presented below.

Free convection over cylinder body and cover. Depending on the orientation of the surfaces of the cylinder body and the top cover, the Nusselt number correlation for free convection over the horizontal surfaces of the top cover and the vertical surfaces of the cylinder body [145] are given in equations (6.23) to (6.25), respectively. As the diameter of the cylinder body is large ($\frac{D}{L} \geq \frac{35}{Gr_L{}^{0.25}}$), the outer surface of the cylinder body is treated as a vertical plate.

For hot horizontal upper surface

$$\overline{Nu}_L = \begin{cases} 0.54Ra_L^{1/4} & , 10^5 \leq Ra_L \leq 10^7 \\ 0.15Ra_L^{1/3} & , 10^7 \leq Ra_L \leq 10^{10} \end{cases} \tag{6.23}$$

For hot horizontal lower surface

$$\overline{Nu}_L = 0.27Ra_L^{1/4} \quad , 10^5 \leq Ra_L \leq 10^{10} \tag{6.24}$$

For vertical isothermal plate

$$\overline{Nu}_L = \begin{cases} 0.68 + \dfrac{0.67Ra_L^{1/4}}{\left[1 + \left(\frac{0.492}{Pr}\right)^{9/16}\right]^{4/9}} & , Ra_L \leq 10^9 \\ \left[0.825 + \dfrac{0.387Ra_L^{1/6}}{\left(1 + \left[\frac{0.492}{Pr}\right]^{9/16}\right)^{8/27}}\right]^2 & , Ra_L > 10^9 \end{cases} \tag{6.25}$$

where

$$\overline{Ra}_L = \frac{g\rho\beta|T_w - T_{sur}|L^3}{\mu\alpha} \tag{6.26}$$

$$Pr = \frac{\mu c_p}{k} \tag{6.27}$$

$$L = \frac{\text{Heat Transfer Area}}{\text{Perimeter}} \tag{6.28}$$

Forced convection in cylindrical suction and discharge tube. As the suction flow and discharge flow in swing vane compressor are not continuous, the average velocity of the gas flow in each pipe and hence, average Reynolds number is

used in the calculation of the Nusselt number using the following correlation [120, 146, 147]. For laminar flow

$$\overline{Nu}_D = 4.36 \tag{6.29}$$

and for turbulent flow

$$\begin{aligned} &\overline{Nu}_D = 5 + 0.015 Re^a Pr^b \quad , 0.1 < Pr < 10^5 \ \& \ 10^4 < Re < 10^6 \\ &\text{For,} \quad a = 0.88 - \frac{0.24}{4 + Pr}, \quad b = \frac{1}{3} + 0.5 e^{-0.6 Pr} \end{aligned} \tag{6.30}$$

Convection between working fluid and cylinder inner wall. Throughout the working cycle, the working fluid involved in the heat transfer undergoes rapid changes to the thermodynamic properties and the gas flow patterns are difficult to be ascertained due to rapid changing boundary-layer developments induced by changing compression and suction volume boundaries. However, the Nusselt number calculated from correlation Equation (6.31), although originally formulated for reciprocating compressor, was tested by Padhy and Dwivedi [120] and was found suitable for modelling the working chamber of rolling piston compressor. Since swing vane and rolling piston compressors are fundamentally similar in the compression and suction operating configurations, the correlation Equation (6.31) is used to model the convective heat transfer in working chambers of the oil-free prototype with the flow assumed to be turbulent.

$$\overline{Nu}_D = 0.053 Re^{0.8} Pr^{0.6} \tag{6.31}$$

Convection between ambient air and rotating shaft components. The modelling of convective heat transfer between the shaft-counterweight and quiescent air is divided into two parts. The high speed rotating shaft is modelled as a rotating cylinder with negligible axial flow [121] as given in Equation (6.32) and the counterweight is modelled as a rotating disc [145] as shown in Equation (6.33) respectively.

$$\overline{Nu}_D = 0.018[(0.5 Re_D^2 + Gr_D) Pr]^{0.315} \tag{6.32}$$

$$\overline{Nu}_D = \frac{RePr\sqrt{C_{dr}/2}}{5Pr + 5ln(5Pr+1) + 2\sqrt{2/C_{dr}} - 14}$$
$$\text{For,} \quad C_{dr} = \frac{1}{-2.05 + 4.07log_{10}Re\sqrt{C_{dr}}} \tag{6.33}$$

Radiation heat transfer to surroundings. The emissivity for metal usually ranges from 0.1 to 0.4 depending on surface conditions and finishing [148]. For aluminium cylinder body that is exposed to oxidisation from ambient surrounding and high temperature of operating condition, it is estimated to be within 0.2 to 0.8. For the polished steel that makes up the shaft assembly including the rotor and the counterweight, its emissivity is estimated to be 0.25. In addition, the temperature of the compressor components are expected to be much higher than that of the surroundings with view factor for the radiation heat transfer to be at unity [148]. The average heat transfer coefficient for radiation is given by equations (6.34) and (6.35).

$$\overline{h}_{rad_{alu}} = 0.4\sigma(T_i + T_{sur})(T_i^2 + T_{sur}^2) \tag{6.34}$$

$$\overline{h}_{rad_{steel}} = 0.25\sigma(T_i + T_{sur})(T_i^2 + T_{sur}^2) \tag{6.35}$$

6.2.4 Heat Generation And Division of Frictional Heat

Heat Generation

Heat generation due to dry rubbing at bearing surfaces can be derived based on the equations of the dynamic frictional forces and sliding velocities presented in Section 4.4 and Section 5.2. The frictional loss or the heat generated at the bearing surface between the split bush and the vane can be derived as shown in (6.36).

$$P_{vsb} = \mu(|F_{vsb1}|+|F_{vsb2}|)\left|\frac{dl_{C_2C_3}}{dt}\right| \tag{6.36}$$

The power loss due to contact rubbing between the split bush and the wall surface of the slit bush slot in the cylinder wall is given as Equation (6.37).

$$P_{csb} = |T_{csb}|\left|\frac{d\phi}{dt}\right| \tag{6.37}$$

The frictional loss at the rotor endface is obtained by integrating the product of sliding shear stress $\vec{f}_r$ (given in (5.39)) and tangential sliding velocity $\vec{v}$ (given

in (5.36)) over the rotor endface, as shown in Equation (6.38). The analytical solution to the double integration in Equation (6.38) is not possible due to the complexity of tangential sliding velocity $\vec{v}$ which is implicitly dependent on other geometrical and kinematic relations and thus, the endface frictional loss has to be numerically iterated.

$$\begin{aligned} P_{r_{ef}} &= \int_{r_{ri}}^{r_{ro}} \int_{0}^{2\pi} (\vec{f}_r \cdot \vec{v}) |\vec{r_{C_2 i}}| d\theta_r d\vec{r_{C_2 i}} \\ &= |\vec{f}_r| \int_{r_{ri}}^{r_{ro}} \int_{0}^{2\pi} \sqrt{|r_{C_2 i}|^2(-\omega_3 - \omega_1)^2 + e^2{\omega_1}^2 - 2e\omega_1 |r_{C_2 i}|(-\omega_3 - \omega_1)\cos(\theta_1 - \theta_r)} \\ &\quad |\vec{r_{C_2 i}}| d\theta_r d\vec{r_{C_2 i}} \end{aligned} \tag{6.38}$$

Heat Distribution at Bearing Surfaces

As the prototype is to operate without the use of oil lubrication, dry sliding at bearing surfaces are friction-reduced by dissimilar self-lubrication material to prevent actual welding of similar metal-to-metal mating surfaces due to the heat generated. However, with the use of dissimilar material at bearing surfaces, the amount of heat generated and distributed to each surface will vary. The amount of heat distributed between two sliding surfaces is governed by the heat partition factor or heat distribution coefficient α where the heat generated through dry sliding $\dot{Q}_T$ is split into surface 1 and surface 2, as given in Equation (6.39) [149–152].

$$\frac{\dot{Q}_1}{\dot{Q}_T} = \frac{\dot{Q}_1}{\dot{Q}_1 + \dot{Q}_2} = \alpha \tag{6.39}$$

Based on the conceptual macroscopic sliding contact thermal model proposed by Bardon [152] and further development by Chantrenne and Raynaud [150], the heat distribution coefficient α between two sliding surfaces can further be simplified into Equation (6.40) that is dependent on the sliding thermal contact resistance R_{sl}, assuming that the heat is only generated at real contact interface or contacting points between asperities.

$$\alpha = \frac{R_{sl,2}}{R_{sl,1} + R_{sl,2}} \tag{6.40}$$

To determine the sliding thermal contact resistance of each surface, Chantrenne and Raynaud [150] have developed a correlation that is based on material physical properties, sliding velocity and the profile of the surface asperities.

The correlation involves determining the dimensionless sliding thermal contact resistance for two rough surface in dry sliding contact, as shown in Equation (6.41). The asperities profile is conceptually modelled as illustrated in Figure 6.16, with the asperities assumed to be periodically uniformed in separation and each surface having the same height H_i and width $2b_i$.

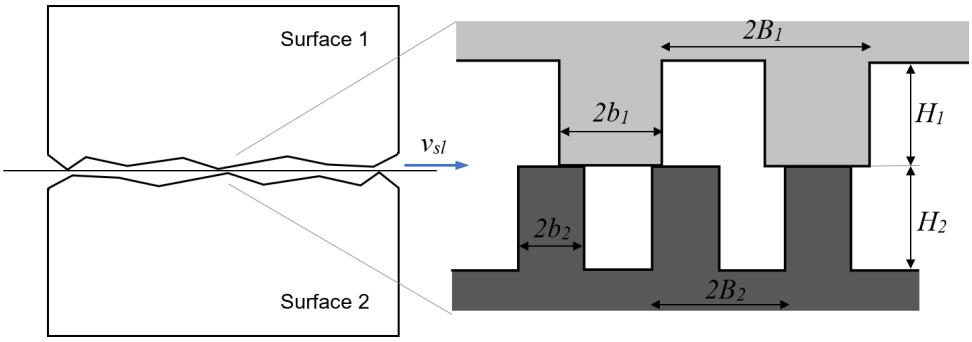

Figure 6.16: Simplified asperities profile at contact interface.

$$R^*_{sl,i} = 0.93\left(\frac{1}{b^*_i} - 1\right)H^*_i + 0.4\left(\frac{1}{v^*_i}\right)^{0.24}\left(\frac{1}{b^*_i} - 1\right) \quad , i = 1, 2 \tag{6.41}$$

$$R_{sl,i} = \frac{2B_i R^*_{sl,i}}{k_i} \tag{6.42}$$

$$v^*_i = \frac{2v_{sl}B_i\rho_i c_{p,i}}{k_i} \tag{6.43}$$

$$H^*_i = \frac{H_i}{2B_i} \tag{6.44}$$

$$b^*_i = \frac{b_i}{B_i} \tag{6.45}$$

where,
$2B$ is the spatial periodicity (μm).
H_i and $2b_i$ are the height and the width of the asperities respectively (μm).
ρ_i is the density of surface i (kg m^{-3}).
$c_{p,i}$ is the specific heat of surface i's material (J kg^{-1}K^{-1}).
k_i is the thermal conductivity of surface i's material (W m^{-1}K^{-1}).

In practice, the surface profiles of the bushings used in the oil-free prototype are constantly changing due to sliding wear from dry rubbing. For ease of modelling, both bearing surfaces 1 and 2 are assumed to have the equal value of average

roughness height H_i, roughness width $2b_i$ and periodic separation $2B_i$ since the surfaces are machined by the same milling, boring and tuning processes [153].

A comparison of the dimensionless sliding thermal contact resistances between C95500 AB2 Nickel-Aluminium Bronze and AISI630 17-4 PH Stainless Steel and between Bearing Grade PEEK and AISI630 17-4 PH Stainless Steel with material properties shown in Table 6.2 is computed for a range of sliding velocities and is illustrated in Figure 6.17. Both pairs of rubbing surfaces are assumed to be machined by the same processes and having the same average asperity dimensions based on average surface finish of the machining processes [153] as shown in Table 6.3.

Table 6.2: Material Properties

AISI630 17-4 PH Stainless Steel [154]	Value
Thermal Conductivity at 260°C (W $m^{-1}K^{-1}$)	22.5
Specific Heat at 100°C (J $kg^{-1}K^{-1}$)	460
Density (kg m^{-3})	7800
C95500 AB2 Nickel-Aluminium Bronze [155, 156]	
Thermal Conductivity at 20°C (W $m^{-1}K^{-1}$)	42
Specific Heat at 20°C (J $kg^{-1}K^{-1}$)	419
Density (kg m^{-3})	7600
PEEK 450G [157]	
Thermal Conductivity based on ISO 22007-4:2008 (W $m^{-1}K^{-1}$)	0.82
Specific Heat Capacity based on ISO 22007-4:2008 (J $kg^{-1}K^{-1}$)	1100
Density (kg m^{-3})	1440

Table 6.3: Asperity properties based on average machining surface roughness [153].

Property	Value (μm)
Height, H	1.6
Width, $2b$	1.2
Periodic Separation, 2B	2.4

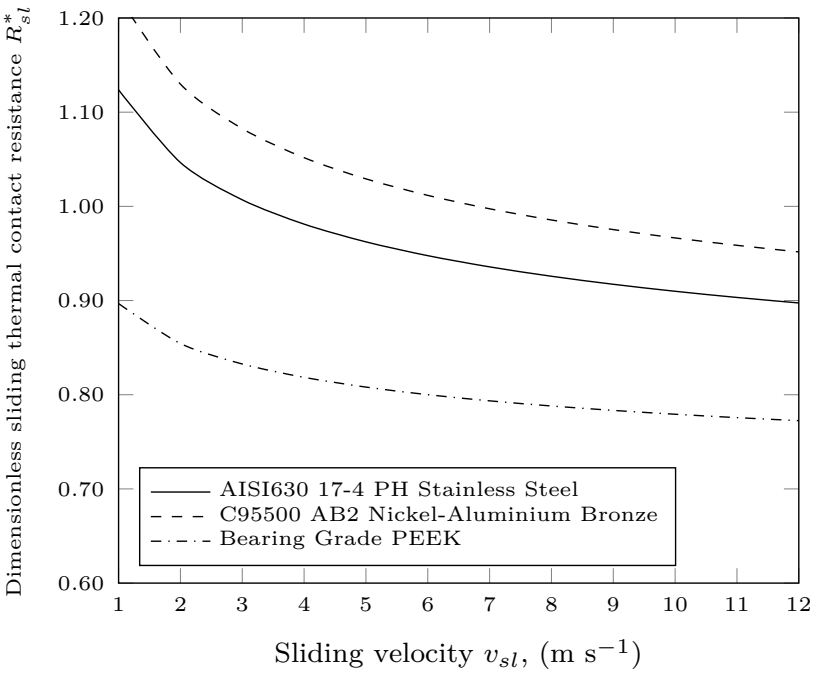

Figure 6.17: Comparison of dimensionless sliding thermal contact resistance between Bronze-Stainless Steel and PEEK-Stainless Steel.

Based on Figure 6.17, it is noted that increasing sliding velocity v_{sl} brings about less significant decrease in the dimensionless sliding thermal contact resistance R^*_{sl}. With reference to the dimensionless sliding thermal contact resistance R^*_{sl} in Equation (6.41), it is clear that the larger the sliding velocity v_{sl} and dimensionless sliding velocity v^*_{sl}, the last term of Equation (6.41) becomes insignificant. This suggests that resultant sliding thermal contact resistance of each surface $R_{sl,i}$ will become invariant to sliding velocity and the overall heat distribution coefficient α can be expressed as:

$$\alpha \cong \frac{1}{1 + \frac{k_2}{k_1}} \tag{6.46}$$

From Figure 6.18, it can be seen that the discrepancies between heat distribution coefficient based on Equations (6.40) and (6.46) for each surface pair are small and therefore, this suggests that simplified expression in Equation (6.46) is sufficient for the estimation of heat distribution coefficient between two mating surfaces. In the study of heat generation and surface temperature analysis in sliding contact systems by Waddad et al. [151], heat distribution coefficient is also found to be directly influenced by the ratio of thermal conductivities of mating surfaces $\frac{k_2}{k_1}$. He and Ovaert [158] and Chantrenne and Raynaud [149]

also observed this trend in their numerical study of thermal properties influence on thermal sliding contact resistances and heat partition coefficient.

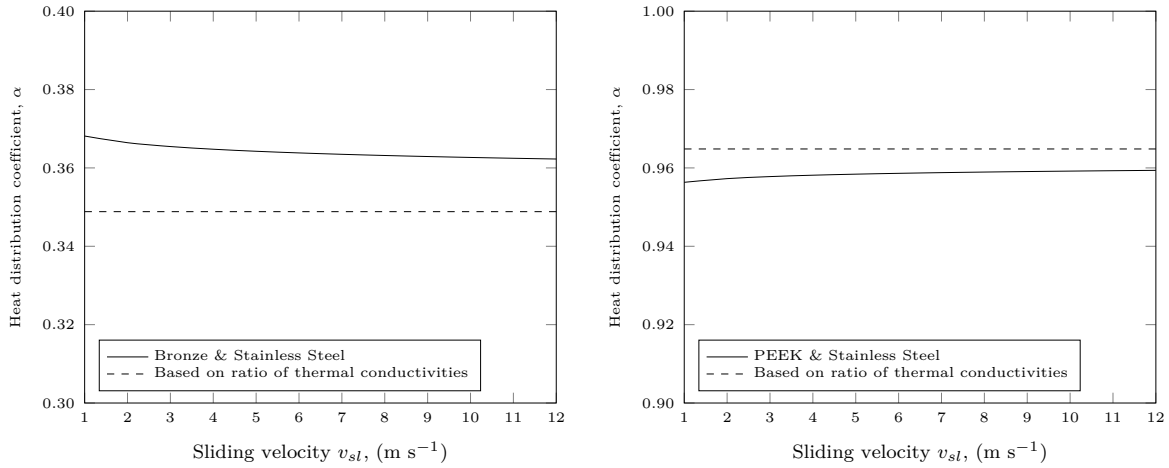

Figure 6.18: Comparison of heat distribution coefficients between different bushing materials and stainless steel surfaces.

Therefore, for the friction heat generated between steel and bronze, 35.6% of the heat generated shall be absorbed by the steel bearing surface. On the other hand, for rubbing with bearing grade PEEK surfaces, the steel surface will take in 96.1% of total heat generated at the PEEK-Steel surface. This is expected since PEEK is polymer-based material and behaves as a thermal insulator as compared to steel which has higher thermal conductivity. For simplicity, the modelling of heat distribution coefficient of two bearing surfaces for the heat transfer analysis will be based on the ratio of the thermal conductivities of both materials in Equation (6.46).

6.2.5 System Of Linear Algebraic Equations

With a system of 38 lumped elements, there will be 38 linear equations in the form of Equation (6.22) that have to be solved in order to obtain the temperature of each element. The equation associated with suction pipe element SP is presented here as an illustration. For suction pipe element SP, it is affected by radiation and free convection with the surrounding air, heat conduction with the cylinder body element $C1$ and convective heat transfer with suction intake flow. Based on energy balance analysis and Equation (6.22), the heat transfer to and from the element SP can be written as shown in (6.47) which is rearranged into

Equation (6.48).

$$-H_{SP,C1}(T_{C1}-T_{SP})+H_{SP,suc}(T_{SP}-T_{suc})+H_{SP,\infty}(T_{SP}-T_{sur})=0 \quad (6.47)$$

$$(H_{SP,C1}+H_{SP,suc}+H_{sp,\infty})T_{SP}-H_{SP,C1}T_{C1}=H_{SP,\infty}T_{sur}+H_{SP,suc}T_{suc} \quad (6.48)$$

where,

$$H_{SP,C1}=\frac{k_{C1}\pi(r_{SPo}^2-r_{SPi}^2)}{l_{C1}/2}+\frac{k_{SP}\pi(r_{SPo}^2-r_{SPi}^2)}{l_{SP}/2} \quad (6.49)$$

$$H_{SP,\infty}=k_{air}\pi l_{SP}(0.53(GrPr)^{0.25})+\epsilon\sigma(T_{SP}+T_{sur})(T_{SP}^2+T_{sur}^2) \quad (6.50)$$

$$H_{SP,suc}=\begin{cases}4.36k_{SP}\pi l_{SP} & \text{, for laminar flow}\\ (5+0.015Re^aPr^b)k_{SP}\pi l_{SP} & \text{, for turbulent flow}\end{cases} \quad (6.51)$$

$$a=0.88-\frac{0.24}{4+Pr},\quad b=\frac{1}{3}+0.5e^{-0.6Pr}$$

In general, the system of 38 linear equations can be expressed in matrix form:

$$\boldsymbol{CX}=\boldsymbol{D} \quad (6.52)$$

where matrix $\boldsymbol{C}$ represents all the lumped thermal conductance terms H and matrix $\boldsymbol{D}$ represents all the heat losses to the surroundings or working fluid and also heat source terms such as the frictional losses. Matrix $\boldsymbol{X}$ represents all the temperature of component elements which are unknown. To solve for matrix $\boldsymbol{X}$, computational linear algebra solver based on Gauss-Jordan approach is used to solve for each unknown temperature. The solution would give the steady-state operating temperature of all the components of the oil-free prototype. With the temperature of the elements in contact with the working fluid, the heat transfer to and from the working fluid $\dot{Q}_{cv}$ required for the thermodynamics iteration in Section 4.5 can be found based on Equation (6.18) and corresponding convective heat transfer coefficient with the working fluid in (6.31). The experimental validation of the predicted temperature distribution within the oil-free compressor will be shown in Chapter 8.

6.3 Summary

The leakage flow and heat transfer analysis models are presented in this chapter and a summary of the chapter is given as follows:

- Radial clearance leakage is modelled as a Fanno flow through an equivalent straight channel with a converging throat.

- Similarly, vane endface leakage is also modelled as a Fanno flow through a straight channel but without the converging section.

- CFD simulation was carried out to justify the adoption of Fanno flow model for vane endface leakge. Both CFD simulation and mathematical model were found to predict similar flow behaviour and a strong agreement was found between the results with an average discrepancy of 3.9% across the rotational angles.

- Equivalent leakage paths of rotor endface clearance are assumed to be the shortest straight line distance, which has the least flow resistance, between compression and suction sides and the leakage flow is also modelled as Fanno flow through a straight channel without the converging throat.

- CFD simulation was carried out to analyse the flow behaviour at the rotor endface clearance. It was found that there were large discrepancies in the leakage mass flow prediction at high pressure ratio and rotational angles beyond 270° with the highest discrepancy of 50.6% and an average discrepancy of 20.5%. This is because of the difference in the assumption of the leakage pathway for both CFD simulation and theoretical modelling — the fluid flow vector in the CFD simulation is assumed to be normal to the inlet of the flow domain and followed a longer curved path from high pressure side to low pressure outlet, while the theoretical model assumed a shorter straight line path which results in higher flow velocity and choked flow.

- Since leakage flow will be much greater in practice due to slip flow and rarefaction effect, especially in an oil-free compressor where clearances are not blocked by oil lubrication, the CFD simulation approach is more conservative in prediction and the theoretical modelling using the shortest

straight path as equivalent flow channel for Fanno flow will be used for the leakage analysis of the oil-free prototype.

- In the temperature prediction of the compressor components, the entire compressor is sub-divided into 38 discrete elements with simpler geometry and lumped thermal conductance approach is used to analyse the heat transfer and temperature distribution of these parts.
- Existing convection heat transfer correlations for standard geometrical configurations are presented and applied in the modelling of heat transfer among the elements.
- The linear heat transfer equations of 38 elements are expressed in matrix form and computational linear algebra solver based on Gauss-Jordan approach is used to solve for the unknown temperature of each element.

In the next chapter, the design specifications of the prototype and the details of the experimental setups will be presented.

Chapter 7

Design Of Prototype And Experiment Setups

The oil-free swing vane compressor prototype was designed with the concepts presented in Chapter 3. The fabrication, dimensioning details and the selection process of the self-lubricating material for bushings, will be first presented in this chapter. The experiment setup for the measurement of prototype performance and the procedures for the experimental study and validation will then be presented in the second half of this chapter.

7.1 Design Specifications and Physical Dimensions of Prototype

For the purpose of experimental study, the compressor prototype was designed with a working volume of 50 cm^3 which is larger than the capacity of an average household compressor (generally a capacity of 28 — 32 cm^3 [159] for an air-conditioning compressor). This is because the prototype operates without oil lubrication and leakage is expected to be significant; in the event of severe leakage due to large clearances from poor fabrication, the mass intake and discharge flow rate can still be effectively measured. To validate the theoretical modellings of the oil-free prototype, the first phase of the experimental validation runs were conducted using air as the working fluid in an open loop which is easier to operate. Afterwards, a closed refrigeration loop which uses refrigerant R134a as the working fluid was designed to study the effects of liquid refrigerant injection cooling. The specifications of the prototype are tabulated in Table 7.1:

Table 7.1: Design Specifications of Prototype

Parameters	
Working fluid	Air (Open loop), R134a (Closed refrigeration loop)
Maximum allowable pressure	2400 kPa
Volumetric displacement	49.5 cm^3 rev^{-1}
Maximum operating speed	1800 rev min^{-1} (rpm)

The exact dimensioning and design of the oil-free swing vane compressor prototype was done by the author and the prototype was fabricated by Time Engineering Sdn Bhd, Malaysia using dissimilar materials for different components to prevent welding of two bearing surfaces during dry rubbing. The components were manufactured with materials as shown in Table 7.2.

Table 7.2: Materials used for each components of the prototype

Component	**Material**
Eccentric Shaft	AISI630 17-4 PH Stainless Steel Condition A [160]
Rotor	AISI630 17-4 PH Stainless Steel Condition A
Counterweight	AISI630 17-4 PH Stainless Steel Condition A
Split Bush	PEEK GF30 [161], C95500 AB2 Nickel-Aluminum Bronze [162]
Cylinder	7075 T651 Aluminium [163]
Endface bushing plates	C95500 AB2 Nickel-Aluminum Bronze Cast Nylon 6 [164] & PTFE [165]
Valve Reed	AISI 304L [166]
Cover	7075 T651 Aluminium
Suction and Discharge Pipes	AISI 304L
Base Plate	6061 T651 Aluminium [163]

The dimensions of each component of the prototype were measured to check for consistency with stated tolerances so that the correct dimensions of the clearance gaps between moving parts can be determined. The major compressor dimensions were measured using micrometer screw gauge and digital vernier caliper with accuracies of ± 0.001 mm and ± 0.01 mm respectively. For complex and inaccessible dimensions, coordinate measurement machine (CMM) with the accuracy of ± 0.1 μm, was used and form tolerances like roundness and angular positions of holes were also measured. Multiple measurements were made for each dimension and the arithmetic mean was taken as the final measured value. The measured dimensions of main components with their design specifications are tabulated in Table 7.3. The asterisks (*) specify that the parts have been reworked to get better fitting for smoother operation.

Table 7.3: Prototype Dimensions

Component/Dimension	**Specification, mm**	**Final measured dimension, mm**
Cylinder		
Inner cylinder wall diameter	101.00 ± 0.06	101.045
Chamber height	35.00 ± 0.02	34.910
Split bush slot diameter	12.00 ± 0.01	12.080
Split bush slot depth	40.50 ± 0.01	40.350
Lower shaft bearing hole diameter	47.00 — (0.02∼0.04)	47.004
Lower shaft bearing hole depth	20.00 + 0.02	20.086
Shaft		
Upper shaft diameter	20.00 — 0.01	19.950
Eccentric diameter	35.00 + 0.01	34.970
Eccentric length	29.00 ± 0.01	28.949
Lower shaft diameter	20.00 — 0.01	19.970
Lower shaft length	26.00 + 0.02	25.975
Total length	164.00 — 0.21 164.00 + 0.23	163.897
Rotor		
Axial length	30.00 ± 0.01	29.897
Outer diameter	90.00 — 0.06	89.918
Vane length	25.10 ± 0.01	25.090
Vane width	6.00 ± 0.01	5.990
Split Bush		
Diameter	12.00 ± 0.01	11.923
Axial length	40.30 ± 0.01	40.327
Vane slot height	30.05 — 0.02	30.072
Vane slot width	6.00 + 0.04	5.913
Valve Reed		
Thickness	0.20 ± 0.10	0.300

Diameter	15.00 + 0.10	15.040
Length of neck section	19.16 ± 0.10	19.010
Width of neck section	8.00 ± 0.10	7.990
Total length	33.00 ± 0.10	33.170
Top Cover		
Diameter of endface bushing slot	101.00 ± 0.06	101.04
Depth of endface bushing slot	5.00 ± 0.10	5.087
Top Endface Bushing*		
Diameter	101.00 — 0.01 101.00 + 0.10	100.940
Thickness	5.00 — 0.02	5.120
Bottom Endface Bushing*		
Diameter	101.00 — 0.01 101.00 + 0.10	100.950
Thickness	5.00 — 0.02	4.85

As mentioned in Chapter 3, ball bearings are used at the eccentric-rotor and shaft-cover bearing surfaces where there are high loadings and frictional losses. The ball bearings used are SKF self-lubricated sealed ball bearings and the dimensions are shown in Table 7.4. The dimensions are based on SKF's specification and can be found in the Appendix F, Section F.14.

Table 7.4: Ball Bearing Specifications

Bearing Designation/Dimension	Specification, mm
Shaft Bearing W6204-2RS1	
Bore diameter	20
Outside diameter	47
Height	14
Radial internal clearance	0.005min. 0.020max.
Eccentric Bearing W6007-2RS1	
Bore diameter	35
Outside diameter	62
Height	14
Radial internal clearance	0.005min. 0.020max.

Based on the measured dimensions in Table 7.3, the clearances which affect various leakage paths were determined and are listed in Table 7.5. The asterisks (**) specify that the particular clearance has been adjusted with the use of shims to get tighter tolerance. It is noted that the radial clearance between the rotor and cylinder and the top endface clearance are the two significant leakage paths identified in the prototype.

Table 7.5: Leakage Path Clearance

Leakage Path	**Clearance, μm**
Radial clearance between rotor and cylinder, δ_{rad}	63.5
Radial clearance between split bush & slot, $\delta_{rad,b}$	157
Clearance between rotor/vane endface & top endface bushing, $\delta_{ef}{}^{**}$	16.0

In addition, the surface roughness of the bearing surfaces between the rotor and bottom bushing plate and between the vane and split bush are measured by surface profilometer which has a resolution of ± 0.001 μm. The measured surface roughness are averaged and tabulated in Table 7.6.

Table 7.6: Measured surface roughness values

Bearing Surface	**Surface Roughness Ra, μm**
Rotor and Bottom Bushing Plate	
Rotor	0.665
Bottom Bushing Plate	1.085
Vane and Split Bush	
Vane	0.356
Split Bush's Vane Slot	2.346

Note that due to manufacturing inaccuracies in the fabrication, the clearances in some dimensions are larger than the design specifications. For example, the dimensions of the axial length of the cylinder, rotor and the thickness of the endface bushing plates exceeded the tolerance specified by a resultant average of 100 μm and shims have to be added to reduce the top endface clearance. Due to the limited resources allocated for this study, only certain components were re-worked and the remaining dimensions are unchanged.

7.2 Prototype Assembly

In this section, the prototype components and the assembly procedure of the prototype are presented photographically. The prototype is made up of 17 major components; a cylinder body, a top cover, a rotor, an eccentric shaft with a counterweight, 2 shaft bearings, 2 eccentric bearings, 2 endface bushings and a split bush made of self-lubricating materials, a valve reed with the stop plate, an injector adaptor, the suction and discharge pipes. Since uneven distribution of rotating masses could contribute to vibratory forces or motions as a result of centrifugal forces, the centre of gravity of the shaft assembly — eccentric shaft, rotor and counterweight — has to be balanced to prevent excessive loading on the ball bearings and unnecessary rubbing between the rotor and the top endface bushing plate due to out-of-plane vibration of the rotor. The procedural steps in balancing the shaft assembly are shown in Appendix E.

The lower shaft bearing was first tight-fitted into the lower bearing hole in the cylinder and secured with bearing retaining collar, as shown in Figure 7.1 in details.

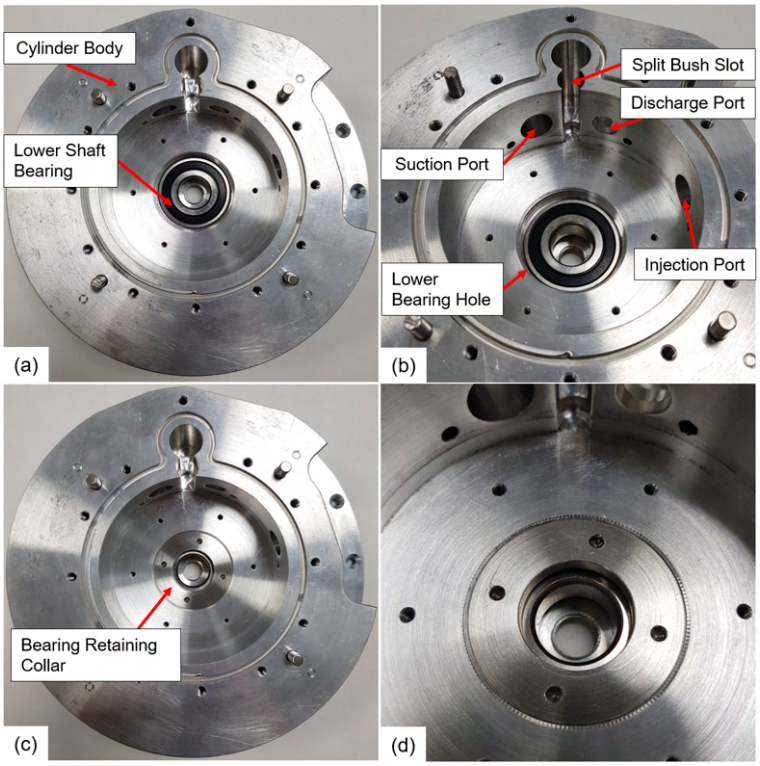

Figure 7.1: Assembling procedure of lower shaft bearing — a) Ball bearing tight-fitted into the bearing hole b) Detailed overall view c) Bearing retaining collar tightened to secure the ball bearing. d) Detailed view of retaining collar.

The bottom endface bushing plate made of self-lubricating material was then mechanically fastened onto the cylinder body, as shown in Figure 7.2, using countersunk screws so as not to pose interference to the bearing surface that rubs with the lower surface of the rotor during operation.

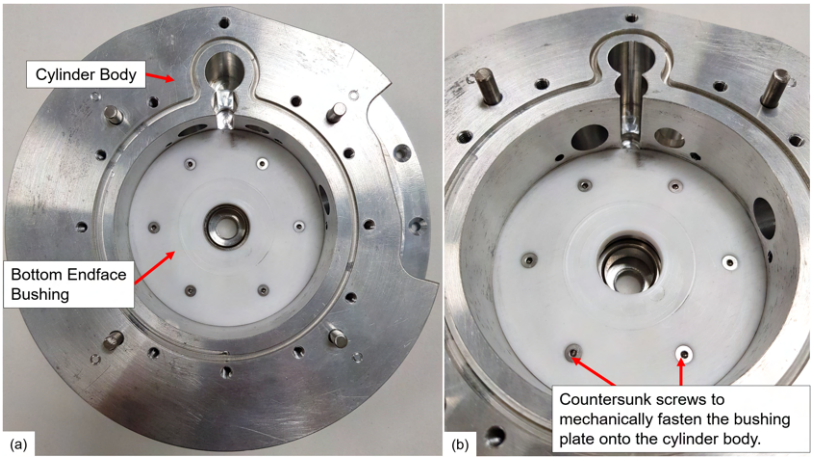

Figure 7.2: Fastening bushing plate onto the cylinder — a) Front view b) Detailed overall view.

Next, the split bush, which is also entirely made of self-lubricating material, was then placed into the split bush slot in the cylinder body, as illustrated by Figure 7.3. For the ease of manufacturing and to ensure accuracy in the vane slot clearance, the split bush was fabricated as a single piece from a rod of self-lubricating material with a vane slot cut in the middle to accommodate the swivelling motion of the vane instead of being fabricated into two individual bushings.

Different self-lubricating materials were fabricated into the split bush and endface bushings and were used in dry runs to evaluate their wear resistance. The evaluation process and testing observations will be shown in the next Section 7.3.

Right after securing the endface bushing and split bush, the shaft was inserted into the lower shaft bearing before the rotor was assembled onto the eccentric with the free end of the vane inserted into the vane slot of the split bush, as shown in Figure 7.4.

The upper shaft ball bearing was then tight-fitted onto the top cover while the top endface bushing plate was mechanically fastened onto the underside, as shown in Figure 7.5a and b. After which, the cover was aligned with dowel pins and assembled onto the cylinder body with M5 screws (see Figure 7.5c). Once the cover was tightened, the shaft seal was driven into the cover and secured

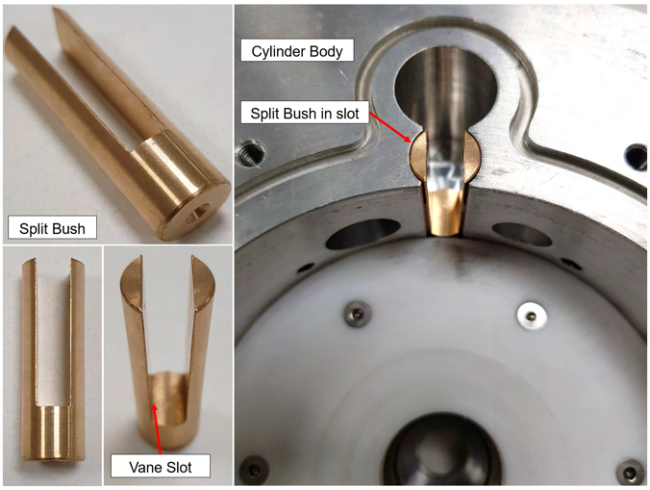

Figure 7.3: Design and positioning of split bush.

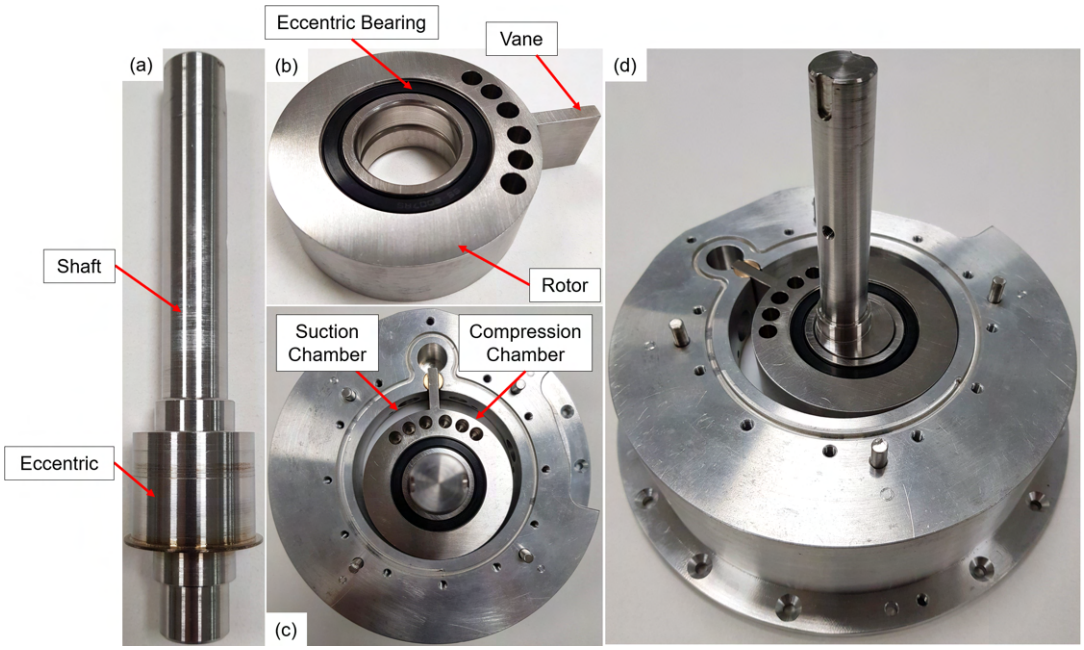

Figure 7.4: Assembly procedure of the rotor and shaft — a) Eccentric shaft b) Rotor c) Front view of assembly d) Overall view.

with the securing plate, as illustrated in Figure 7.5d and e.

The valve reed was then installed over the discharge port to cover the port hole, as shown in Figure 7.6a and c, and the discharge and suction pipes were then assembled onto the cylinder body at the discharge and suction ports respectively (as seen in Figure 7.6d). Lastly, the injector adaptor was screwed into the injector port, as shown in Figure 7.6e.

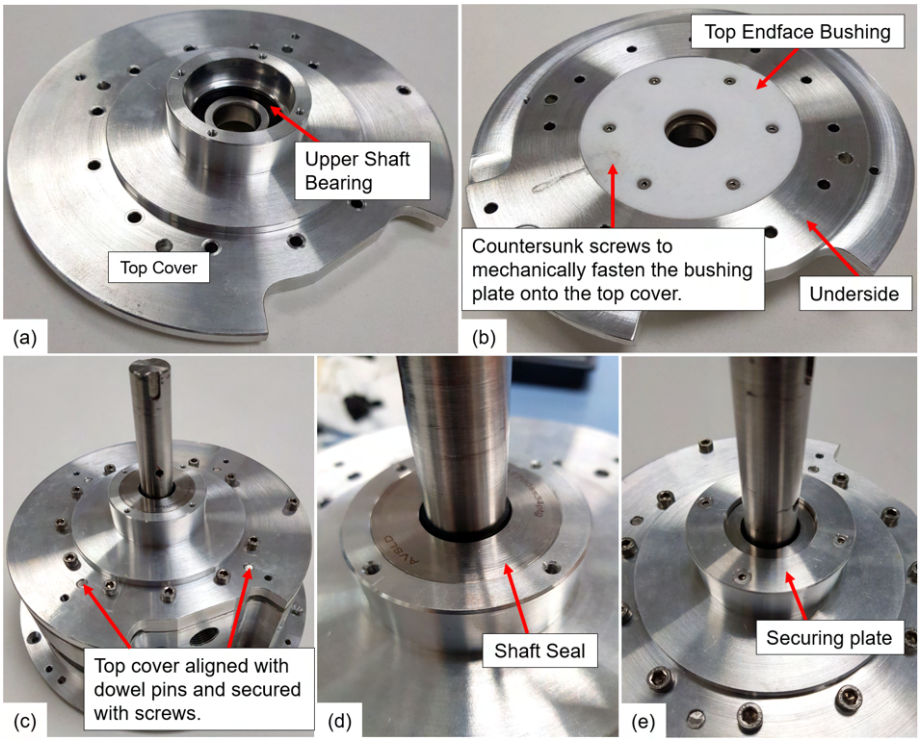

Figure 7.5: Assembly procedure of the top cover — a) Upper shaft bearing tight-fitted onto the top cover b) Top endface bushing fastened onto the underside of top cover c) Top cover aligned by dowel pin and fastened by screws d) Shaft seal tight-fitted onto the top cover e) Securing plate to secure the shaft seal.

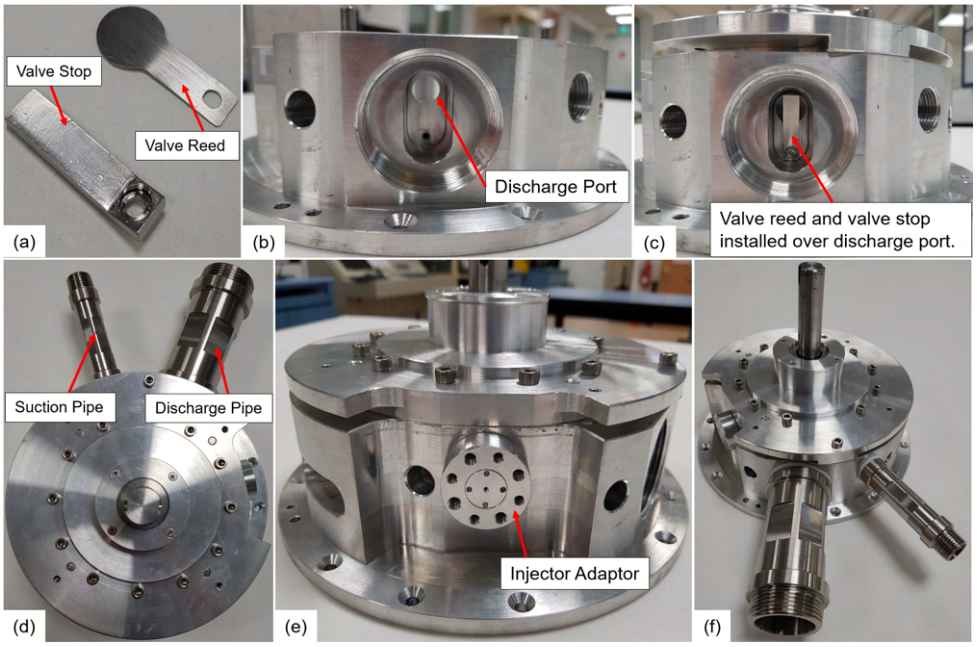

Figure 7.6: Assembly procedure of the valve reed, injector adaptor and discharge and suction pipes — a) Valve reed and valve stop b) Discharge port c) Valve reed and valve stop installed to cover the discharge port d) Suction and discharge pipe assembled onto the cylinder body f) Injector adaptor screwed onto the injector port f) Overall view.

7.3 Selection Of Bushing Materials

In this section, the results of the wear resistance testing of each self-lubricating materials, namely, PEEK GF30 [161], Cast Nylon 6 [164], PTFE [165] and C95500 AB2 Nickel-Aluminium Bronze [162], will be shown photographically.

7.3.1 Sample Preparations

Each self-lubricating material was cut to the specifications of the endface bushings and split bush, as previously tabulated in Table 7.3. Three self-lubricating materials, which include Cast Nylon 6, PTFE and C95500 AB2 Nickel-Aluminium Bronze, were fabricated into the endface bushing plates, as shown in Figure 7.7. On the other hand, two materials with higher wear resistance and hardness, specifically PEEK GF30 and C95500 AB2 Nickel-Aluminium Bronze were fabricated into the split bush since it bears higher loadings from gas pressure, as shown in Figure 7.8. PEEK GF30 was not chosen to be fabricated into endface bushing as a large bulk material of PEEK GF30 is required for the fabrication and it is costly for such testing.

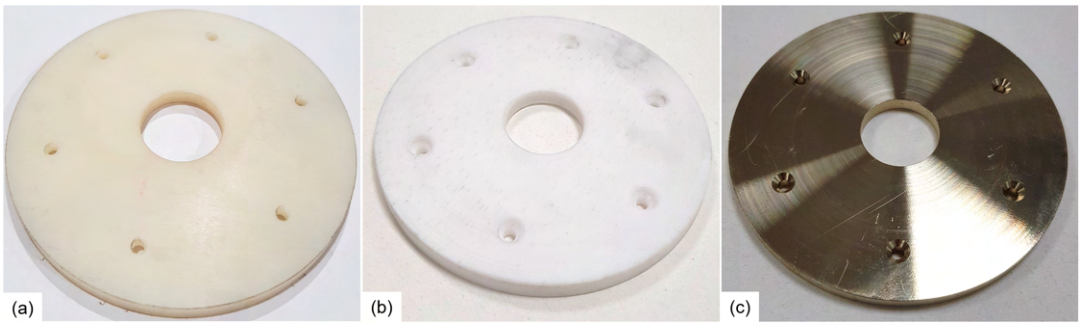

Figure 7.7: Samples of endface bushing plate — a) Cast Nylon 6 b) PTFE c) C95500 AB2 Nickel-Aluminium Bronze.

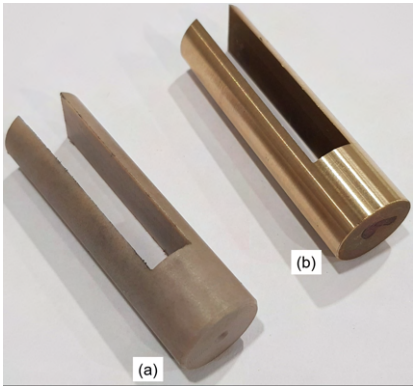

Figure 7.8: Samples of split bush — a) PEEK GF30 b) C95500 AB2 Nickel-Aluminium Bronze.

7.3.2 Wear Test

For the endface bushing of diameter 101 mm, the maximum sliding speed can reach up to 15.86 ms $^{-1}$ at 3000 rpm while the sliding speed between the vane and split bush is approximately 1.72 ms $^{-1}$, which are operating speeds that are beyond some testing range conducted in studies reviewed in Section 2.4. Therefore, the dry sliding wear behaviour of each material was studied by assembling and using the sample in the prototype for actual runs, as shown in Figure 7.9 and Figure 7.10, in order to test its wear resistance and reliability under the practical dynamic loadings and harsh working temperature of an average compressor's operating condition.

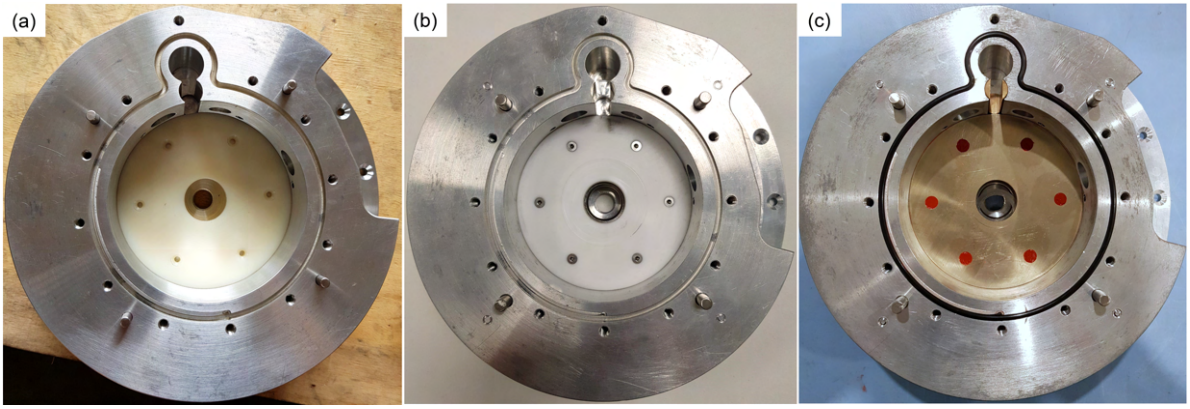

Figure 7.9: Testing on each bushing plate sample — a) Cast Nylon 6 b) PTFE c) C95500 AB2 Nickel-Aluminium Bronze.

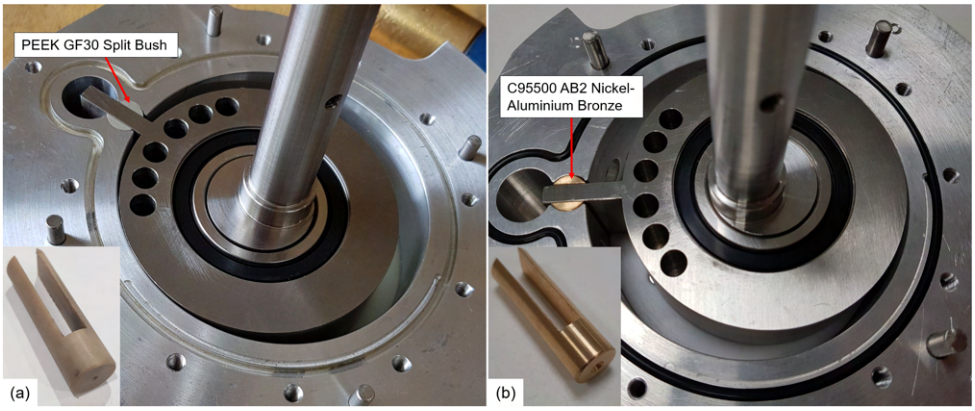

Figure 7.10: Testing on each split bush sample — a) PEEK GF30 b) C95500 AB2 Nickel-Aluminium Bronze.

The prototype was coupled to a motor and setup, as shown in Figure 7.11, and the testing was conducted on an open loop using air as the working fluid. The run time of each testing was 15 minutes with the operating speed of the

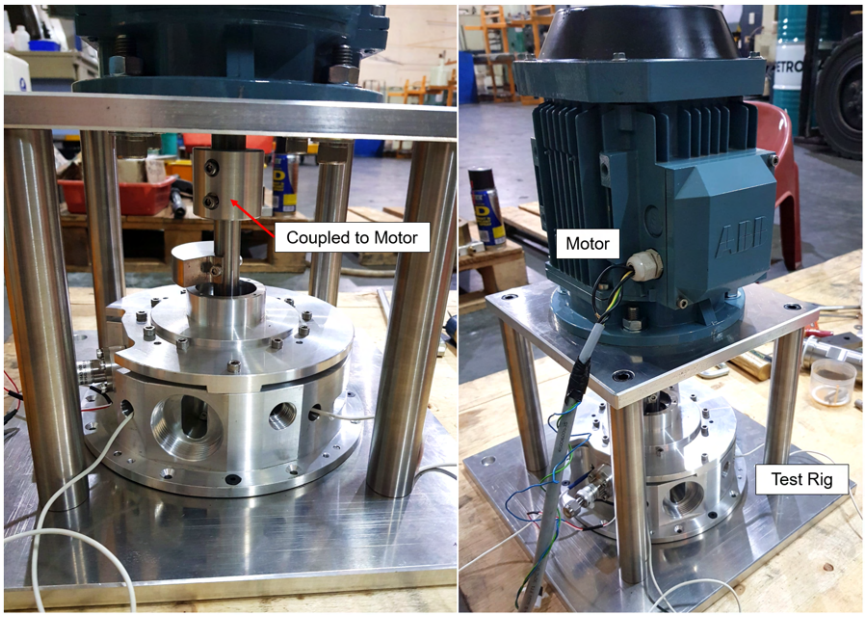

Figure 7.11: Dry Testing Setup.

motor increased progressively every 5 minutes until a maximum rotational speed of 3000 rpm was achieved while the pressure ratio was maintained at the range of 1.2 to 1.4. The wear behaviour and the worn surfaces of each sample will be shown in Subsection 7.3.3.

7.3.3 Worn Surface Characterisation

Throughout the testing, some runs were terminated due to seizure of the compressor. After each testing, observations of the worn surfaces were carried out.

Both the worn surfaces of Cast Nylon 6 and PTFE bushing in Figure 7.12a and b showed that severe plastic deformations and plough marks contribute to most of the surface modifications with melting and thermal-oxidation observed at the inner portion of the endface bushing where dry sliding with the eccentric occurs. The melted surface and thermal-oxidised debris generated in both polymer-based samples suggest that the interfacial temperature at the sliding contact points between the bushing and rotating components might have exceeded the melting temperature of the self-lubricating materials. The worn surfaces of the AB2 Nickel-Aluminium Bronze sample in Figure 7.12c, on the other hand, did not show any melted surface and thermal-oxidised debris.

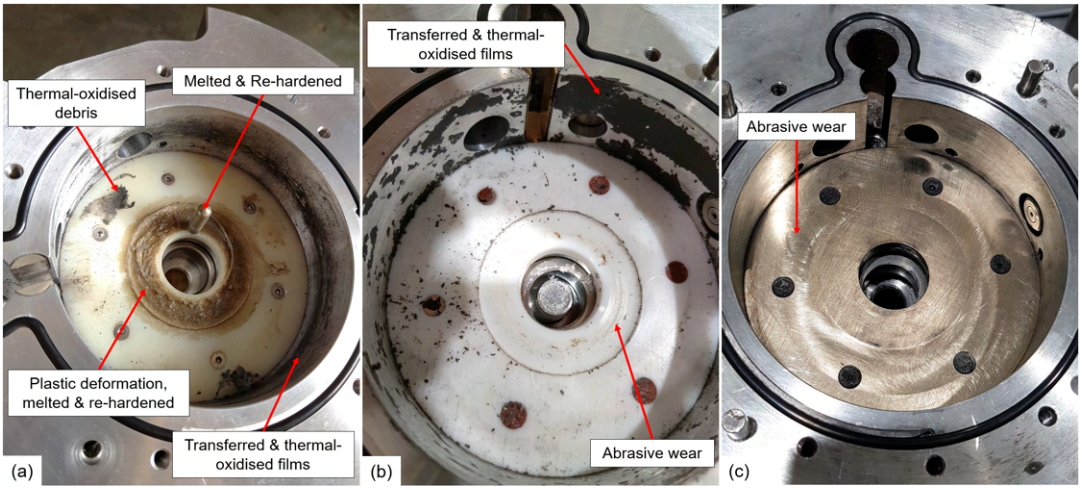

Figure 7.12: Worn surface of bottom endface bushing plate — a) Cast Nylon 6 b) PTFE c) C95500 AB2 Nickel-Aluminium Bronze.

Based on thermal properties tabulated in Table 7.7, the interfacial temperature could have risen beyond the temperature of 335°C but stayed below the melting temperature of AB2 Nickel-Aluminium Bronze at 1038°C. The low thermal conductivity of the polymers might be the cause of the slow dissipation of the friction-induced heat at the sliding interface, which in turn has led to a drastic increase in the interfacial temperature during dry sliding due to the accumulation of heat at the interface. Deep wear furrows caused by the ploughing motion from dry rubbing with the eccentric of the shaft were clearly seen at the inner portion of PTFE sample of Figure 7.12b, suggesting that the vibration and tilting of the eccentric shaft do occur during rotation. Large fragments of transferred PTFE films found on the cylinder wall also show that PTFE's low wear resistance is unsuitable for use as a bottom endface bushing where frequent contacts with the rotor and eccentric occur. Furthermore, the substantial region of melted and thermal-oxidised surface observed in Cast Nylon 6 sample indicates that it is not suitable to be used as a bushing for the high operating speed of the compressor as the interfacial temperature at the bearing surface can easily rise beyond its melting temperature. The bottom endface bushing of AB2 Nickel-Aluminium Bronze, on the other hand, only suffered abrasive wear with minimal wear fragments observed.

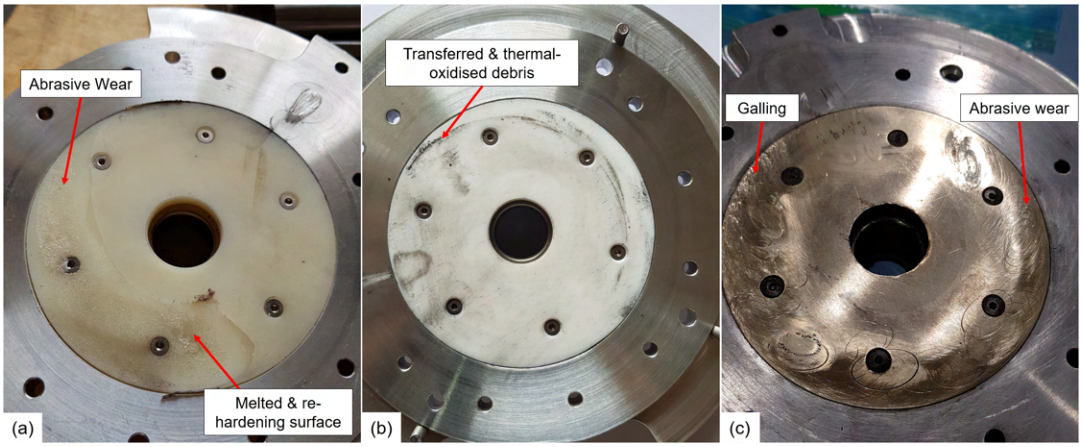

Figure 7.13: Worn surface of upper endface bushing plates — a) Cast Nylon 6 b) PTFE c) C95500 AB2 Nickel-Aluminium Bronze.

As there is a clearance between the upper endface bushing and rotor, the top bearing surfaces are designed not to experience constant dry friction sliding. However, due to vibration and tilting of the shaft, the rotor vibrates out of its rotation plane and undergoes some dry rubbing with the upper endface bushing. This is evident from the abrasive wear marks observed from worn surfaces of each sample, as shown in Figure 7.13. From Figure 7.13a, it can be observed that Cast Nylon 6 surface experienced massive peeling and tearing caused by the dry sliding with the rotor top surface. As compared to the bottom endface sample shown in Figure 7.12c, the upper endface bushing made of AB2 Nickel-Aluminium Bronze (see Figure 7.13c) also exhibited signs of abrasive wear with severe galling. This might be caused by the increased intensity of ploughing and knocking from the vibrating rotor against the top endface bushing due to the presence of the clearance gap between both surfaces. The large deposits of transferred AB2 Nickel-Aluminium Bronze on the rotor surface, as shown in Figure 7.14, further confirmed that adhesive wear does occur between the stainless steel surface of rotor and the AB2 Nickel-Aluminium Bronze bushing. This also indicates that seizure of compressor due to welding of bronze deposits on both sides of the mating surfaces can occur and this might be the possible cause of seizure during some test run.

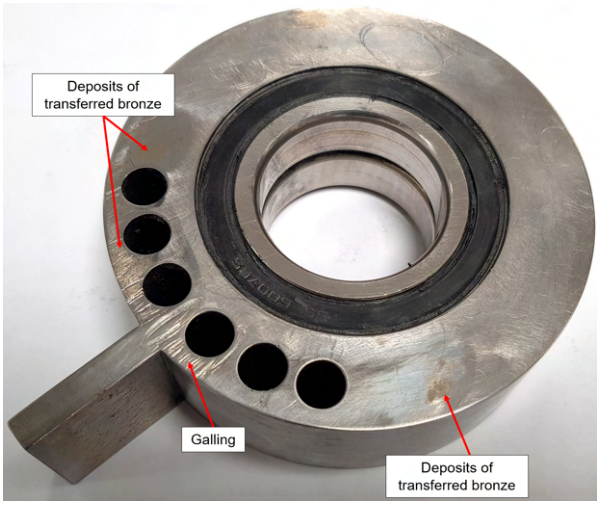

Figure 7.14: Transferred layers of C95500 AB2 Nickel-Aluminium Bronze onto rotor surface.

The worn surface of PEEK GF30 in Figure 7.15a, showed severe melting and thermal oxidation along the ploughs at the edge of the vane slot where there is high contact loading from the vane. This indicates that the interfacial temperature at the sliding contact between the split bush and vane sides had risen beyond 335°C during the testing. From wear marks on the vane side in Figure 7.16a and b, it can be ascertained that adhesive wear also does occur during the wear process of PEEK GF30 sample as large deposits of transferred layer was seen on the vane side with severe scuffing marks. Furthermore, the friction-induced heat has also caused the warping of the vane slot of the PEEK GF30 split bush, as seen in Figure 7.15b. Warping is detrimental to the reliability of the compressor as the drastic dimension change may cause severe mechanical interference. The AB2 Nickel-Aluminium Bronze split bush, on the other hand, showed no sign of melting but it has suffered severe galling from the dry sliding with the side of the vane under high contact loading from gas pressure, as shown in Figure 7.15. Approximately 0.37 mm enlargement in the width of the vane slot is measured after a 15 minutes of dry run.

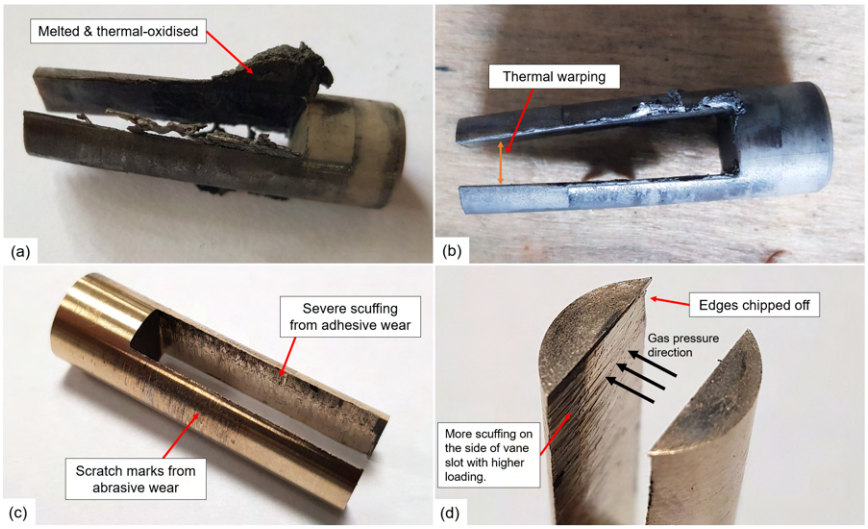

Figure 7.15: Worn surface of split bush — a) PEEK GF30 b) C95500 AB2 Nickel-Aluminium Bronze.

Table 7.7: Thermal properties of self-lubricating materials

Cast Nylon 6 [80, 167]	Value
Melting Point (°C)	214
Thermal conductivity at 23°C (W $m^{-1}K^{-1}$)	0.28
PTFE [168]	
Melting Point (°C)	335
Thermal conductivity at 25°C (W $m^{-1}K^{-1}$)	0.25
PEEK GF30 [77, 169]	
Melting Point (°C)	340
Thermal conductivity at 25°C (W $m^{-1}K^{-1}$)	0.43
C95500 AB2 Nickel-Aluminium Bronze [155, 156]	
Melting Point (°C)	1038
Thermal conductivity at 20°C (W $m^{-1}K^{-1}$)	41.9

From the straw to deep straw colour of the rotor and vane side surfaces, as shown in Figure 7.16b, c and d, it can be concluded that the resultant rotor and vane can easily reach a temperature beyond 200°C due to the friction-induced heat from dry sliding. When steel is heated in contact with air at certain temperature in the tempering range, the surface of the steel takes on various temper colour due to the formation of thin oxide layers on the surface. As an example, the temper colour of common steels at different temperature ranges are given in Table 7.8. Hence, based on the temper colour tabulated in Table 7.8, the rotor could have reached 220 to 240°C due to friction-induced heat.

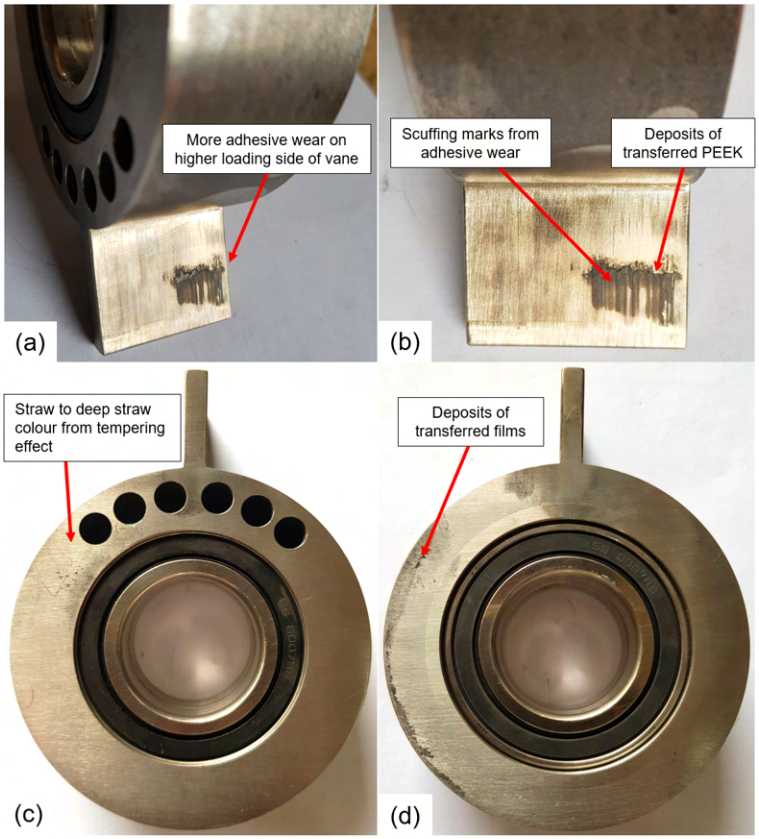

Figure 7.16: Temper colour of rotor due to high rubbing heat and exposure to air — a) Side view of rotor b) Deposits of PEEK polymer due to scuffing on high loading side of vane c) Top surface of rotor d) Bottom surface of rotor.

Table 7.8: Tempering colour of steel [170, 171]

Heating temperature °C	Colour
204.4	Faint straw
226.7	Straw
246.1	Deep straw
271.1	Bronze
282.2	Peacock
310.0	Full blue
337.8	Light blue

Based on the above observations of each worn surface, C95500 AB2 Nickel-Aluminium Bronze exhibits better wear resistance and thermal stability against the high friction-induced heat and dynamic loading conditions of the prototype as compared to other polymer-based self-lubricating material. In addition, the severe melting in Cast Nylon 6 and high wear characteristic of PTFE showed that they are unsuitable for such application. PEEK GF30, which has the

highest melting point and wear resistance among the polymer bushings, showed sign of thermal oxidation and melting even though its melting temperature is 340°C, suggesting that the interfacial temperature at the bearing surfaces of a compressor is unsuitable for most polymer-based self lubricating materials that have melting points within 400°C. In conclusion, C95500 AB2 Nickel-Aluminium Bronze was chosen as the material of choice for the fabrication of both the endface bushings and the split bush that will be used in the experimental runs due to its high wear-resistance and high melting point.

7.4 Experimental Setup

Two experimental setups for both open air loop and refrigeration loop were designed to validate the theoretical modellings from Chapters 4 to 6 and to study the effects of liquid refrigerant injection cooling respectively. For simplicity, the prototype was first employed in an open air loop to measure its performance for the validation of theoretical modellings. Once the theoretical models were validated in Chapter 8, Section 8.1 to Section 8.3, the models were then used to predict the effect of the liquid refrigerant injection cooling, which were also further validated by comparison with the measurements obtained from refrigeration runs of the oil-free prototype in the second part of the experimental study in Chapter 8, Section 8.4.

7.4.1 Experimental Setup For Open Air Loop

Figure 7.17 is the schematic of the experimental setup for open air loop and Figure 7.18 shows the actual experiment setup. The discharge pressure, volumetric flow rate of discharge air, pressure variation of working chambers, temperature of prototype's components and the total power input to the prototype are to be measured.

In the experiment, the prototype was driven by an ABB 2.2 kW two-pole induction motor with a frequency controller to regulate the rotational speed of the motor. However, due to motor slippage or the lag between the synchronous speed of the electric motor's magnetic field and the shaft rotating speed, the actual output speed of the motor differed from the stated speed indicated by the frequency controller by 1.35% to 1.86%. As a result, a tachometer of TM1100 model, which has a measuring resolution of 0.01 rpm with an accuracy of 0.02%, was used to validate the resultant operating speed of the compressor. The

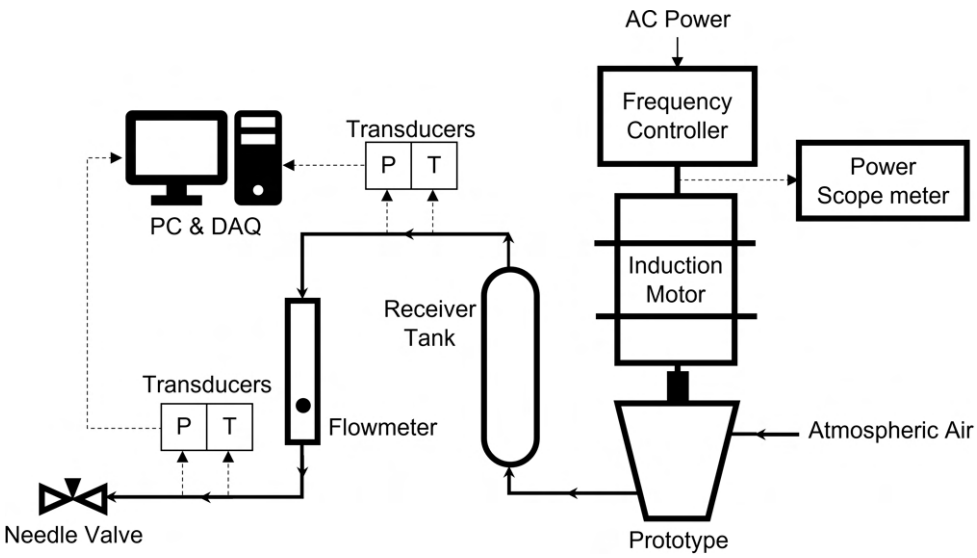

Figure 7.17: Schematic diagram of the experimental setup for open air loop.

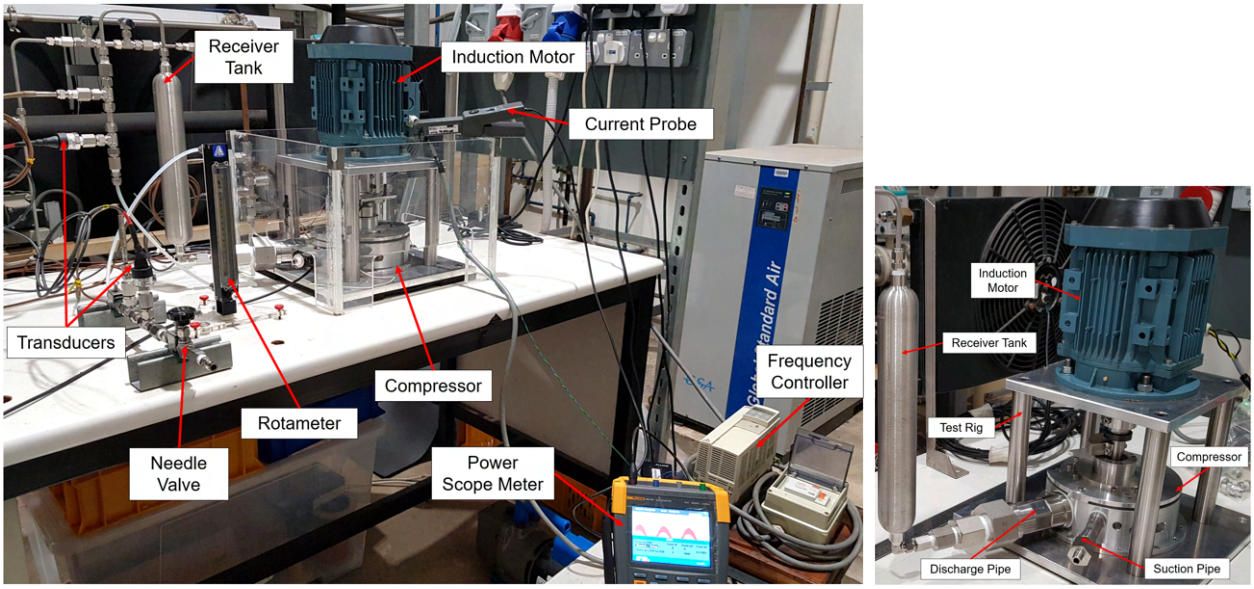

(a) Overall view. (b) Detailed view.

Figure 7.18: Actual experimental setup for open air loop.

power and current input into the compressor were measured using Fluke MDA-510 Power Scope Meter and current probe, as shown in Figure 7.18a where the probe was clamped onto the current input wire of the motor. During the operation, atmospheric air was directly drawn into the prototype for compression and the compressed air was discharged into a 0.5 litre Swagelok 304L-HDF4-500 receiver tank in which the discharge pressure was measured by a WIKA A-10 series pressure transducer with a measurement range of up to 40 bar. Meanwhile, the compressed air temperatures at both the outlets of the receiver

tank and flowmeter were measured by standard Type T thermocouples which have a temperature tolerance of ±1°C. Throughout the working cycle, the pressure fluctuations of both suction and compression chambers were measured by two Endevco 8530B-200 and 8530B-500 piezoresistive pressure transducers respectively, which were inserted into the prototype's chamber wall. The pressure transducers with high sensitivity (0.2 ± 0.07 & 0.09 ± 0.03 mV/kPa) are able to record the pressure at a sampling rate of more than 500 kHz. To determine the volumetric efficiency of the prototype, the volumetric flow rate of the discharge air was measured using Aalborg 044-40-GL 150 mm flowtube rotameter with a 1/4"(6.35 mm) diameter Tantalum float. The flowmeter has a measurement range between 2015 – 69940 ml min^{-1}. A pair of pressure transducer and Type T thermocouple were employed at the inlet and outlet of the flowmeter in order to measure the pressure drop and temperature change so as to determine the density of the discharge air. A needle valve was installed at the end of the loop after the flowmeter to regulate the discharge flow rate and the discharge pressure. To validate the heat transfer model, the steady temperature of the top cover, cylinder body, suction and discharge pipes were also measured using standard Type K thermocouple which has a temperature tolerance of ±2.2°C. The signals from all sensors were captured by National Instrument data acquisition system (DAQ) and the measurements were taken at the maximum sampling rate of 25kHz. The specifications of all the experimental equipment and calibration data can be found in Appendix F and Appendix G, respectively. The uncertainties of the measuring devices based on equipment specifications are summarised in Table 7.9.

Table 7.9: Uncertainties of Measuring Equipment

Equipment	Uncertainty
WIKA Pressure transducer (model: A-10)	±20 kPa
Type T thermocouple [172]	±1°C
Type K thermocouple [172]	±2.2°C
Endevco piezoresistive pressure transducers (model: 8530B-200)	±6.89 kPa
Endevco piezoresistive pressure transducers (model: 8530B-500)	±17.24 kPa
Fluke power scope meter & current probe (model: MDA-510 & 80i110s)	±0.215 A
Aalborg 044-40-GL Rotameter	±1312.5 ml min^{-1}
Tachometer TM1100	±0.02% of reading

7.4.2 Experimental Setup For Refrigeration Loop

The refrigeration loop, as shown in the Figure 7.19, was designed to measure the COP of the vapour-compression cycle, the performance of the prototype under the effect of liquid refrigerant injection cooling and to validate the prediction results from the theoretical modelling. This mainly involves the measurement of the input power to the prototype and the temperature of the prototype components using the power scope meter and the standard Type K thermocouples, respectively. Furthermore, the discharge pressure, the volumetric flow rate of discharge R134a and the pressure variation of working chambers are also measured for model validation.

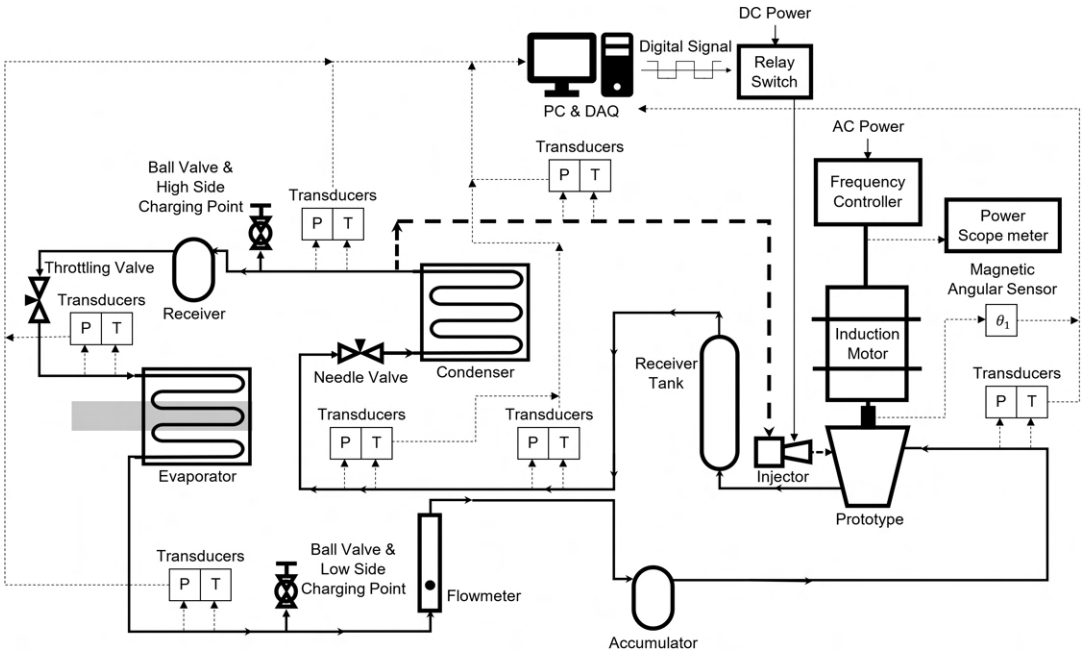

Figure 7.19: Schematic diagram of the experimental setup for refrigeration loop.

Figure 7.20 shows the actual experimental setup of the refrigeration loop. Along the cycle, pressure transducers and Type T thermocouples were installed to capture the properties of the refrigerant R134a so as to determine its thermodynamic state in the vapour-compression cycle. As no oil lubrication was employed in the experimental runs, lubrication components such as oil filter, oil sump or oil regulator was not required in the refrigeration cycle setup.

As explained in Subsection 3.2.2, the liquid refrigerant injection was electronically-controlled based on the angular position of the shaft and the compression phase. To detect the exact angular position of the shaft, a MR200 magnetic ring was mounted onto the shaft and a MSK210 Rotativ magnetic sensor with a maximum

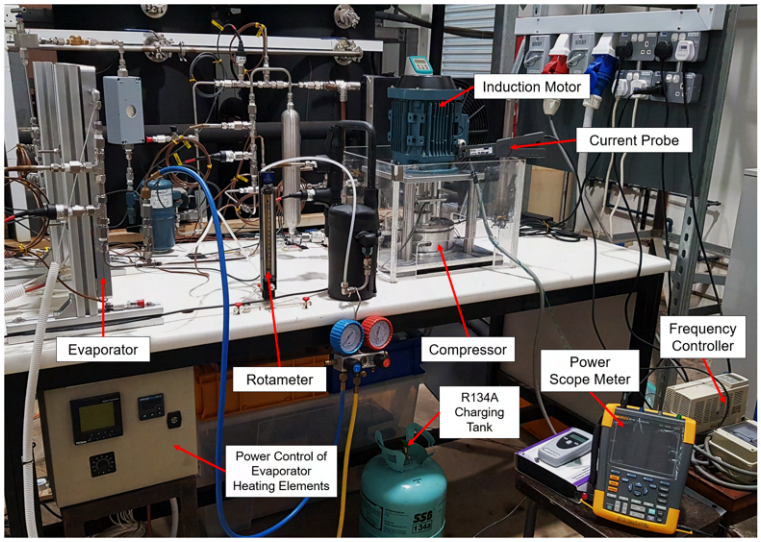

(a) Front view.

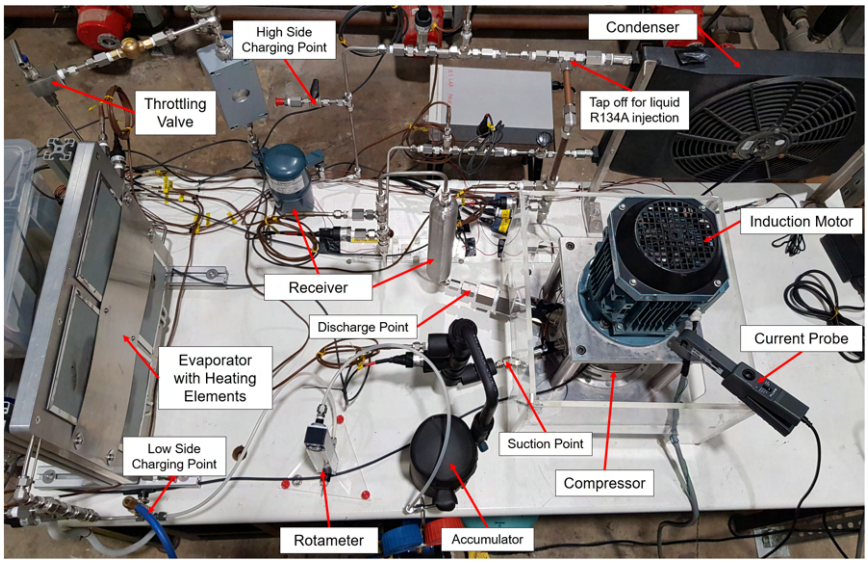

(b) Overall view.

Figure 7.20: Actual experimental setup for refrigeration loop.

resolution of 0.045° was positioned close to the magnetic ring to capture the polarity change due to the shaft rotation, as shown in Figure 7.21. The polarity change was in turn converted to analogue signal by the magnetic sensor which was sent to the DAQ. The DAQ system would trigger the AQY221R6V MOSFET relay switch via a digital signal once the analogue signal from the magnetic sensor had signalled the injection angular position of the shaft. The solenoid pulse valve (model: Parker Hannifin 009-1643-900) was opened once the replay switch was closed and the DC power source was switched on. To channel the liquid refrigerant into the compressor, a small quantity of subcooled/saturated

liquid R134a from the outlet of the condenser was tapped off from the main flow and channelled to the injector, as shown in Figure 7.22, and was injected into the compression chamber once the solenoid valve was opened. The injected liquid refrigerant was atomised into droplets once the liquid had passed through the hydraulic atomising nozzle (model:1/4M-SS8).

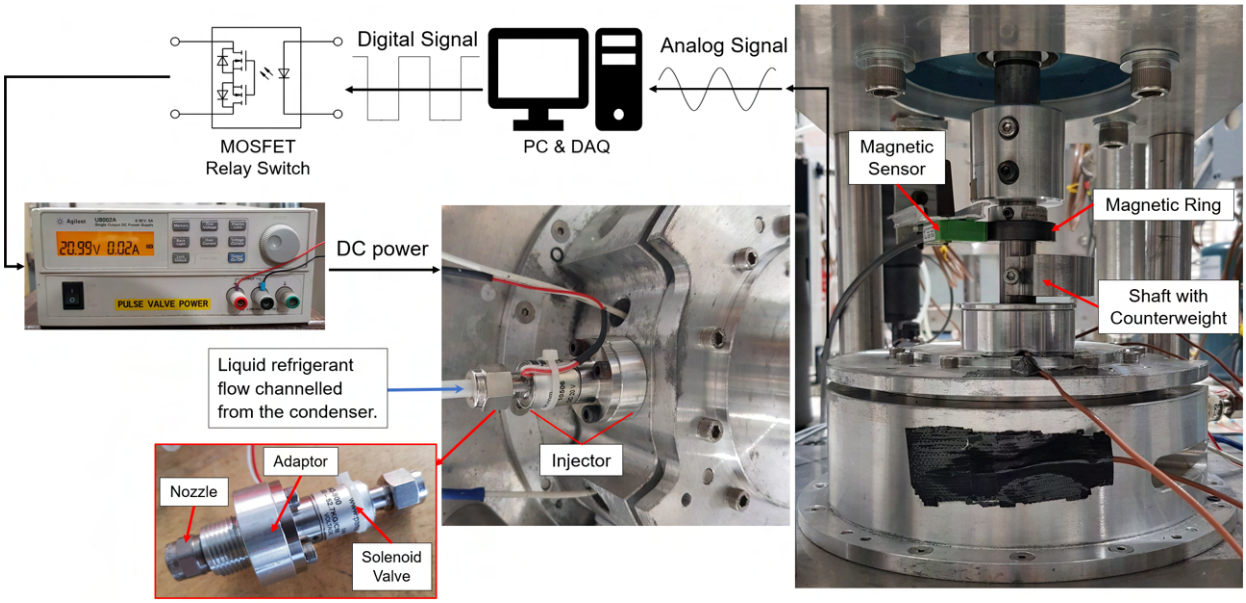

Figure 7.21: Actual experimental setup — Liquid refrigerant injection controls.

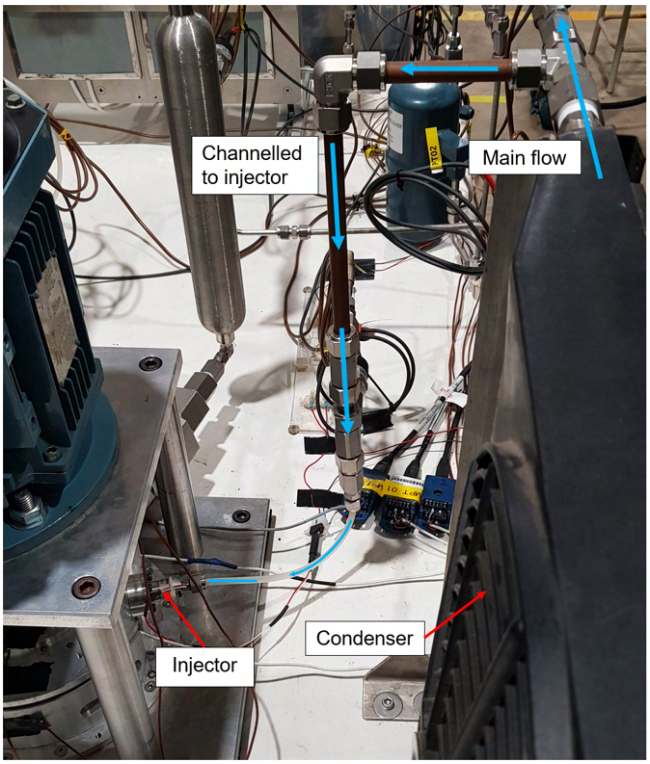

Figure 7.22: Actual experimental setup — Channelling liquid refrigerant from condenser outlet to the injector for liquid injection cooling.

7.5 Experimental Procedure

In this section, the experimental procedures for the performance analysis of the oil-free prototype are presented.

In the experimental test, a steady state is reached when the following conditions of measuring equipment are achieved:

1. The variation in the discharge pressure measured by WIKA pressure transducer (at the outlet of the discharge receiver and at the inlet and outlet of the condenser and evaporator) is within the transducer's uncertainty of ±20 kPa for a duration of 5 minutes.

2. The fluctuation of the float inside the rotameter is within ±2 mm of the reading scale for a duration of 5 minutes.

3. The temperature variation measured by the Type K thermocouples, attached onto the body of the prototype, is within the thermocouple's uncertainty of ±2.2°C for a duration of 5 minutes.

4. The temperature variation measured by the Type T thermocouples (at the outlet of the receiver and at the inlet and outlet of the condenser and evaporator) is within the thermocouple's uncertainty of $\pm 1^{\circ}C$ for a duration of 5 minutes.

Before actual experiments were conducted and measurement results were recorded, a preliminary test was conducted at a constant operating speed of 1620 rpm for more than 30 minutes to identify the appropriate duration of time required for the system to reach steady state. It was found that a duration of 15 minutes for experiment conducted with air was sufficient to achieve the conditions of steady state as mentioned above. For experiments conducted with air, the prototype was operated from 1080 rpm to 1800 rpm with an interval of 180 rpm for a duration of 15 minutes for each run in order to ensure that the steady state of the operating conditions was reached. Beyond this range of operating speed and duration, vibration and chattering of components were observed, and the prototype would be very prone to seizure before reaching the steady state. In order to prevent vibration and seizure during the initial startup phase of the compressor, a thin film of anti-seize grease was applied on the bushing surface to prevent galling. The grease was observed to be pushed aside by the rotor and vane after each run and was unable to stick onto the mating surface to provide long-term lubrication. This means that the mating surfaces were already dry rubbing once the steady operating speed of the compressor was reached. Each run was proceeded with caution to prevent overheating of the compressor and the runs were terminated if the chattering of moving parts was intense. The experimental procedures for open air loop runs are described below:

1. Components of the prototype, pipe fittings and the measuring instruments were adequately cleaned with isopropyl alcohol before assembly.

2. The piping of the loop was then checked for secure connection. Any major leakage was identified by bubble leak test (pressurised air at 900 kPa Absolute) and the leakage points were rectified by tightening of the fittings or sealing of the connections with high temperature silicone gasket sealant.

3. The motor frequency controller was set to the testing frequency and the motor was accelerated to the corresponding operating speed in order to shorten the duration of the transient startup phase of the compressor.

4. The needle valve at the end of the air loop was regulated to build up the pressure in the air receiver.

5. The operating conditions were maintained for 15 minutes so that the temperature distribution within the prototype and the pressure profile of the working chambers can be stabilised (steady state).

6. Once the steady state condition has been achieved, the needle valve was adjusted such that the flowmeter reading was maintained and stabilised at 10 mm for the first measurement. The pressure and temperature readings from the discharge tank, the pressure profile of the working chambers and the surface temperature of the prototype components were recorded by the DAQ system at a frequency of 25 kHz for a duration of 20s. The current into the motor was also recorded using the scope meter for a duration of 20s.

7. After the first measurement, the flow rate was increased by adjusting the needle valve. The flowmeter reading was increased by increments of 5 mm and experiments for a total of 5 flowmeter readings (10 mm, 15 mm, 20 mm, 25 mm and 30 mm) were conducted. Between each interval, the flow was allowed to be stabilised before the measurements were taken. Each recorded reading was then converted to its corresponding volumetric flow rate and mass flow rate based on the gas properties, the rotameter calibration scale reading data and the gas correction factor, as shown in Section F.4.

8. After the measurements for 5 flow rates (readings at 10 mm, 15 mm, 20 mm, 25 mm and 30 mm), the motor was switched off to cool the prototype for about 30 minutes before running the prototype at the next operating speed.

9. The experimental procedures from step 3 to 7 were repeated for each input operating speed (1080 rpm, 1260 rpm, 1440 rpm, 1620 rpm and 1800 rpm).

From the preliminary run to identify the appropriate duration of time required for the R134a refrigeration loop to reach steady state, it was found that a duration of 20 minutes for the system to achieve the conditions of steady state. For experiments conducted with R134a, the prototype was operated at an input operating speed of 1620 rpm with the suction dew point of the low side of the

refrigeration loop maintained at 7.2°C for 20 minutes based on AHRI standard 540 reference rating condition for high load refrigeration [173]. The discharge dew point of the high side of the refrigeration loop, however, was not controlled and was maintained at 54.4°C based on the standard as the corresponding discharge pressure of the prototype has to be maintained above the saturation pressure of R134a at 1469.8 kPa. This discharge pressure can only be attained when the prototype is operating beyond 2000 rpm. The prototype would not be able to operate at this speed for more than 15 minutes without the sliding interface heating up excessively; the prototype would have easily seized and the moving parts would have been irreparably damaged due to the severe galling from wear. The experimental procedures for refrigeration runs are described below:

1. Similarly, the bubble leakage test was conducted on the refrigeration closed loop using pressurised air (900 kPa Absolute) to identify the leakage points. Tightening or re-sealing of connections was also done to rectify these leakage points.

2. The evaporator with the heating elements was switched on and maintained at 45 — 50°C by adjusting the power control of the heating elements.

3. The refrigeration loop was then vacuumed using a vacuum pump to evacuate the air-moisture contents in the loop. The prototype was operated at 600 rpm during the vacuuming process in order to purge out the remaining air inside the chambers and pipings.

4. Once the total pressure of the entire loop had reached below 30 kPa, the vacuum pump was then isolated from the loop. The manifold and the R134a charging tank were then connected to the loop via the high and low side charging points, as shown in Figure 7.20b.

5. The liquid refrigerant from the R134a charging tank was then charged in until the high and low side pressure had equalised. Throughout the charging process, the prototype was operating at 600 rpm to move the refrigerant through the entire loop.

6. The system was then left idle for 15 minutes to allow vaporisation of any liquid refrigerant that the throttling valve had released into the evaporator.

7. After 15 minutes, the prototype was operated at input operating speed of 1620 rpm for more than 10 minutes with the throttling valve adjusted

until the low side pressure had stabilised around 377.2 kPa which is the saturation pressure of R134a at 7.2°C and the subcooled condition was achieved at the evaporator inlet. This process ensured that the maximum amount of liquid was charged into the receiver.

8. Once the refrigeration loop was fully charged, the experimental testing were carried out.

9. For the measurement of the prototype performance on refrigeration loop, the prototype was operated at input operating speed of 1620 rpm with operating conditions maintained for 20 minutes to ensure steady state is reached.

10. The refrigerant at the inlet of the evaporator was ensured to be in the subcooled/ saturated liquid state with the low side pressure stabilised at around 377.2 kPa before measurements were recorded by the DAQ system at a frequency of 25 kHz for a duration of 20s. The power scope meter and current probe were also used to measure the average current drawn by the motor for 20s.

11. The system was also shut down for about 30 minutes to cool down the prototype before experiments with liquid refrigerant injection cooling were conducted.

12. With the injector controls switched on and with the start and end injection positions set, the experimental procedures from step 8 to 10 were repeated for run with liquid refrigerant injection cooling.

7.6 Summary

The design details of the prototype, the selection process of self-lubricating materials for the fabrication of bushings, the experimental setups and the measurement procedures are presented in this chapter. Four commercially available self-lubricating materials, namely, Cast Nylon 6, PTFE, PEEK GF30 and C95500 AB2 Nickel-Aluminium Bronze were tested in the prototype runs. Based on the wear behaviour and wear resistance of each self-lubricating material, C95500 AB2 Nickel-Aluminium Bronze material exhibits better wear performance at high rotation speeds and prolonged sliding durations. It was chosen as the material of choice for the fabrication of the bushings and split bush that undergo dry friction rubbing. The experimental results and validations of the theoretical models will be shown and discussed in the next chapter.

Chapter 8

Experimental Study and Validation

In this chapter, the results from experimental study will be presented. The pressure profile of the working chambers, the discharge mass flow rate, the power input and the temperature of prototype components were the main measurements obtained from the experimental runs. These measured results were compared with the predicted results to validate the mathematical models formulated in Chapter 4 to 6. The overall measured results from the experiments are presented in Appendix D Section D.2.

8.1 Validation of Thermodynamics and Leakage Models Using Results From Testing With Air

To validate the theoretical thermodynamics and leakage model presented in Chapter 4 and Chapter 6, the average discharge mass flow rate of the compressed air and the instantaneous pressure profile of the working chambers from experimental runs with air were compared with the predicted results from the theoretical models. The simulations of the thermodynamics properties of the compressed air throughout the suction and compression cycles were carried out using the simulation parameters and measured operating speeds tabulated in Table 8.1, Table 8.2 and Table 8.3.

Table 8.1: Flow coefficients and effective dead volume used in the predictions for air

Simulation parameters	Value
Suction flow coefficient, $C_{d,suc}$	0.0755
Discharge coefficient, $C_{d,disc}$	0.8
Effective dead volume	17.05 cm^3

Table 8.2: Mechanical properties of valve reed and valve parameters used in the predictions for air

Simulation parameters	Value
AISI 304 Stainless Steel	
Density of valve reed material	7800 kg m^{-3}
Young's Modulus, E	210 GPa
Damping ratio, ζ	0.2

Table 8.3: Measured motor speed and slippage at each input operating speed

Input operating speed*, rpm	**Measured operating speed**, ω_1, rpm**	% of slippage, s
1080	1063	1.57
1260	1243	1.35
1440	1413.2	1.86
1620	1592	1.73
1800	1772	1.56

*: **Operating speed input to the frequency controller of motor.**
: **Operating speed measured by tachometer and used in simulation.

Of particular note, the value of the suction flow coefficient is very small as a pipe reducer is used to connect the suction pipe of the compressor to other equipment which are sized with 1/4"(6.35mm) fittings; the suction flow area is approximately reduced 3.7 times from the suction port diameter of 16mm to the pipe reducer inner diameter of 4.35mm. The detailed validations of the flow coefficients and the effective dead volume used in the modellings are shown in Appendix B. The overall process of the numerical simulation based on all the theoretical models presented, is also illustrated in the program flow diagram in Appendix C.

The comparison between the measured and the predicted mass flow rates of air at different pressure ratios and operating speeds is presented in Figure 8.1. From Figure 8.1, it is observed that the measured mass flow rates at the input operating speed of 1080 rpm are generally lower than the corresponding predicted mass flow rates while the measured mass flow rates are much higher than the predictions at input operating speeds greater than 1440 rpm. In general, this discrepancy is mainly due to the use of a constant suction flow coefficient, $C_{d,suc}$, in the theoretical simulations for all testing conditions with the assumption that the suction flow coefficient does not change under varying suction flow behaviour and operating speeds. From the computational modelling of the pulsatile suction flow shown in Appendix B, Section B.1, it was found that the suction flow coefficient generally increases with increasing input operating speeds from 1080 rpm to 1800 rpm. For all simulation runs, an average suction flow coefficient of

0.0755 for air was used and it is the corresponding flow coefficient of suction flow condition at input operating speed close to 1440 rpm. Hence, the amount of suction mass intake simulated and the subsequent discharge mass flow would be underpredicted with the relatively small suction flow coefficient for higher input operating speeds beyond 1440 rpm while the discharge mass flow for input operating speeds much lower than 1440 rpm would generally be overpredicted.

As expected, both the predicted and measured mass flow rate decreases with the pressure ratio at a given operating speed. This is because a higher pressure ratio between the discharge and suction pressure indicates greater leakages from the compression chamber to the suction chamber at a given operating speed since the internal leakages are pressure-driven flows. For a constant pressure ratio, on the other hand, the discharge mass flow rate increases with increasing operating speed under similar suction condition. This is because a shorter working cycle at higher operating speed would mean a larger average mass flow discharged per cycle with lesser leakage due to a shorter leakage duration for the compressed air to leak from the compression chamber into the suction side. From Figure 8.1, it can be seen that the mass flow rate at the input operating speed of 1800 rpm is the highest as compared to other operating speed for any given pressure ratio.

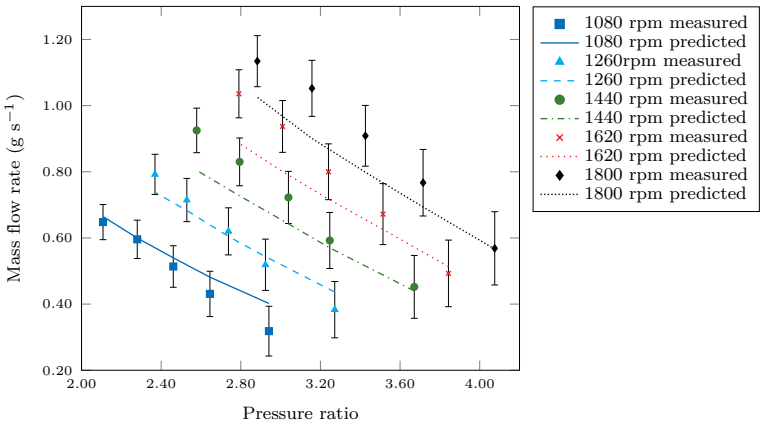

Figure 8.1: Comparison of the measured and predicted mass flow rates at different pressure ratios.

To account for greater internal leakages due to the lack of sealing from oil lubrication and wider clearances from machining inaccuracies, the predicted mass flow rates were calculated by assuming a constant 26% increment in the leakage flow rate. In other words, a constant average leakage coefficient, C_{leak}, of 1.26 was used as an experimental fitting parameter to account for leakages caused by the lack of oil lubrication sealing and wider leakage gaps from the

fabrication imprecision of the clearances. One such machining inaccuracies is the noncircularity of the rotor outer surface (will be explained in greater detail later), as shown in Figure 8.8, where radial clearances at certain region along the rotor and the cylinder wall were found to be 20 μm greater than the existing measured radial clearance of 63.5 μm (shown in Table 7.5). From the numerical simulation of the prototype, an increase of 20 μm in the radial clearance would easily bring about a decrease in the predicted average mass flow rate, ranging from 19.2% to 34.3% for pressure ratios from 2.79 to 3.84 at an operating speed of 1620 rpm. With the constant average leakage coefficient, C_{leak}, the overall predicted and measured mass flow rates were found to be in good agreement with most of the discrepancies within ±15%, as shown in Figure 8.2.

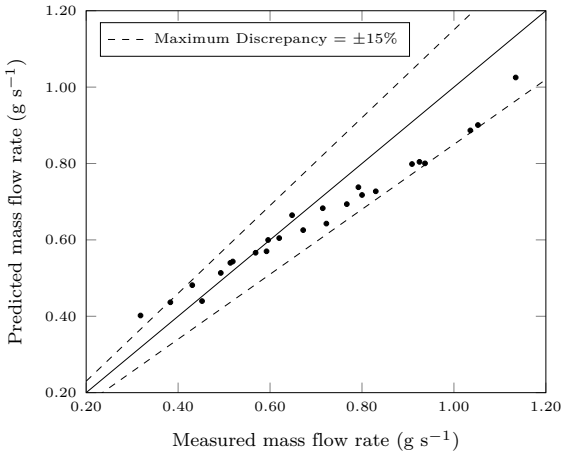

Figure 8.2: Overall discrepancy between predicted and measured mass flow rates.

The measured volumetric efficiency is defined as the ratio of the measured discharge mass flow rate to the theoretical mass flow rate of the prototype with no dead volume and internal leakage and is expressed as shown in (8.1). The predicted volumetric efficiency, on the other hand, is defined as the ratio of the average discharge mass flow rate simulated to the theoretical mass flow rate of the prototype with no dead volume and internal leakages, as shown in (8.2). The uncertainties determined for the measured volumetric efficiency are presented in Appendix D, Section D.1.

$$\eta_{vol,measured} = \frac{\rho_{measured}\dot{V}_{measured}}{\rho_{suc}V_{ideal}\frac{\omega_1}{60}} \tag{8.1}$$

$$\eta_{vol,predicted} = \frac{\dot{m}_{avg,predicted}}{\rho_{suc}V_{ideal}\frac{\omega_1}{60}} \tag{8.2}$$

Figure 8.3 shows the volumetric efficiencies of the prototype at various operational speeds and pressure ratios, which were measured to be ranging from 30.9% to 67.5%. Among the measured data, the lowest measured volumetric efficiency of 30.9% was recorded when the input operating speed was at 1080 rpm with a pressure ratio of 2.94, whereas the highest measured volumetric efficiency of 67.5% is observed at the input operating speed of 1440 rpm with a pressure ratio of 2.58. Similarly, poor volumetric efficiencies at low operating speed at high pressure ratio are also mainly due to the greater internal leakage which results in reduced amount of discharge mass flow. The reason for the overprediction of volumetric efficiencies at input operating speed below 1440 rpm and the underprediction above 1440 rpm is also mainly due to the use of constant suction flow coefficient for all simulation runs at different operating speed.

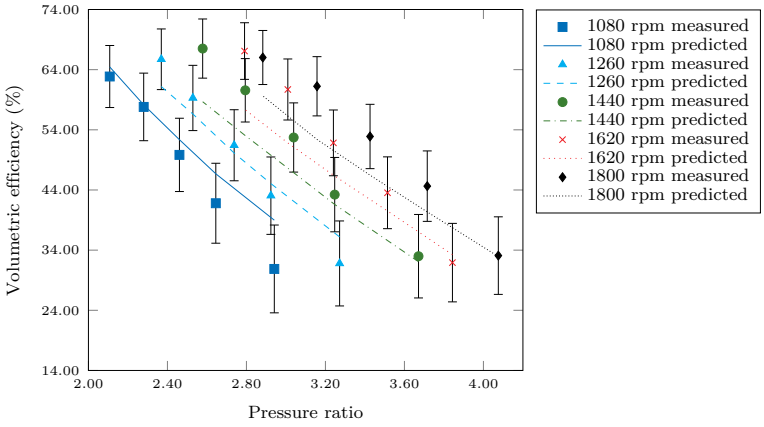

Figure 8.3: Comparison of the measured and predicted volumetric efficiencies at different pressure ratios.

To validate the prediction of the instantaneous pressure variations of the working chambers, the pressure of both suction and compression chambers were also measured using pressure transducers which are inserted in the sensor ports of the prototype that are located on the radial wall of the cylinder. The positions of the sensor port were designed to be as close to the suction and discharge ports as possible to measure a more complete duration of the suction and compression process. However, as the rotor rotates through the entire working cycle, the pressure transducers are covered by the radial face of the rotor at certain angular positions, as illustrated in Figure 8.4. With respect to the shaft's angular position, θ_1, the suction pressure transducer can measure an approximate range of 50° to 23°(383°) while the compression pressure transducer can measure an approximate range of 345° to 672°(312°). As a result, the instantaneous pressure variations

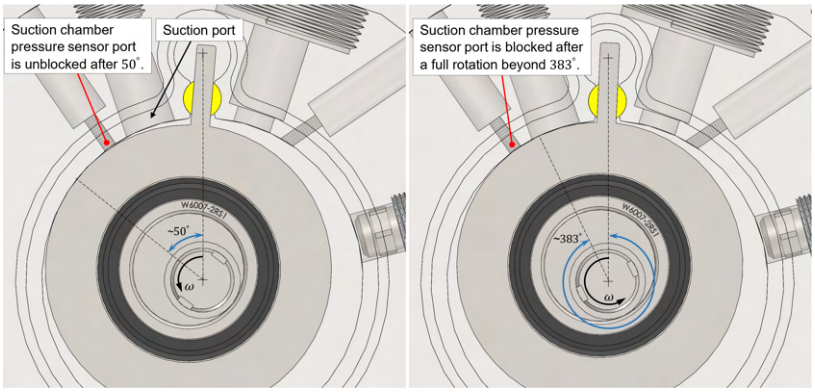

(a) Suction chamber sensor port blocked from 23° to 50°.

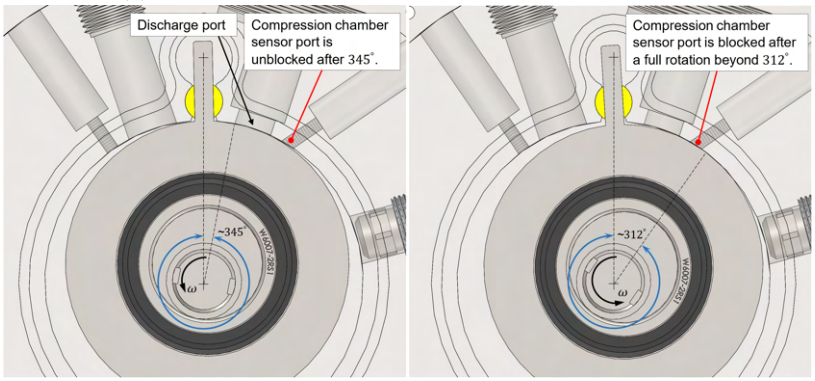

(b) Compression chamber sensor port blocked from 312° to 345°.

Figure 8.4: Pressure transducers blocked by the rotor at different rotational angle range.

of the working chambers will be presented in the common measurement range of 50° to 312° for both suction and compression process. The comparison between the predicted and measured pressure variations of the working chambers at input operating speeds of 1080 rpm, 1440 rpm and 1800 rpm are presented in Figure 8.5 to Figure 8.7. The rest of the comparison for input operating speeds of 1260 rpm and 1620 rpm are presented in Appendix D, Section D.2. It is observed that the predicted and measured pressure profiles of the working chambers are in good agreement with a maximum mean discrepancy of 2.36% and an average mean discrepancy of 1.68%. The mean discrepancy is calculated based on the following formula:

$$\sigma_{dis} = \frac{\sum_{i=1}^{n} \sqrt{\frac{(Y_{measured} - Y_{predicted})^2}{{Y_{measured}}^2}}}{n} \tag{8.3}$$

where

σ_{dis} is the average discrepancy $(-)$.

n is the total number of data points $(-)$.

$Y_{measured}$ is the magnitude of the measured pressure (kPa).

$Y_{predicted}$ is the magnitude of the predicted pressure (kPa).

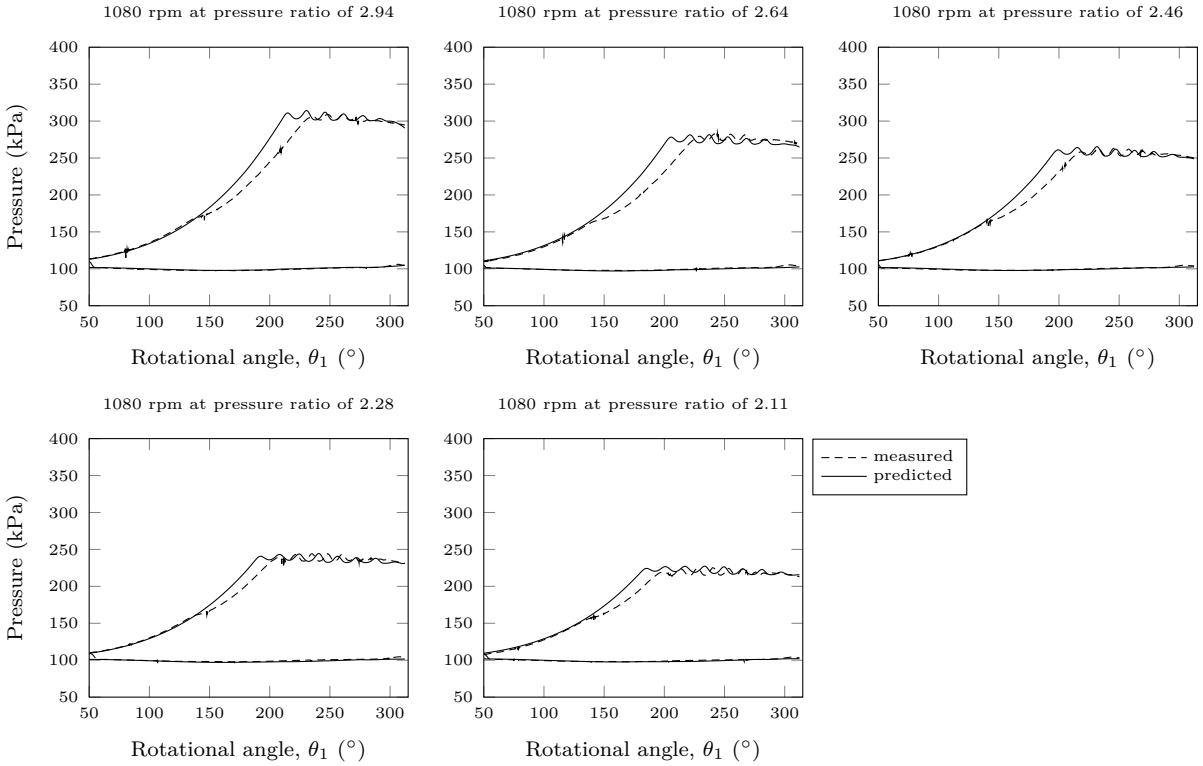

Figure 8.5: Comparison of the measured and predicted instantaneous pressure of the working chambers at input operating speed of 1080 rpm.

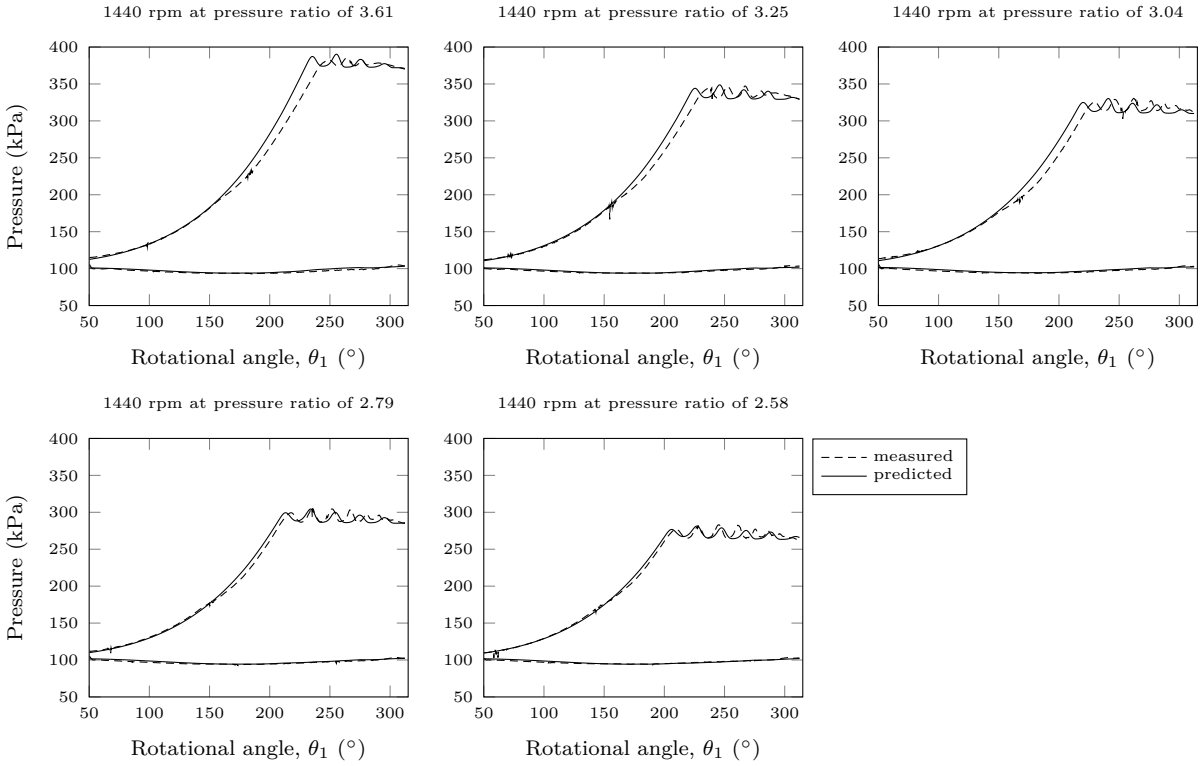

Figure 8.6: Comparison of the measured and predicted instantaneous pressure of the working chambers at input operating speed of 1440 rpm.

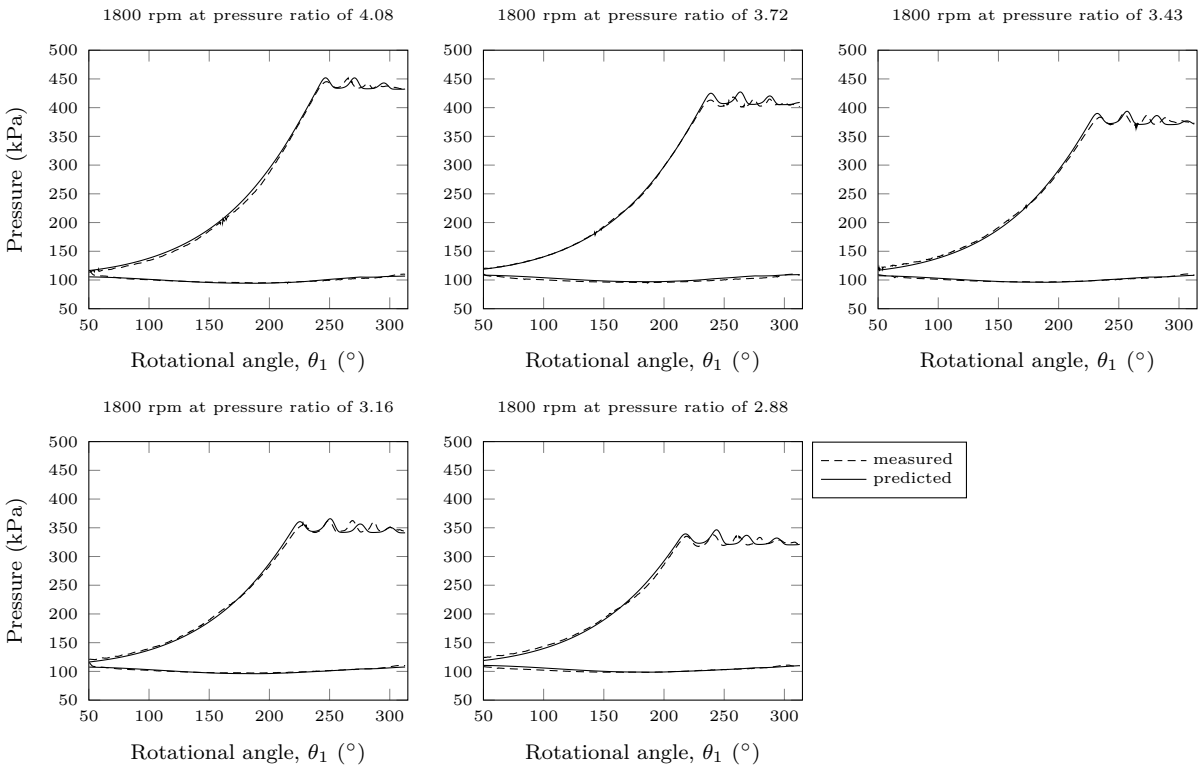

Figure 8.7: Comparison of the measured and predicted instantaneous pressure of the working chambers at input operating speed of 1800 rpm.

From Figure 8.5, it is observed that there is an abrupt deviation between the measured and the predicted pressure profile at angle between 150° to 220° from pressure ratio of 2.94 to 2.11 where there is a sudden decrease in the rate of pressure increase of the measured pressure variation and a delayed discharge process. This similar deviation is also spotted in Figure 8.6 from pressure ratio of 3.61 to 2.58, where the measured compression pressure profile has a sudden reduction in the rate of pressure increase while the predicted pressure profile continues to increase at an increasing rate. This sudden deviation and drop in pressure is believed to be caused by the internal leakage through the radial clearance as a result of noncircularity of the outer rotor surface due to unexpectedly high machining inaccuracy which has caused an abrupt increase in the radial clearance between the rotor and the cylinder wall, as depicted in Figure 8.8.

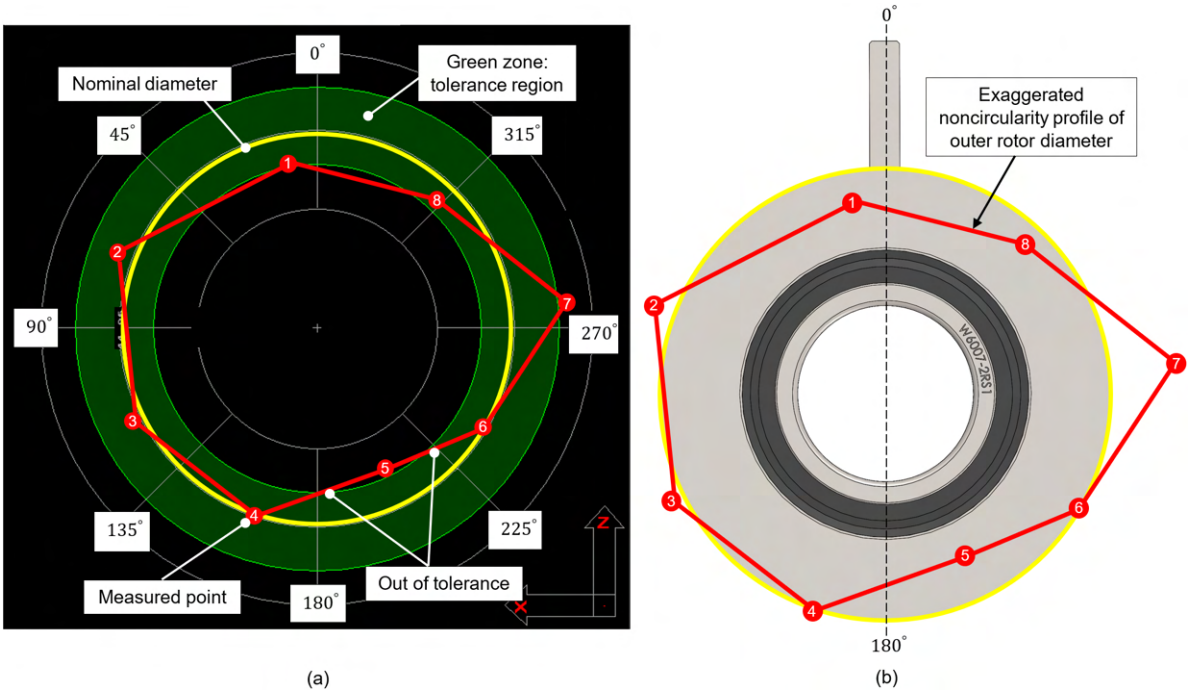

Figure 8.8: Out of tolerance of outer rotor diameter at region near 180° to 225°.

Figure 8.8a shows the measured circularity using coordinate measuring machine (CMM) while Figure 8.8b shows the corresponding circularity on the actual rotor. A total of 8 points have been measured to inspect the circularity of the rotor outer surface. It is noted that the nominal outer diameter of the rotor is measured to be 89.918 mm which is 80 μm smaller than the specified 90mm outer diameter of the rotor, as shown previously in Table 7.3. Within a tolerance zone of ± 20 μm with respect to the nominal diameter, the region near 180° to 225° of the rotor, namely point 5, is about 20μm less than the nominal diameter. This means that the resultant radial clearance near the rotational angle θ_1 of 150° to 220° would be more than 83.5 μm including the existing radial clearance of 63.5 μm, based on Table 7.5. Therefore, this abrupt drop in the measured pressure during the compression process would most likely to be caused by the sudden increase in the radial leakage as a result of the enlarged radial clearance between the rotor and cylinder wall. Furthermore, this abrupt deviation of measured pressure is also observed to decrease with decreasing pressure ratio as well as increasing operating speed. As seen in Figure 8.6, the abrupt decrease in the pressure gradient of the compression pressure variations at pressure ratio of 2.58 is almost negligible as compared to that at pressure ratio of 3.61. From Figure 8.7, the pressure variations were measured at high input operating speed of 1800 rpm and no significant abrupt deviation between the measurements and

predictions can be seen for all pressure ratios. This reconfirms that the sudden drop in the measured compression pressure variations is caused by the sudden increase in the radial leakage as a result of the enlarged radial clearance between the rotor and cylinder wall since high operating speed reduces internal leakage due to shorter leakage duration while the reverse is true for cases of high pressure ratios. This also suggest that the use of a constant average leakage coefficient of 1.26 for the entire cycle may underpredict the internal leakage at position near rotational angle θ_1 of 150° to 220° and the coefficient should increase with the widening of the clearance at these positions to simulate this abrupt deviation.

8.2 Validation of Dynamic Model Using Results From Testing With Air

The dynamics modelling of the compressor was conducted based on the friction coefficients tabulated in Table 8.4.

Table 8.4: Friction coefficients and lip seal friction in used in the predictions

Simulation parameters	Value
Friction coefficient between split bush (Bronze) and slot wall in cylinder (Aluminium) [174]	0.5
Friction coefficient between split bush (Bronze) and vane (Steel) [175] [176]	0.45
Shaft seal tangential friction per unit of circumference, ϕ [177]	3800 N m^{-1}

In order to prevent leakage of the compressed fluid through the clearance between the shaft and the cover, a shaft lip seal was used. As the seal was used under dry rubbing condition without lubrication, the lip seal's friction coefficient is 15 times greater than that under oil-lubricated condition (see Section F.13). As a result, the tangential friction per unit of circumference of the shaft seal is also increased by 15 times as compared to that of oil-lubricated lip seals [177].

Although the lip seal prevents possible leakage through the clearance between the shaft and the cover, it results in high frictional force due to dry rubbing between the PTFE material and the shaft surface. In addition to the frictional losses discussed in Subsection 6.2.4, the frictional losses at the shaft-seal interface have to be accounted for. The power loss due to the shaft-seal friction can be calculated based on equation (8.4) which was proposed by Muller and Nau [177].

$$P_{f,seal} = 2\pi r_s^2 \phi \omega_1 \tag{8.4}$$

The predicted power input to the compressor prototype is determined by multi-

plying the calculated input torque with the operating speed:

$$P_{predicted} = T_m \omega_1 \tag{8.5}$$

The total mechanical power input to the prototype is calculated based on equations (8.6) and (8.7) as proposed by Bhimbhra [178]. To determine the resultant power input to the prototype P_m, the total power available at the air-gap of the induction motor P_g, has to be first determined and is expressed as equation (8.6). From equation (8.6), m is the number of poles in the induction motor, I is the stator current and R_f is the resistance experienced by the stator due to the rotating air-gap field. Detailed derivation of R_f is shown in Section D.1. The resultant power input to the prototype P_m, is dependent on the motor slippage s, and is determined by equation (8.7).

$$P_g = mI^2 R_f \tag{8.6}$$

$$P_m = (1 - s)P_g \tag{8.7}$$

From the motor catalogue (see Section F.1), $m = 2$ and s is based on the values tabulated in Table 8.3 which are measured using a tachometer. The current I is the current measured by the Fluke power scope meter and current probe.

The comparison between the measured and the predicted average power input per cycle at different operating speeds and pressure ratios is shown in Figure 8.9. It is observed that the measured average power input increases with increasing operating speed. Furthermore, at any given operating speed, the measured average power input increases as the pressure ratio rises. This is because higher compression work is required to drive the rotor against the higher differential pressure force between the suction and compression chambers in order to compress the fluid. From Figure 8.9, it is also observed that the measured average power input is generally higher than the predictions. This discrepancy might be due to the use of constant friction coefficients. In practice, the surface profiles of the bushings are continuously changing and are worn out due to the prolonged experimental runs under dry condition. Scuffing and galling accumulated on the surface of the bushings after each experimental testing, as seen previously in Subsection 7.3.3, might contribute to an increase in the friction coefficients. As a result, the theoretical modelling will be underpredicting the average power input to the prototype with the use of constant friction coefficients

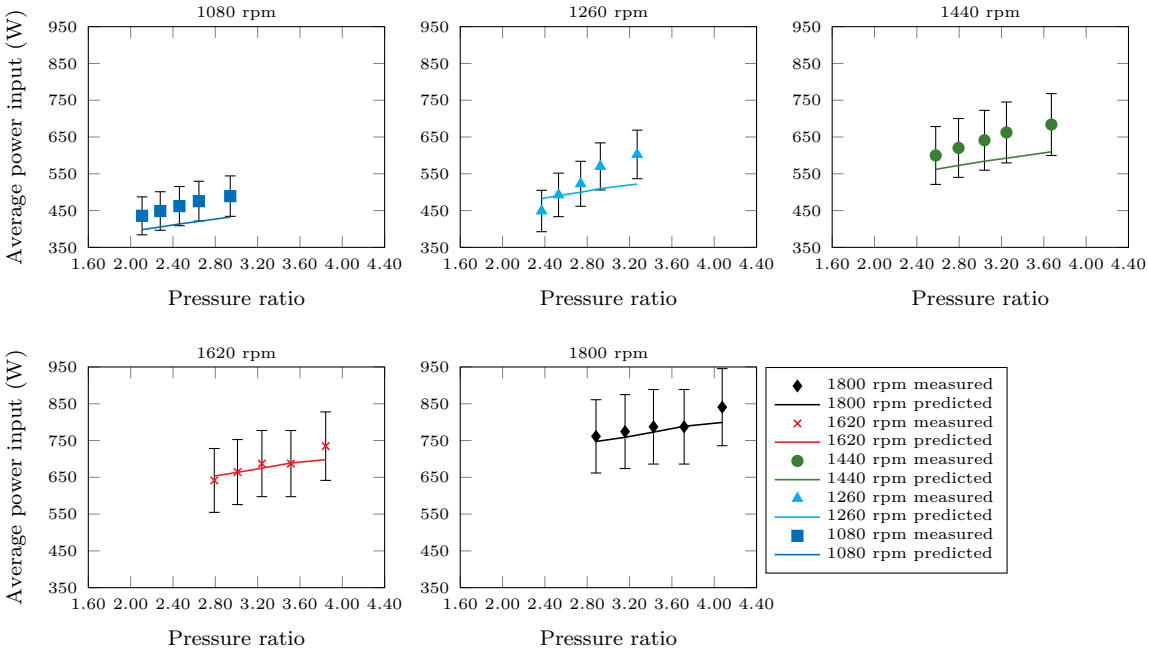

Figure 8.9: Comparison of the measured and predicted average power inputs at different input operating speeds and pressure ratios.

of lower values.

In general, the average power inputs are predicted within the uncertainties of the measured average power input. The uncertainty calculation for power input is presented in Appendix D, Section D.1. Figure 8.10 shows the overall discrepancy between the measured and the predicted average power input, and it is noticed that all predictions fall within a maximum discrepancy of ±15%. Overall, good agreement is observed between the predicted and measured power inputs with a maximum discrepancy of 13.37% and an average discrepancy of 6.09%. This indicates that the use of constant friction coefficients in the theoretical modelling is sufficiently accurate in predicting the dynamics of the prototype even when the surface profiles of the bushings are changing throughout the runs. The only downside to the use of constant friction coefficients is the underprediction of the actual power input over the long runs when the bushings are worn out.

The mechanical efficiency is defined as the ratio of the net compression work done to the theoretical total work input into the prototype and is expressed as shown in equation (8.8).

$$\eta_{mech} = \frac{-\oint_{V_{com}} p_{com} dV - \oint_{V_{suc}} p_{suc} dV}{\oint T_m \omega_1 dt} \tag{8.8}$$

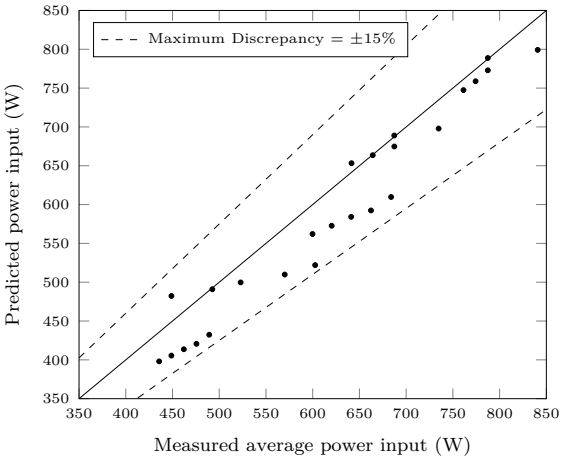

Figure 8.10: Overall discrepancy between predicted and measured average power inputs.

The predicted mechanical efficiencies for different operating speeds and pressure ratios are shown in Figure 8.11. From Figure 8.11, it can be seen that the mechanical efficiency of the prototype is still on the rising trend as the testing range of the pressure ratio is limited to a range of 2.11 to 4.08. Any higher testing range of pressure ratio would require the prototype to operate at a higher rotational speed of more than 1800 rpm since there is severe internal leakage in the oil-free prototype. However, to prevent any overheating and irreparable damage to the prototype, the input operating speeds are kept below 1800 rpm. In general, the predicted mechanical efficiency of the oil-free prototype ranges from 19.31% to 30.3%. Such a low range of mechanical efficiencies is mainly due to the dry rubbing of the bearing surfaces which contributes to the higher frictional losses.

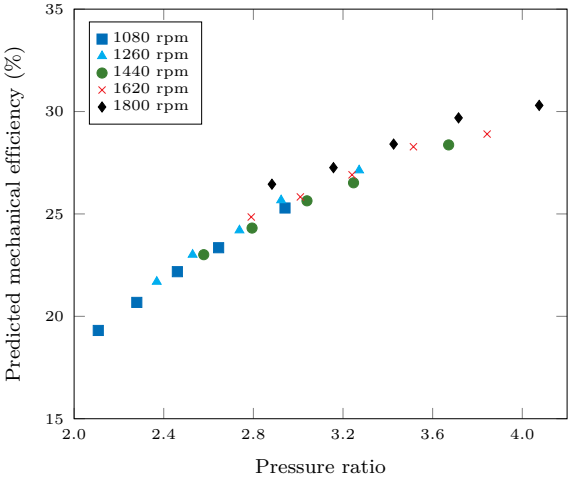

Figure 8.11: Predicted mechanical efficiencies at different input operating speeds and pressure ratios.

8.3 Validation of Thermal Model Using Results From Testing With Air

To validate the prediction of the temperature profile of the prototype, Type K thermocouples were fixed onto some components of the prototype and measurements were carried during the experimental runs. Out of the 38 discrete elements (see Figure 6.15) that were modelled in Section 6.2, only 4 stationary components were measured, namely the compressor top cover, the cylinder body, the suction and the discharge pipes. The rest of the assembly were either too difficult, if not impossible to measure as they were rotating, such as the rotor and the shaft, or were parts inside the compressor and were inaccessible. Figure 8.12 shows the locations where temperature measurements were taken.

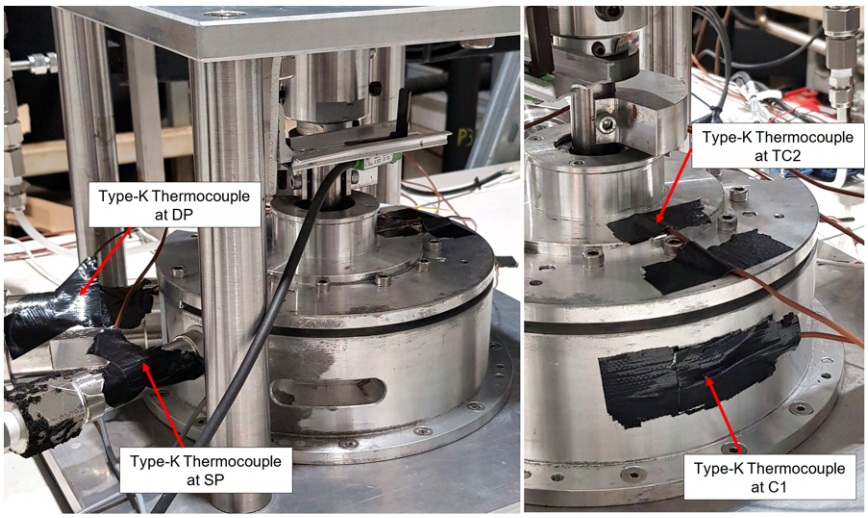

Figure 8.12: Locations where temperatures were measured.

In order to ensure that the steady state temperatures of the prototype components were measured, the prototype was operated until no drastic change in the temperature measurements within $\pm 2.2°C$ was detected before the measurements were logged for each run at different input operating speeds from 1440 rpm to 1800 rpm. DAQ system was used to log the measured data over an extended period of time to ensure steady state measurements were collected. As prolonged operations would induce more wear on the moving components, all tests were carried out at pressure ratios lower than 3.0 to reduce the gas pressure force and the resultant frictional forces acting on the bearing surfaces so as to minimise the risk of seizure.

The comparison of the predicted and measured results is shown in Table 8.5.

In general, the predictions are in reasonably good agreement with the temperature measurements, as shown in Figure 8.13. Discrepancies were mostly less than 10% with the highest discrepancy at 13.91% and an average discrepancy of 7.04% throughout all runs at three operating speeds. This suggests that the assumptions of constant friction coefficients based on Table 8.4 and the approximation of the heat distribution coefficients between two sliding surfaces based on the ratio of the thermal conductivities of both materials, as presented in Equation 6.2.4, are reasonable in predicting components' temperature. It is believed that the discrepancies are the result of the simplifications made in discretising the prototype components into elements of simple geometry and due to the assumptions made in the application of the convection heat transfer correlations and the assumptions of heat transfer between isothermal and lumped elements.

Table 8.5: Comparison of the predicted and measured temperature profiles at input operating speeds of 1440 rpm, 1620 rpm and 1800 rpm

	1440 rpm, Pressure ratio of 2.59			1620 rpm, Presssure ratio of 2.78			1800 rpm, Presssure ratio of 2.87		
Elements	Predicted	Measured	% Discrepancy	Predicted	Measured	% Discrepancy	Predicted	Measured	% Discrepancy
Shaft section1, S1	109.18	Not measured		116.14	Not measured		122.74	Not measured	
Counterweight, CW	84.88	Not measured		88.31	Not measured		91.38	Not measured	
Shaft section 2, S2	256.31	Not measured		284.34	Not measured		312.06	Not measured	
Shaft bearing 1, B1	50.54	Not measured		53.68	Not measured		56.35	Not measured	
Top cover element 4, TC4	47.80	Not measured		50.61	Not measured		52.94	Not measured	
Endface bushing 1, EB1	47.78	Not measured		50.59	Not measured		52.92	Not measured	
Eccentric, EC	191.21	Not measured		206.45	Not measured		221.20	Not measured	
Eccentric bearings, B2	197.29	Not measured		212.53	Not measured		227.29	Not measured	
Rotor, R	195.01	Not measured		209.89	Not measured		224.31	Not measured	
Cylinder layer 9, C9	47.86	Not measured		50.67	Not measured		53.01	Not measured	
Vane, V	244.05	Not measured		279.07	Not measured		318.40	Not measured	
Split bush, SB	563.19	Not measured		692.81	Not measured		841.19	Not measured	
Suction pipe, SP	34.45	32.5	6.06	35.46	33.0	7.59	36.29	32.8	10.63
Discharge pipe, DP	49.20	43.2	13.91	51.94	48.1	7.95	54.03	49.0	10.17
Endface bushing 2, EB2	48.10	Not measured		50.94	Not measured		53.30	Not measured	
Shaft section 3, S3	74.78	Not measured		79.92	Not measured		84.55	Not measured	
Shaft bearing 2, B3	48.47	Not measured		51.34	Not measured		53.74	Not measured	
Cylinder bottom layer 9, BC9	47.87	Not measured		50.69	Not measured		53.03	Not measured	
Test rig, TR	47.90	Not measured		50.71	Not measured		53.05	Not measured	
Top cover element 1, TC1	47.76	Not measured		50.57	Not measured		52.90	Not measured	
Top cover element 2, TC2	47.77	44.4	7.60	50.57	48.6	3.98	52.90	50.0	5.73
Top cover element 3, TC3	47.78	Not measured		50.58	Not measured		52.91	Not measured	
Cylinder layer 1, C1	47.86	45.8	4.57	50.67	50.4	0.51	53.01	50.1	5.81
Cylinder layer 2, C2	47.86	Not measured		50.67	Not measured		53.01	Not measured	
Cylinder layer 3, C3	47.86	Not measured		50.67	Not measured		53.01	Not measured	
Cylinder layer 4, C4	47.86	Not measured		50.68	Not measured		53.02	Not measured	
Cylinder layer 5, C5	47.86	Not measured		50.68	Not measured		53.02	Not measured	
Cylinder layer 6, C6	47.87	Not measured		50.68	Not measured		53.03	Not measured	
Cylinder layer 7, C7	47.87	Not measured		50.69	Not measured		53.04	Not measured	
Cylinder layer 8, C8	47.88	Not measured		50.70	Not measured		53.05	Not measured	
Cylinder bottom layer 1, BC1	47.84	Not measured		50.65	Not measured		52.99	Not measured	
Cylinder bottom layer 2, BC2	47.86	Not measured		50.67	Not measured		53.01	Not measured	
Cylinder bottom layer 3, BC3	47.87	Not measured		50.69	Not measured		53.03	Not measured	
Cylinder bottom layer 4, BC4	47.88	Not measured		50.70	Not measured		53.04	Not measured	
Cylinder bottom layer 5, BC5	47.89	Not measured		50.71	Not measured		53.06	Not measured	
Cylinder bottom layer 6, BC6	47.91	Not measured		50.73	Not measured		53.07	Not measured	
Cylinder bottom layer 7, BC7	47.93	Not measured		50.74	Not measured		53.09	Not measured	
Cylinder bottom layer 8, BC8	47.95	Not measured		50.77	Not measured		53.12	Not measured	

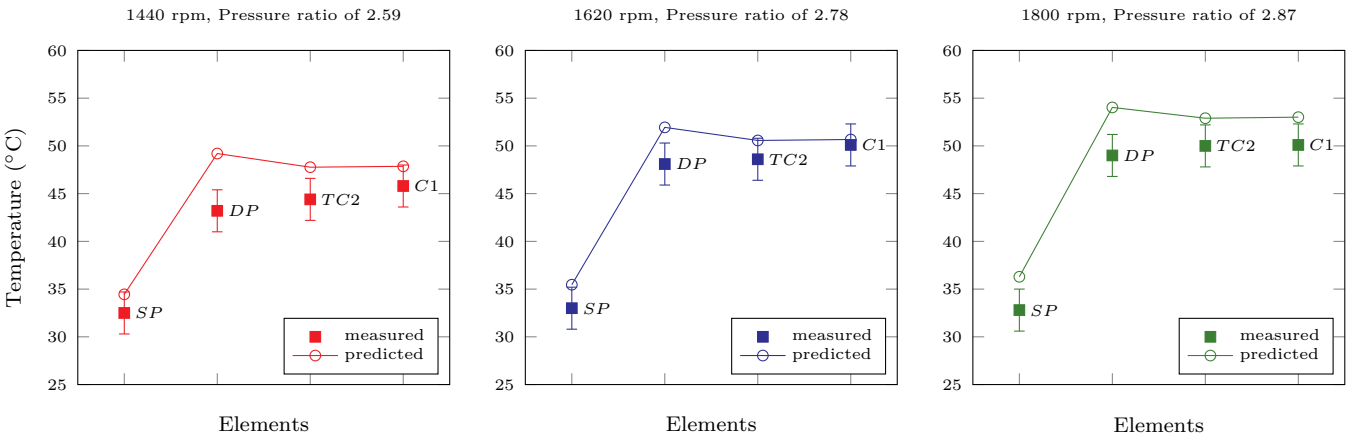

Figure 8.13: Measured and predicted temperature of the prototype components at different input operating speeds.

From the predictions of the temperature profile of the prototype, it can also be observed that the predicted temperatures of the split bush for all operating speeds are the highest among all elements and the predicted temperatures are above 500°C but below C95500 AB2 Nickel-Aluminium Bronze's melting point of 1038°C. This could explain why melting is not observed in the split bush sample of C95500 AB2 Nickel-Aluminium Bronze during the wear test based on Figure 7.15c and d. The high temperature is mainly because all surfaces of the split bush structure undergo dry rubbing with the vane sides and the slot wall, causing heat to be generated at all surfaces. Furthermore, it is made of thermally conductive C95500 AB2 Nickel-Aluminium Bronze and has a small heat capacity due to its small dimensions. Extreme heat generated from the interfacial sliding layer would have easily conducted through the whole structure. This also partly explains why the severe thermal-oxidation of the PEEK GF30 split bush, as seen in Figure 7.15a and b, were all localised at the interfacial surface and only partial thermal warping of the vane slot corners was observed since PEEK GF30 is an insulative material and heat from interfacial layer would not have easily conducted through the polymer structure.

From Table 8.5, it can also be observed that the predicted bulk temperatures of the endface bushings for all operating speeds are ranging from 47.78°C to 53.30°C, which are close to the temperature of the cylinder cover and body. In comparison with the predicted bulk temperature of the split bush, the predicted temperatures of the endface bushings are much lower than that of the split bush and this might be due to the larger dimensions of the endface bushings and the larger heat capacity. In addition, each endface bushing has only one bearing

surface that bears a lower frictional force from the dry rubbing with the rotor as compared to the split bush which bears a higher loading from the gas pressure force. Furthermore, the endface bushings are also mechanically fastened onto the large aluminium cover and body which have large heat capacities and are highly thermal conductive. Heat generated at the interface between the rotor and the endface bushings would have been easily conducted through the large surface area of the bushing structure and be conducted away by the aluminium bodies, thus, resulting in a lower bulk temperature that is close to the temperature of the adjacent aluminium bodies.

It is also observed that the predicted temperatures of the vane and the rotor ranged from 195.01°C to 318.40°C. This could explain why the rotor and the vane took on the temper colour of straw to deep straw variations, as seen in Figure 7.16, after dry rubbing with the bushing samples during the wear test. Steel, which is the material of the rotor and vane, exhibits straw temper colour when the heating temperature is raised beyond 226.7°C, based on the temper colour results shown in Table 7.8.

8.4 Results of Prototype Testing with R134a

In this section, the measured results from the R134a runs will be presented. With the validation of the theoretical models in previous sections, the validated simulation model was also used to predict the performance of the prototype in a R134a vapour-compression refrigeration cycle. The simulation was carried out using the simulation parameters tabulated in Table 8.6. The validations of the flow coefficients and the effective dead volume used are shown in Appendix B.

Table 8.6: Simulation parameters used in the predictions for R134a vapour-compression cycle

Simulation parameters	Value
Suction flow coefficient, $C_{d,suc}$	0.0975
Discharge coefficient, $C_{d,disc}$	0.8
Effective dead volume	9.0312 cm^3
Damping ratio, ζ	0.5
Shaft seal tangential friction per unit of circumference	7500 N m^{-1}
Measured operating speed, ω_1	1592 rpm

The measurements were carried out with the test conditions as tabulated in Table 8.7. The tests were conducted at the input operating speed of 1620 rpm as any lower operating speed will result in low discharge pressure and temperature which in turn results in low condenser subcooling. Low refrigerant flow due to low operating speed may also lead to the overheating of the prototype. On the other hand, the high flow rate of R134a at high operating speed requires greater superheating from the evaporator for complete vaporisation. It was found to be extremely challenging to control the throttle valve and the heating rate of the evaporator manually in order to prevent the suction and slugging of liquid refrigerant in the prototype when the input operating speed was set beyond 1620 rpm. Furthermore, higher operating speeds mean greater risk of the prototype seizure. Hence, the testing with R134a were all conducted at a reasonable input operating speed of 1620 rpm.

Table 8.7: Testing condition of R134a refrigeration cycle

Test conditions	
Input operating speed/Measured speed	1620/1592 rpm
Pressure	
Discharge pressure	945.8kPa
Suction inlet pressure	305.4kPa
Evaporator inlet pressure	389.7kPa
Evaporator outlet pressure	358.9kPa
Condenser inlet pressure	944.1kPa
Condenser outlet pressure	937.5kPa
Temperature	
Suction inlet temperature	26.7°C
Evaporator inlet temperature	6.8°C
Evaporator outlet temperature	30.1°C
Condenser inlet temperature	37.1°C
Condenser outlet temperature	32.1°C
Compressor cylinder surface temperature	46.7°C
Ambient temperature	27.3°C

As mentioned earlier in Section 7.5, the suction dew point of the low side of the refrigeration loop was maintained at around 7.2°C based on AHRI standard 540 reference rating condition for high load refrigeration [173]. However, the discharge dew point of the high side of the refrigeration loop was not controlled and maintained at 54.4°C as the corresponding discharge pressure has to be maintained above the saturation pressure of R134a at 1469.8 kPa. This discharge pressure cannot be attained with the prototype running at the input operating speed of 1620 rpm and a discharge pressure of 945.83 kPa was achieved instead during the testing due to significant internal leakages caused by lack of sealing from oil lubrication and the large clearances from machining inaccuracies.

The test results from the experimental run with R134a and the predictions from the simulation are shown in Table 8.8. From the results tabulated, it can be seen that the predicted and measured mass flow rates are in good agreement with a discrepancy of 1.68% which is within the uncertainty of 3.29%. In addition, the discrepancy between the predicted and measured average power input is found to be 3.52% which is within the uncertainty of 9.44%. The coefficients of performance for both measurement and prediction were determined to be around 1.25 and the volumetric efficiencies were more than 50%. The low COP and volumetric efficiency are mostly due to the non-lubricated operating condition since high friction loss and internal leakages are expected.

The comparison of the measured and predicted instantaneous pressure of

Table 8.8: Results of R134a refrigeration cycle at input operating speed of 1620 rpm

Output results	Measured	Predicted	% Discrepancy
Average discharge mass flow rate, g s^{-1}	9.6	9.44	1.68
Average power input, W	1360.3	1312.44	3.52
Cooling load, W	1704.7	1676.11	1.68
Efficiencies			
Coefficient of performance (COP)	1.25	1.28	1.90
Volumetric efficiency, η_{vol}, %	55.5	54.59	1.68
Mechanical efficiency, η_{mech}, %	-	35.56	-
Isentropic efficiency	-	0.70	-

the working chambers are shown in Figure 8.14. Discrepancies between the prediction and measurements are mostly less than 5% with an average mean discrepancy of 3.08%. From Figure 8.14, the measured compression pressure profile is observed to deviate from the prediction at angle between 150° to 220° and this deviation is also observed when air was used as the working fluid in the open loop testing. As explained in Section 8.1, the noncircularity of the rotor due to machining inaccuracies was found to be the most probable cause to this sudden divergence as the noncircularity has led to the widening of the radial clearance at 150° which would have caused a sudden surge in the radial leakage.

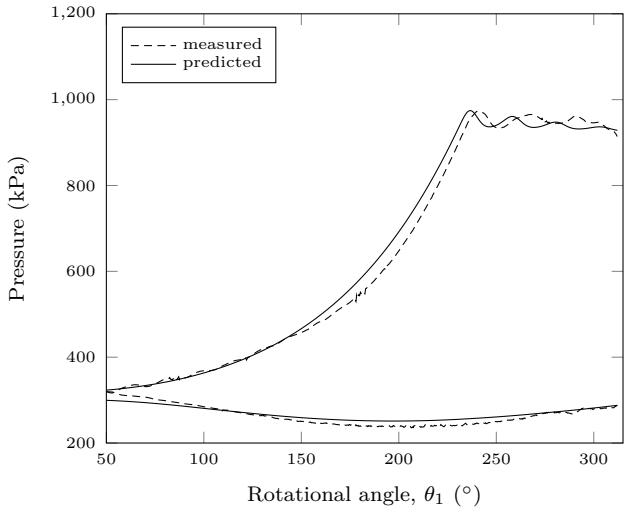

Figure 8.14: Comparison of the measured and predicted instantaneous pressure of the working chambers at input operating speed of 1620 rpm for R134a.

8.5 Effect of Liquid Refrigerant Injection Cooling

In this section, the measured and predictions of the R134a runs with liquid refrigerant injection cooling are presented. Two injection conditions were tested and these are:

- Injection of liquid refrigerant starts at $\theta_1 = 100°$ and cuts off at $\theta_1 = 150°$ with an injection duration of 0.005s.
- Injection of liquid refrigerant starts at $\theta_1 = 100°$ and cuts off at $\theta_1 = 200°$ with an injection duration of 0.01s.

Liquid refrigerant was injected at $\theta_1 = 100°$ because the pressure in the compression chamber ($\sim$ 360 kPa) is much lower than that of the injector inlet (above 900 kPa) at this angular position while the predicted temperature of the R134a in the compression chamber ($\sim$ 28.8°C) is higher than that of the two-phase flow after injection ($\sim$ 7.03°C). This ensures that there are substantial pressure and temperature differences between the injected refrigerant and the existing chamber gas for injection flow and effective cooling to take place. Similarly, the compressor was operated at an input operating speed of 1620 rpm with the evaporating conditions kept around 366.86 kPa and 6.7°C. The test conditions for each run are tabulated in Table 8.9. To predict the effect of liquid refrigerant injection cooling under each condition, the simulation was also carried out using the simulation parameters tabulated in Table 8.6 with the discharge coefficients of spray nozzle at 0.3 (see Appendix B, Section B.3).

The overall measured and predicted results are shown in Table 8.10. Measurements without liquid refrigerant injection cooling are used as the control run or the reference for comparison. The predictions are in good agreement with those of the measurements. From Table 8.10, the discrepancies between the predicted and measured average suction mass flow rate are 7.16% and 7.81% while the discrepancies between the predicted and the measured average power input are 4.16% and 4.19%. It is also observed that the predicted pressure variations in the working chambers for both injection conditions, as shown in Figure 8.15, also agree well with the measurements where the maximum mean discrepancy is 3.38% and the average mean discrepancy is 3.28%. In addition, the discrepancies between the predictions and the measured temperature of each prototype component, as shown in Figure 8.16 and Table 8.11, were mostly less than 10% with the highest discrepancy of 15.40%.

Table 8.9: Testing conditions of R134a refrigeration cycle under different conditions of liquid refrigerant injection cooling at input operating speed of 1620 rpm

Test condition	**No liquid injection (Control)**	**Injection duration of 0.005s**	**Injection duration of 0.01s**
Pressure			
Discharge pressure	945.8kPa	980.0kPa	980.0kPa
Suction inlet pressure	305.4kPa	313.65kPa	311.1kPa
Evaporator inlet pressure	389.7kPa	400.0kPa	399.9kPa
Evaporator outlet pressure	358.9kPa	369.4kPa	366.7kPa
Condenser inlet pressure	944.1kPa	983.6kPa	992.95kPa
Condenser outlet pressure	937.5kPa	975.3kPa	983.8kPa
Injector inlet pressure	-	977.0kPa	985.8kPa
Temperature			
Suction inlet temperature	26.7°C	29.1°C	25.1°C
Evaporator inlet temperature	6.8°C	6.7°C	6.7°C
Evaporator outlet temperature	30.1°C	34.7°C	26.7°C
Condenser inlet temperature	37.1°C	35.3°C	36.6°C
Condenser outlet temperature	32.1°C	32.8°C	33.6°C
Injector inlet temperature	-	32.4°C	34.2°C
Compressor cylinder surface temperature	46.7°C	39.7°C	37.1°C
Ambient temperature	27.3°C	27.3°C	27.3°C

Table 8.10: Results of R134a refrigeration cycle under different conditions of liquid refrigerant injection cooling at input operating speed of 1620 rpm

	No liquid injection (Control)		**Injection duration of 0.005s**			**Injection duration of 0.01s**		
	Pressure ratio of 3.06		**Pressure ratio of 3.18**			**Pressure ratio of 3.18**		
Output results	Measured	Predicted	Measured	Predicted	% Discr.	Measured	Predicted	% Discr.
Average suction mass flow rate ($\dot{m}_{avg,suc}$), g/s	9.6	9.44	9.94	9.23	7.16	10.40	9.59	7.81
Average injected liquid refrigerant ($\dot{m}_{avg,inj}$), g/s	-	-	-	0.88	-	-	1.26	-
Ratio of $\dot{m}_{avg,inj}$ to $\dot{m}_{avg,suc}$	-	-	-	0.096	-	-	0.13	-
Average power input, W	1360.3	1312.44	1393.26	1335.31	4.16	1393.26	1334.93	4.19
% increment in power based on control	-	-	2.42	-	-	2.42	-	-
Cooling load, W	1704.7	1676.11	1772.23	1645.41	7.16	1804.83	1663.95	7.81
Efficiencies								
Coefficient of performance (COP)	1.25	1.28	1.27	1.23	3.13	1.30	1.25	3.78
Volumetric efficiency, η_{vol}, %	55.5	54.59	57.78	56.80	7.16	60.93	58.40	7.81
Mechanical efficiency, η_{mech}, %	-	35.56	-	36.00	-	-	36.56	-
Isentropic efficiency	-	0.70	-	0.76	-	-	0.90	-

Although the pressure ratios of the runs with liquid refrigerant injections were greater than that of the control run (without liquid refrigerant injection), the measured average power inputs of both runs with injections are almost unaffected where the percentage increment in power input was only found to be 2.42% with respect to the control run even though excess power should

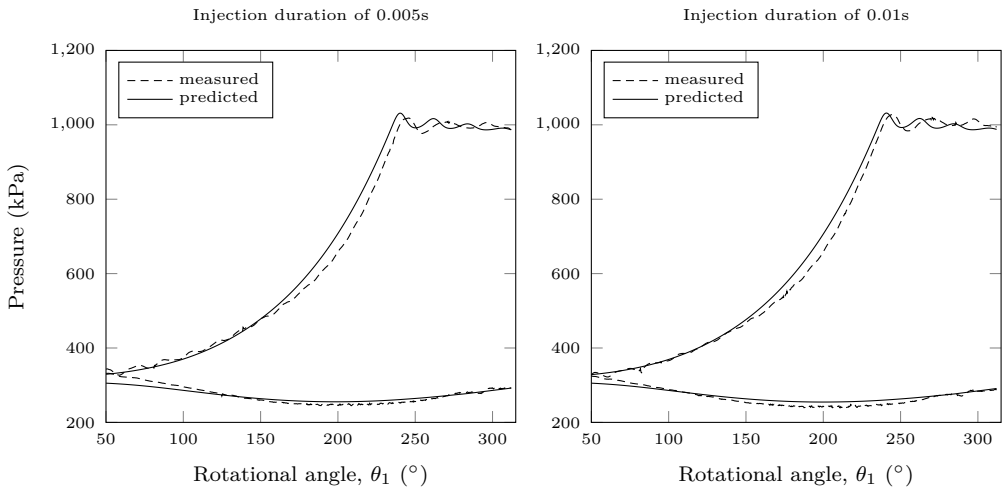

Figure 8.15: Comparison of the measured and predicted instantaneous pressure of the working chambers under different conditions of liquid refrigerant injection cooling.

be required to compress the additional injected refrigerant. Furthermore, no significant change to the COPs is observed for testing with injections and the pressure in the compression chamber for both injection conditions, as shown in Figure 8.15, does not show any significant variations. This might be because the amount of injected liquid refrigerant is negligible as compared to the total capacity of the prototype. The predicted amount of the injected mass flow for both testing conditions at injection durations of 0.005s and 0.01s only constitute 9.6% and 13% of the predicted average suction mass flow respectively. It also seems to suggest that cooling effects from the vaporisation of the liquid injected may have even balanced out the additional compression work needed to compress the injected refrigerant.

Even though the injected refrigerant is relatively small in quantity, the prototype parts were found to be cooled significantly by the injections. From Figure 8.16, the surface temperature of the discharge pipe, DP was reduced from 52.8 to 47.2°C while the surface temperature of the cylinder body, $C1$, was significantly reduced from 43.6 to 37.1°C when the injection duration was 0.01s. As these temperature measurements were taken from the surface of the components, as seen in Figure 8.12, a 6.5 degree reduction in the surface temperature of the cylinder body or a 8.1 degrees decrease in the surface temperature of the top cover would mean that the internal parts would also have been significantly cooled down by the injected liquid refrigerant since the vaporisation of the liquid refrigerant occurs in the working chambers. The reduction in the surface temperature of the discharge pipe may also mean that the temperature of the discharged

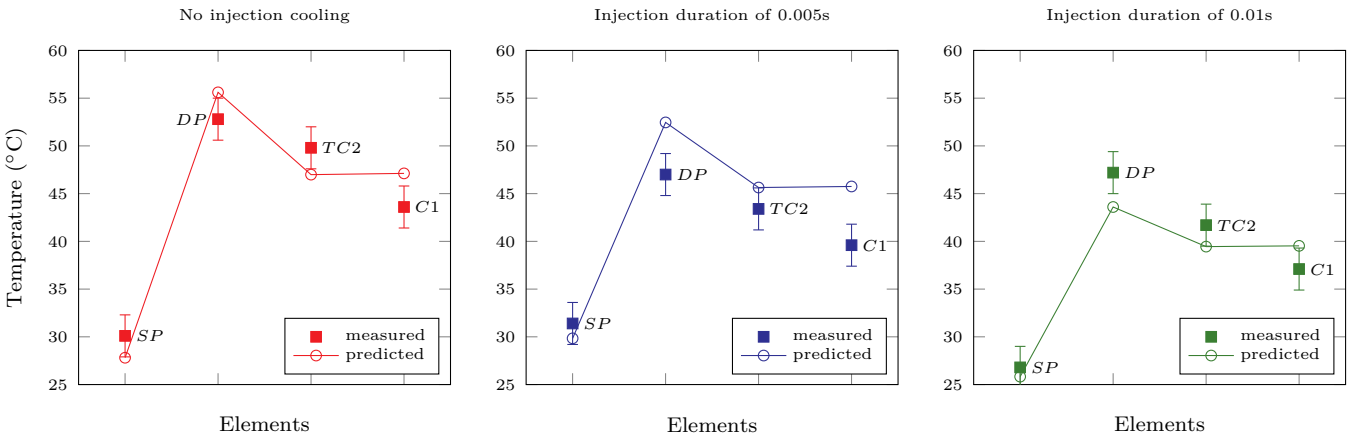

Figure 8.16: Measured and predicted temperatures of the prototype components at different injection conditions.

gases would have been reduced significantly with the injections. These significant reductions in the components' temperature may also suggest that a small portion of the injected refrigerant may have remained in the saturated liquid state after injection due to metastability characteristic and increasing pressure condition in the compression chamber; this metastable refrigerant may have impinged onto the surface of the internal components and was then evaporated by absorbing heat from the components' surface, thereby resulting in significant temperature reduction of the components. Overall, the results show that liquid refrigerant injection can effectively cool down the dry rubbing parts without negatively affecting the power input of the compressor and the chamber pressure even with a liquid injection of up to 13% of the suction intake.

From Table 8.11, a large reduction in the overall predicted temperature profile of the prototype with increasing duration of liquid refrigerant injection from 0.005 to 0.01s can be observed. The bulk temperature of the split bush is predicted to be reduced by 24.43 degrees from 237.22°C to 212.79°C while the endface bushings are generally cooled down by 7 degrees. This significant reduction in the predicted temperature of the split bush might be caused by the simplification made in the thermal modelling in considering the entire split bush as one lumped element instead of discretising it further into smaller elements. In general, the temperature reductions based on the measurements and predictions suggest that the use of liquid injection cooling would have been useful in reducing the risk of seizure since the cooling effect would prevent the overheating of moving parts that may lead to severe thermal expansion and mechanical interference of the bearing surfaces.

Table 8.11: Overall measured and predicted temperatures of the prototype at different injection conditions

	Without liquid injection (Control)			Injection duration of 0.005s			Injection duration of 0.01s		
Elements	Predicted	Measured	% Discrepancy	Predicted	Measured	% Discrepancy	Predicted	Measured	% Discrepancy
Shaft section1, S1	174.49	Not measured		173.97	Not measured		171.93	Not measured	
Counterweight, CW	128.16	Not measured		127.80	Not measured		126.41	Not measured	
Shaft section 2, S2	458.53	Not measured		456.96	Not measured		450.78	Not measured	
Shaft bearing 1, B1	52.40	Not measured		51.04	Not measured		44.85	Not measured	
Top cover element 4, TC4	47.03	Not measured		45.67	Not measured		39.47	Not measured	
Endface bushing 1, EB1	47.00	Not measured		45.65	Not measured		39.45	Not measured	
Eccentric, EC	128.08	Not measured		124.99	Not measured		116.86	Not measured	
Eccentric bearings, B2	108.93	Not measured		105.61	Not measured		97.19	Not measured	
Rotor, R	100.07	Not measured		96.70	Not measured		88.19	Not measured	
Cylinder layer 9, C9	47.12	Not measured		45.75	Not measured		39.52	Not measured	
Vane, V	184.56	Not measured		182.92	Not measured		173.99	Not measured	
Split bush, SB	237.22	Not measured		226.77	Not measured		212.79	Not measured	
Suction pipe, SP	27.81	30.1	7.58	29.84	31.4	5.12	25.83	26.8	3.61
Discharge pipe, DP	55.61	52.8	5.30	52.46	47.0	11.61	43.60	47.2	7.59
Endface bushing 2, EB2	47.22	Not measured		45.86	Not measured		39.63	Not measured	
Shaft section 3, S3	61.85	Not measured		60.16	Not measured		53.53	Not measured	
Shaft bearing 2, B3	47.42	Not measured		46.05	Not measured		39.80	Not measured	
Cylinder bottom layer 9, BC9	47.12	Not measured		45.75	Not measured		39.53	Not measured	
Test rig, TR	47.12	Not measured		45.75	Not measured		39.54	Not measured	
Top cover element 1, TC1	46.99	Not measured		45.63	Not measured		39.44	Not measured	
Top cover element 2, TC2	46.99	49.8	5.59	45.64	43.4	5.12	39.45	41.7	5.43
Top cover element 3, TC3	47.00	Not measured		45.65	Not measured		39.45	Not measured	
Cylinder layer 1, C1	47.12	43.6	8.18	45.75	39.6	15.40	39.53	37.1	6.55
Cylinder layer 2, C2	47.12	Not measured		45.75	Not measured		39.53	Not measured	
Cylinder layer 3, C3	47.12	Not measured		45.75	Not measured		39.52	Not measured	
Cylinder layer 4, C4	47.11	Not measured		45.75	Not measured		39.52	Not measured	
Cylinder layer 5, C5	47.11	Not measured		45.74	Not measured		39.52	Not measured	
Cylinder layer 6, C6	47.10	Not measured		45.74	Not measured		39.52	Not measured	
Cylinder layer 7, C7	47.11	Not measured		45.74	Not measured		39.52	Not measured	
Cylinder layer 8, C8	47.11	Not measured		45.75	Not measured		39.53	Not measured	
Cylinder bottom layer 1, BC1	47.12	Not measured		45.75	Not measured		39.52	Not measured	
Cylinder bottom layer 2, BC2	47.12	Not measured		45.75	Not measured		39.52	Not measured	
Cylinder bottom layer 3, BC3	47.12	Not measured		45.75	Not measured		39.53	Not measured	
Cylinder bottom layer 4, BC4	47.12	Not measured		45.75	Not measured		39.53	Not measured	
Cylinder bottom layer 5, BC5	47.12	Not measured		45.76	Not measured		39.54	Not measured	
Cylinder bottom layer 6, BC6	47.13	Not measured		45.76	Not measured		39.54	Not measured	
Cylinder bottom layer 7, BC7	47.14	Not measured		45.77	Not measured		39.55	Not measured	
Cylinder bottom layer 8, BC8	47.15	Not measured		45.78	Not measured		39.56	Not measured	

8.6 Post-Experiment Prototype Inspection

The oil-free prototype was dismantled and the components were inspected after all the experimental runs. Figure 8.17 shows the surface condition of the shaft and eccentric after all the experimental runs. The dry rubbing with the lip seal has produced a ring of wear mark with slight straw to bluish temper colour due to extreme heat generated. It is also observed that there are deposits of bronze on the shaft collar that were transferred from the top endface bushing, indicating that there are shaft tilting and vibration during operations which have caused the shaft collar to rub against the bushing. Wear marks are also seen on the eccentric on which the eccentric ball bearings were fitted. This suggest that there is also slippage between the eccentric and the inner race of the ball bearings during rotations which has resulted in dry rubbing since the resultant measured diameter of the eccentric is smaller than the design specification. The fitting between the ball bearings and the eccentric is too loose.

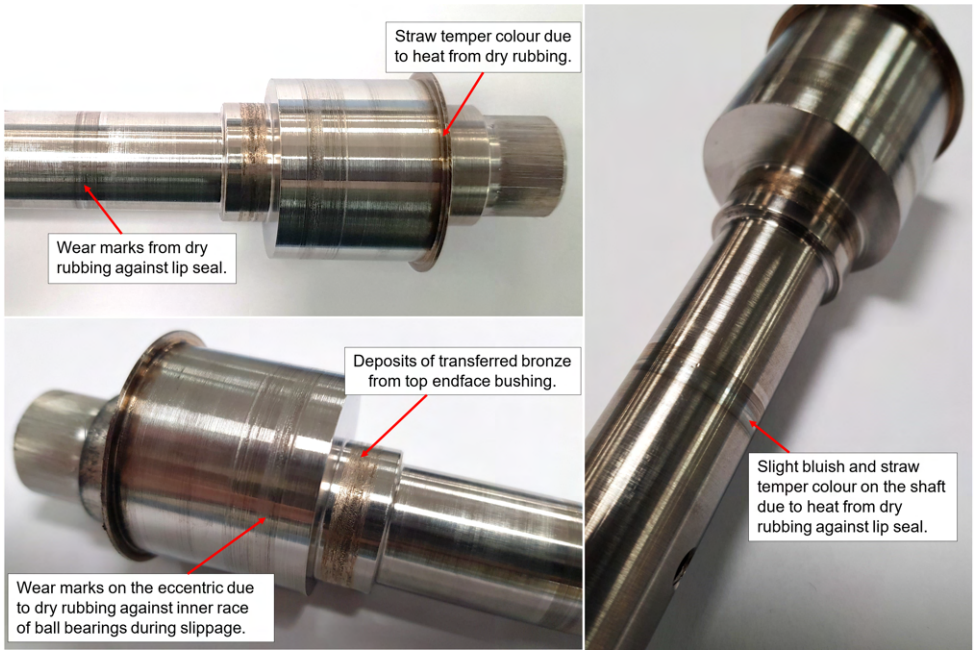

Figure 8.17: Wear marks of shaft and eccentric after experiments.

The rotor and the vane have also suffered from dry rubbing with the endface bushings and split bush, as seen in Figure 8.18. The left side of the vane which bears the loading from the high gas pressure force (see Figure 8.18a) has the most severe adhesive and abrasion wear with deep galling and scuffing marks. Protruding layers of bronze deposits were also found on both sides of the vane,

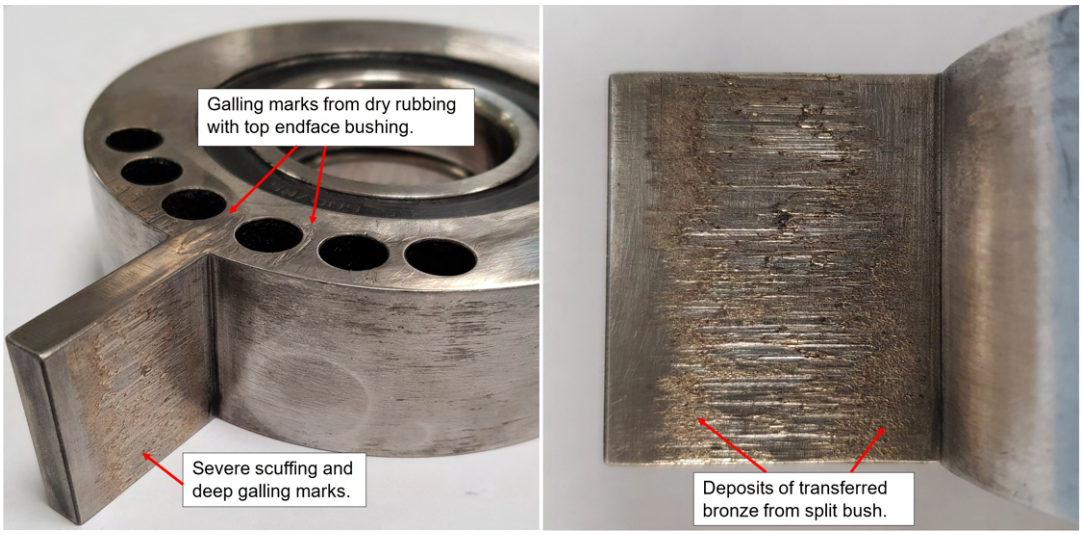

(a) Vane side with high loading from gas pressure (left).

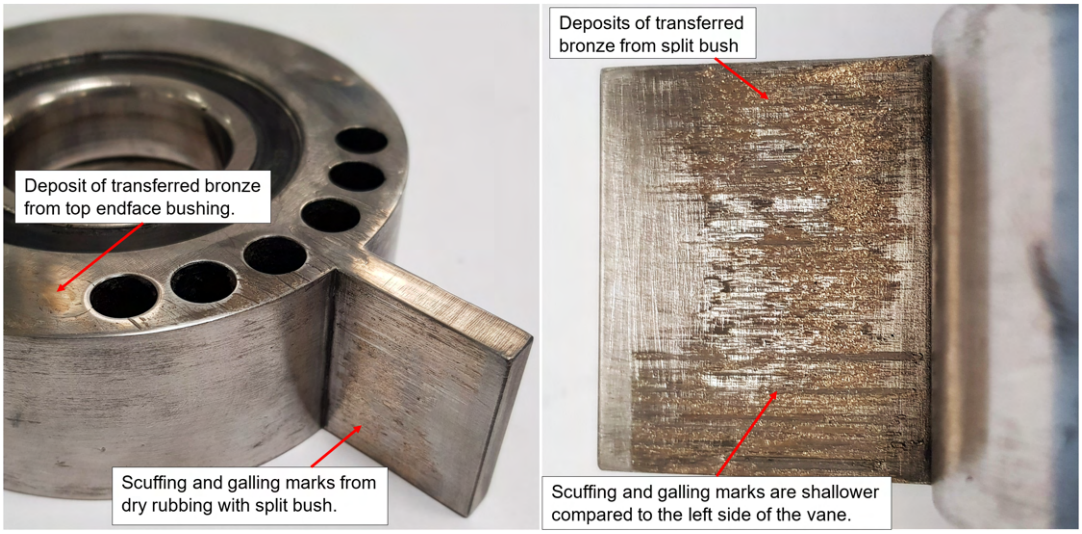

(b) Vane side (right).

Figure 8.18: Wear marks of rotor and vane after experiments.

suggesting that the seizures experienced during some runs might be highly due to the friction welding of similar bronze layers on both sides of the vane and split bush especially when the interfacial temperature is found to be higher 300°C (as explained in Subsection 7.3.3). Furthermore, post-experiment surface roughness measurements based on arithmetical mean roughness value (Ra value) have shown that the surface roughness of the vane and rotor have approximately increased by 10 times from 0.356 μm to 3.572 μm.

8.7 Summary

The performance of the prototype using air and R134a as the working fluids were experimentally determined and the theoretical modellings have been validated with the collected data. The predicted and measured mass flow rate and average power input are in good agreement for both air and 134a with most discrepancies within ±15%. For the measurement of the instantaneous pressure profile of the working chambers, it was observed that there was an abrupt pressure drop between 150° to 220° of the rotational angle, θ_1, during the compression phase. This is because the rotor was machined with an out-of-tolerance outer diameter which has led to a sudden widening of the radial clearance between the rotor and the cylinder and a sudden increase in radial leakage. With better tolerance control during fabrication, this leakage can be improved. The effects of liquid refrigerant injection cooling were also studied and it was observed that the cooling from the injections were able to bring down the surface temperature of prototype components by 5 to 8 degrees. A reduction of 7 to 24°C in the bulk temperature of the bearings and the internal moving parts were also predicted to be possible with liquid refrigerant injection cooling. The measured pressure variation of the working chambers does not show significant changes when the injected mass is increased from 9.6% to 13%. In addition, 2.4% of power increment was measured with injection cooling. In general, liquid refrigerant injection cooling is found to be able to cool down the oil-free prototype significantly without noticeable increase in power consumption for compression work.

Chapter 9

Conclusions and Recommendations for Future Work

In this research study, an oil-free swing vane compressor with liquid refrigerant injection cooling was developed and studied. A summary of the developmental work and the key findings from the predictions and measured results are presented in the first half of this chapter, followed by the recommendations for future work.

9.1 Developmental Work

The developmental work carried out in this study on oil-free compressor includes the conceptual design in reducing the friction acting on the rubbing components of the compressor mechanism, designing the injector and its control, mathematical modelling, prototype fabrication, building of the experimental setups and experimental testing.

9.1.1 Compressor and Injector Design

Various types of positive-displacement vane type compressor mechanisms have been reviewed.

- The swing vane mechanism was reviewed to be the most suitable design of all positive-displacement vane type compressor mechanisms for dry operations as it is easy to be incorporated with self-lubricating material for friction-reduction without drastic re-designing of each compressor component.

- Bearing surfaces that undergo dry rubbing were replaced with self-lubricating material to reduce excessive frictional wear and heating which may lead to seizure due to friction welding of rubbing surfaces. For rotor-eccentric and shaft bearing surfaces which experience high gas forces and frictional losses, sealed ball bearings were used in order to ensure the reliability of the overall mechanism.

- A wear test has been carried out to select a suitable self-lubricating material for the fabrication of endface wear bushings and split bush. All the self-lubricating materials were machined into bushings and tested in the prototype under the practical test conditions. Among all commercially available self-lubricating material, namely, Cast Nylon 6, PTFE, PEEK GF30 and C95500 AB2 Nickel-Aluminium Bronze, the latter was chosen for its wear-resistance and high melting point that are needed to withstand high frictional force and extreme heat generated at the dry rubbing interfaces.

- An injector and its control were designed and incorporated into the compressor prototype for liquid refrigerant injection into the compression chamber at a specified phase of the compression process based on the angular position of the shaft. The injector is electronically-controlled by the PC & DAQ system that detects the specified angular position of the shaft via magnetic angular position sensor and controls the onset and opening duration of the solenoid valve for the injection of liquid refrigerant.

9.1.2 Mathematical Modelling

- A comprehensive mathematical model describing the working process of both the suction and compression chambers of the compressor was developed to determine the performance characteristics of the lubricant-free compressor. The model accounts for the dynamics of the swing vane mechanism under dry rubbing conditions, the internal leakages at the radial and endface clearances, the suction and discharge flow analysis, the operation of the discharge reed valve and the liquid refrigerant injection cooling of the compressor chamber. The latter employs homogeneous frozen two-phase orifice flow model to account for the mass flow of the injected liquid refrigerant.

- The lumped thermal conductance method was used to predict the compo-

nents' temperature as a result of significant frictional heat generated due to the absence of lubricant.

- CFD simulation was carried out to supplement the determination of the suction flow coefficient of the transient pulsatile flow in the suction pipe.

9.2 Key Findings and Observations

Experiments have been carried out to determine the performance of the prototype compressor operating under lubricant-free operational conditions. The open loop was used to operate the compressor with air as the working fluid. In the open air loop, the prototype was successfully operated at 1080 to 1800 rpm and has attained a range of pressure ratios from 2.11 to 4.08. In the case of R134a, a vapour-compression refrigeration cycle was set up. The prototype was operated in this refrigeration cycle with R134a as the working fluid at an input operating speed of 1620 rpm and a pressure ratio of 3.1 was attained. Liquid refrigerant injection was also tested during the experimental runs with R134a and it was found to be effective in cooling the components of the compressor. Key findings and observations from the measured and simulation results are presented as follows:

- The average discharge mass flow rate of air was found to increase with operating speed as expected while it decreases with the pressure ratio. The average discharge mass flow of air was also found to be underpredicted at high operating speed beyond 1440 rpm and overpredicted at speed below 1440 rpm. This was caused by the use of constant suction flow coefficient which is the average value of all the CFD-determined flow coefficients at operating speed from 1080 rpm to 1800 rpm. The average discrepancy between the predicted and measured flow rates of air is 8.73%.

- The volumetric efficiencies of testing with air were measured to range from 30.9% to 67.5%. It was observed that high pressure ratio and low operating speeds would yield lower volumetric efficiencies and vice versa.

- The instantaneous pressure variations of the working fluid in both the suction and compression chambers were measured and compared with the predictions. The comparisons show that the maximum and average mean discrepancies for testing with air as the working fluid are 2.36% and

1.68%, respectively. For experimental runs with R134a, the average mean discrepancy at input operating speed of 1620 rpm is 3.08%.

- When comparing measured and predicted power input with air as the working fluid, the maximum and average discrepancies of power input are 13.37% and 6.08%, respectively.
- Using the lumped conductance model, the predicted and measured temperature of components show that most of the discrepancies are smaller than 10% and the highest discrepancy is at 13.91%.
- The COP and the volumetric efficiency of the R134a in the vapour-compression cycle at input operating speed of 1620 rpm were measured to be 1.25 and 55.52%, respectively. The low performance was largely due to substantial internal leakages in the absence of sealing from oil lubrication.
- The prototype was tested with liquid refrigerant injection cooling for a duration of 0.005s and 0.01s and it was found that the injections had effectively reduced the components' temperatures of the prototype. The surface temperature of the cylinder was cooled down by 6.5°C from 43.6°C to 37.1°C while the cylinder top cover was cooled by 8.1°C from 49.8°C to 41.7°C. Since the vaporisation of injected liquid refrigerant occurs internally in the working chambers, a significant reduction in surface temperature of the components would indicate that the internal parts were also significantly cooled by the injected liquid refrigerant. The use of liquid refrigerant injection was found to contribute an additional 2.4% increment in the average power input.
- The isentropic efficiency of the prototype was predicted to improve from 0.70 to 0.90 with liquid refrigerant injection cooling for a duration of 0.01s. The isentropic efficiency of the prototype achieved under the effects of liquid refrigerant injection cooling for a duration of 0.005s is 0.76. The overall improvement in the isentropic efficiency is mainly due to the reduction in the compression work required to compress the gas after cooling.

9.3 Research Contributions

In this study, a conceptual design of an oil-free swing vane compressor has been successfully tested with air and R134a as the working fluids. Liquid refrigerant

was also injected into the compression chamber during the compression process to cool the prototype and the temperature measurements of the liquid refrigerant injected prototype has shown that the refrigerant injection was able to cool the compressor significantly without increasing the compression power input and decreasing the compressor efficiency. Such cooling technique can be utilised in the developmental work of other oil-free compressor types to prevent overheating and seizure of the compressor.

Furthermore, the performance of the oil-free swing vane compressor was simulated using existing models that have been used in the modelling of conventional oil-lubricated positive displacement vane type compressors. One of the main contributions of this study is the validations of the accuracy of these existing models for the simulation of an oil-free positive displacement swing vane compressor using experimental results. Both leakage and heat transfer models that are based on Fanno flow and lumped conductance method, respectively, were able to predict the volumetric efficiency and temperatures of the prototype components with discrepancies less than 15%.

Secondly, a two-phase flow model was used in the modelling of the flashing process of the liquid refrigerant during its flow from the condenser to the injector and this has not been done in previous studies where injected refrigerant is usually assumed to be in subcooled or saturated state. A simple analysis model, in which the liquid refrigerant of the two-phase flow is assumed to evaporate immediately after injection and the resultant vapour to be mixed homogeneously with the chamber gas, was also applied. The discrepancies between the temperature prediction of each prototype component and the experimental measurements under the effects of different injection durations were mostly less than 15%. The power input and the instantaneous pressure variations of the working chambers were also predicted accurately using the simple analysis model. By using such these models, the computational time for the simulation of the effect of liquid refrigerant injection cooling on an oil-free compressor can be shortened without compromising the accuracy in the predictions.

Thirdly, in this study, the dead volumes of the prototype are found to be causing fluctuation in the pressure of the suction chamber due to the re-expansion of the trapped fluid in the dead volumes. This has led to the formation of pulsatile suction flow in the suction port. Details of this finding are shown in Appendix B Section B.1. CFD simulations were conducted to model the pulsatile suction flow and it was found that it reduces the suction flow and volumetric efficiency

of the compressor. Furthermore, it was observed that the flow reducing effect decreases with increasing operating speed of the compressor. This suggests that lower operating speed allows greater re-expansion of compressed fluid from dead volume, resulting in larger adverse pressure gradient across the suction port and greater pulsatile flow. Such finding is important for the thermodynamic modelling of a compressor especially an oil-free type where the dead volumes are unsealed in the absence of oil lubrication and can greatly affect the volumetric efficiency of the oil-free compressor.

Furthermore, the surface temperature of dry rubbing interfaces has been found to range from 200°C to 300°C based on the tempering colour of the steel components. This would help in narrowing the selection of self-lubricating materials in the developmental work for the design of other oil-free positive displacement vane type compressors.

9.4 Recommendations for Future Work

From the findings of the experimental study of the oil-free swing vane compressor presented in Chapter 8, the efficiencies of the oil-free prototype were observed to be poor as compared to that of the conventional oil-lubricated compressors and the durability was far from being operational based on the severity of the wear marks on each moving component. Throughout the experimental tests, the compressor was prone to seizure, vibration and significant internal leakages. The occasional onset of vibration is partly due to the imbalance of rotating components caused by machining inaccuracies and temporary mechanical binding and unbinding of worn-out rubbing surfaces. As such, there are areas of improvement. The recommendations for further development of an oil-free compressor are presented as follows:

- Fabrication of each prototype components with better tolerance control is needed to ensure smoother operations with reduced vibrational chattering and shaft tilting. Additionally, the circularity and cylindricity inaccuracies of the rotor have to be reduced in order to minimise the amount of radial leakages in the prototype. Moreover, it is also advisable to have the surfaces of the rubbing components to be case-hardened by heat treatments so as to increase the surface hardness and wear resistance of the rubbing surfaces to prevent excessive wear.

- Using the current simulation model, parametric studies can be systematically conducted to identify critical design variables which have significant effects on the performance of the oil-free compressor. Following which, constrained multi-variables and multi-objectives optimisation methods such as genetic algorithm, complex optimisation method can be used to identify combinations of design variables that provide an optimum performance for given objective functions. For an oil-free compressor, an improved mechanical efficiency with reduced frictional losses should be the priority for the choice of objective functions.

- More in-depth studies can be carried out in the study of the effects of liquid refrigerant injection on the compressor performance, in particular the reduction of components' temperature, especially in the absence of oil lubrication. It is believed that the injection of liquid refrigerant is one mechanism that allows cooling of rubbing components to be achieved and at the same time, it may also have the effects of improving overall compressor performance due to less compression work needed for the compression of less energetic and cooled working fluid when the injection is applied appropriately. The effects of liquid refrigerant injection and the amount of temperature reduction achievable are affected by a few parameters, mainly, the injection positions and the amount of liquid injected. Others such as states of the injected liquid, the droplet sizes and distributions and the injection angle also play an important part in maximising the liquid injection effects for improved reliability and better performance of the compressor.

- Liquid refrigerant can also be injected directly onto the rubbing surfaces in order to bring down the interfacial temperature. This would help to prevent the overheating of the rubbing surfaces and reduce the risk of seizure due to wear, thermal expansion and dimensional interference.

- Although the adaptation of sealed ball bearings to the dry compressor design would assist in friction-reduction at dry rubbing surfaces and minimises the chances of seizure which are caused by the friction welding of dry rubbing components. The limitation, however, is that the applications of sealed ball bearing is mostly restricted to rotating components only. For linear rubbing surfaces, surface hardening and coatings may be applicable.

- Materials with better wear characteristics such as low friction and wear rate with high thermal resistance (e.g. high performance alloy Inconel 600 or Alumina ceramics), will certainly be needed to improve the performance and reliability of the lubricant-free compressors. The use of these materials for friction-reduction of the linear rubbing interface between the vane and the split bush is of particular interest since sealed bearing cannot be applied. It is inadvisable to use any polymer-based material that has a melting point below 500°C as the low thermal conductivity of polymer and high frictional heat generated would lead to high rubbing surface temperature and melting.

- Re-designing of the vane and the split bush to incorporate the use of linear bearings are also recommended as the sliding interface between the vane and the split bush suffers the most severe wear among all rubbing surfaces.

The successful development of an oil-free compressor for vapour-compression refrigeration systems would provide an alternative to the solutions of small-scale portable cooling and heating applications with high COP. Although the scope of the developmental work in designing and testing an oil-free compressor is indeed overwhelming due to the many practical design challenges and problems to be resolved as mentioned in this thesis, the author is hopeful that the studies presented in this thesis would lay a good foundation in the future development of an oil-free positive displacement compressor and help to realise the success of a portable small capacity oil-free vapour-compression refrigeration system.

References

[1] D. F. G. Hampson, "Compressor Lubrication," in *Lubrication in Practice*, London: Palgrave Macmillan UK, 1972, pp. 67–74, ISBN: 978-1-349-81550-0. DOI: 10.1007/978-1-349-81550-0_9.

[2] E. Sloman, "Lubrication," in *Plant Engineer's Reference Book*, Elsevier, 2002, pp. 40–1–40–46. DOI: 10.1016/b978-075064452-5/50095-x.

[3] H. Kerpicci, A. Yagci, and S. U. Onbasioglu, "Investigation of oil flow in a hermetic reciprocating compressor," *International Journal of Refrigeration*, vol. 36, no. 1, pp. 215–221, 2013. DOI: https://doi.org/10.1016/j.ijrefrig.2012.09.002.

[4] B. J. Hamrock, S. R. Schmid, and B. O. Jacobson, *Fundamentals of Fluid Film Lubrication*. Taylor and Francis Inc, Mar. 15, 2004, 728 pp., ISBN: 9780824753719. [Online]. Available: https://www.ebook.de/de/product/3883164/bernard_j_ohio_state_university_columbus_usa_hamrock_bo_o_lund_university_sweden_jacobson_steven_r_university_of_notre_dame_indiana_usa_schmid_fundamentals_of_fluid_film_lubrication.html.

[5] L. Cremaschi, Y. Hwang, and R. Radermacher, "Experimental investigation of oil retention in air conditioning systems," *International Journal of Refrigeration*, vol. 28, no. 7, pp. 1018–1028, 2005. DOI: https://doi.org/10.1016/j.ijrefrig.2005.03.012.

[6] S. Moorhouse, E. Rodriguez, and D. Turner, "Variable speed oil-freemagnetic bearingcentrifugal compressors," *ASHRAE Journal*, pp. 54–60, Apr. 2020. [Online]. Available: https://www.ashrae.org/filelibrary/technicalresources/ashraejournal/125thanniversaryarticles/54-61_clausen_historical_danfoss.pdf.

[7] TCBU Editorial, "Meeting world-class efficiency standards with oil-free compressors," *Thermal Control Business Update*, May 2020. [Online]. Available: https://thermalcontrolmagazine.com/technology/meeting-world-class-efficiency-standards-with-oil-free-compressors/.

[8] D. Turbocor, *Oil-free compressors maintain consistent performance over time - case study*, Jan. 2019. [Online]. Available: https://www.danfoss.com/en-us/service-and-support/case-studies/dcs/oil-free-compressors-maintain-consistent-performance-over-time/.

[9] R. Conry, L. Whelan, and J. Ostman, "Magnetic Bearings, Variable Speed Centrifugal Compression And Digital Controls Applied In A Small Tonnage Refrigerant Compressor Design," *International Compressor Engineering Conference*. Paper 1500, (2002). [Online]. Available: https://docs.lib.purdue.edu/icec/1500.

[10] W. Zhang and H. Zhu, "Radial magnetic bearings: An overview," *Results in Physics*, vol. 7, pp. 3756–3766, 2017. DOI: https://doi.org/10.1016/j.rinp.2017.08.043.

[11] S. M. Darbandi, M. Behzad, H. Salarieh, and H. Mehdigholi, "Linear Output Feedback Control of a Three-Pole Magnetic Bearing," *IEEE/ASME Transactions on Mechatronics*, vol. 19, no. 4, pp. 1323–1330, 2014, ISSN: 1941-014X. DOI: 10.1109/TMECH.2013.2280594.

[12] T. Schuhmann, W. Hofmann, and R. Werner, "Improving Operational Performance of Active Magnetic Bearings Using Kalman Filter and State Feedback Control," *IEEE Transactions on Industrial Electronics*, vol. 59, no. 2, pp. 821–829, 2012, ISSN: 1557-9948. DOI: 10.1109/TIE.2011.2161056.

[13] T. Tritt, "Thermoelectric Materials: Principles, Structure, Properties, and Applications," in *Encyclopedia of Materials: Science and Technology*, Elsevier, 2002, pp. 1–11. DOI: https://doi.org/10.1016/B0-08-043152-6/01822-2.

[14] M. Mirmanto, S. Syahrul, and Y. Wirdan, "Experimental performances of a thermoelectric cooler box with thermoelectric position variations," *Engineering Science and Technology*, vol. 22, no. 1, pp. 177–184, 2019. DOI: https://doi.org/10.1016/j.jestch.2018.09.006.

[15] J. Vián and D. Astrain, "Development of a thermoelectric refrigerator with two-phase thermosyphons and capillary lift," *Applied Thermal Engineering*, vol. 29, no. 10, pp. 1935–1940, 2009. DOI: https://doi.org/10.1016/j.applthermaleng.2008.09.018.

[16] S. A. Abdul-Wahab, A. Elkamel, A. M. Al-Damkhi, I. A. Al-Habsi, H. S. Al-Rubai'ey', A. K. Al-Battashi, A. R. Al-Tamimi, K. H. Al-Mamari, and M. U. Chutani, "Design and experimental investigation of portable solar thermoelectric refrigerator," *Renewable Energy*, vol. 34, no. 1, pp. 30–34, 2009. DOI: https://doi.org/10.1016/j.renene.2008.04.026.

[17] G. Min and D. Rowe, "Experimental evaluation of prototype thermoelectric domestic-refrigerators," *Applied Energy*, vol. 83, no. 2, pp. 133–152, 2006. DOI: https://doi.org/10.1016/j.apenergy.2005.01.002.

[18] Y. Dai, R. Wang, and L Ni, "Experimental investigation and analysis on a thermoelectric refrigerator driven by solar cells," *Solar Energy Materials and Solar Cells*, vol. 77, no. 4, pp. 377–391, 2003. DOI: https://doi.org/10.1016/S0927-0248(02)00357-4.

[19] T. Yanagisawa, T. Shimizu, I. Chu, and K. Ishijima, "Motion Analysis of Rolling Piston in Rotary Compressor," *International Compressor Engineering Conference*. Paper 392, (1982). [Online]. Available: http://docs.lib.purdue.edu/icec/392.

[20] Z. L. He, X. Z. Yang, D. T. Li, and W. F. Wu, "Dynamic characteristics of a swing compressor for an air conditioning system at different discharge pressures," *International Journal of Refrigeration*, vol. 112, pp. 125–135, 2020. DOI: https://doi.org/10.1016/j.ijrefrig.2019.12.021.

[21] K. T. Ooi and Y. L. Teh, "REVOLVING VANE COMPRESSOR AND METHOD FOR ITS MANUFACTURE," English, U.S. Patent US 8,905,737 B2, Feb. 2014. [Online]. Available: https://patents.google.com/patent/US8905737.

[22] J. D. Tromblee, "Performance Analysis of a Sliding -Vane Rotary Compressor for a Household Refrigerator/Freezer," *International Compressor Engineering Conference*. Paper 432, (1984). [Online]. Available: https://docs.lib.purdue.edu/icec/432.

[23] W. Q. Chen, Z. W. Xing, H. Tang, and H. G. Wu, "Theoretical and experimental investigation on the performance of screw refrigeration compressor under part-load conditions," *International Journal of Refrigeration*, vol. 34, no. 4, pp. 1141–1150, 2011. DOI: https://doi.org/10.1016/j.ijrefrig.2011.01.020.

[24] K. Tojo, M. Ikegawa, M. Shiibayashi, A. Arai, and N. Uchikawa, "A Scroll Compressor for Air Conditioners," *International Compressor Engineering Conference*. Paper 496, (1984). [Online]. Available: http://docs.lib.purdue.edu/icec/496.

[25] G. Hundy, A. Trott, and T. Welch, "Compressors," in *Refrigeration, Air Conditioning and Heat Pumps*, Elsevier, 2016, pp. 59–87. DOI: https://doi.org/10.1016/B978-0-08-100647-4.00004-8.

[26] T. Yanagisawa and T. Shimizu, "Friction losses in rolling piston type rotary compressors. III," *International Journal of Refrigeration*, vol. 8, no. 3, pp. 159–165, 1985. DOI: https://doi.org/10.1016/0140-7007(85)90156-2.

[27] T. Matsuzaka and S. Nagatomo, "Rolling Piston Type Rotary Compressor Performance Analysis," *International CompressorEngineering Conference*. Paper 386., (1982). [Online]. Available: https://docs.lib.purdue.edu/icec/386.

[28] Y. Liu and J. Kosco, ‘‘Vane Dynamics Analysis of a Tilted Vane Rotary Compressor,’’ *International Compressor Engineering Conference*. Paper 1273, (1998). [Online]. Available: https://docs.lib.purdue.edu/icec/1273.

[29] K. T. Ooi, T. N. Wong, and E. C.Kwek, ‘‘Effects of Vane Spring Stiffness on Compressor Performance,’’ *International Compressor Engineering Conference*. Paper 1034, (1994). [Online]. Available: https://docs.lib.purdue.edu/icec/1034.

[30] S. Fujimoto, K. Sakitani, and M. Watada, ‘‘Tribology Analysis in Rolling Piston Type Compressor,’’ *International Compressor Engineering Conference*. Paper 477, (1984). [Online]. Available: https://docs.lib.purdue.edu/icec/477.

[31] M. Takebayashi, H. Hata, T. Iizuka, A. Ishiyama, and H. Kohsokabe, ‘‘A Study on Wear Characteristics of a Rolling-Piston-Type Rotary Compressor,’’ *International Compressor Engineering Conference*. Paper 1378, (2000). [Online]. Available: https://docs.lib.purdue.edu/icec/Paper1378.

[32] H. C. Sung, ‘‘Tribological characteristics of various surface coatings for rotary compressor vane,’’ *Wear*, vol. 221, no. 2, pp. 77–85, 1998. DOI: https://doi.org/10.1016/S0043-1648(98)00244-0.

[33] Y. Z. Lee and S. D. Oh, ‘‘Friction and wear of the rotary compressor vane–roller surfaces for several sliding conditions,’’ *Wear*, vol. 255, no. 7-12, pp. 1168–1173, 2003. DOI: https://doi.org/10.1016/S0043-1648(03)00278-3.

[34] S. D. Oh, J. W. Kim, and Y. Z. Lee, ‘‘Friction and Wear Characteristics of TiN Coated Vane for the Rotary Compressor in a R410A Refrigerant,’’ *Tribology Transactions*, vol. 47, no. 1, pp. 29–33, 2004. DOI: https://doi.org/10.1080/05698190490279065.

[35] G. Bianchi and R. Cipollone, ‘‘Theoretical modeling and experimental investigations for the improvement of the mechanical efficiency in sliding vane rotary compressors,’’ *Applied Energy*, vol. 142, pp. 95–107, 2015. DOI: https://doi.org/10.1016/j.apenergy.2014.12.055.

[36] P. Shu, B. Guo, L. Li, and J.Hu, ‘‘Influence of Vane Slot Back-Pressure on the Characteristic of Vane Motion in Rotary Vane Compressor,’’ *International Compressor Engineering Conference*. Paper 1275, (1998). [Online]. Available: https://docs.lib.purdue.edu/icec/1275.

[37] K. Tojo, T. Kan, and A. Arai, ‘‘Dynamic Behavior of Sliding Vane in Small Rotary Compressors,’’ *International Compressor Engineering Conference*. Paper 242, (1978). [Online]. Available: https://docs.lib.purdue.edu/icec/Paper242.

[38] O. Al-Hawaj, "Theoretical modeling of sliding vane compressor with leakage," *International Journal of Refrigeration*, vol. 32, no. 7, pp. 1555–1562, 2009. DOI: https://doi.org/10.1016/j.ijrefrig.2009.07.005.

[39] G. Bianchi and R. Cipollone, "Friction power modeling and measurements in sliding vane rotary compressors," *Applied Thermal Engineering*, vol. 84, pp. 276–285, 2015. DOI: https://doi.org/10.1016/j.applthermaleng.2015.01.080.

[40] M. Masuda, K. Sakitani, Y. Yamamoto, T.Uematsu, and A. Mutoh, "Development of Swing Compressor for Alternative Refrigerants," *International Compressor Engineering Conference*. Paper 1154, (1996). [Online]. Available: https://docs.lib.purdue.edu/icec/1154.

[41] X. Hu, Z. Qu, X. Yang, and J. Sun, "Theoretical study on frictional losses of a novel automotive swing vane compressor," *International Journal of Refrigeration*, vol. 36, no. 3, pp. 758–767, 2013. DOI: https://doi.org/10.1016/j.ijrefrig.2012.11.001.

[42] Y. Teh and K. Ooi, "Theoretical study of a novel refrigeration compressor – Part I: Design of the revolving vane (RV) compressor and its frictional losses," *International Journal of Refrigeration*, vol. 32, no. 5, pp. 1092–1102, 2009. DOI: https://doi.org/10.1016/j.ijrefrig.2008.09.006.

[43] K. Tan and K. Ooi, "A novel revolving vane compressor with a fixed-vane," *International Journal of Refrigeration*, vol. 34, no. 8, pp. 1980–1988, 2011. DOI: https://doi.org/10.1016/j.ijrefrig.2011.06.010.

[44] Y. Teh, K. Ooi, and D. W. Djamari, "Theoretical study of a novel refrigeration compressor – Part II: Performance of a rotating discharge valve in the revolving vane (RV) compressor," *International Journal of Refrigeration*, vol. 32, no. 5, pp. 1103–1111, 2009. DOI: https://doi.org/10.1016/j.ijrefrig.2008.09.007.

[45] K. R. Heng, K. T. Ooi, and W. K. Chan, "Performance of a non-uniform width rotating discharge valve in the revolving vane (RV) compressor," *IIR International congress of refrigeration*. Manuscript 347, (2019). [Online]. Available: https://cm.icr2019.org/webapp/bio/1100.

[46] K.-K. Ha, C. H. Lee, C. M. Kim, S. H. Kim, and B. K. Ahn, "A Study on the Characteristics of an Oil-Free Centrifugal Compressor for Fuel Cell Vehicles," *SAE International Journal of Alternative Powertrains*, vol. 5, no. 1, pp. 167–174, 2016. DOI: https://doi.org/10.4271/2016-01-1184.

[47] Danfoss Turbocor, *Making a world of difference - Danfoss Turbocor oil-free centrifugal compressors for air-conditioning systems*, Brochure, 2018. [Online]. Available: https://assets.danfoss.com/documents/DOC272566793555/DOC272566793555.pdf.

[48] S. Shimao Ni and D. K. Cai, ‘‘Oil-Free “Floating Scroll” Compressor,’’ *International Compressor Engineering Conference*. Paper 1599, (2002). [Online]. Available: https://docs.lib.purdue.edu/icec/1599/.

[49] S. Ni, ‘‘‘‘Floating Scroll” Technology for Fuel Cell Air Management System,’’ 2003. DOI: https://doi.org/10.1115/FUELCELL2003-1748.

[50] Y. N. He, L. F. Xing, Y. Q. Zhang, J. Zhang, F. Cao, and Z. W. Xing, ‘‘Development and experimental investigation of an oil-free twin-screw air compressor for fuel cell systems,’’ *Applied Thermal Engineering*, vol. 145, pp. 755–762, 2018. DOI: https://doi.org/10.1016/j.applthermaleng.2018.09.064.

[51] K. Kitagawa, Y. Hirao, Y. Yanagi, and Y. Ikeda, ‘‘Development of Helium Oil Free Screw Compressor,’’ in *Proceedings of the Sixteenth International Cryogenic Engineering Conference/International Cryogenic Materials Conference*, Elsevier, 1997, pp. 211–214. DOI: https://doi.org/10.1016/B978-008042688-4/50049-1.

[52] K. Liang, ‘‘A review of linear compressors for refrigeration,’’ *International Journal of Refrigeration*, vol. 84, pp. 253–273, 2017. DOI: 10.1016/j.ijrefrig.2017.08.015.

[53] ——, ‘‘Analysis of oil-free linear compressor operated at high pressure ratios for household refrigeration,’’ *Energy*, vol. 151, pp. 324–331, 2018. DOI: 10.1016/j.energy.2018.03.068.

[54] K. Liang, R. Stone, M. Dadd, and P. Bailey, ‘‘A novel linear electromagnetic-drive oil-free refrigeration compressor using R134a,’’ *International Journal of Refrigeration*, vol. 40, pp. 450–459, 2014. DOI: 10.1016/j.ijrefrig.2013.11.027.

[55] A. Jomde, A. Anderson, V. Bhojwani, S. Kedia, N. Jangale, K. Kolas, and P. Khedkar, ‘‘Modeling and measurement of a moving coil oil-free linear compressor performance for refrigeration application using R134a,’’ *International Journal of Refrigeration*, vol. 88, pp. 182–194, 2018. DOI: 10.1016/j.ijrefrig.2018.01.002.

[56] Z. H. Li, K. Liang, and H. Y. Jiang, ‘‘Thermodynamic analysis of linear compressor using R1234yf,’’ *International Journal of Refrigeration*, vol. 104, pp. 530–539, 2019. DOI: 10.1016/j.ijrefrig.2019.05.001.

[57] Z. H. Li, H. Y. Jiang, X. W. Chen, and K. Liang, ‘‘Optimal refrigerant charge and energy efficiency of an oil-free refrigeration system using R134a,’’ *Applied Thermal Engineering*, vol. 164, p. 114 473, 2020. DOI: 10.1016/j.applthermaleng.2019.114473.

[58] C. Z. Li, J. G. Li, L. F. Tang, J. Sun, H. M. Zou, and J. H. Cai, ''Effects of the driving voltage waveform on the performance of vapor compression cycle system driven by the moving coil oil-free linear compressor,'' *International Journal of Refrigeration*, vol. 108, pp. 200–208, 2019. DOI: 10.1016/j.ijrefrig.2019.08.036.

[59] H. K. Lee, G. Y. Song, J. S. Park, E. P. Hong, and W. H. Jung, ''Development of the Linear Compressor for a Household Refrigerator,'' *International Compressor Engineering Conference*. Paper 1364, (2000). [Online]. Available: https://docs.lib.purdue.edu/icec/1364.

[60] H. K. Lee, S. S. Jeong, C. W. Lee, and H. K. Lee, ''Linear Compressor for Air-Conditioner,'' *International Compressor Engineering Conference*. Paper 1667, (2004). [Online]. Available: https://docs.lib.purdue.edu/icec/1667.

[61] K. T. Ooi, ''International Conference on Compressors and Their Systems 2005,'' in. Chichester: Wiley, 2005, ch. The effects of liquid injection on performance of a rotary compressor, pp. 151–161, ISBN: 978-0-470-02576-5.

[62] A. K. Dutta, T. Yanagisawa, and M. Fukuta, ''An investigation of the performance of a scroll compressor under liquid refrigerant injection,'' *International Journal of Refrigeration*, vol. 24, no. 6, pp. 577–587, 2001. DOI: https://doi.org/10.1016/S0140-7007(00)00041-4.

[63] H. Yamazaki, T. Itoh, K. Sato, H. Kobayashi, and M. Kawada, ''High performance scroll compressor with liquid refrigerant injection,'' *International Compressor Engineering Conference*. Paper 1596, (2002). [Online]. Available: https://docs.lib.purdue.edu/icec/1596/.

[64] I. Tosun, ''Evaluation of Transfer Coefficients: Engineering Correlations,'' in *Modeling in Transport Phenomena*, Elsevier, 2007, pp. 59–115. DOI: 10.1016/b978-044453021-9/50005-1.

[65] K. G. Mclaren and D. Tabor, ''Visco-Elastic Properties and the Friction of Solids: Friction of Polymers: Influence of Speed and Temperature,'' *Nature*, vol. 197, no. 4870, pp. 856–858, 1963. DOI: 10.1038/197856a0.

[66] S. Biswas and K. Vijayan, ''Friction and wear of PTFE — a review,'' *Wear*, vol. 158, no. 1-2, pp. 193–211, 1992. DOI: 10.1016/0043-1648(92)90039-b.

[67] J. Ye, H. Khare, and D. Burris, ''Transfer film evolution and its role in promoting ultra-low wear of a PTFE nanocomposite,'' *Wear*, vol. 297, no. 1-2, pp. 1095–1102, 2013. DOI: 10.1016/j.wear.2012.12.002.

[68] M. Conte, B. Pinedo, and A. Igartua, ''Role of crystallinity on wear behavior of PTFE composites,'' *Wear*, vol. 307, no. 1-2, pp. 81–86, 2013. DOI: 10.1016/j.wear.2013.08.019.

[69] K. Tanaka, Y. Uchiyama, and S. Toyooka, "The mechanism of wear of polytetrafluoroethylene," *Wear*, vol. 23, no. 2, pp. 153–172, 1973. DOI: 10.1016/0043-1648(73)90081-1.

[70] S. Wang and B. Cao, "Torsion Tribological Behavior of Polytetrafluoroethylene Composites under Dynamic Normal Load: Effect of Dynamic Normal Load Amplitude," *Tribology Transactions*, vol. 59, no. 3, pp. 462–468, 2016. DOI: 10.1080/10402004.2015.1086934.

[71] S. Bahadur and D. Tabor, "The wear of filled polytetrafluoroethylene," *Wear*, vol. 98, pp. 1–13, 1984. DOI: 10.1016/0043-1648(84)90213-8.

[72] B. Briscoe, M. Steward, and A. Groszek, "The effect of carbon aspect ratio on the friction and wear of PTFE," *Wear*, vol. 42, no. 1, pp. 99–107, 1977. DOI: 10.1016/0043-1648(77)90171-5.

[73] A. Schelling, H. Kausch, and A. Roulin, "Friction behaviour of polyetheretherketone under dry reciprocating movement," *Wear*, vol. 151, no. 1, pp. 129–142, 1991. DOI: 10.1016/0043-1648(91)90353-v.

[74] Y. P. Khanna, "The melting temperature of polytetrafluoroethylene," *Journal of Materials Science Letters*, vol. 7, no. 8, pp. 817–818, 1988. DOI: 10.1007/bf00723770.

[75] Vanderveer Industrial Plastics, *Technical Datasheet for Teflon (Polytetrafluoroethylene)*, Vanderveer Industrial Plastics, 515 South Melrose Street Placentia, CA 92870. [Online]. Available: https://www.vanderveerplastics.com/assets/docs/Technical-Date-Sheets-PEEK-Revised.pdf?r=false.

[76] D. Puhan and J. S. Wong, "Properties of Polyetheretherketone (PEEK) transferred materials in a PEEK-steel contact," *Tribology International*, vol. 135, pp. 189–199, 2019. DOI: 10.1016/j.triboint.2019.02.028.

[77] Vanderveer Industrial Plastics, *Technical Datasheet for Polyetheretherketone (PEEK)*, Vanderveer Industrial Plastics, 515 South Melrose Street Placentia, CA 92870. [Online]. Available: https://www.vanderveerplastics.com/assets/docs/Technical-Date-Sheets-PEEK-Revised.pdf?r=false.

[78] H. Voss and K. Friedrich, "On the wear behaviour of short-fibre-reinforced peek composites," *Wear*, vol. 116, no. 1, pp. 1–18, 1987. DOI: 10.1016/0043-1648(87)90262-6.

[79] B. Briscoe, L. H. Yao, and T. Stolarski, "The friction and wear of poly(tetrafluoroethylene)-poly (etheretherketone) composites: An initial appraisal of the optimum composition," *Wear*, vol. 108, no. 4, pp. 357–374, 1986. DOI: 10.1016/0043-1648(86)90013-x.

[80] theplasticshop.co.uk, *Technical Datasheet for Nylon 66 Rod, Sheet & Tube*, (2011). [Online]. Available: https://www.theplasticshop.co.uk/plastic_technical_data_sheets/nylon_66_technical_data_sheet.pdf.

[81] H. Czichos, ''Influence of adhesive and abrasive mechanisms on the tribological behaviour of thermoplastic polymers,'' *Wear*, vol. 88, no. 1, pp. 27–43, 1983. DOI: 10.1016/0043-1648(83)90310-1.

[82] J. Byett and C. Allen, ''Dry sliding wear behaviour of polyamide 66 and polycarbonate composites,'' *Tribology International*, vol. 25, no. 4, pp. 237–246, 1992. DOI: 10.1016/0301-679x(92)90061-q.

[83] S. Alam, R. Marshall, and S. Sasaki, ''Metallurgical and tribological investigations of aluminium bronze bushes made by a novel centrifugal casting technique,'' *Tribology International*, vol. 29, no. 6, pp. 487–492, 1996. DOI: 10.1016/0301-679x(95)00108-g.

[84] V. K. Sharma, R. Singh, and R. Chaudhary, ''Experimental Study of Tribological Behavior of Casted Aluminium-Bronze,'' *Materials Today: Proceedings*, vol. 5, no. 14, pp. 28 008–28 017, 2018. DOI: 10.1016/j.matpr.2018.10.041.

[85] S. A. Ajeel, R. S. Yaseen, and A. Keqal, ''The Behavior of Dry Sliding Wear for Aluminium Bronze Alloy Reinforced by Al2O3 and TiO2 Nanoparticles,'' *IOP Conference Series: Materials Science and Engineering*, vol. 518, p. 032 045, 2019. DOI: 10.1088/1757-899x/518/3/032045. [Online]. Available: https://doi.org/10.1088%2F1757-899x%2F518%2F3%2F032045.

[86] D. Sımsek, N. Y. Colak, I. Sımsek, and D. Ozyurek, ''Dry Sliding Wear Behaviors of Iron Addition to Nickel–Aluminum Bronze Produced by Mechanical Alloying,'' *Transactions of the Indian Institute of Metals*, vol. 73, no. 2, pp. 319–326, 2019. DOI: 10.1007/s12666-019-01837-3.

[87] S. Tjong and K. Lau, ''Tribological behaviour of SiC particle-reinforced copper matrix composites,'' *Materials Letters*, vol. 43, no. 5-6, pp. 274–280, 2000. DOI: 10.1016/s0167-577x(99)00273-6.

[88] W. Zhai, W. Lu, P. Zhang, M. Zhou, X. Liu, and L. Zhou, ''Microstructure, mechanical and tribological properties of nickel-aluminium bronze alloys developed via gas-atomization and spark plasma sintering,'' *Materials Science and Engineering: A*, vol. 707, pp. 325–336, 2017. DOI: 10.1016/j.msea.2017.09.047.

[89] R. Bayer, *Mechanical Wear Fundamentals and Testing*, ser. Mechanical engineering (Marcel Dekker, Inc.), 172. Marcel Dekker, New York, (2004).

[90] B. Gavtash, H. K. Versteeg, G. Hargrave, B. Myatt, D. Lewis, T. Church, and G. Brambilla, "Transient flashing propellant flow models to predict internal flow characteristics, spray velocity, and aerosol droplet size of a pMDI," *Aerosol Science and Technology*, vol. 51, no. 5, pp. 564–575, 2017. DOI: https://doi.org/10.1080/02786826.2017.1282151.

[91] ——, "Transient aerodynamic atomization model to predict aerosol droplet size of pressurized metered dose inhalers (pMDI)," *Aerosol Science and Technology*, vol. 51, no. 8, pp. 998–1008, 2017. DOI: 10.1080/02786826.2017.1327121. eprint: https://doi.org/10.1080/02786826.2017.1327121. [Online]. Available: https://doi.org/10.1080/02786826.2017.1327121.

[92] ——, "A model of transient internal flow and atomization of propellant/ethanol mixtures in pressurized metered dose inhalers (pMDI)," *Aerosol Science and Technology*, vol. 52, no. 5, pp. 494–504, 2018. DOI: 10.1080/02786826.2018.1433814. eprint: https://doi.org/10.1080/02786826.2018.1433814. [Online]. Available: https://doi.org/10.1080/02786826.2018.1433814.

[93] B. Myatt, D. Lewis, T. Church, G. Brambilla, G. K. Hargrave, H. K. Versteeg, E. J. Long, and B. Gavtash, "PDA Analysis of HFA/Ethanol pMDI Aerosols: An Improved Test Protocol and New Findings," *ICLASS 2015, 13th Triennial International Conference on Liquid Atomization and Spray Systems*, (2015).

[94] B. Myatt, R. Newton, D. Lewis, T. Church, G. Brambilla, G. K. Hargrave, H. K. Versteeg, B. Gavtash, and E. J. Long, "PDA and High Speed Image Analysis Of HFA/Ethanol pMDI Aerosols: New Findings," *Ddl 26*, (2015), pp. 73–77.

[95] Y. Chen, N. P. Halm, E. A. Groll, and J. E. Braun, "Mathematical modeling of scroll compressors—part I: compression process modeling," *International Journal of Refrigeration*, vol. 25, no. 6, pp. 731–750, 2002. DOI: 10.1016/s0140-7007(01)00071-8.

[96] P. N. Pandeya and W. Soedel, "Rolling Piston Type Rotary Compressors with Special Attention to Friction and Leakage," *International Compressor Engineering Conference*. Paper 268., (1978). [Online]. Available: https://docs.lib.purdue.edu/icec/268/.

[97] T Yanagisawa and T Shimizu, "Leakage losses with a rolling piston type rotary compressor. I. Radical clearance on the rolling piston," *International Journal of Refrigeration*, vol. 8, no. 2, pp. 75–84, 1985. DOI: 10.1016/0140-7007(85)90077-5.

[98] N. K. Cho, Y. Youn, B. C. Lee, and M. K. Min, "The Characteristics of Tangential Leakage in Scroll Compressors for Air-Conditioners," *International Compressor Engineering Conference*. Paper 1466., (2000). [Online]. Available: https://docs.lib.purdue.edu/icec/1466/.

[99] G. W. Kim, K. Y. Noh, B. C. Min, S. J. Song, and S. K. Na, ''Prediction of Leakage Flow of Radial Clearance in a Rolling Piston Rotary Compressor,'' *International Compressor Engineering Conference*. Paper 2493., (2016). [Online]. Available: https://docs.lib.purdue.edu/icec/2493.

[100] G. Kim, B. Min, S. Na, G. Choi, and D. Kim, ''Estimation of leakage through radial clearance during compression process of a rolling piston rotary compressor,'' *Journal of Mechanical Science and Technology*, vol. 31, no. 12, pp. 6033–6040, 2017. DOI: 10.1007/s12206-017-1147-4.

[101] E. Silva, M. F. Nicoluzzi, M. Rojas-Cardenas, and C. J. Deschamps, ''Analysis of Viscous Slip at the Wall in Gas Flows of R134a and R600a through Metallic Microtubes,'' *International Compressor Engineering Conference*. Paper 2459., (2016). [Online]. Available: https://docs.lib.purdue.edu/icec/2459/.

[102] X. Guo, C. Huang, A. Alexeenko, and J. Sullivan, ''Numerical and experimental study of gas flows in 2D and 3D microchannels,'' *Journal of Micromechanics and Microengineering*, vol. 18, no. 2, p. 025 034, 2008. DOI: 10.1088/0960-1317/18/2/025034.

[103] M. J. McNenly, M. A. Gallis, and I. D. Boyd, ''Empirical slip and viscosity model performance for microscale gas flow,'' *International Journal for Numerical Methods in Fluids*, vol. 49, no. 11, pp. 1169–1191, 2005. DOI: 10.1002/fld.1012.

[104] K. T. Ooi and K. K. Phua, ''Effects of Materials on Temperature Distribution of a Compressor,'' *International Compressor Engineering Conference*. Paper 1352., (1998). [Online]. Available: https://docs.lib.purdue.edu/icec/1352/.

[105] R. P. Adair, E. B. Qvale, and J. T. Pearson, ''Instantaneous Heat Transfer to the Cylinder Wall in Reciprocating Compressors,'' *International Compressor Engineering Conference*. Paper 45., (1972). [Online]. Available: https://docs.lib.purdue.edu/icec/45/.

[106] G. Woschni, ''A Universally Applicable Equation for the Instantaneous Heat Transfer Coefficient in the Internal Combustion Engine,'' in *SAE Technical Paper Series*, SAE International, 1967. DOI: 10.4271/670931.

[107] W. J. D. Annand, ''Heat Transfer in the Cylinders of Reciprocating Internal Combustion Engines,'' *Proceedings of the Institution of Mechanical Engineers*, vol. 177, no. 1, pp. 973–996, 1963. DOI: 10.1243/pime_proc_1963_177_069_02.

[108] T. Lefeuvre, P. S. Myers, and O. A. Uyehara, ''Experimental Instantaneous Heat Fluxes in a Diesel Engine and Their Correlation,'' 1969.

[109] R. Liu and Z. Zhou, "Heat Transfer Between Gas and Cylinder Wall of Refrigerating Reciprocating Compressor," *International Compressor Engineering Conference*. Paper 441., (1984). [Online]. Available: https://docs.lib.purdue.edu/icec/441/.

[110] K. Tan and K. Ooi, "Heat transfer in compression chamber of a revolving vane (RV) compressor," *Applied Thermal Engineering*, vol. 31, no. 8-9, pp. 1519–1526, 2011. DOI: 10.1016/j.applthermaleng.2011.01.041.

[111] F. Fagotti, M. L. Todescat, R. T. S. Ferreira, and A. T. Prata, "Heat Transfer Modeling in a Reciprocating Compressor," *International Compressor Engineering Conference*. Paper 1043., (1994). [Online]. Available: https://docs.lib.purdue.edu/icec/1043/.

[112] S. W. Brok, S. Touber, and J. S. Van der Meer, "Modeling of Cylinder Heat Transfer - Large Effort, Little Effect?," *International Compressor Engineering Conference*. Paper 305., (1980). [Online]. Available: https://docs.lib.purdue.edu/icec/305.

[113] J. F. Hamilton and W. Ray, *Extensions of Mathematical Modeling of Positive Displacement Type Compressors*. West Lafayette, IN : Purdue University School of Mechanical Engineering Ray W. Herrick Laboratories, 1974.

[114] J. Polman, "Heat transfer in a piston cylinder system," *International Journal of Heat and Mass Transfer*, vol. 24, no. 1, pp. 184–187, 1981. DOI: 10.1016/0017-9310(81)90108-3.

[115] J. Tuhovcak, J. Hejcik, and M. Jicha, "Comparison of heat transfer models for reciprocating compressor," *Applied Thermal Engineering*, vol. 103, pp. 607–615, 2016. DOI: 10.1016/j.applthermaleng.2016.04.120.

[116] F. P. Disconzi, C. J. Deschamps, and E. L. L. Pereira, "Development of an In-Cylinder Heat Transfer Correlation for Reciprocating Compressors," *International Compressor Engineering Conference*. Paper 2103., (2012). [Online]. Available: https://docs.lib.purdue.edu/icec/2103/.

[117] R. Aigner and H. Steinruck, "Modelling Fluid Dynamic, Heat Transfer and Valve Dynamics in Reciprocating Compressor," *5th Conference of the EFRC*, Prague, Czech Republic, (2007).

[118] E. L. L. Pereira, C. J. Deschamps, and F. A. Ribas, "Numerical Analysis of Heat Transfer inside the Cylinder of Reciprocating Compressors in the Presence of Suction and Discharge Processes," *International Compressor Engineering Conference*. Paper 1995., (2010). [Online]. Available: https://docs.lib.purdue.edu/icec/1995/.

[119] B. Launder and D. Spalding, "The numerical computation of turbulent flows," *Computer Methods in Applied Mechanics and Engineering*, vol. 3, no. 2, pp. 269–289, 1974. DOI: 10.1016/0045-7825(74)90029-2.

[120] S. K. Padhy and S. N. Dwivedi, ''Heat transfer analysis of a rolling-piston rotary compressor,'' *International Journal of Refrigeration*, vol. 17, no. 6, pp. 400–410, 1994. DOI: 10.1016/0140-7007(94)90075-2.

[121] K. T. Ooi, ''Heat transfer study of a hermetic refrigeration compressor,'' *Applied Thermal Engineering*, vol. 23, no. 15, pp. 1931–1945, 2003. DOI: 10.1016/s1359-4311(03)00150-9.

[122] Q. Wang, ''Seizure failure of journal-bearing conformal contacts,'' *Wear*, vol. 210, no. 1-2, pp. 8–16, 1997. DOI: 10.1016/s0043-1648(97)00064-1.

[123] I. Corni, N. Neumann, D. Eifler, and A. Boccaccini, ''Polyetheretherketone (PEEK) Coatings on Stainless Steel by Electrophoretic Deposition,'' *Advanced Engineering Materials*, vol. 10, no. 6, pp. 559–564, 2008. DOI: 10.1002/adem.200800010.

[124] G. H. Junker, ''New Criteria for Self-Loosening of Fasteners Under Vibration,'' *SAE Transactions*, vol. 78, pp. 314–335, 1969, ISSN: 0096736X, 25771531. [Online]. Available: http://www.jstor.org/stable/44563013.

[125] J. A. F. Grandt, ''Materials Degradation and Fatique in Aerospace Structures,'' Purdue University, School of Aerospace of Aeronuatics and Astronuatics, Tech. Rep., (1997).

[126] D. Dunn, ''Update on Engineering and Structural Adhesives,'' in *Update on Engineering and Structural Adhesives*. Shrewsbury, U.K: ISmithers, 2010, ch. Chapter 5: Durability of Adhesively Bonded Structures, pp. 137–154, ISBN: 978-1-84735-480-8.

[127] H. Park, S.-J. Kim, J. Lee, J. H. Kim, and D. Kim, ''Delamination behavior analysis of steel/polymer/steel high-strength laminated sheets in a V-die bending test,'' *International Journal of Mechanical Sciences*, vol. 173, p. 105 430, 2020. DOI: 10.1016/j.ijmecsci.2020.105430.

[128] K. Ooi and T. Wong, ''A computer simulation of a rotary compressor for household refrigerators,'' *Applied Thermal Engineering*, vol. 17, no. 1, pp. 65–78, 1997. DOI: 10.1016/1359-4311(96)00013-0.

[129] A. Subiantoro and K. T. Ooi, ''Introduction of the Revolving Vane Expander,'' *HVAC&R Research*, vol. 15, no. 4, pp. 801–816, 2009. DOI: 10.1080/10789669.2009.10390865.

[130] K. S. Yap, K. T. Ooi, and A. Chakraborty, ''Analysis of the novel cross vane expander-compressor: Mathematical modelling and experimental study,'' *Energy*, vol. 145, pp. 626–637, 2018. DOI: 10.1016/j.energy.2017.12.097.

[131] P. Shakya and K. T. Ooi, ''Introduction to Coupled Vane compressor: Mathematical modelling with validation,'' *International Journal of Refrigeration*, vol. 117, pp. 23–32, 2020. DOI: 10.1016/j.ijrefrig.2020.01.027.

[132] Y. D. Lim and K. T. Ooi, "Performance analysis of a U-Vane compressor," *Applied Thermal Engineering*, vol. 178, p. 115 570, 2020. DOI: 10.1016/j.applthermaleng.2020.115570.

[133] M. J. Moran and H. N. Shapiro, *Fundamentals of Engineering Thermodynamics: SI version*. Chichester: John Wiley, (1998).

[134] S. C. Chapra and R. P. Canale, *Numerical Methods for Engineers*, 6th ed. Mcgraw-Hill Higher Education, 2010.

[135] E. Lemmon and M. Huber, *NIST Reference Fluid Thermodynamic and Transport Properties Database (REFPROP): Version 9.1*, 2010.

[136] Y. A.Cengel and M. A. Boles, *Thermodynamics: An Engineering Approach*, 7th ed. Mcgraw-Hill Higher Education, 2011.

[137] M. Potter, *Mechanics of Fluids*. Stamford, CT: Cengage Learning, 2012, ISBN: 9780495667735.

[138] K. Nilpueng and S. Wongwises, "Experimental investigation of two-phase flow characteristics of HFC-134a through short-tube orifices," *International Journal of Refrigeration*, vol. 32, no. 5, pp. 854–864, 2009. DOI: 10.1016/j.ijrefrig.2008.12.003.

[139] K. Nilpueng, C. Supavarasuwat, and S. Wongwises, "Flow pattern, mass flow rate, pressure distribution, and temperature distribution of two-phase flow of HFC-134a inside short-tube orifices," *International Journal of Refrigeration*, vol. 32, no. 8, pp. 1864–1875, 2009. DOI: 10.1016/j.ijrefrig.2009.08.002.

[140] L. Meirovitch, *Fundamentals of Vibrations*, International Edition 2001. Boston: McGraw-Hill, 2001, ISBN: 0070413452.

[141] L. F. Moody, "Friction Factors for Pipe Flow," *Journal of Mechanical Design - Transactions of the ASME*, vol. vol. 66. 1944.

[142] L. Y. Lim, *Investigation of leakage flow in compressor clearances*, 2020. [Online]. Available: https://hdl.handle.net/10356/141487.

[143] T Yanagisawa and T Shimizu, "Leakage losses with a rolling piston type rotary compressor. II. Leakage losses through clearances on rolling piston faces," *International Journal of Refrigeration*, vol. 8, no. 3, pp. 152–158, 1985. DOI: https://doi.org/10.1016/0140-7007(85)90155-0.

[144] C. F. Costa, R. T. S. Ferreira, and A. T. Prata, "Considerations About the Leakage Through theMinimal Clearance in a Rolling Piston Compressor," *International Compressor Engineering Conference*. Paper 780., (1990). [Online]. Available: https://docs.lib.purdue.edu/icec/780.

[145] F. Kreith, *Principles of Heat Transfer*. Stamford, CT Singapore: Cengage Learning, 2011, ISBN: 9780495667704.

[146] J. P. Holman, *Heat Transfer*. Boston Mass: McGraw Hill Higher Education, 2010, ISBN: 9780073529363.

[147] L. Burmeister, *Convective Heat Transfer*. John Wiley & Sons, Inc., Sep. 10, 1993, 640 pp., ISBN: 047157709X. [Online]. Available: https://www.ebook.de/de/product/3602720/louis_burmeister_convective_heat_transfer.html.

[148] F. Incropera, *Fundamentals of Heat and Mass Transfer*. Hoboken, NJ: John Wiley, 2007, ISBN: 9780471457282.

[149] P. Chantrenne and M. Raynaud, "A microscopic thermal model for dry sliding contact," *International Journal of Heat and Mass Transfer*, vol. 40, no. 5, pp. 1083–1094, 1997. DOI: https://doi.org/10.1016/0017-9310(96)00152-4.

[150] P. Chantrenne and M. Raynaud, "Study of a macroscopic sliding contact thermal model from microscopic models," *International Journal of Thermal Sciences*, vol. 40, no. 7, pp. 603–621, 2001. DOI: https://doi.org/10.1016/S1290-0729(01)01251-0.

[151] Y. Waddad, V. Magnier, P. Dufrénoy, and G. D. Saxcé, "Heat partition and surface temperature in sliding contact systems of rough surfaces," *International Journal of Heat and Mass Transfer*, vol. 137, pp. 1167–1182, 2019. DOI: https://doi.org/10.1016/j.ijheatmasstransfer.2019.04.015.

[152] J. P. Bardon, "Bases physiques des conditions de contactthermique imparfait entre milieu en glissement relatif," *Revue Generale de Thermique*, pp. 85–92, 1994.

[153] K. C. John, *Textbook of Machine Drawing*. New Delhi: PHI Learning, 2009, ISBN: 9788120337213.

[154] AKSteel, *17-4ph Stainless Steel Product Data*, AKSteel, Dec. (2016). [Online]. Available: https://www.aksteel.com/sites/default/files/2018-01/174ph201706.pdf.

[155] G. Alloys, *Product Data of C95500 Nickel-Aluminum Bronze*, 14315 State Route 113, Wakeman, OH 44889. [Online]. Available: https://www.concast.com/files/C95500.pdf.

[156] Copper Alloys Ltd., *Material Properties of ASTM B 505 C95500 Aluminium Bronze*, Online Website. [Online]. Available: https://www.copperalloys.net/alloys/astm-b-505-c95500?gclid=CjwKCAjwztL2\/BRATEiwAvnALcgPNKlNO-Ix1a8af1JUHC2DhBeB3RTQvZGq36ULFQPwsXYiW9\/UCg2BoCqLEQAvD_BwE.

[157] E. Group, *Product Data of TECAPEEK PVX black*, Ensinger Group, Feb. (2018). [Online]. Available: https://www.ensingerplastics.com/en-sg/shapes/products/peek-tecapeek-pvx-black.

[158] L. He and T. C. Ovaert, "Heat Partitioning Coefficient Calculations for Sliding Contacts with Friction," *Tribology Transactions*, vol. 51, no. 1, pp. 12–18, 2008. DOI: 10.1080/10402000701739248.

[159] Danfoss Turbocor, *Danfoss scrolls, H-Series Residential and light commercial*, Online Website, 2016. [Online]. Available: https://assets.danfoss.com/documents/DOC159886428252/DOC159886428252.pdf.

[160] A. M. Supplies, *Data sheet for 17-4PH Stainless Steel*, Advance Materials Supplies. [Online]. Available: http://www.advancematerials.com.sg/wp-content/uploads/2017/06/Alloy-17-4PH.pdf.

[161] RSPRO, *Datasheet of RS Pro Beige Polyetheretherketone (PEEK) Rod*, RSPRO. [Online]. Available: https://docs.rs-online.com/346a/0900766b8157f668.pdf.

[162] Ban Soon Cheong Pte Ltd., *Product Data of Aluminium Nickel Bronze Rod AB2, C95500*, Online Website, 2020. [Online]. Available: http://www.copper.sg/products/Bronze-\&-Bronze-alloys/Nickel-Aluminium-Bronze,-Aluminium-Nickel-Bronze-\&-Aluminium-Bronze/Nickel-Aluminium-Bronze-Rod-AB2,-C95500-\&-C95810.

[163] *Datasheet of Aluminium Alloys*, Lian Cheong Hardware Pte Ltd., 2020. [Online]. Available: http://www.liancheong.com/UploadedImg/files/20032017_24826_PM_aluminium.pdf.

[164] RSPRO, *Datasheet of RS Pro Cast Nylon 6*, RSPRO. [Online]. Available: https://docs.rs-online.com/269a/0900766b815803a8.pdf.

[165] ——, *Datasheet of RS Pro PTFE*, RSPRO. [Online]. Available: https://docs.rs-online.com/bac9/0900766b81677682.pdf.

[166] ASM Aerospace Specification Metals Inc., *Product Data of AISI Type 304L Stainless Steel*, Online Website. [Online]. Available: http://asm.matweb.com/search/SpecificMaterial.asp?bassnum=MQ304L.

[167] X. C. Hu and H. H. Yang, "Polyamide and Polyester Fibers," in *Comprehensive Composite Materials*, Elsevier, 2000, pp. 327–344. DOI: 10.1016/b0-08-042993-9/00060-7.

[168] Laminated Plastics, *Technical Data Sheet of Teflon (PTFE)*, Laminated Plastics. [Online]. Available: https://laminatedplastics.com/teflon.pdf.

[169] Sterling Plastics Inc., *Product Datasheet for PEEK (POLYETHERETHERKETONE) – 30Glass Filled*, Online website, (2012). [Online]. Available: http://sterlingplasticsinc.com/materials/peek-polyetheretherketone-30-glass-filled/.

[170] "Temper Colors for Steels," in *Heat Treating of Irons and Steels*, ASM International, 2014, pp. 550–551. DOI: 10.31399/asm.hb.v04d.a0005997.

[171] *Heat Treating Data Book*, 10th ed. SECO/Warwick Corporation, 2011. [Online]. Available: https://www.secowarwick.com/wp-content/uploads/2017/03/HeatTreatingDataEBook.2011.pdf.

[172] OMEGA Engineering Inc., *Thermocouple types*, Online website, Apr. (2019). [Online]. Available: https://www.omega.com/en-us/resources/thermocouple-types.

[173] AHRI, *2015 Standard for Performance Rating of Positive Displacement Refrigerant Compressors and Compressor Units*, Air-Conditioning, Heating, and Refrigeration Institute, 2015. [Online]. Available: http://www.ahrinet.org/App_Content/ahri/files/STANDARDS/AHRI/AHRI_Standard_540_I-P_and_SI_2015.pdf.

[174] A. Kovalchenko, P. Blau, J. Qu, and S. Danyluk, "Scuffing tendencies of different metals against copper under non-lubricated conditions," *Wear*, vol. 271, no. 11-12, pp. 2998–3006, 2011. DOI: 10.1016/j.wear.2011.06.009.

[175] I. Boromei, L. Ceschini, C. Martini, and R. Sola, "Aluminium bronze-steel sliding contact in packaging applications: Failure analysis and lab-scale tribological tests," *Engineering Failure Analysis*, vol. 112, p. 104 528, 2020. DOI: 10.1016/j.engfailanal.2020.104528.

[176] D. Fuller, *Theory and Practice of Lubrication for Engineers*. Wiley, 1956.

[177] H. K. Müller and B. S. Nau, *Fluid Sealing Technology*. Routledge, 2019. DOI: 10.1201/9780203755716.

[178] P. S. Bimbhra, *Electrical Machinery : Theory, Performance and Applications*. New Delhi: Khanna, 2003, ISBN: 8174091734.

[179] ANSYS, Inc., *ANSYS Fluent Theory Guide*, 2019 R2, 2019.

[180] T. H. Shih, W. Liou, A. Shabbir, Z. Yang, and J. Zhu, "A New eddy-viscosity model for high Reynolds number turbulent flows: model development and validation," *Computers Fluids*, vol. 24, pp. 227–238, (1995).

[181] ANSYS, Inc., *ANSYS Fluent User's Guide*, Releaser 15.0, 2013.

[182] S. Hayashi, T. Matsui, and T. Ito, "Study of Flow and Thrust in Nozzle-Flapper Valves," *Journal of Fluids Engineering*, vol. 97, no. 1, pp. 39–50, 1975. DOI: 10.1115/1.3447213.

[183] J. Rigola, O. Lekmuhl, C. D. Perez-Segarra, and A. Oliva, "Numerical Simulation of Fluid Flow Through Valve Reeds Based on Large Eddy Simulation Models (LES)," *International Compressor Engineering Conference*. Paper 1917., (2008). [Online]. Available: https://docs.lib.purdue.edu/icec/1917/.

[184] T. S. Ferreira and J. Lainor, "Analysis of the Influence of Valve Geometric Parameters on the Effective Flow and Force Areas," *International Compressor Engineering Conference*. Paper 558., (1986). [Online]. Available: https://docs.lib.purdue.edu/icec/558/.

[185] C. J. Deschamps, R. T. S. Ferreira, and A. T. Prata, "Turbulent Flow Through Valves of Reciprocating Compressors," *International Compressor Engineering Conference*. Paper 1135., (1996). [Online]. Available: https://docs.lib.purdue.edu/icec/1135/.

[186] R. L. Ferreira and J. L. Gasche, "Effective force area and discharge coefficient for reed type valves: A comprehensive data set from a numerical study," *International Journal of Refrigeration*, vol. 103, pp. 287–300, 2019. DOI: 10.1016/j.ijrefrig.2019.04.017.

[187] A. K. Colaciti, L. M. V. López, H. A. Navarro, and L. Cabezas-Gómez, "Numerical simulation of a radial diffuser turbulent airflow," *Applied Mathematics and Computation*, vol. 189, no. 2, pp. 1491–1504, 2007. DOI: 10.1016/j.amc.2006.12.029.

[188] C. J. Deschamps, A. T. Prata, and R. T. S. Ferreira, "Modeling of turbulent flow through radial diffuser," *Journal of the Brazilian Society of Mechanical Sciences*, vol. 22, no. 1, pp. 31–41, 2000. DOI: 10.1590/s0100-73862000000100003.

[189] A. Radcliffe, "The Performance of a Type of Swirl Atomizer," *Proceedings of the Institution of Mechanical Engineers*, vol. 169, no. 1, pp. 93–106, 1955. DOI: 10.1243/pime_proc_1955_169_022_02.

[190] V. G. M. Arthur H. Lefebvre, *Atomization and Sprays*. Taylor & Francis Ltd., Mar. 27, 2017, 300 pp., ISBN: 1498736262. [Online]. Available: https://www.ebook.de/de/product/28789927/arthur_h_lefebvre_vincent_g_mcdonell_atomization_and_sprays.html.

[191] N. Rizk and A. Lefebvre, "Internal flow characteristics of simplex swirl atomizers," *Journal of Propulsion and Power*, vol. 1, no. 3, pp. 193–199, 1985. DOI: 10.2514/3.22780.

[192] D. R. Carlisle, "Communication on the performance of atype of swirl atomizer," *Proceedings of the Institution of Mechanical Engineers*, vol. 169, p. 101, 1955.

[193] G. I. Taylor, "The boundary layer in the converging nozzle of a swirl atomizer," *The Quarterly Journal of Mechanics and Applied Mathematics*, vol. 3, no. 2, pp. 129–139, 1950. DOI: 10.1093/qjmam/3.2.129.

Appendix A

Theoretical Modelling Detailed Derivations

A.1 Additional Geometrical Detailed Derivations

The detailed derivations (based on Figure 4.1) required for the calculation of correctional volume $V_{correc1}, V_{correc2}, V_{correc3}$ are shown in this section.

$$l_{C_1G} = \begin{cases} \sqrt{\left(\frac{w_v}{2}\right)^2 + (r_c + r_{sb})^2 - 2(r_c + r_{sb})\frac{w_v}{2}\cos(\frac{\pi}{2} + |\phi|)} & \phi < 0 \\ \sqrt{\left(\frac{w_v}{2}\right)^2 + (r_c + r_{sb})^2 - 2(r_c + r_{sb})\frac{w_v}{2}\cos(\frac{\pi}{2} - |\phi|)} & \phi \geq 0 \end{cases} \tag{A.1}$$

$$\varepsilon_2 = \cos^{-1}\left(\frac{(r_c + r_{sb})^2 - \left(\frac{w_v}{2}\right)^2 - {l_{C_1G}}^2}{-l_{C_1G} w_v}\right) \tag{A.2}$$

$$\varepsilon_3 = \pi - \sin^{-1}\left(\frac{l_{C_1G}\sin(|\frac{\pi}{2} - \varepsilon_2|)}{r_c}\right) \tag{A.3}$$

$$\varepsilon_4 = \pi - \sin^{-1}\left(\frac{l_{C_1H}\sin(|\frac{\pi}{2} - \varepsilon_1|)}{r_c}\right) \tag{A.4}$$

A.2 Detailed Derivations of Correctional Volumes

The detailed derivations (based on Figure 4.1 and Figure 4.2) of correctional volumes $V_{correc1}, V_{correc2}, V_{correc3}$ which are mentioned in Section 4.2, are shown in this section.

$$Area\ of\ \triangle GC_1C_3 = \begin{cases} \frac{1}{2}(r_c + r_{sb}) l_{C_1G} \sin(\frac{\pi}{2} - \varepsilon_2 - |\phi|) & , \phi < 0 \\ \frac{1}{2}(r_c + r_{sb}) l_{C_1G} \sin(\frac{\pi}{2} - \varepsilon_2 + |\phi|) & , \phi \geq 0 \end{cases} \tag{A.5}$$

$$Area\ of\ \triangle GC_1F = \frac{1}{2} r_c l_{C_1G} \left(-|\frac{\pi}{2} - \varepsilon_2| + \sin^{-1} \left(\frac{l_{C_1G} \sin(|\frac{\pi}{2} - \varepsilon_2|)}{r_c} \right) \right) \tag{A.6}$$

$$Area of sector FC_1J = \begin{cases} \begin{cases} \frac{1}{2} {r_c}^2 \left| -\phi - \sin^{-1} \left(\frac{l_{C_1G} \sin(|\frac{\pi}{2} - \varepsilon_2|)}{r_c} \right) \right| & , \phi < 0 \\ \frac{1}{2} {r_c}^2 \left| \phi - \sin^{-1} \left(\frac{l_{C_1G} \sin(|\frac{\pi}{2} - \varepsilon_2|)}{r_c} \right) \right| & , \phi \geq 0 \end{cases} \\ , (\frac{\pi}{2} - \varepsilon_2) < 0 \\ \begin{cases} \frac{1}{2} {r_c}^2 (-\phi + \sin^{-1} \left(\frac{l_{C_1G} \sin(|\frac{\pi}{2} - \varepsilon_2|)}{r_c} \right)) & , \phi < 0 \\ \frac{1}{2} {r_c}^2 (\phi + \sin^{-1} \left(\frac{l_{C_1G} \sin(|\frac{\pi}{2} - \varepsilon_2|)}{r_c} \right)) & , \phi \geq 0 \end{cases} \\ , (\frac{\pi}{2} - \varepsilon_2) \geq 0 \end{cases} \tag{A.7}$$

$$Area\ of\ \triangle HC_1C_3 = \begin{cases} \frac{1}{2}(r_c + r_{sb}) l_{C_1H} \sin(\frac{\pi}{2} - \varepsilon_2 + |\phi|) & , \phi < 0 \\ \frac{1}{2}(r_c + r_{sb}) l_{C_1H} \sin(\frac{\pi}{2} - \varepsilon_2 - |\phi|) & , \phi \geq 0 \end{cases} \tag{A.8}$$

$$Area\ of \triangle HC_1I = \frac{1}{2} r_c l_{C_1H} \left(-|\frac{\pi}{2} - \varepsilon_2| + \sin^{-1}\left(\frac{l_{C_1H} \sin(|\frac{\pi}{2} - \varepsilon_1|)}{r_c} \right) \right) \quad \text{(A.9)}$$

$$Areaof sector IC_1J = \begin{cases} \begin{cases} \frac{1}{2} {r_c}^2 \left| \phi - \sin^{-1}\left(\frac{l_{C_1H} \sin(|\frac{\pi}{2} - \varepsilon_1|)}{r_c} \right) \right| & , \ \phi < 0 \\ \frac{1}{2} {r_c}^2 \left| -\phi - \sin^{-1}\left(\frac{l_{C_1H} \sin(|\frac{\pi}{2} - \varepsilon_1|)}{r_c} \right) \right| & , \ \phi \geq 0 \end{cases} \\ , \ (\frac{\pi}{2} - \varepsilon_1) < 0 \\ \begin{cases} \frac{1}{2} {r_c}^2 (\phi + \sin^{-1}\left(\frac{l_{C_1H} \sin(|\frac{\pi}{2} - \varepsilon_1|)}{r_c} \right)) & , \ \phi < 0 \\ \frac{1}{2} {r_c}^2 (-\phi + \sin^{-1}\left(\frac{l_{C_1H} \sin(|\frac{\pi}{2} - \varepsilon_1|)}{r_c} \right)) & , \ \phi \geq 0 \end{cases} \\ , \ (\frac{\pi}{2} - \varepsilon_1) \geq 0 \end{cases} \quad \text{(A.10)}$$

$$V_{correc1} = \begin{cases} l_{com}(Area\ of \triangle HC_1C_3 - Area\ of \triangle HC_1I \\ -Area\ of\ sector\ IC_1J) \qquad , \ (\frac{\pi}{2} - \varepsilon_1) < 0 \\ l_{com}(Area\ of \triangle HC_1C_3 + Area\ of \triangle HC_1I \\ -Area\ of\ sector\ IC_1J) \qquad , \ (\frac{\pi}{2} - \varepsilon_1) \geq 0 \end{cases} \quad \text{(A.11)}$$

$$V_{correc2} = l_{com} \left({r_{ro}}^2 \sin^{-1}(\frac{w_v}{2r_{ro}}) - \frac{w_v}{2} \sqrt{{r_{ro}}^2 - \frac{{w_v}^2}{2}} \right) \quad \text{(A.12)}$$

$$V_{correc3} = \begin{cases} l_{com}[w_v \left(l_{C_2C_3} - \sqrt{{r_{ro}}^2 - \frac{{w_v}^2}{2}} \right) - Area\ of \triangle GC_1C_3 \\ + Area\ of \triangle GC_1 + Area\ of\ sector\ FC_1J - V_{correc1}] \quad , (\frac{\pi}{2} - \varepsilon_2) < 0 \\ l_{com}[w_v \left(l_{C_2C_3} - \sqrt{{r_{ro}}^2 - \frac{{w_v}^2}{2}} \right) - Area\ of \triangle GC_1C_3 \\ - Area\ of \triangle GC_1 + Area\ of\ sector\ FC_1J - V_{correc1}] \quad , (\frac{\pi}{2} - \varepsilon_2) \geq 0 \end{cases} \tag{A.13}$$

A.3 Detailed Derivations of Sonic Velocity

Since speed of sound, v_{ss} in a medium is expressed as:

$${v_{ss}}^2 = \left.\frac{dp}{d\rho}\right|_{isentropic} \tag{A.14}$$

for saturated mixture with constant vapour quality q,

$$\frac{1}{{v_{ss}}^2} = \frac{d}{dp}\left(\frac{\rho_{g_{cr}}\rho_f}{q\rho_f + (1-q)\rho_{g_{cr}}}\right) \tag{A.15}$$

Using isentropic gas law $\rho_{g_{cr}} = \left(\frac{p_{cr}}{C}\right)^{\frac{1}{\gamma}}$, $C = Const.$ and assuming $\frac{d\rho_f}{dp} = 0$,

$$\begin{aligned} \frac{1}{{v_{ss}}^2} &= \frac{\frac{\rho_f}{C\gamma}\left(\frac{p_{cr}}{C}\right)^{\frac{1-\gamma}{\gamma}}\left(q\rho_f + (1-q)\rho_{g_{cr}}\right) - (1-q)\left(\frac{p_{cr}}{C}\right)^{\frac{1-\gamma}{\gamma}}\frac{\rho_{g_{cr}}\rho_f}{C\gamma}}{\left(q\rho_f + (1-q)\rho_{g_{cr}}\right)^2} \\ &= \frac{\frac{\rho_{g_{cr}}}{p_{cr}\gamma}\left(q\rho_f + (1-q)\rho_{g_{cr}}\right) - (1-q)\frac{{\rho_{g_{cr}}}^2}{p_{cr}\gamma}}{\left(q\rho_f + (1-q)\rho_{g_{cr}}\right)^2} \\ &= \frac{\rho_{g_{cr}}}{qp_{cr}\gamma\left(1 + \left(\frac{1-q}{q}\right)\frac{\rho_{g_{cr}}}{\rho_f}\right)^2} \\ v_{ss} &= \sqrt{\left(\frac{q\gamma p_{cr}}{\rho_{g_{cr}}}\right)\left(1 + \left(\frac{1-q}{q}\right)\left(\frac{\rho_{g_{cr}}}{\rho_f}\right)\right)^2} \end{aligned} \tag{A.16}$$

To derive equation (4.40):

$$
\begin{aligned}
(\rho_{cr} v_{ss})^2 &= {\rho_{cr}}^2 \frac{q p_{cr} \gamma}{\rho_{g_{cr}}} \left(1 + \left(\frac{1-q}{q}\right)\left(\frac{\rho_{g_{cr}}}{\rho_f}\right)\right)^2 \\
&= \frac{{\rho_{g_{cr}}}^2 {\rho_f}^2}{\left(q\rho_f + (1-q)\rho_{g_{cr}}\right)^2} \frac{q p_{cr} \gamma}{\rho_{g_{cr}}} \left(1 + \left(\frac{1-q}{q}\right)\left(\frac{\rho_{g_{cr}}}{\rho_f}\right)\right)^2 \\
&= \frac{\gamma p_{cr} \rho_{g_{cr}}}{q} \\
\rho_{cr} v_{ss} &= \sqrt{\frac{\gamma p_{cr} \rho_{g_{cr}}}{q}}
\end{aligned}
\tag{A.17}
$$

The transcendent equation (4.44) for the solving of critical pressure ratio r_{cr} is derived by equating equation (4.36) to (4.39):

$$
\begin{aligned}
& v_{so} = v_{ss} \\
& 2\left[\frac{1-q}{\rho_f}(p_{cv} - p_{cr}) + \frac{q p_{cv}^{\frac{1}{\gamma}}}{\rho_g\left(1-\frac{1}{\gamma}\right)}\left(p_{cv}^{1-\frac{1}{\gamma}} - p_{cr}^{1-\frac{1}{\gamma}}\right)\right] \div p_{cv} \\
& = \left(\frac{q\gamma p_{cr}}{\rho_{g_{cr}}}\right)\left(1 + \left(\frac{1-q}{q}\right)\left(\frac{\rho_{g_{cr}}}{\rho_f}\right)\right)^2 \div p_{cv} \\
& 2\left[\frac{1-q}{\rho_f}(1 - r_{cr}) + \frac{q p_{cv}^{-1+\frac{1}{\gamma}}}{\rho_g\left(1-\frac{1}{\gamma}\right)}\left(p_{cv}^{1-\frac{1}{\gamma}} - p_{cr}^{1-\frac{1}{\gamma}}\right)\right] \\
& = \left(\frac{q\gamma r_{cr}}{\rho_{g_{cr}}}\right)\left(1 + \left(\frac{1-q}{q}\right)\left(\frac{\rho_{g_{cr}}}{\rho_f}\right)\right)^2 \\
& 2\left[\frac{1-q}{\rho_f}(1 - r_{cr}) + \frac{q}{\rho_g\left(1-\frac{1}{\gamma}\right)}\left(1 - r_{cr}^{1-\frac{1}{\gamma}}\right)\right] \\
& = \left(\frac{q\gamma r_{cr}}{\rho_{g_{cr}}}\right)\left(1 + \left(\frac{1-q}{q}\right)\left(\frac{\rho_{g_{cr}}}{\rho_f}\right)\right)^2 \\
& 2\left[\frac{1-q}{\rho_f}(1 - r_{cr}) + \frac{q}{\rho_g\left(1-\frac{1}{\gamma}\right)}\left(1 - r_{cr}^{1-\frac{1}{\gamma}}\right)\right] \div q
\end{aligned}
$$

$$= \left(\frac{{r_{cr}}^{1-\frac{1}{\gamma}} q\gamma}{\rho_g} \right) \left(1 + \left(\frac{1-q}{q} \right) \left(\frac{\rho_g}{\rho_f} \right) \right)^2 \div q \quad where\ \rho_{g_{cr}} = \rho_g {r_{cr}}^{\frac{1}{\gamma}}$$

$$2 \left[\frac{1}{X_{cr}\rho_{g_{cr}}}(1 - r_{cr}) + \frac{1}{\rho_g \left(1 - \frac{1}{\gamma} \right)}(1 - {r_{cr}}^{1-\frac{1}{\gamma}}) \right] \times X_{cr} \quad where\ X_{cr} = \left(\frac{q}{1-q} \right) \left(\frac{\rho_f}{\rho_{g_{cr}}} \right)$$

$$= \left(\frac{{r_{cr}}^{1-\frac{1}{\gamma}} \gamma}{\rho_g} \right) \left(1 + \frac{1}{X_{cr}} \right)^2 \times X_{cr}$$

$$2 \left[\frac{1}{\rho_{g_{cr}}}(1 - r_{cr}) + \frac{X_{cr}}{\rho_g \left(1 - \frac{1}{\gamma} \right)}(1 - {r_{cr}}^{1-\frac{1}{\gamma}}) \right] \div {r_{cr}}^{1-\frac{1}{\gamma}}$$

$$= \left(\frac{{r_{cr}}^{1-\frac{1}{\gamma}} \gamma X_{cr}}{\rho_g} \right) \left(1 + \frac{1}{X_{cr}} \right)^2 \div {r_{cr}}^{1-\frac{1}{\gamma}}$$

$$2 \left[\frac{{r_{cr}}^{\frac{-1}{\gamma}}}{\rho_g}({r_{cr}}^{\frac{1}{\gamma}-1} - {r_{cr}}^{\frac{1}{\gamma}}) + \frac{X_{cr}}{\rho_g \left(1 - \frac{1}{\gamma} \right)}({r_{cr}}^{\frac{1}{\gamma}-1} - 1) \right]$$

$$= \left(\frac{\gamma X_{cr}}{\rho_g} \right) \left(1 + \frac{1}{X_{cr}} \right)^2$$

$$2 \left[(\frac{1}{r_{cr}} - 1) + \frac{X_{cr}}{\left(1 - \frac{1}{\gamma} \right)}({r_{cr}}^{\frac{1}{\gamma}-1} - 1) \right]$$

$$= \gamma X_{cr} \left(1 + \frac{1}{X_{cr}} \right)^2 \tag{A.18}$$

A.4 Finite Element Method For Modal Analysis Of Reed Valve Vibration

Figure A.1 shows a typical finite element j of the arbitrarily shaped reed valve in transverse vibration, where represents the dimensionless local coordinate defined by (A.19). As the dimensionless displacement $Y(\xi)$ within the interval $(j-1)h < x < jh$ consists of contributions from the translations Y_{j-1}, Y_j and rotations Θ_{j-1}, Θ_j from both ends of the nodes, the dimensionless displacement

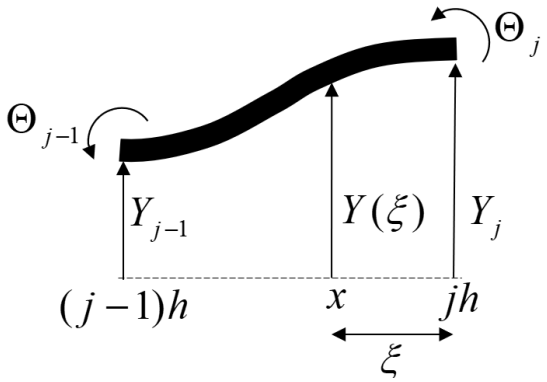

Figure A.1: Finite element of the reed valve in bending showing nodal displacements.

$Y(\xi)$ is defined as:

$$\xi = \frac{(jh - x)}{h} \tag{A.19}$$

$$Y(\xi) = \phi_1(\xi)Y_{j-1} + \phi_2(\xi)h\Theta_{j-1} + \phi_3(\xi)Y_j + \phi_4(\xi)h\Theta_j = \phi^T(\xi)\mathrm{a}_j \tag{A.20}$$

where $\phi(\xi) = [\phi_1(\xi)\ \phi_2(\xi)\ \phi_3(\xi)\ \phi_4(\xi)]^T$ is a vector of interpolation functions and $\mathrm{a}_j = [Y_{j-1}\ h\Theta_{j-1}\ Y_j\ h\Theta_j]^T$ is vector of nodal displacements. The interpolation functions are defined by approximating dimensionless displacement $Y(\xi)$ as Hermite Cubic since the differential equation of motion for beam vibration is of order four:

$$Y(\xi) = c_1 + c_2\xi + c_3\xi^2 + c_4\xi^3 \tag{A.21}$$

with conditions on both nodal ends as:

$$\begin{aligned} Y(0) &= Y_j \qquad \Theta_j = -\frac{1}{h}\frac{dY(\xi)}{d\xi}\bigg|_{\xi=0} \\ Y(1) &= Y_{j-1} \quad \Theta_{j-1} = -\frac{1}{h}\frac{dY(\xi)}{d\xi}\bigg|_{\xi=1} \end{aligned} \tag{A.22}$$

The interpolation functions are defined as:

$$\begin{aligned} \phi_1(\xi) &= 3\xi^2 - 2\xi^3 \qquad \phi_2(\xi) = \xi^2 - \xi^3 \\ \phi_3(\xi) &= 1 - 3\xi^2 + 2\xi^3 \quad \phi_4(\xi) = -\xi + 2\xi^2 - \xi^3 \end{aligned} \tag{A.23}$$

Several methods can be employed to obtain the vector of nodal displacements which depicts the mode shape. In this paper, Rayleigh-Ritz method will be used. Considering the energy form of Rayleigh's quotient,

$$\lambda_n = \frac{U_{\max}}{T_{ref}} \tag{A.24}$$

The maximum potential energy stored in the deformed reed valve is expressed as a sum over k number of individual finite elements:

$$\begin{aligned} U_{\max} &= \frac{1}{2}\sum_{j=1}^{k}(\tau(t))^2 \int_{(j-1)h}^{jh} EI(x)\left[\frac{d^2Y(x)}{dx^2}\right]^2 dx \\ &= \frac{1}{2}\sum_{j=1}^{k}(\tau(t))^2 \frac{1}{h^3}\int_0^1 EI_j(\xi)\mathrm{a}_j^T \frac{d^2\phi(\xi)}{d\xi^2}\frac{d^2\phi^T(\xi)}{d\xi^2}\mathrm{a}_j d\xi \\ &= \frac{1}{2}\sum_{j=1}^{k}(\tau(t))^2 \mathrm{a}_j^T K_j \mathrm{a}_j \end{aligned} \tag{A.25}$$

where individual element stiffness matrix is:

$$\begin{aligned} K_j &= \frac{1}{h^3}\int_0^1 EI_j(\xi)\frac{d^2\phi(\xi)}{d\xi^2}\frac{d^2\phi^T(\xi)}{d\xi^2}d\xi \\ &= \frac{1}{h^3}\int_0^1 EI_j(\xi)\begin{bmatrix} 6-12\xi \\ 2-6\xi \\ -6+12\xi \\ 4-6\xi \end{bmatrix}\begin{bmatrix} 6-12\xi \\ 2-6\xi \\ -6+12\xi \\ 4-6\xi \end{bmatrix}^T d\xi \end{aligned} \tag{A.26}$$

And the reference kinetic energy as:

$$\begin{aligned} T_{ref} &= \frac{1}{2}\sum_{j=1}^{k}\left(\frac{d\tau}{dt}\right)^2 \int_{(j-1)h}^{jh} m(x)Y^2(x)dx \\ &= \frac{1}{2}\sum_{j=1}^{k}\left(\frac{d\tau}{dt}\right)^2 h\int_0^1 m_j(\xi)\mathrm{a}_j^T\phi(\xi)\phi^T(\xi)\mathrm{a}_j d\xi \\ &= \frac{1}{2}\sum_{j=1}^{k}\left(\frac{d\tau}{dt}\right)^2 \mathrm{a}_j^T M_j \mathrm{a}_j \end{aligned} \tag{A.27}$$

where individual element mass matrix is:

$$M_j = h\int_0^1 m_j(\xi)\phi(\xi)\phi^T(\xi)d\xi = h\int_0^1 m_j(\xi)\begin{bmatrix} 3\xi^2-2\xi^3 \\ \xi^2-\xi^3 \\ 1-3\xi^2+2\xi^3 \\ -\xi+2\xi^2-\xi^3 \end{bmatrix} d\xi \tag{A.28}$$

By rearranging (A.24) of Rayleigh's quotient, an eigenvalue problem is obtained:

$$K\mathrm{a} = \lambda^2 M\mathrm{a} \tag{A.29}$$

where the first and last individual element matrices for clamped and free conditions are expressed in (A.30), assuming constant EI_j within each element:

$$K_1 = \frac{EI_1k^3}{L^3}\begin{bmatrix} 12 & -6 \\ -6 & 4 \end{bmatrix} \qquad M_1 = \frac{m_1L}{420k}\begin{bmatrix} 156 & -22 \\ -22 & 4 \end{bmatrix}$$

$$K_k = \frac{EI_kk^3}{L^3}\begin{bmatrix} 12 & 6 & -12 & 6 \\ -12 & -6 & 12 & -6 \\ 6 & 2 & -6 & 4 \end{bmatrix} \quad M_k = \frac{m_kL}{420k}\begin{bmatrix} 156 & 22 & 54 & -13 \\ 22 & 4 & 13 & -3 \\ 54 & 13 & 156 & -22 \\ -13 & -3 & -22 & 4 \end{bmatrix} \tag{A.30}$$

and the first and last individual element matrices for clamped and pinned conditions when the reed valve hits the stop plate are expressed in (A.31), assuming constant EI_j within each element:

$$K_1 = \frac{EI_1k^3}{L^3}\begin{bmatrix} 12 & -6 \\ -6 & 4 \end{bmatrix} \qquad M_1 = \frac{m_1L}{420k}\begin{bmatrix} 156 & -22 \\ -22 & 4 \end{bmatrix}$$

$$K_k = \frac{EI_kk^3}{L^3}\begin{bmatrix} 12 & 6 & 6 \\ 6 & 4 & 2 \\ 6 & 2 & 4 \end{bmatrix} \quad M_k = \frac{m_kL}{420k}\begin{bmatrix} 156 & 22 & -13 \\ 22 & 4 & -3 \\ -13 & -3 & 4 \end{bmatrix} \tag{A.31}$$

The assembly of global matrices from individual element matrices for both clamped-free and clamped-pinned conditions are as follows:

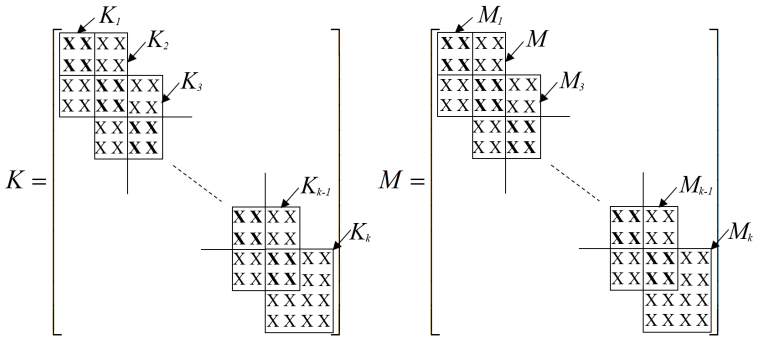

(A.32)

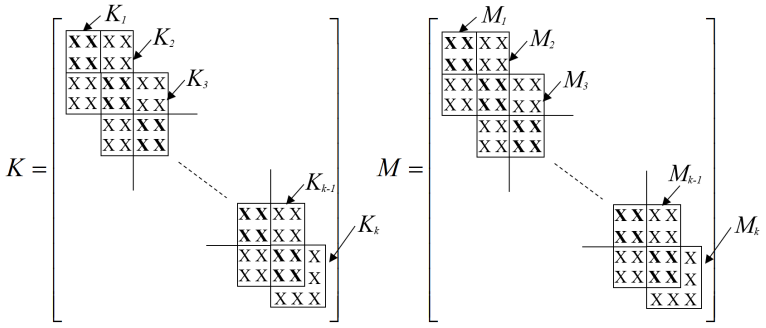

(A.33)

To this end, the free vibration mode shape Y_n, and natural frequencies λ_n, can be obtained by solving the eigenvalue problem, (A.29). The approximated eigenvalues and associated eigenvectors of (A.29) are the natural frequencies and the nodal displacements and rotations respectively. Due to the nature of excitation of the valve, only the first mode shape corresponding to the lowest natural frequency or eigenvectors associated to λ_1 are considered. With the mode 1 nodal displacements or eigenvectors associated to λ_1, polynomial functions that are approximations of the free vibration mode shapes can be obtained via multiple linear regression method. The mode shapes are approximated by polynomial functions of fourth-order or higher in the form as:

$$Y(x) = D_1 x + D_2 x^2 + D_3 x^3 + \cdots + D_q x^q \tag{A.34}$$

The polynomial functions are optimised by minimising the sum of the squares of the residuals between the nodal displacement valves and the polynomial approximated values,

$$\begin{aligned} S &= \textstyle\sum_{j=1}^{k} \left(Y_j - D_1 x_j - D_2 x_j^2 - D_3 x_j^3 - \cdots - D_q x_j^q\right)^2 \\ \tfrac{\partial S}{\partial D_1} &= 2 \textstyle\sum_{j=1}^{k} (-x_j) \left(Y_j - D_1 x_j - D_2 x_j^2 - D_3 x_j^3 - \cdots - D_q x_j^q\right) \\ &\vdots \\ \tfrac{\partial S}{\partial D_q} &= 2 \textstyle\sum_{j=1}^{k} \left(-x_j^q\right) \left(Y_j - D_1 x_j - D_2 x_j^2 - D_3 x_j^3 - \cdots - D_q x_j^q\right) \end{aligned} \tag{A.35}$$

The coefficients D_q, yielding the minimum sum of the squares of the residuals are obtained by setting the partial derivatives equal to zero and expressing the

result in matrix form as:

$$\begin{bmatrix} \sum_{j=1}^{k} x_j^2 & \cdots & \sum_{j=1}^{k} x_j^{q+1} \\ \vdots & \ddots & \vdots \\ \sum_{j=1}^{k} x_j^{q+1} & \cdots & \sum_{j=1}^{k} x_j^{2q} \end{bmatrix} \begin{bmatrix} D_1 \\ D_2 \\ D_3 \\ \vdots \\ D_q \end{bmatrix} = \begin{bmatrix} \sum_{j=1}^{k} x_j Y_j \\ \sum_{j=1}^{k} x_j^2 Y_j \\ \sum_{j=1}^{k} x_j^3 Y_j \\ \vdots \\ \sum_{j=1}^{k} x_j^q Y_j \end{bmatrix} \tag{A.36}$$

Appendix B

Flow Coefficients and Simulation Parameters

B.1 Suction Flow Coefficient

In order to connect the prototype to the low side of the refrigeration loop where components such as the accumulator and evaporator are sized with 1/4" fittings, the suction pipe of the protype was fitted with pipe reducer, as illustrated in Figure B.1. During the actual experimental run, the pressure of the suction chamber was found to be fluctuating drastically, as shown in Figure B.2, due to re-expansion of the trapped fluid in the dead volume of the prototype and due to restricted fluid inflow caused by the reduced flow area of the reducer inlet. This means that the actual flow in the suction pipe should behave like a transient pulsatile flow with periodic variations since the outlet pressure of the pipe is fluctuating over the working cycle of the prototype. In order to accurately determine the suction flow coefficient of such pulsatile fluid flow in the suction pipe with the reducer, CFD simulations was used to model the suction pipe flow. With the flow area drastically reduced by the pipe reducer, as shown in the dimensions tabulated in Table B.1, flow separations with recirculation regions at the diverging portion of the pipe are also expected in the actual flow. As a result, turbulence model will be used in the flow simulation. Out of all commonly used turbulence model, namely, the standard k-ϵ, realisable k-ϵ and SST-kω models, the realisable k-ϵ model is preferred in this application due to its robustness in predicting compressible flows with high Reynolds number [179, 180]. As such, the pulsatile suction flow through the pipe with reducer inlet was simulated based on realisable k-ϵ turbulence model with enhanced wall treatment and pressure gradient effects near the walls, assuming transient and axisymmetric

compressible flow. The time step taken to simulate the transient condition was 4.00×10^{-5} s.

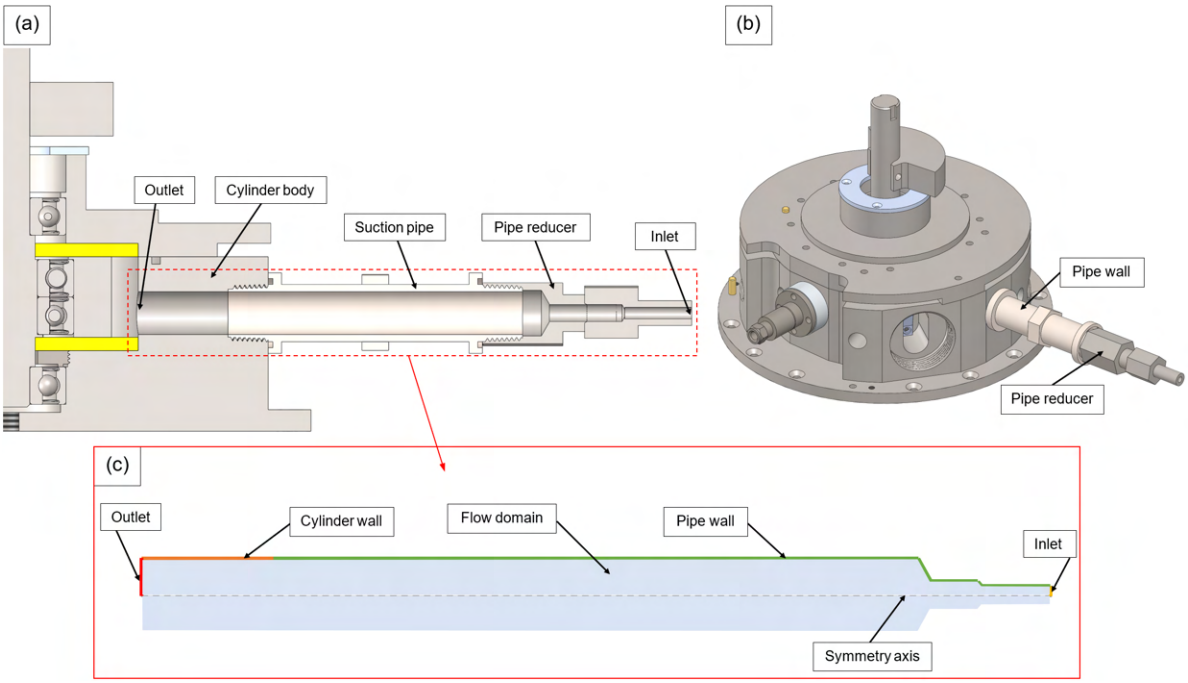

Figure B.1: Modelling of suction flow through the suction pipe with reducer — a) Cutaway view b) Overall view c) Simplified 2D geometry of the fluid flow domain.

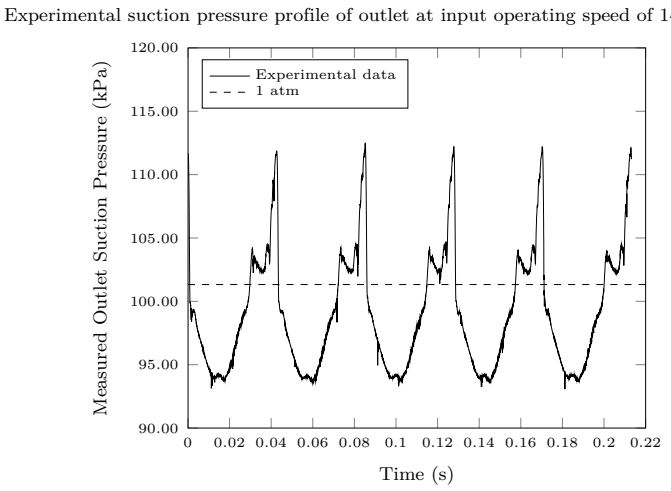

Figure B.2: An example of suction pressure profile for transient pressure outlet condition.

In order to simulate the actual pipe flow, only the geometry of flow domain was setup, as shown in Figure B.1, with the actual pipe dimensions tabulated in Table B.1. The boundary of the flow domain was further discretised into different boundary zones with each zone prescribed with different boundary conditions, as

illustrated in Table B.2. The pressure inlet boundary condition was prescribed to the pipe inlet with constant pressure; for air flow, the inlet boundary was set at constant atmospheric pressure of 101.325 kPa. As mentioned previously, the outlet condition was fluctuating and so the experimental measurement of the suction pressure was used as the transient pressure condition of the outlet in order to simulate actual condition of the pipe flow.

Table B.1: Dimensions of the flow domain.

Zone	**Dimension, mm**
Length of cylinder section	33.50
Length of pipe section	160.58
Inlet diameter	4.35
Outlet diameter	16.00

Table B.2: Zone type and boundary conditions based on experimental measurements for the flow domain.

Zone	**Type**	**Pressure, kPa**	**Temperature, K**
Symmetry axis	Axis	-	-
Cylinder wall	Wall	-	316.15
Pipe wall	Wall	-	303.15
Inlet	Pressure inlet	101.325(Air)/284.349(R134a)	300.15
Outlet	Pressure outlet	Transient pressure profile	300.15

Before the flow simulation, a mesh convergence study was also conducted using air experimental data to determine the optimal mesh density. With an optimal mesh, the solution should be independent of the mesh density where the solution no longer varies significantly with increasing mesh refinement. While higher number of elements generally result in increased accuracy of the solution, the computational time required is also greatly increased. Hence, a compromise has to be established between the two where the accuracy of the solution and computational time expenses are reasonable. The mesh convergence study was conducted by running the simulation with increasing cell counts while maintaining the average skewness below 0.9 and average aspect ratio below 40 [181], except in the inflation layers near the walls, as shown in Figure B.3. The results of the mesh convergence study for the pipe flow are shown in Table B.3. From the results, the mesh with 41779 elements was selected due to the good compromise between solution accuracy and computational time. With this mesh, the solution based on resultant suction flow coefficient $C_{d,suc}$ was reasonably accurate (less than 3%) with only 1.7% discrepancy in the suction flow coefficient

as compared to the solution of the finest mesh. The suction flow coefficient $C_{d,suc}$ is defined as the ratio of average mass flow rate at the outlet boundary (as illustrated in Table B.2) to the theoretical ideal mass flow rate based on the ideal orifice equation (4.29) using atmospheric density and flow area of the outlet. The ideal isentropic flow velocity is determined using equation (4.28) with the upstream enthalpy at atmospheric condition and the downstream enthalpy based on the measured pressure of the suction chamber and upstream entropy. In terms of computational time required, increasing the mesh from 41,779 elements to 73,458 elements resulted in an increase in simulation run time by 31.8%. Thus, for practicality, the mesh with 41,779 elements was selected.

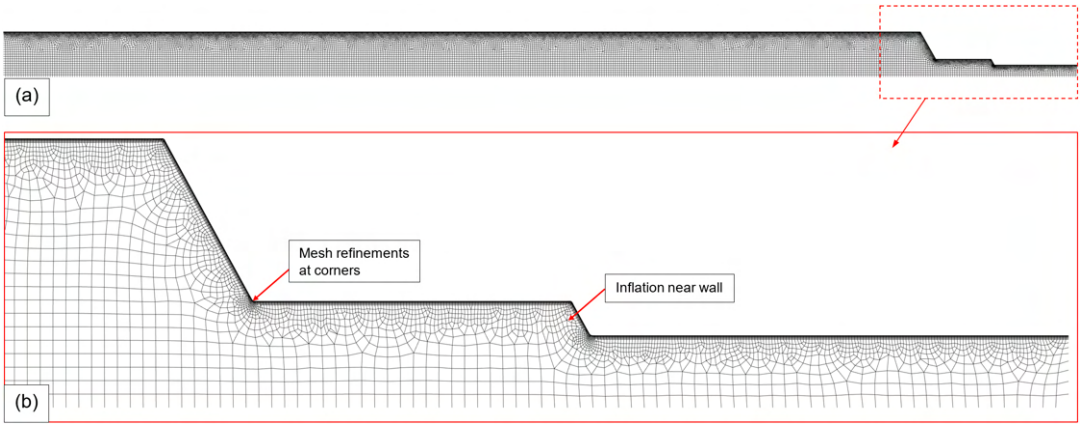

Figure B.3: Meshed geometry of flow domain — a) Overall view b) Close-up of the highlighted region.

Table B.3: Mesh convergence study results using air experimental results of suction pressure at input operating speed of 1440 rpm.

	No. of elements		
	9078	41779	73458
Average skewness/aspect ratio	0.0672/4.704	0.0746/5.675	0.0747/5.515
Average outlet mass flow, kg s^{-1}	4.29980×10^{-4}	10.88895×10^{-4}	10.70646×10^{-4}
Ideal orifice flow, kg s^{-1} (Based on Equation 4.29)	144.69622×10^{-4}	144.69622×10^{-4}	144.69622×10^{-4}
Computational time, hours	3	7.5	11
Suction flow coefficient, $C_{d,suc}$	0.0297	0.0753	0.0740
% discrepancy in $C_{d,suc}$ (Based on finest mesh)	59.84	1.70	-

The flow simulations were conducted with different set of experimentally measured suction pressure profile for the outlet boundary condition. Each set of the experimental measurements were obtained from open air loop runs of the prototype at various input operating speeds, ranging from 1080 rpm to 1800 rpm, and from R134a refrigeration loop runs at 1620 rpm. Figure B.4 below shows an example of velocity magnitude contour of the flow domain based on

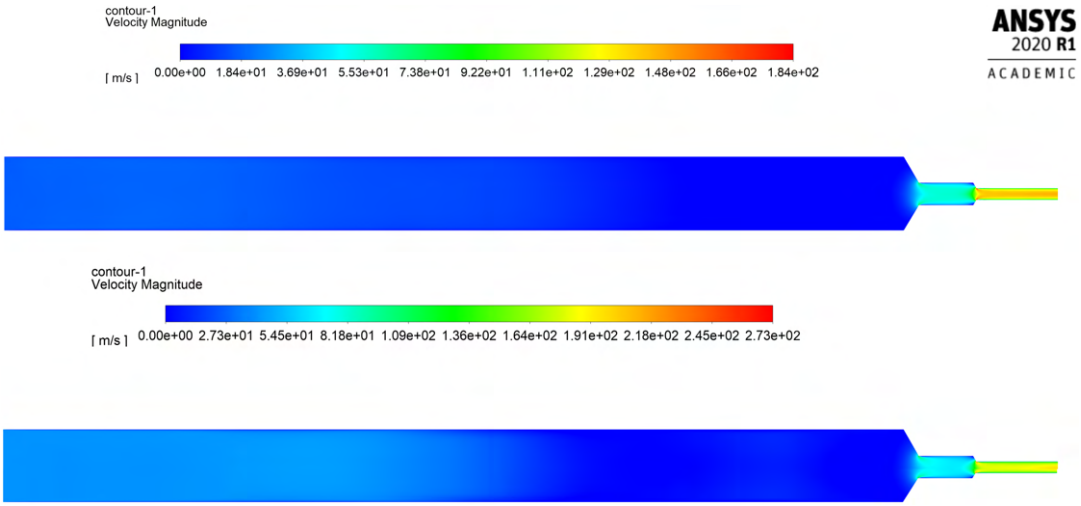

Figure B.4: An example of velocity magnitude contour of flow domain.

outlet suction pressure of air measured at input operating speed of 1440 rpm. As previously predicted that the actual flow would be fluctuating under periodically varying boundary conditions, the CFD simulation confirms that the flow is pulsatile with some regions along the pipe accelerating and decelerating in speed, as illustrated in the contour plot of Figure B.4.

The resultant average mass flow rate and suction flow coefficient $C_{d,suc}$ for both air and R134a at the outlet for each input operating speed was computed and tabulated in Table B.4 and Table B.5. The arithmetic mean of the set of suction flow coefficient $C_{d,suc}$ for air at each input operating speed was taken as the average suction flow coefficient $C_{d,suc}$ that was used in the predictions of the experimental runs with air, as shown in Chapter 8.

Overall, the average suction flow coefficient $C_{d,suc}$ for air was found to be 0.0755. It is very small in value because the flow reduction caused by the use of pipe reducer at the suction pipe inlet is relatively large. Based on dimensions in Table B.1, the suction flow area is approximately reduced 3.7 times from the outlet diameter of 16mm to the inlet diameter of 4.35mm. Furthermore, the suction flow coefficient is observed to increase with increasing operating speed, as shown in Table B.4, suggesting that lower operating speed tends to allow greater re-expansion of fluid from the dead volume which will result in larger adverse pressure gradient between the suction inlet and outlet and greater pulsatile flow. Based on the experimental suction pressure profiles, adverse pressure gradient occurs 34.8% of the suction cycle duration at 1080 rpm while it occurs only 19.9% of the suction cycle duration at 1440 rpm. For suction flow

of R134a at input operating speed of 1620 rpm, suction flow coefficient $C_{d,suc}$ was determined to be 0.0975.

Table B.4: Suction mass flow rates of air at different input operating speeds based on CFD simulations and ideal orifice flow.

	Mass flow rate of air, kg s^{-1}		
Input operating speed, rpm	**CFD**	**Ideal orifice flow (Based on Equation 4.29)**	$C_{d,suc}$
1080	3.47121×10^{-4}	79.72005×10^{-4}	0.0435
1260	4.05217×10^{-4}	88.0974×10^{-4}	0.0460
1440	10.88895×10^{-4}	144.69622×10^{-4}	0.0753
1620	9.58074×10^{-4}	110.62107×10^{-4}	0.0866
1800	10.77133×10^{-4}	85.35441×10^{-4}	0.1262
Average suction flow coefficient, $C_{d,suc}$			0.0755

Table B.5: Suction mass flow rate of R134a at input operating speed of 1620 rpm based on CFD simulation and ideal orifice flow.

	Mass Flow Rate of R134a, kg s^{-1}		
Input operating speed, rpm	**CFD**	**Ideal orifice flow (Based on Equation 4.29)**	$C_{d,suc}$
1620	235.02762×10^{-4}	2410.90505×10^{-4}	0.0975

B.2 Discharge Coefficient of Flow Through Reed Type Valve

Determination of the discharge coefficient of the flow through reed type valves is not a simple task because the flow behaviour is dependent on the geometry of the discharge port and the vibrational dynamics of the valve reed. The complex flow through the valve can be simulated based on fluid-structure interaction (FSI) problem, in which the flow behaviour and the vibrational motion of the valve are solved simultaneously, or through a simplified quasi steady flow model, where fluid motion is uncoupled from the dynamics of the valve. Either way, FSI simulations requires extremely long computational time. On the other hand, simplified modellings of the complex valve reed system as a simple radial diffuser, as illustrated in Figure B.5, have been proven to provide sufficiently accurate and fast solutions to the determination of the discharge coefficient and other flow parameters such as effective force area and flow areas in studies of compressors with reed type valve system [182–185]. Modelling the valve reed system as simplified radial diffuser only depends on a few dimensionless parameters, namely, the diameter ratio, D/d , and the lift ratio between the frontal disk and the seat, s/d, as shown in Figure B.5c.

Ferreira and Gasche [186] have presented a comprehensive numerical data set of flow parameters including discharge coefficient of flow for a wide range of incompressible flow with Mach number less than 0.3. The turbulence effects at the diffuser zone (Figure B.5c) are modelled based on RNG k-ϵ and k-ω SST models which are the recommended models for the solving of such flow [187], [188]. The results for discharge coefficient, $C_{d,disc}$, at different lift ratio, s/d, and Reynolds number, Re, are shown in Figure B.6.

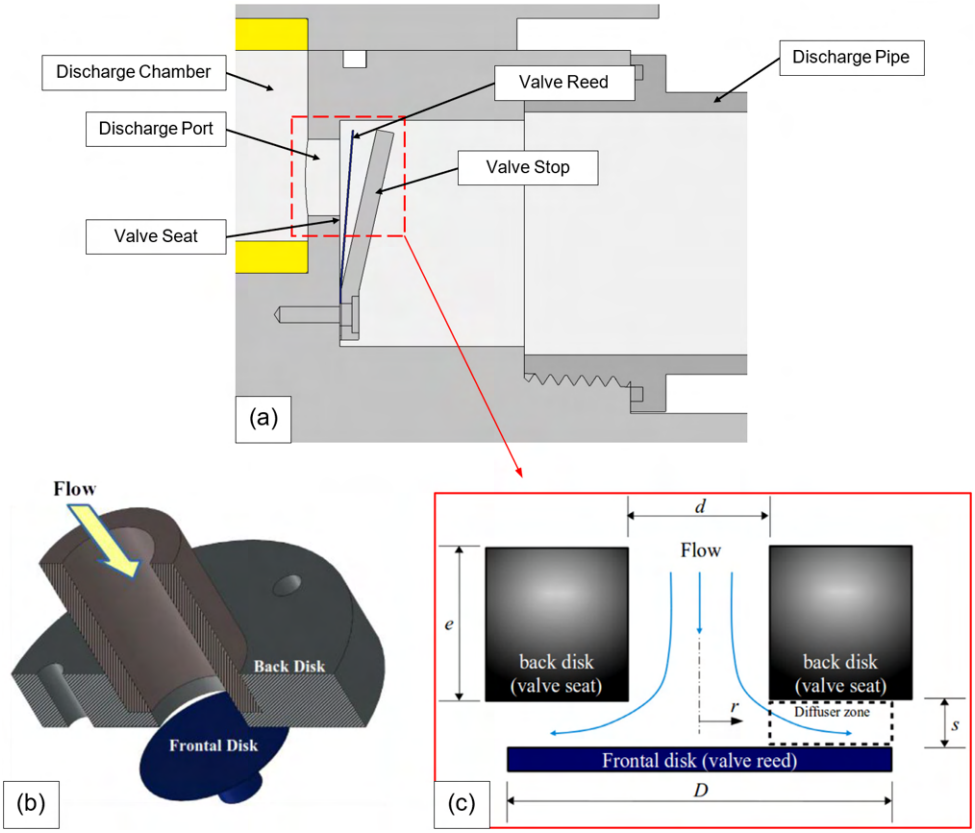

Figure B.5: Modelling of discharge flow through the reed type valve as simplified radial diffuser — a) Cutaway view of the discharge port of the prototype b) Actual 3D radial diffuser [186] c) Main parameters of a radial diffuser [186].

Using ideal orifice flow equation (4.28), theoretical calculations of the ideal flow velocity through the discharge port and the Mach numbers at different experimental conditions have shown that the flow through the reed type valve is safe to be assumed as incompressible flow. The maximum ideal Mach numbers obtained are less than 0.3, as shown in the calculations tabulated in Table B.6 and Table B.7.

Table B.6: Theoretical calculation of ideal orifice flow velocity for different input operating speeds of the prototype based on experimental air discharge conditions.

Input operating speed, rpm	**Pre-set discharge pressure, kPa Based on experiment**	**Maximum ideal orifice flow velocity, m s^{-1} (Based on Equation 4.28)**	**Speed of sound, m s^{-1}**	**Max. Mach no.**	**Average Re**
1080	269	123.543	429.568	0.290	830,075
1260	307	126.089	436.994	0.291	898,346
1440	326	126.629	441.624	0.296	877,127
1620	369	123.659	451.083	0.275	826,790
1800	409	122.746	459.132	0.269	816,299

Table B.7: Theoretical calculation of ideal orifice flow speed for input operating speed of 1620 rpm based on experimental R134a discharge condition.

Input operating Speed, rpm	**Pre-set discharge pressure, kPa Based on experiment**	**Maximum ideal orifice flow velocity, m s^{-1} (Based on Equation 4.28)**	**Speed of sound, m s^{-1}**	**Max. Mach no.**	**Average Re**
1620	1007	44.457	153.321	0.290	7.98×10^{6}

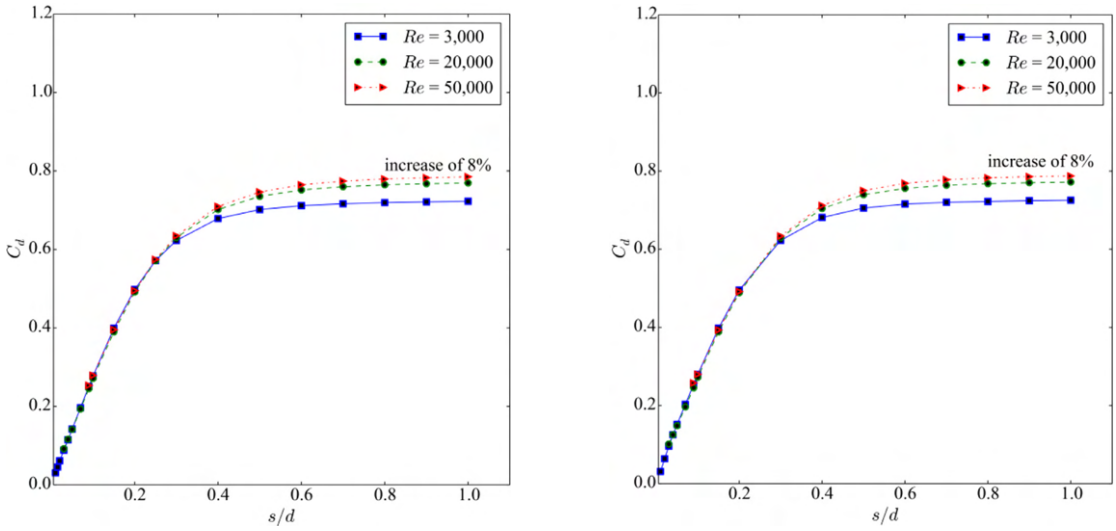

(a) D/d=1.15 (b) D/d=1.3

Figure B.6: Discharge coefficient as a function of the lift, s, and Reynolds number, Re.

The dimensions of the reed type valve designed for the prototype is tabulated in Table B.8. With the dimensions of the valve system, the dimensionless parameters for the equivalent radial diffuser can be calculated, as shown in Table B.9, and the discharge coefficient, $C_{d,disc}$ for the prototype's reed type valve is determined to be 0.8.

Table B.8: Dimensions of the prototype's reed type valve.

Parameter	**Dimension, mm**
Length of discharge port, e	4.50
Diameter of discharge port/ feeding orifice, d	12.00
Maximum valve lift/ Height of valve stop, s	5.00
Diameter of reed valve head/ frontal disk, D	15.00

Table B.9: Dimensionless parameters of the reed type valve of the prototype.

Dimensionless ratio	
Diameter ratio, D/d	1.25
Maximum lift ratio, s/d	0.417
Average Reynold number range, Re	>50,000

B.3 Discharge Coefficient of Hydraulic Atomising Spray Nozzle

The hydraulic atomising spray nozzle used in the liquid refrigerant injection is a form of swirl atomiser and its discharge coefficient is inevitably low due to the presence of the gaseous core in the centre of spray cone which effectively blocks off the centre portion of the orifice. It was found that the discharge coefficient of swirl atomiser typed spray nozzle is practically independent of the fluid flow behaviour and viscosity for flow with Reynolds number larger than 3000 [189]. Thus, for liquid refrigerant injection application where the refrigerant is of low viscosity and the Reynold number is typically more than 10,000, the atomising spray nozzle is assumed to have constant discharge coefficient. Furthermore, based solely on Bernoulli's equation, studies have shown that the discharge coefficient of swirl atomisers is only dependent on atomiser dimensions at high Reynold flow. The discharge coefficient is only dependent on the total cross-sectional area of inlet ports, A_p, in the swirl chamber of the nozzle, diameter of the swirl chamber, D_s, and the orifice diameter of the nozzle, d_o, as shown in Figure B.7.

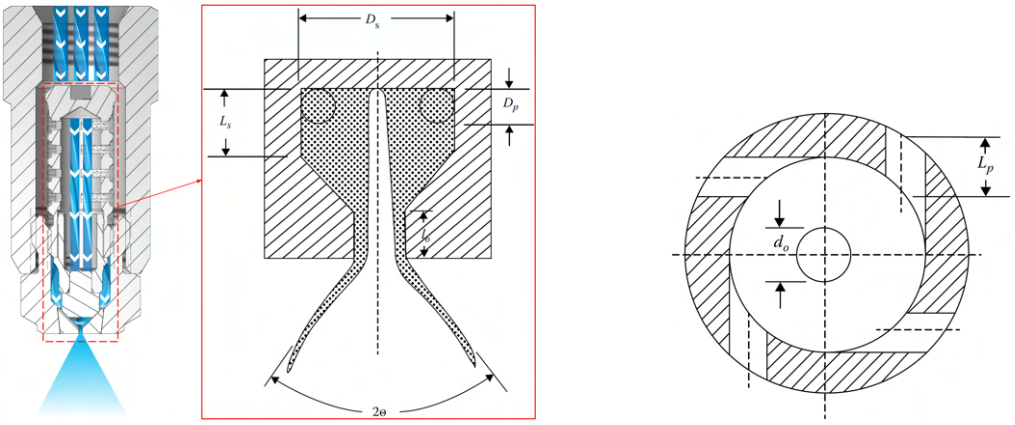

(a) Cutaway side view. (b) Cutaway front view.

Figure B.7: Schematic view of a simplex swirl chamber of a pressure-swirl atomising nozzle [190].

Rizk and Lefebvre [191] has correlated the atomiser dimensions with the discharge coefficients based on their experimental data and derived the following relationship for $C_{d,spray}$:

$$C_{d,spray} = 0.35 \left(\frac{A_p}{D_s d_o}\right)^{0.5} \left(\frac{D_s}{d_o}\right)^{0.25} \tag{B.1}$$

Based on Carlisle's [192] evidence for the effect of D_s/d_o and L_s/D_s on discharge coefficient and Taylor's [193] discharge coefficient correlation for inviscid flow, another relationship [190] for $C_{d,spray}$ can be obtained:

$$C_{d,spray} = \sqrt{0.0616 \left(\frac{D_s}{d_o}\right) \left(\frac{A_p}{D_s d_o}\right)} \tag{B.2}$$

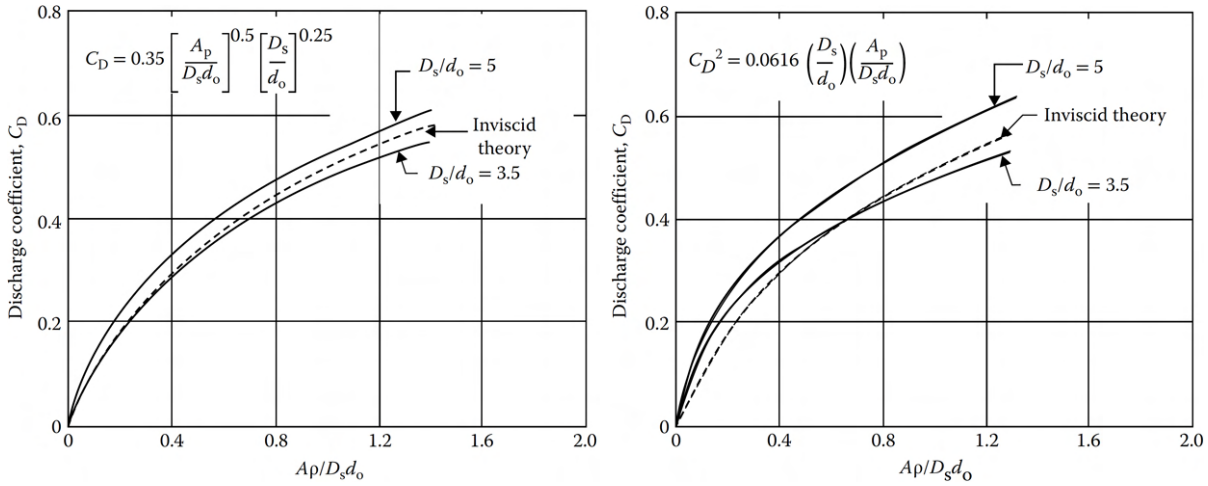

(a) Rizk and Lefebvre [191].

(b) Carlisle and Taylor [190, 192, 193].

Figure B.8: Practical relationship between discharge coefficient and atomizer dimensions.

Both relationship are illustrated in Figure B.8. Based on both equations (B.1) and (B.2), assumptions from previous studies [190] on the discharge coefficient of pressure-swirl atomiser and the dimensions of the hydraulic atomising spray nozzle (as shown in Table B.10 and Section F.9) used in the experimental runs, the discharge coefficient of the spray nozzle used is approximately determined to be 0.3.

Table B.10: Dimensions of hydraulic atomising spray nozzle's swirl chamber.

Parameter	**Dimension, mm**
Model: 1/4M-SS8 (Section F.9)	
Diameter of swirl chamber, D_s	3.00
Diameter of 2 inlet ports, D_p	1.524
Diameter of orifice, d_0	1.524

B.4 Validation Of Dead Volume In The Prototype

Although the prototype is designed with a maximum swept volume or volumetric displacement of 50 cm^3, as mentioned in Section 7.1, there are clearances designed in the prototype to allow necessary working spaces for the extraction/installation of the bearings, endface bushing plates, pressure sensors and the injector. These clearances are dead volume where a portion of compressed fluid is trapped inside. The locations of the dead volume and the approximated volume are shown in Figure B.9 and Table B.11 respectively.

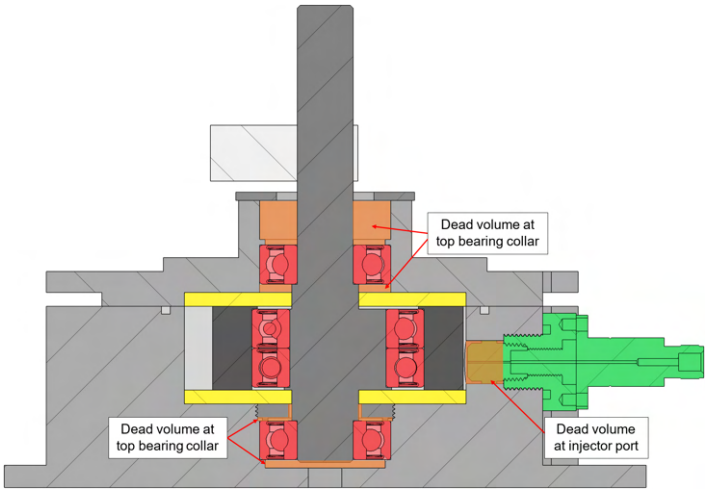

(a) Cutaway view.

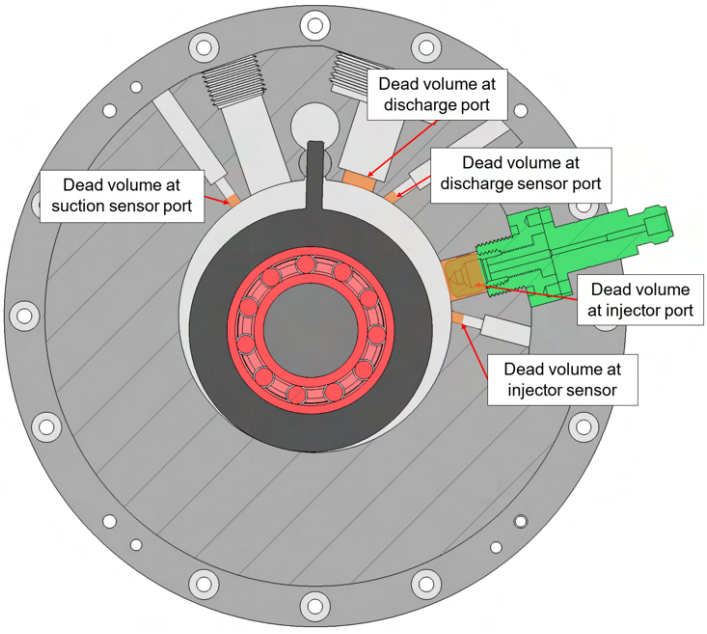

(b) Front view.

Figure B.9: Locations of dead volume in the prototype hightlighted in orange colour.

Table B.11: Approximated dead volume in the prototype.

Dead Volume Location	Volume, cm^3/cc
3 Sensor ports	0.077
Injector port clearance	1.33
Total clearance at top bearing collar	17.33
Total clearance at bottom bearing collar	4.07
Discharge port	0.51
Total approximated dead volume	23.31

The total approximated dead volume is determined to be at least 23.31 cm^3 which is about 46.6% of the maximum volumetric displacement of the prototype. In practice, however, the effective dead volume occupied by the compressed fluid will be much smaller than the total approximated dead volume. This is because some locations of the dead volume (e.g the clearance at the top bearing collar) are not directly linked to the working chamber, and it takes time for the compressed fluid to leak through the micro-gaps and occupy these spacings. Furthermore, the response time of the compressed fluid to occupy the dead volume depends on the operating speed of the compressor and the flow behaviour through the micro-gaps which can be rarefied gas flow in slip and transition flow regimes [101, 102]. In other words, different gas will occupy different effective dead volume. For the experimental runs on open air loop, the effective dead volume is experimentally determined to be approximately 17.05 cm^3 for the range of operating speed from 1080 rpm to 1800 rpm. For the experimental runs with refrigerant R134a, the effective dead volume is experimentally determined to be approximately 9.0312 cm^3 for the input operating speed of 1620 rpm.

Appendix C

Program Flow Chart of Simulation

The overall numerical simulation of the prototype performance based on the mathematical models presented in Chapter 4 to 6 are translated and written in codes using FORTRAN f90 programming language. FORTRAN was selected as it is especially suited to numeric computation and scientific computing. Furthermore, it allows the ease of evaluating the thermodynamic states of the working fluid during the working cycle of the compression process via flash subroutines from the NIST Reference Fluid Thermodynamic and Transport Properties Database (REFPROP) [135] which are written in FORTRAN f90 programming language. The program flow chart of the simulation is presented in Figure C.1 and the program flow chart of the simulation for vapour-compression cycle with liquid refrigerant injection cooling is presented in Figure C.2.

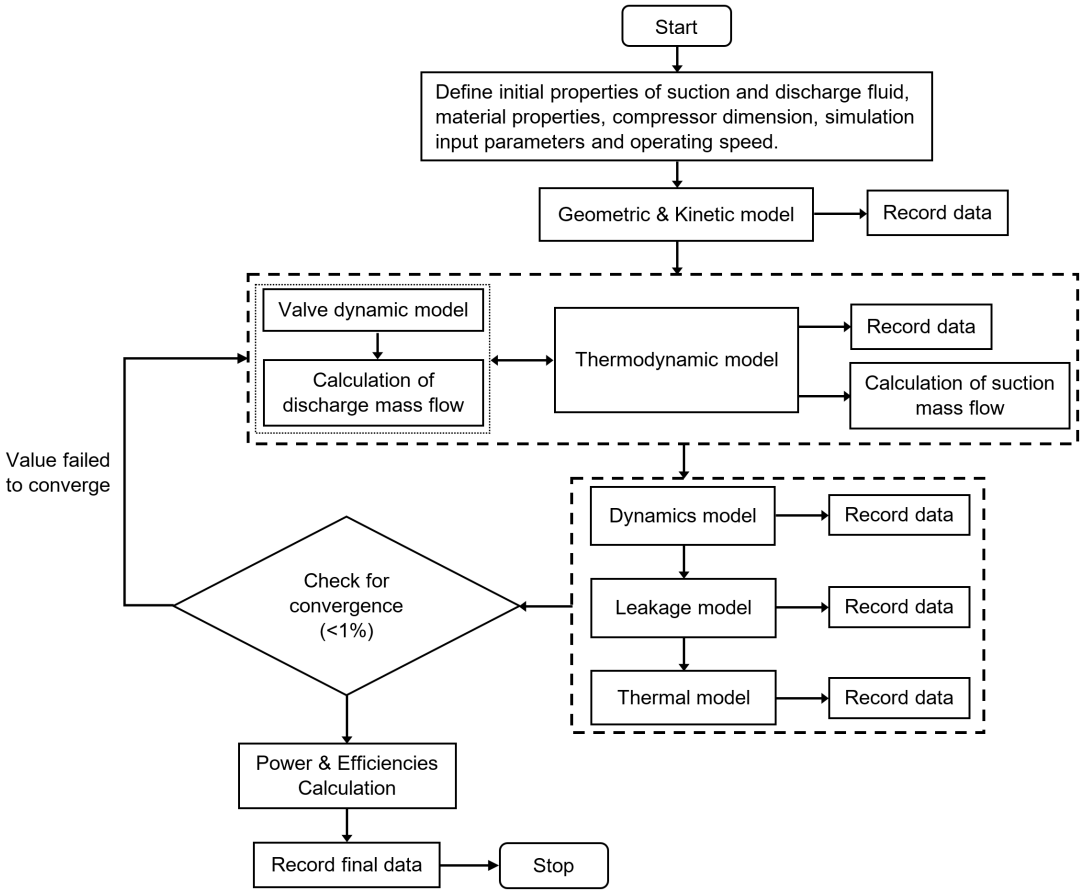

Figure C.1: Program flow chart of the overall numerical simulation.

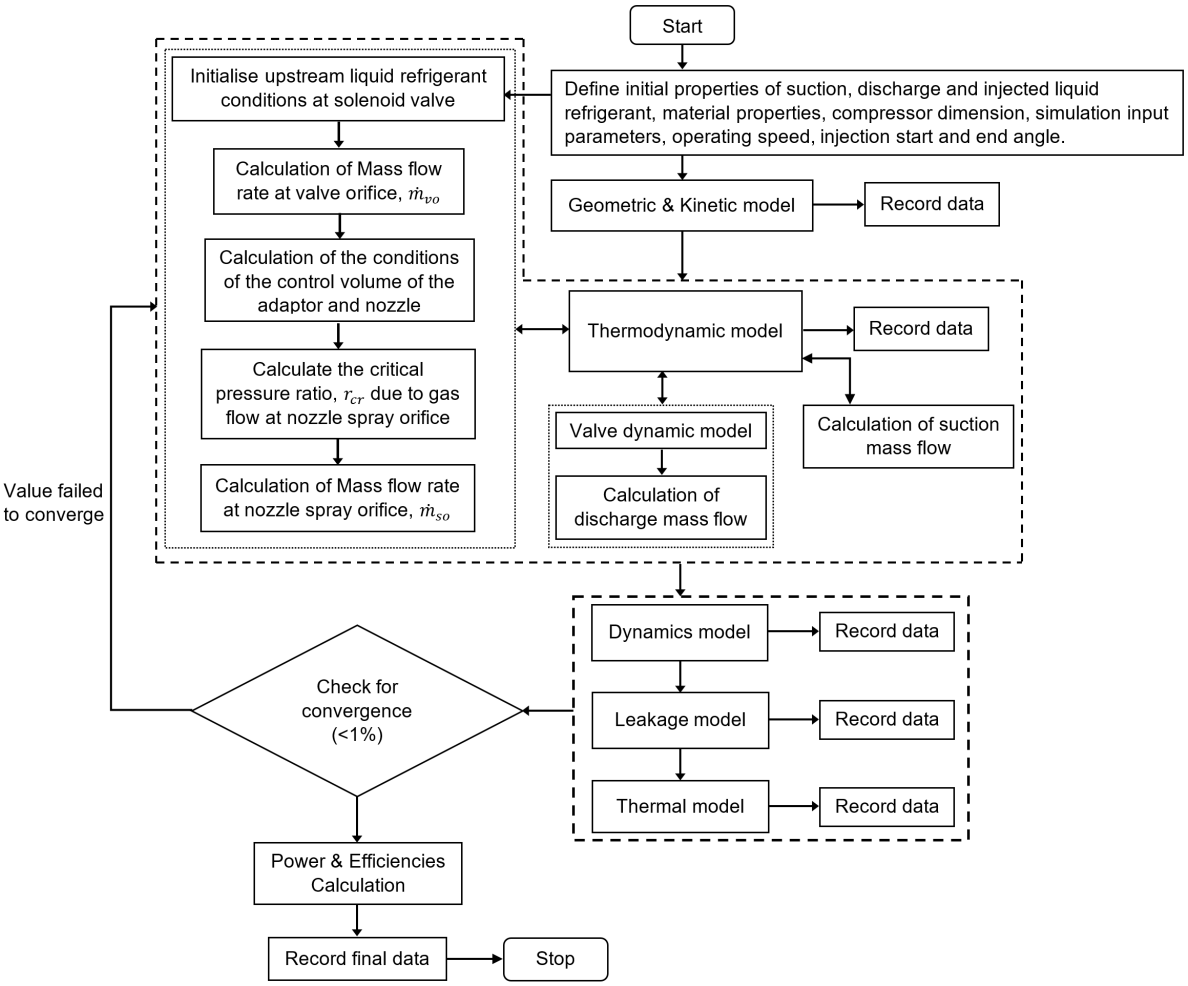

Figure C.2: Program flow chart of the overall numerical simulation for vapour-compression cycle with liquid refrigerant injection cooling.

Appendix D

Uncertainty Analysis, Measurement Data and Theoretical Predictions

D.1 Uncertainty Analysis

The uncertainties of various measuring instruments used in the measurements of mass flow rate and average power input of the prototype are shown in Table D.1 and Table D.2.

Table D.1: Measurement uncertainties

Equipments	Uncertainty
Fluke power scope meter (model: MDA-510) ΔI	$\pm$0.215A
Aalborg 044-40-GL Rotameter, $\Delta \dot{V}$	$\pm$1312.5 ml min^{-1}
Tachometer TM1100	$\pm$0.02% of reading

Table D.2: Uncertainty of motor operating speed

Input operating speed*, rpm	**Measured operating speed**, ω_1, rpm**	Uncertainty $\Delta\omega_1$	% of slippage, s
1080	1063	21.26	1.57
1260	1243	24.86	1.35
1440	1413.2	28.26	1.86
1620	1592	31.84	1.73
1800	1772	35.44	1.56

*: **Operating speed input to the frequency controller of motor.**
: **Operating speed measured by tachometer and used in simulation.

The uncertainty of the measured volumetric efficiency, $\Delta\eta_{measured}$, are calculated based on the following approximations:

$$\begin{aligned}
\eta_{vol,measured} &= \frac{\rho_{measured}\dot{V}_{measured}}{\rho_{suc}V_{ideal}\frac{\omega_1}{60}} \\
\Delta\eta_{vol,measured} &\approx \sqrt{\left(\frac{\partial\eta_{measured}}{\partial\dot{V}_{measured}}\Delta\dot{V}_{measured}\right)^2 + \left(\frac{\partial\eta_{measured}}{\partial\omega_1}\Delta\omega_1\right)^2} \\
&= \sqrt{\left(\frac{\rho_{measured}}{\rho_{suc}V_{ideal}\frac{\omega_1}{60}}\Delta\dot{V}_{measured}\right)^2 + \left(-\frac{\rho_{measured}\dot{V}_{measured}}{\rho_{suc}V_{ideal}\frac{{\omega_1}^2}{60}}\Delta\omega_1\right)^2}
\end{aligned} \tag{D.1}$$

The uncertainty of the average measured power input, ΔP_m, are calculated based on the following approximations:

$$\begin{aligned}
P_m &= (1-s)mI^2R_f \\
\Delta P_m &\approx \sqrt{\left(\frac{\partial P_m}{\partial I}\Delta I\right)^2 + \left(\frac{\partial P_m}{\partial R_f}\Delta R_f\right)^2} \\
&\approx (1-s)mI\sqrt{(2\Delta I R_f)^2 + (I\Delta R_f)^2}
\end{aligned} \tag{D.2}$$

where, s is the percentage of motor slippage, m is the number of poles and I is the current input to the motor that is measured by the power scope meter. R_f is the resistance experienced by the stator due to the rotating air-gap field which varies with the operating motor frequency, f_m. Based on the inductance-resistance series circuitry of the induction motor from the datasheet in Section F.1, the impedance of the induction motor is expressed as:

$$\begin{aligned}
Z_f &= R_f + jX_f \\
&= \frac{\left(\frac{f_m}{f_R}\right)^2\left(\frac{r_2{X_m}^2{R_{ir}}^2}{s} + \frac{{r_2}^2{X_m}^2R_{ir}}{s^2}\right) + \left(\frac{f_m}{f_R}\right)^4{X_m}^2{x_2}^2R_{ir}}{\left(\frac{R_{ir}r_2}{s} - \left(\frac{f_m}{f_R}\right)^2X_mx_2\right)^2 + \left(\frac{f_m}{f_R}\right)^2\left(R_{ir}x_2 + R_{ir}X_m + \frac{r_2}{s}X_m\right)^2} \\
&+ j\left[\frac{\left(\frac{f_m}{f_R}\right)\left(\frac{{R_{ir}}^2{r_2}^2}{s^2}\right)X_m + \left(\frac{f_m}{f_R}\right)^3{R_{ir}}^2{x_2}^2X_m + \left(\frac{f_m}{f_R}\right)^3{R_{ir}}^2{X_m}^2x_2}{\left(\frac{R_{ir}r_2}{s} - \left(\frac{f_m}{f_R}\right)^2X_mx_2\right)^2 + \left(\frac{f_m}{f_R}\right)^2\left(R_{ir}x_2 + R_{ir}X_m + \frac{r_2}{s}X_m\right)^2}\right]
\end{aligned} \tag{D.3}$$

where, f_m is the motor operating frequency, f_r is the rated motor frequency (50Hz), r_2 is the rotor ohmic loss, x_2 is the leakage impedance at the rotor and

X_m is the magnetizing reactance. R_f is expressed as follows:

$$R_f = \frac{\left(\frac{f_m}{f_R}\right)^2 \left(\frac{r_2 {X_m}^2 {R_{ir}}^2}{s} + \frac{{r_2}^2 {X_m}^2 R_{ir}}{s^2}\right) + \left(\frac{f_m}{f_R}\right)^4 {X_m}^2 {x_2}^2 R_{ir}}{\left(\frac{R_{ir} r_2}{s} - \left(\frac{f_m}{f_R}\right)^2 X_m x_2\right)^2 + \left(\frac{f_m}{f_R}\right)^2 \left(R_{ir} x_2 + X_m R_{ir} + \frac{r_2}{s} X_m\right)^2} \tag{D.4}$$

D.2 Measured Data and Theoretical Predictions

The overall measured data from experiments with air is presented in Table D.3. The suction pressure measured is within a range due to the pulsatile backflow in the suction port.

Table D.3: Overall measured data from experiments with air

Input operating speed, rpm	**Measured Suction pressure (kPa)**	**Measured discharge pressure (kPa)**	**Measured suction temperature (°C)**	**Pressure ratio**	**Measured mass flow rate (g s^{-1})**	**Measured average power input (W)**	**Predicted mechanical efficiency**	**Measured volumetric efficiency**	**Predicted isentropic efficiency**
1080	97.1-111.3	297.7	28.0	2.94	0.32	489.3	0.25	0.31	0.52
1080	97.4-109.4	271.3	28.0	2.64	0.43	475.6	0.23	0.42	0.57
1080	97.1-110.0	249.1	28.0	2.46	0.51	462.1	0.22	0.50	0.61
1080	96.8-109.1	230.1	28.1	2.28	0.60	448.8	0.21	0.58	0.65
1080	96.6-108.5	211.8	28.1	2.11	0.65	435.7	0.19	0.62	0.68
1260	95.6-112.4	336.5	27.7	3.27	0.38	602.6	0.27	0.32	0.54
1260	98.0-113.3	306.7	27.7	2.92	0.52	570.1	0.26	0.43	0.58
1260	96.4-111.0	281.8	27.8	2.74	0.62	522.9	0.24	0.51	0.62
1260	96.3-111.0	259.2	27.8	2.53	0.72	492.6	0.23	0.59	0.66
1260	97.0-110.2	241.8	27.7	2.37	0.79	448.8	0.22	0.66	0.69
1440	92.7-113.3	374.8	26.6	3.67	0.45	683.9	0.28	0.33	0.55
1440	93.7-111.7	334.0	26.6	3.25	0.59	662.4	0.27	0.43	0.61
1440	93.6-111.6	311.6	26.6	3.04	0.72	641.2	0.26	0.53	0.64
1440	92.5-111.0	285.7	26.6	2.79	0.83	620.3	0.24	0.61	0.68
1440	92.6-110.6	267.1	26.6	2.58	0.93	599.8	0.23	0.68	0.7
1620	92.8-117.9	397.1	26.6	3.84	0.49	734.7	0.29	0.32	0.46
1620	94.3-113.4	363.6	26.6	3.51	0.67	687.3	0.28	0.44	0.49
1620	94.2-116.3	333.3	26.6	3.24	0.80	687.4	0.27	0.52	0.53
1620	95.2-114.6	309.9	26.6	3.01	0.94	664.3	0.26	0.61	0.56
1620	94.7-114.1	288.0	26.6	2.79	1.04	641.5	0.25	0.67	0.59
1800	92.3-121.4	437.5	26.6	4.08	0.57	840.7	0.30	0.33	0.61
1800	94.0-118.3	397.4	26.6	3.72	0.77	787.4	0.30	0.45	0.64
1800	96.2-120.0	363.2	26.6	3.43	0.91	787.4	0.28	0.53	0.67
1800	97.2-115.7	334.8	26.6	3.16	1.05	774.3	0.27	0.61	0.69
1800	97.7-119.8	306.4	26.6	2.88	1.13	761.4	0.26	0.66	0.71

The measured and predicted mass flow rates with the corresponding calculated uncertainties from experiments with air are presented in Table D.4.

Table D.4: Measured and predicted mass flow rates with the calculated uncertainties

Input operating speed, rpm	**Pressure ratio**	**Measured mass flow rate (g s^{-1})**	**Predicted mass flow rate (g s^{-1})**	**Measured volumetric efficiency (%)**	**Predicted volumetric efficiency (%)**	**Uncertainties** $\eta_{vol,measured}$ **(%)**
1080	2.94	0.32	0.402	30.9	38.98	7.30
1080	2.64	0.43	0.481	41.8	46.69	6.64
1080	2.46	0.51	0.540	49.8	52.36	6.09
1080	2.28	0.60	0.600	57.8	58.16	5.62
1080	2.11	0.65	0.665	62.9	64.45	5.16
1260	3.27	0.38	0.437	31.8	36.2	7.06
1260	2.92	0.52	0.543	43.1	45.06	6.43
1260	2.74	0.62	0.605	51.4	50.14	5.91
1260	2.53	0.72	0.683	59.3	56.63	5.42
1260	2.37	0.79	0.738	65.7	61.19	5.04
1440	3.67	0.45	0.440	33.0	32.08	6.94
1440	3.25	0.59	0.570	43.2	41.59	6.18
1440	3.04	0.72	0.643	52.7	46.88	5.75
1440	2.79	0.83	0.727	60.6	53.04	5.27
1440	2.58	0.93	0.804	67.5	58.67	4.92
1620	3.84	0.49	0.514	31.9	33.25	6.52
1620	3.51	0.67	0.626	43.5	40.5	5.97
1620	3.24	0.80	0.718	51.8	46.46	5.47
1620	3.01	0.94	0.800	60.7	51.82	5.07
1620	2.79	1.04	0.887	67.1	57.41	4.71
1800	4.08	0.57	0.566	33.1	32.94	6.45
1800	3.72	0.77	0.694	44.6	40.35	5.86
1800	3.43	0.91	0.799	52.9	46.46	5.35
1800	3.16	1.05	0.901	61.2	52.4	4.92
1800	2.88	1.13	1.025	66.0	59.64	4.49

The measured and predicted average power input with the corresponding calculated uncertainties are presented in Table D.5.

Table D.5: Measured and predicted average power input with the calculated uncertainties

Input operating speed, rpm	Pressure ratio	Measured average power input (W)	Predicted average power input (W)	Uncertainties (W)	Uncertainties (%)
1080	2.94	489.3	432.37	54.97	11.23
1080	2.64	475.6	420.67	54.12	11.38
1080	2.46	462.1	413.66	53.28	11.53
1080	2.28	448.8	405.51	52.44	11.69
1080	2.11	435.7	398.05	51.61	11.84
1260	3.27	602.6	522.04	66.00	10.95
1260	2.92	570.1	509.91	64.02	11.23
1260	2.74	522.9	499.74	61.09	11.68
1260	2.53	492.6	490.96	59.14	12.01
1260	2.37	448.8	482.34	56.26	12.53
1440	3.67	683.9	609.74	84.15	12.30
1440	3.25	662.4	592.43	82.77	12.50
1440	3.04	641.2	584.18	81.38	12.69
1440	2.79	620.3	572.73	80.00	12.90
1440	2.58	599.8	562.07	78.62	13.11
1620	3.84	734.7	697.92	93.08	12.67
1620	3.51	687.3	688.98	89.93	13.08
1620	3.24	687.4	674.79	89.94	13.08
1620	3.01	664.3	663.57	88.37	13.30
1620	2.79	641.5	653.30	86.80	13.53
1800	4.08	840.7	799.20	104.84	12.47
1800	3.72	787.4	788.76	101.35	12.87
1800	3.43	787.4	772.92	101.35	12.87
1800	3.16	774.3	758.79	100.48	12.98
1800	2.88	761.4	747.39	99.61	13.08

The comparison between the measured and predicted pressure profile of the working chambers at input operating speeds of 1260 rpm and 1620 rpm are shown in Figure D.1 and Figure D.2.

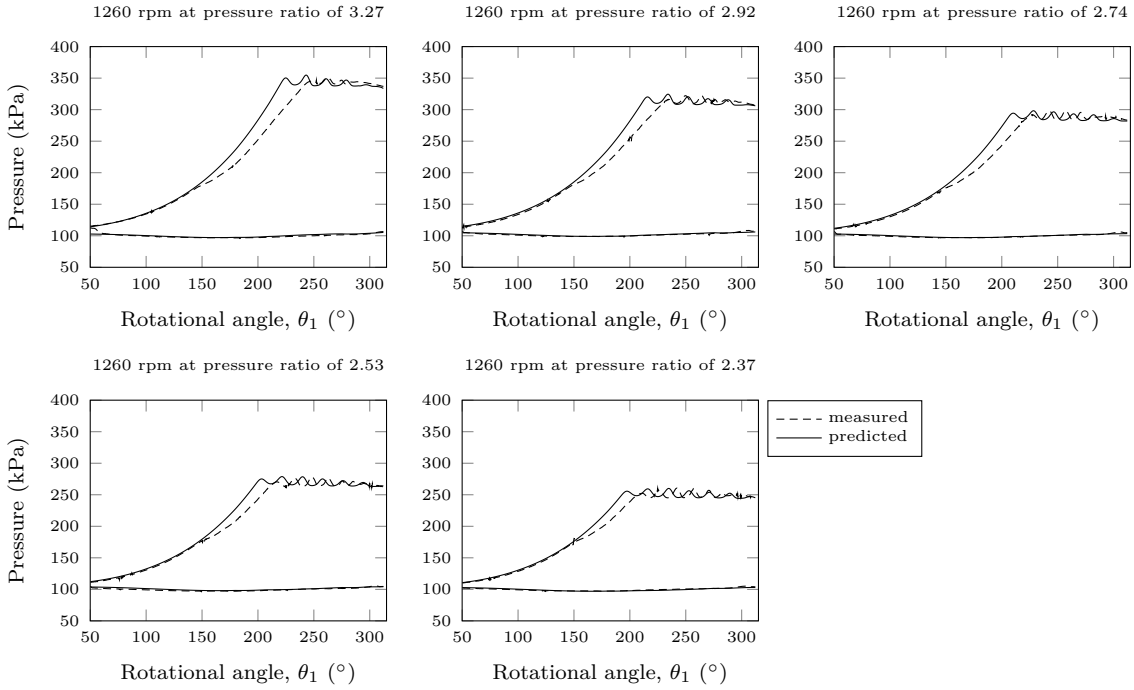

Figure D.1: Comparison of the measured and predicted instantaneous pressure of the working chambers at input operating speed of 1260 rpm.

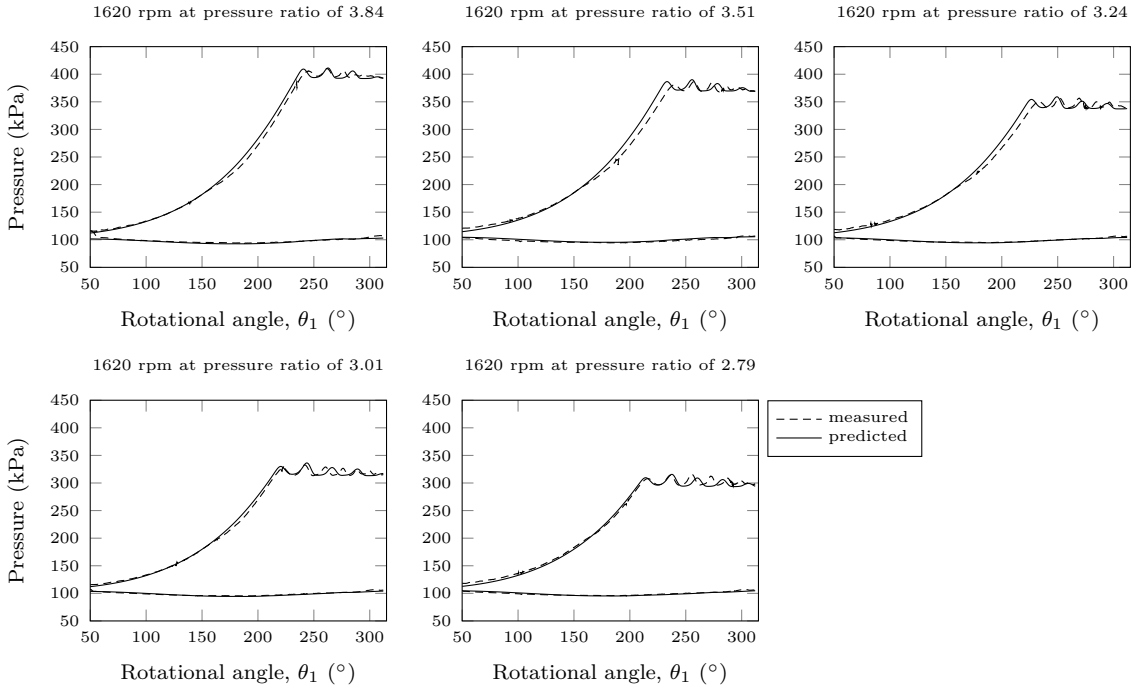

Figure D.2: Comparison of the measured and predicted instantaneous pressure of the working chambers at input operating speed of 1620 rpm.

Appendix E

Balancing of the Shaft Assembly

This section describes the procedural steps in balancing the shaft assembly.

E.1 Balancing of Rotor

Before the fabrication of the rotor, the centre of gravity (CG) of the rotor was first analysed and calculated in SolidWorks Simulation 2019. Since the rotor was designed with a fixed vane, six holes have to be drilled into the rotor (as shown in Figure E.1) at precise locations to remove required quantities of material that were simulation-computed so as to restore the CG of rotor back to the centre of rotation, C_2, within a radius of 0.1μm.

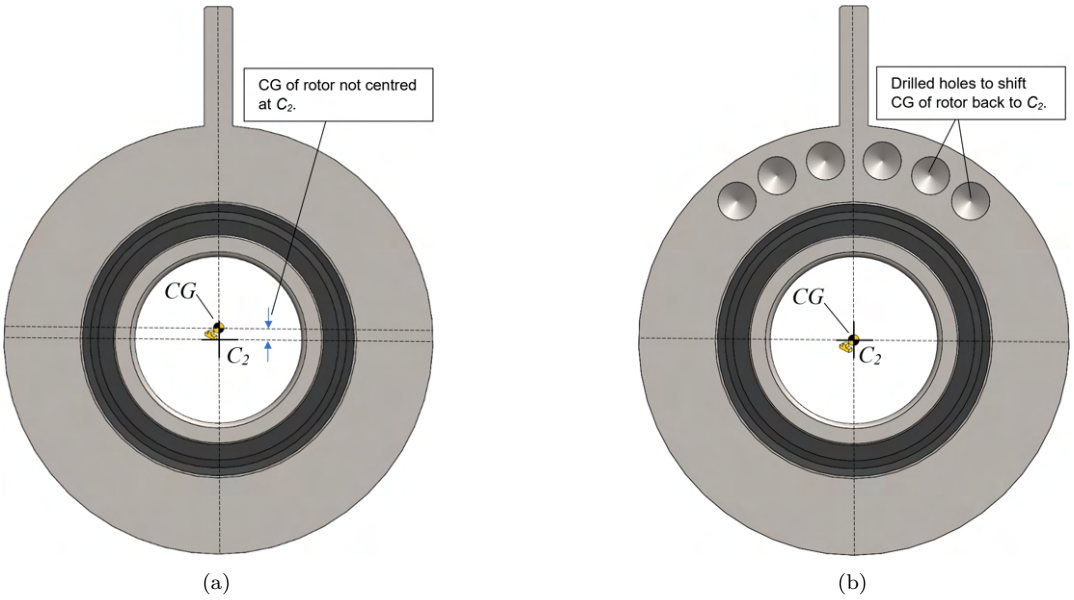

Figure E.1: CG Position of Rotor — (a) Before balancing (b) After balancing by mass removal through drilling of holes on the rotor.

After fabrication, the rotor was statically balanced on a granite surface plate to ensure an even mass distribution about the centre of rotation, C_2, of the rotor was achieved. A statically balanced rotor will remain stationary in any position, with the axis horizontal, and has no tendency to rotate under its own weight, as shown in Figure E.2.

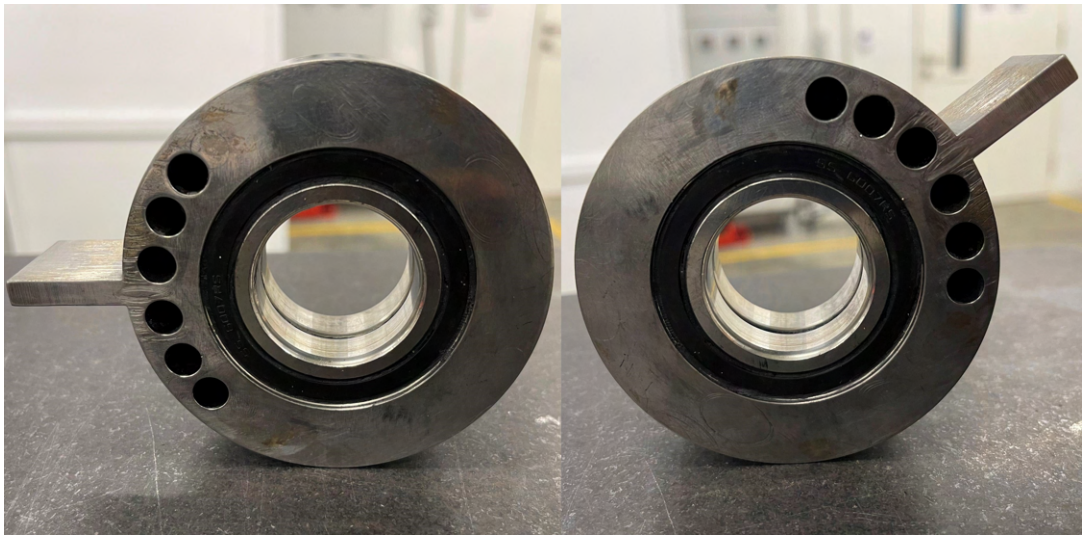

Figure E.2: Rotor in static equilibrium at any position.

E.2 Balancing of the shaft assembly with a counterweight

With the rotor pivoted about the centre of the eccentric of the shaft, the CG of the assembly was offset from the rotation axis of the shaft, C_1, and had to be corrected with a counterweight, as shown in Figure E.3. To design the counterweight, the required mass distribution of the counterweight was determined through the use of SolidWorks simulation to shift the CG of the overall shaft assembly back to the shaft's centre of rotation, C_1, within a radius of 0.1μm.

To ensure that the overall masses of the shaft assembly were evenly distributed, the assembly was statically balanced on gauge blocks on both ends to check if the assembly would rotate under any residual offset loadings. Figure E.4 shows that the balanced shaft assembly with its counterweight is in static equilibrium where the assembly remains stationary in any position with the axis horizontal.

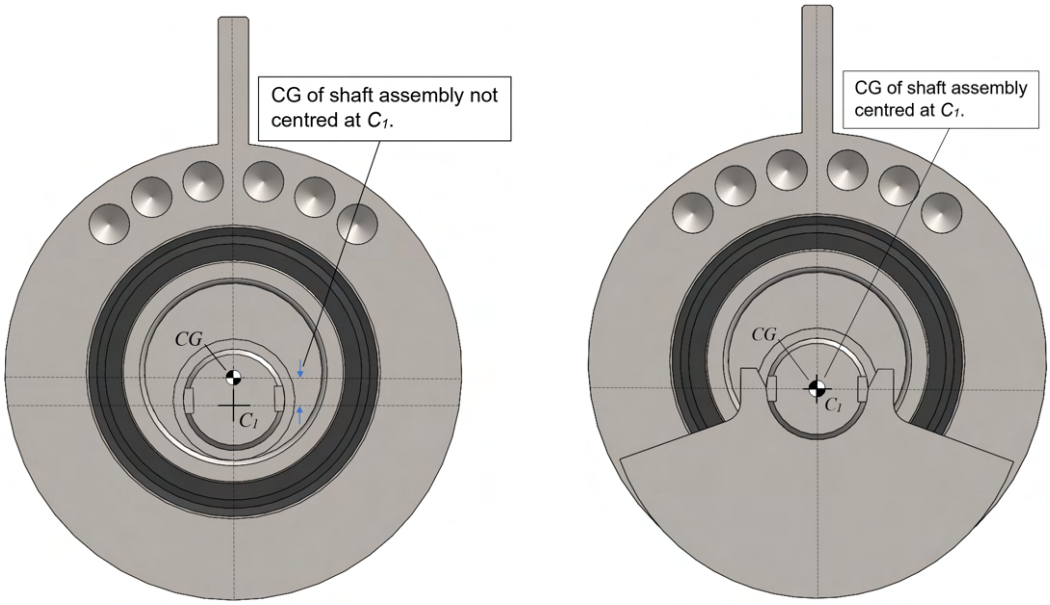

(a) (b)

Figure E.3: CG Position of Shaft Assembly — (a) Before balancing (b) After balancing with the addition of a counterweight.

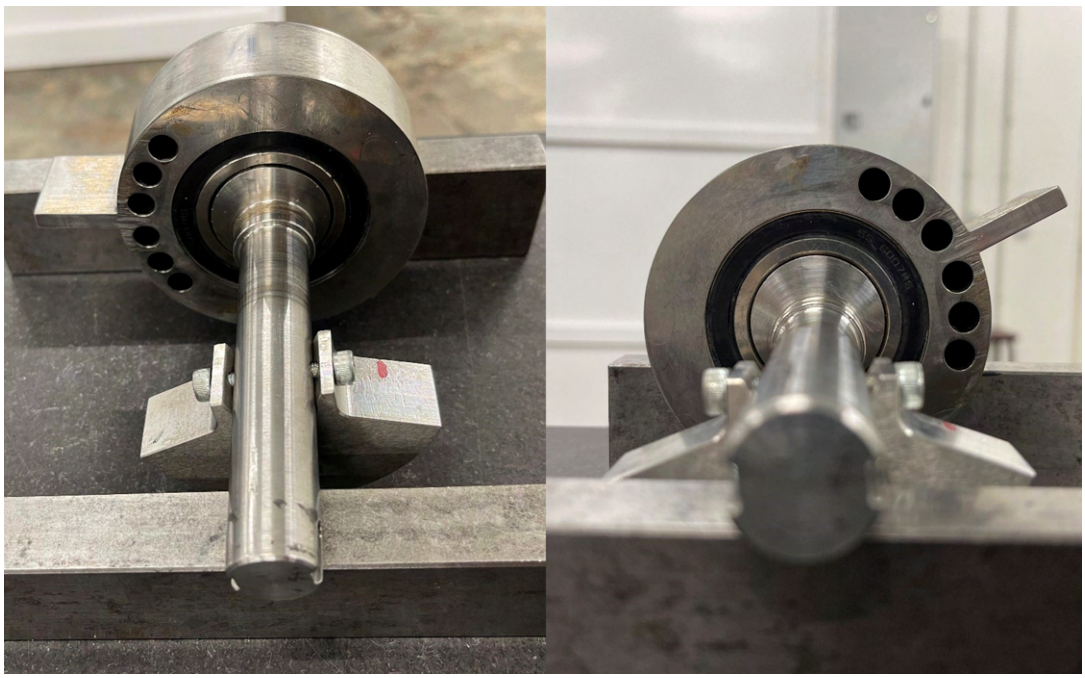

Figure E.4: Shaft assembly in static equilibrium at any position.

Appendix F

Specifications of Experimental Devices

F.1 Induction Motor Specifications

ABB Motors and Generators	Diagram for equivalent-star connected motor				
	Project		Location		
Department/Author	Customer name		Customer ref.		Item name: 1.00001
Our ref.	Rev/Changed by: A	Date of issue: 4/4/2018	Saving ident: untitled.xls		Pages
Product	*TEFC, 3-phase, squirrel cage induction motor*				
Type/Frame	*M2AA 90LB 2*				
Product code	*3GAA 091 213-ASE*		Calc. ref.	GEN_3GAA091213-E_D	
Rated output P_N	*2.2*	kW			
Duty	*S1(IEC) 100%*				
Actual Motor:					
Voltage (V) **400 D**		Current I_N (A)	**4.4**	Power factor at P_N	**0.85**
Frequency (Hz) **50**		Speed (r/min)	**2875**	Efficiency (%) at P_N	**84.6**
Equivalent motor Volt/phase	**231 V**	R1s [Ohms]	**2.7**	X1s [Ohms]	**3.1**
		Xmagnetizing [Ohms]	**144**	Rfriction+iron [Ohms]	**1559**
		X2 r nom [Ohms]	**3.9**	R2 r nom [Ohms]	**2.4**
		X2 start [Ohms]	**3.1**	R2 start [Ohms]	**2.3**
		X2 max [Ohms]	**3.2**	R2 max [Ohms]	**2.3**

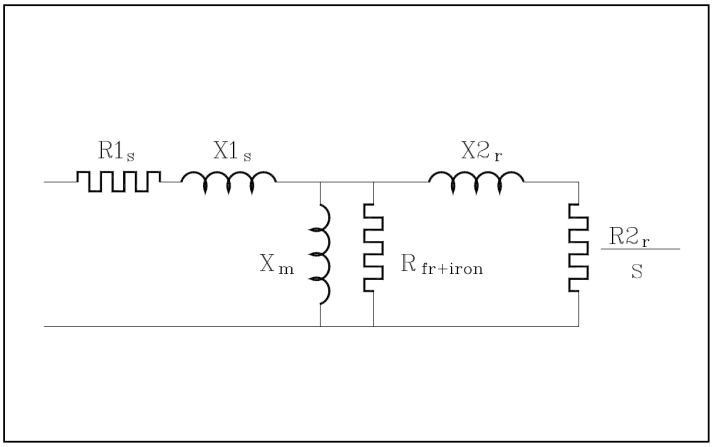

Data based on situation 5/17/2016
All data subject to tolerances in accordance with IEC

F.2 WIKA Pressure Transducer Specifications

Electronic pressure measurement

Pressure transmitter for general industrial applications Model A-10

WIKA data sheet PE 81.60

Applications

- Machine building
- Machine tools
- Measurement and control technology
- Hydraulics and pneumatics
- Pumps and compressors

Special features

- Measuring ranges from 0 … 1 to 0 … 600 bar
- Non-linearity 0.25 % or 0.5 %
- Output 4 ... 20 mA, DC 0 ... 10 V, DC 0 ... 5 V and others
- Electrical connection: Angular connector form A and C, circular connector M12 x 1, cable outlet 2 m
- Process connection G ¼ A DIN 3852-E, ¼ NPT and others

Pressure transmitter model A-10

Description

The model A-10 pressure transmitter for general industrial applications is not only notable for its compact design, but it also offers excellent quality at an extremely competitive price.

The user can choose between a non-linearity of 0.25 % and 0.5 %. A free test certificate provides information on the measuring points recorded during manufacture.

The model A-10 is set up for worldwide use through the international cULus and GOST certification. The various pressure units and process connections required for particular operating conditions are available at short notice.

Data sheets showing similar products:
Pressure transmitter for general applications; model S-10; see data sheet PE 81.01

Part of your business

Measuring ranges

Relative pressure								
bar	**Measuring range**	**0 ... 1**	**0 ... 1.6**	**0 ... 2.5**	**0 ... 4**	**0 ... 6**	**0 ... 10** [1]	**0 ... 16** [1]	**0 ... 25** [1]
	Overpressure limit	2	3.2	5	8	12	20	32	50
	Measuring range	**0 ... 40**	**0 ... 60**	**0 ... 100**	**0 ... 160**	**0 ... 250**	**0 ... 400**	**0 ... 600**	
	Overpressure limit	80	120	200	320	500	800	1,200	
psi	**Measuring range**	**0 ... 15**	**0 ... 25**	**0 ... 30**	**0 ... 50**	**0 ... 100**	**0 ... 160** [1]	**0 ... 200** [1]	**0 ... 300** [1]
	Overpressure limit	30	60	60	100	200	290	400	600
	Measuring range	**0 ... 500**	**0 ... 1,000**	**0 ... 1,500**	**0 ... 2,000**	**0 ... 3,000**	**0 ... 5,000**	**0 ... 10,000**	
	Overpressure limit	1,000	1,740	2,900	4,000	6,000	10,000	17,400	

Absolute pressure								
bar	**Measuring range**	**0 ... 1**	**0 ... 1.6**	**0 ... 2.5**	**0 ... 4**	**0 ... 6**	**0 ... 10**	**0 ... 16**	**0 ... 25**
	Overpressure limit	2	3.2	5	8	12	20	32	50
psi	**Measuring range**	**0 ... 15**	**0 ... 25**	**0 ... 30**	**0 ... 50**	**0 ... 100**	**0 ... 150**	**0 ... 200**	**0 ... 300**
	Overpressure limit	30	60	60	100	200	290	400	600

Vacuum and +/- measuring range						
bar	**Measuring range**	**-1 ... 0**	**-1 ... +0.6**	**-1 ... +1.5**	**-1 ... +3**	**-1 ... +5**
	Overpressure limit	2	3.2	5	8	12
	Measuring range	**-1 ... +9**	**-1 ... +15**	**-1 ... +24**		
	Overpressure limit	20	32	50		
psi	**Measuring range**	**-30 inHG ... 0**	**-30 inHG ... +15**	**-30 inHG ... +30**	**-30 inHG ... +60**	**-30 inHG ... +100**
	Overpressure limit	30	60	60	150	250
	Measuring range	**-30 inHG ... +160**	**-30 inHG ... +200**	**-30 inHG ... +300**		
	Overpressure limit	350	450	600		

1) If the medium water is measured, a higher overpressure limit is recommended.

The given measuring ranges are also available in kg/cm², MPa and kPa.
Other measuring ranges available on request

Vacuum resistance
Yes

Output signal

Signal type	Signal
Current (2-wire)	4 ... 20 mA
Voltage (3-wire)	DC 0 ... 10 V
	DC 0 ... 5 V
	DC 1 ... 5 V
	DC 0.5 ... 4.5 V
Ratiometric (3-wire)	DC 0.5 ... 4.5 V

Other output signals available on request

Depending on the signal type the following loads apply:

Signal type	Load in Ω
Current (2-wire)	≤ (power supply - 8 V) / 0.02 A
Voltage (3-wire)	> maximum output signal / 1 mA
Ratiometric (3-wire)	> 4.5k

Voltage supply

Power supply

Output signal	Power supply	
	Standard	Option
4 ... 20 mA	DC 8 ... 30 V	DC 8 ... 35 V [1]
DC 0 ... 10 V	DC 14 ... 30 V	DC 14 ... 35 V
DC 0 ... 5 V	DC 8 ... 30 V	DC 8 ... 35 V
DC 1 ... 5 V	DC 8 ... 30 V	DC 8 ... 35 V
DC 0.5 ... 4.5 V	DC 8 ... 30 V	DC 8 ... 35 V
DC 0.5 ... 4.5 V ratiometric	DC 5 V ± 10 %	-

1) Not possible with non-linearity 0.25 % BFSL

The power supply for the pressure transmitter must be made via an energy-limited electrical circuit in accordance with section 9.3 of UL/EN/IEC 61010-1, or an LPS to UL/EN/IEC 60950-1, or class 2 in accordance with UL1310/UL1585 (NEC or CEC). The power supply must be suitable for operation above 2,000 m should the pressure transmitter be used at this altitude.

Total current consumption

Signal type	Total current consumption
Current (2-wire)	Signal current, max. 25 mA
Voltage (3-wire)	8 mA
Ratiometric (3-wire)	8 mA

Accuracy

Optionally the model A-10 is available with an improved non-linearity. Depending on the selected non-linearity the following values result:

	Standard	Option
Non-linearity per BFSL (IEC 61298-2)	≤ ±0.5 % of span	≤ ±0.25 % of span
Measuring deviation of the zero signal	Typical: ≤ ±0.5% of span Maximum: ≤ ±0.8 % of span	Typical: ≤ ±0.15% of span Maximum: ≤ ±0.4 % of span
Accuracy at room temperature [1]	≤ ±1 % of span	≤ ±0.5 % of span ≤ ±0.6 % of span (at DC 0 ... 5 V)

1) Including non-linearity, hysteresis, zero offset and end value deviation (corresponds to measured error per IEC 61298-2), calibrated in vertical mounting position with process connection facing downwards

Non-repeatability
≤ 0.1 % of span

Signal noise
≤ ±0.3 % of span

Temperature error at 0 ... 80 °C
- Typical: 1 % of span
- Maximum: 2.5 % of span

Long-term drift
≤ ±0.1 % of span

Time response

Settling time
< 4 ms

Switch-on time
< 15 ms

Operating conditions

Ingress protection (per IEC 60529)
see table "Specifications"

Vibration resistance
- 10 g (IEC 60068-2-6, under resonance)
- 20 g available on request

Shock resistance
500 g (IEC 60068-2-27, mechanical)

Service life
10 million load cycles

Temperatures

Permissible temperature ranges		
	Standard	Option
Ambient	0 ... +80 °C	-30 ... +100 °C
Medium	0 ... +80 °C	-30 ... +100 °C
Storage	-20 ... +80 °C	-30 ... +100 °C

Reference conditions (per IEC 61298-1)

Temperature
15 ... 25 °C

Atmospheric pressure
860 ... 1,060 mbar

Humidity
45 ... 75 % relative

Power supply
DC 24 V

Mounting position
as required

Process connections

Standard	Thread size
EN 837	G ⅛ B [1]
	G ¼ B
	G ¼ female
	G ⅜ B
	G ½ B
DIN 3852-E [2]	G ¼ A
	G ½ A
	M14 x 1.5
ANSI/ASME B1.20.1	⅛ NPT [1]
	¼ NPT
	¼ NPT female
	½ NPT
DIN 16288	M20 x 1.5
ISO 7	R ¼
	R ⅜
	R ½
KS	PT ¼
	PT ½
	PT ⅜
SAE [2] [3]	7/16-20 UNF O-ring BOSS
	9/16-18 UNF O-ring BOSS

1) Maximum measuring range 400 bar
2) Maximum overpressure limit of 600 bar
3) Maximum permissible temperature -10 ... +100 °C

All process connections are available, as standard, with an entry bore of diameter 3.5 mm.
Optional diameters for:
- G ¼ A DIN 3852-E: Ø 6 mm, Ø 0.6 mm, Ø 0.3 mm
- ¼ NPT: Ø 6 mm, Ø 0.6 mm, Ø 0.3 mm

Sealings
For the process connections of the following standards the listed sealing materials are available.

Standard	Standard	Option
EN 837	Copper	Stainless steel
DIN 3852-E	NBR	FKM
SAE	FKM	-

The sealings listed under "Standard" are included in the delivery.

F.3 Endevco Pressure Transducer Specifications

Endevco

Model 8530B
Piezoresistive pressure transducer

Features

- 200 to 1000 psia
- Absolute reference

M37 electrical receptacle

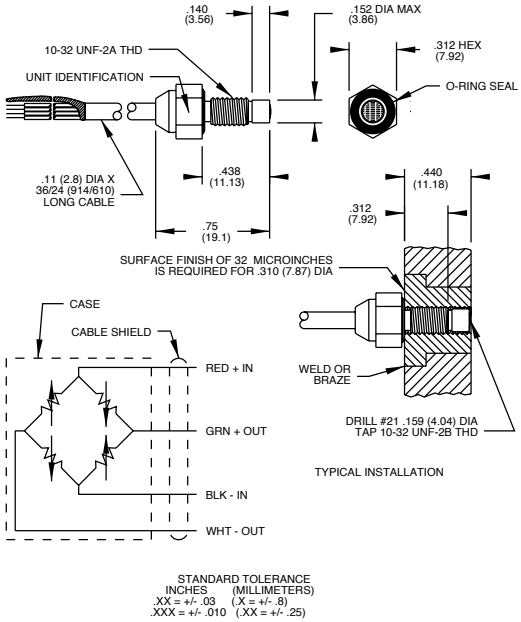

Description

The Endevco® model 8530B is a miniature, high sensitivity piezoresistive pressure transducer for measuring absolute pressure. The volume behind the diaphragm is evacuated and glass sealed to provide an absolute pressure reference. Full scale output is 300 mV with high overload capability and high frequency response. It is available in ranges from 200 psia to 1000 psia. See model 8530C for lower pressure ranges.

Endevco pressure transducers feature an active four-arm strain gage bridge diffused into a sculptured silicon diaphragm for maximum sensitivity and wideband frequency response. Self-contained hybrid temperature compensation provides stable performance over the temperature range of 0°F to 200°F (-18°C to +93°C). Endevco transducers also feature excellent linearity and provide stable performance over the temperature range of 0°F to 200°F (-18°C to +93°C). Endevco transducers also feature excellent linearity (even to 3X range), high shock resistance, and high stability during temperature transients.

The model 8530B is available with metric M5X0.8 mounting threads as 8530B-XXM5 on special orders. Also available with integral four-pin connector as model 8530B-XXM37. The standard cable length is 30 inches. Alternate lengths are available in quantity by using part number 8530B-XXX-ZZZ where "XXX" is the pressure range and "ZZZ" is the cable length in inches

Endevco model 136 three-channel system, model 4428A or 4430A signal conditioner, or OASIS 2000 computer-controlled system are recommended as signal conditioner and power supply.

MEGGiTT
smart engineering for
extreme environments

Model 8530B
Piezoresistive pressure transducer

Endevco

Specifications

	Units	-200	-500	-1000
Range	psia	0–200	0–500	0–1000
Sensitivity [1]	mV/psi	1.5 ±0.5	0.6 ±0.2	0.3 ±0.1
Combined: non-linearity,				
non repeatability, pressure hysteresis [2]	% FSO RSS max	0.50	0.50	1.0
Non-linearity, independent	% FSO typ	0.2	0.2	0.2
Non-repeatability	% FSO typ	0.1	0.1	0.1
Pressure hysteresis	% FSO typ	0.1	0.1	0.1
Zero measurand output [3]	mV max	±10	±10	±10
Zero shift after 3X over range	±% 3X FSO max (typ)	0.2 (0.05)	0.2 (0.05)	
after 2.5X over range	±% 2.5X FSO max (typ)			0.2 (0.1)
Thermal zero shift				
From 0 to 200°F (-18°C to +93°C)	±% FSO max	3	3	3
Thermal sensitivity shift				
From 0 to 200°F (-18°C to +93°C)	±% max	4	4	4
Resonant frequency	Hz	750 000	1 000 000	› 1 000 000
Non-linearity at 3X over range	% 3X FSO	1.5	2.0	2.0 @ % 2.5X FSO
Thermal transient response per	psi / °F	0.02	0.02	0.04
ISA-S37.10, PARA. 6.7, procedure I	psi / °C	0.04	0.04	0.07
Photoflash response [4]	equiv psi	5	10	20
Warm-up time [5]	ms	1	1	1
Acceleration sensitivity	equiv. psi/g	0.0003	0.0002	0.0002
Burst pressure (diaphragm)	psia min	800	2000	4000
Case pressure [6]	psia min	1000	5000	5000

Electrical

Full scale output	300 ±100 mV at 10.0 Vdc
Supply voltage [7]	10.0 Vdc recommended, 18 Vdc maximum
Electrical configuration	Active four-arm piezoresistive bridge
Polarity	Positive output for increasing pressure
Resistance	
Input	2000 ±800 ohms
Output	1600 ±500 ohms
Isolation	100 megohms minimum at 50 Volts, leads to case, leads to shield, shield to case
Noise	5 microvolts rms typical, DC to 50 000 Hz; 50 microvolts rms maximum, DC to 50 000 Hz

Mechanical

Case, material	Stainless steel (17-4 PH CRES)
Cable, integral	Four conductor No. 32 AWG Teflon insulated leads, braided shield, silicone jacket
Dead volume port (+)	0.0003 cubic inches (0.005 cc)
Mounting/torque	10-32 UNF-2A threaded case 0.438 inch (11.12 mm) long / 15 ±5 lbf-in (1.7 ±0.6 Nm)
Weight	2.3 grams (cable weighs 9 grams/meter)

Environmental

Media [8] [9]	Clean dry gas. Contact factory for protective modifications for other media.
Temperature [10]	-65°F to +250°F (-54°C to +121°C)
Vibration	1000 g pk
Acceleration	1000 g
Shock	20 000 g, 100 microsecond haversine pulse
Humidity	Isolation resistance greater than 100 megohms at 50 V when tested per MIL-STD-202E, method 103B, test condition B

Calibration data [11]

Data supplied for all parameters in Certified Performance section. Optional calibrations available for all parameters in Typical Performance section

Included accessories

EHR93	O-ring, Viton

Optional accessories

EHR96	O-ring, Fluorosilicone
24328-3	4 conductor shielded cable, white

Notes:

1. 1 psi = 6.895 kPa = 0.069 bar.
2. FSO (Full Scale Output) is defined as transducer output change from 0 to + full scale pressure.
3. Zero Measurand Output (ZMO) is the transducer output with 0 psia applied.
4. Per ISA-S37.10, Para. 6.7, Proc. II.
5. Warm-up time is defined as elapsed time from excitation voltage "turn on" until the transducer output is within ±1% of reading accuracy.
6. Case pressure identifies media containment pressure in the event of diaphragm rupture.
7. Use of excitation voltages other than 10.0 Vdc requires manufacture and calibration at that voltage since thermal errors increase with high excitation voltages.
8. Internal seals are epoxy and are compatible with clean dry gas media. Media in measurand port is exposed to CRES, Parylene C, epoxy and the Viton O-ring. Not suitable for use with high pH or low pH liquids, long term exposure to water, or exposure to solvents which may attack epoxies.
9. O-ring, Parker 5-125, compound V747-75 (Viton®) is supplied unless otherwise specified on purchase order. Fluorosilicone O-ring, for leak tight operation below 0°F is available on special order.
10. Units can be compensated over any 200°F (93°C) span from -65°F to +250°F (-54°C to +121°C) on special order.
11. Maintain high levels of precision and accuracy using Endevco's factory calibration services. Call Endevco's inside sales force at 800-982-6732 for recommended inervals, pricing and turn around time for these services as well as for quotations on our standard products.

APPLIES TO CALIFORNIA FACILITY

(800) 982-6732 • (949) 493-8181 fax (949) 661-7231 • www.endevco.com • Email: applications@endevco.com
021708

MEGGiTT
smart engineering for
extreme environments

F.4 Flowmeter Specifications

044-40-TA FLOWMETER CALIBRATION DATA 044/255

CUSTOMER	CUST. P.O. No	REF. CURVE NUMBER
		0313-02-02

Max. Flow	Min. Flow	Units	Metering Fluid	Date
65625	3281	std. ml/min	Air	05-Mar-2013

Model Number		**Metering Temperature**	70.0 °F
Tube Number	044-40-TA	**Metering Pressure**	14.70 psia
Serial Number		**Metering density**	0.0012 g/ml
Float Material	Tantalum	**Metering Viscosity**	0.01812 cp
Float Density	16.58 g/ml	**Density at STD.Cond**	0.0012 g/ml
STD. Conditions	STP: 1 atm @ 70 °	**Accuracy**	+/-2%FS
Room Temperature	70.0 °F	**Barometric Pressure**	14.70 psia

SCALE READINGS AT CENTER OF FLOAT

Scale Reading (mm)	Flow
150	65625
140	61052
130	55641
120	51018
110	46019
100	41525
90	36977
80	32420
70	28186
60	23838
50	19320
40	15235
30	11250
20	6944
10	3281

AALBORG INSTRUMENTS & CONTROLS, INC.
20 Corporate Drive, Orangeburg, NY 10962 USA * http://www.aalborg.com
Phone: +1 (845) 770-3000 * Toll-free (800) 866-3837 * FAX: +1 (845) 770-3010

METER SIZING FOR P, PX, T, TX AND S METERS

Flow capacity tables 6, 7, 8, 9 and 10 (pages 61 to 64) are based on calibrations at standard conditions, meaning 14.7 psia (1 atm) pressure and 70 °F (21.1 °C).

Tables list maximum flow rates of flow tubes. The usable range of meters is at least 10:1, often more. Thus, as a rule of thumb, to estimate the minimum metering limit divide the flow rates listed, by ten.

For gases or liquids with fluid properties not greatly different from the calibration media, tables apply directly, when working pressure and temperature are also approximately standard.

Where the above conditions do not apply the maximum flow rates of the metered fluids are converted to equivalent standard flow rates of air or water.

To do this calculate "K" as shown in charts, multiply the maximum flow rate with this factor, and select the appropriate flow tube size from the Flow Capacity tables 6, 7, 8, 9 and 10 (pages 61 to 64).

gas flow

$$Q_{air} = K_{gas} \times Q_{gas}$$

$$K_{gas} = \sqrt{G \times \frac{T_{act}}{T_o} \times \frac{P_o}{P_{act}}}$$

where:

Q_{air} = equivalent air flow capacity at Standard Conditions (SPT).
Q_{gas} = maximum flow of metered gas.
G = specific gravity of metered gas (from table 5).
T_{act} = absolute temperature at flow condition, deg R or deg K.
T_o = absolute temperature at Standard Conditions. (STP) deg R (530) or deg K (294).
P_{act} = pressure at flow conditions, psia.
P_o = pressure at Standard Conditions (STP), (14.7 psia).

liquid flow

$$Q_{water} = K_{liq} \times Q_{liq}$$

$$K_{liq} = \sqrt{\frac{(d_F - d_W)}{(d_F - d_L)} \times \frac{d_L}{d_W}}$$

where:

Q_{water} = equivalent water flow capacity at Standard Conditions (STP).
Q_{liq} = maximum flow of metered liquid.
d_F = density of float selected, (see table 3), (g/ml).
d_L = density of metered liquid, (g/ml).
d_W = density of water at Standard Conditions (STP) (1.0 g/ml).

CALCULATION VS. CALIBRATION FOR P, PX, S, T AND TX METERS

In case of liquid flows at each major point along the scale, sample volumes are collected in a buret of a volumetric flask during measured time intervals. Volumes are interpolated to a unit of time such as for example [mL/min] or [cu. ft/hr] etc. A table or a graph is then constructed to establish a complete set of calibration data. In case of gas flows, calibration data can be similarly developed, except that collection of sample volumes is accomplished by means of gas sampling devices, the simplest of which is a "soap bubble" meter.

It is very important that the correction factors as calculated from the accompanying equations are used for sizing only. These relationships are greatly simplified and will not provide precise predictable flow corrections. It is always best practice to calibrate meters for non-standard conditions on site, by using reliable means of calibration.

F.5 Tachometer Specifications

ACISION®

Non-Contact & Contact

TACHOMETER

TM1100

Measuring Range

Non-Contact: 1.00 - 99,999 rpm

Contact: 1.00 - 19,999 rpm

The Acision TM1100 Combination Hand-Held Digital Tachometer combines the best features of both contact and noncontact models to accurately measure RPM, surface speed and length.

When using the non-contact mode, rotational speed (RPM) is measured using a visible beam of light. The Acision TM1100 can be up to 24 inches away from the small piece of reflective tape that is affixed to the rotating element. In the contact operating mode, the speed is sensed by directly contacting the rotating device using the cone tip or surface speed wheel supplied with the instrument.

The Acision TM1100 rugged construction, portability and outstanding features make It an ideal choice for maintenance personnel, machine operators or others in a wide variety of machinery and material handling applications. nd material handling applications.

FEATURES

- Measures speeds from 1.00 up to 99,999 rpm
- Accuracy of 0.02% with a resolution up to 0.01 rpm
- Built-in memory stores maximum, minimum, average and last reading for recall to the display
- Take accurate measurements from up to 24 inches away from rotating equipment
- NEW - **Molded Rubber Shell** provides additional physical and environmental protection
- NEW - Now includes larger 6 inch circumference Surface Speed Wheel standard
- NEW - Can be set for use with 2 optional-sized surface speed wheels (12 in. or 10 cm circumference)

over ➡

TM1100

Data & Specifications

Specifications

Resolution	.01 from 0 –100 .1 from 100 – 1,000 1 from 1000 – 99,999
Accuracy	± 0.02% of reading or ±1 digit
Display	5-Digit LCD, 10mm high
Decimal Point	Automatic
Memory System	Maximum, minimum, average and last reading (retained in memory for the life of batteries)
Measurement System	
Non-Contact	Visible LED light beam
Contact	Contact adapter
Engineering units	
RPM	RPM
Surface Speed	Feet/min, inches/min and meters/min
Length	Feet, inches, meters

Sensing Distance	Up to 24 inches (60 cm)
Display Update Time	0.5 seconds or one measuring period
Auto Power Off	After 30 seconds of non-use (minimum, maximum average, and last reading retained in memory)
Battery Life	40 hours continuous use (approx.) with alkaline batteries
Battery Type	2 AA (1.5 V) or rechargeable
Weight	6 ounces (170 grams)
Housing Material	ABS Plastic
Operating Temperature	32 to 122° F (0 to 50° C)
Storage Temperature	– 4 to 158° F (–20 to 70° C)

Measuring Ranges – rpm

Optical	1 – 99,999 rpm
Mechanical	1 – 99,999 rpm

Measuring Ranges – speed

Wheel Size	6"	12"	0.1 m
m/min	0.10–1524	0.40–609.6	0.10–1999
ft/min	0.40–5000	0.40–2000	0.40–6550
in/min	4.0–60.00	4.00–24.000	4.00–78.700
m/sec	0.10–25.40	0.10–10.16	0.10–33.30
ft/sec	0.10–83.33	0.10–33.33	0.10–109

Measuring Ranges – length

0 – 99,999 m, / 0 – 99,999 ft / 0 – 99,999 in

1. **Units of Measure Indicators** show the user-selected units of measure.
2. **Contact Indicator** shows if contact or non-contact operation is selected.
3. **Low Battery Indicator** alerts the operator if the batteries are low.
4. **On-Target Indicator** confirms that the measurements are reliable.
5. **Memory Indicators** are illuminated when the maximum, minimum, average and last readings are recalled to the display for viewing.

The TM1100 is supplied as a complete kit including: Gauge, contact adapter, cone tip adapter, 6" circumference universal surface speed wheel, reflective tape, operating instructions and foam-fitted, hard-plastic carrying case.

ACISION

FOR ADDITIONAL INFORMATION OR TO PLACE AN ORDER CALL

F.6 Fluke power scope meter Specifications

FLUKE®

TECHNICAL DATA

Fluke MDA-510 and MDA-550 Motor Drive Analyzer

KEY MEASUREMENTS
Inverter output voltage, DC bus voltage and ripple voltage, harmonics, unbalance

THREE POWERFUL TEST TOOLS IN ONE
Motor-drive analyzer, waveform analyzer and recording data logger all in one

HIGHEST SAFETY RATING IN THE INDUSTRY
600 V CAT IV/1000 V CAT III rated for use at the service entrance and downstream

Simplify complex motor-drive troubleshooting with guided test setups and automated drive measurements that provide reliable, repeatable test results.

The new Fluke MDA 510 and MDA 550 Motor-Drive Analyzers save time and eliminate the hassle of setting up complex measurements, while simplifying the troubleshooting process. Simply select a test and the step-by-step guided measurements show you where to make voltage and current connections, while the preset measurement profiles ensure you will capture all the data you need for each critical motor-drive section—from the input to the output, the DC bus, and the motor itself. From basic to advanced measurements, the MDA-500 Series has you covered, and with a built-in report generator you can quickly and easily generate as-found, and as-left reports with confidence.

The MDA-510 and MDA-550 are the ideal portable motor-drive analysis test tools, and can help safely locate and troubleshoot typical problems on inverter type motor-drive systems.

- **Measure key motor-drive parameters** including voltage, current, DC Bus voltage level and AC ripple, voltage and current unbalance and harmonics (MDA-550), voltage modulation, and motor shaft voltage discharges (MDA-550).
- **Perform extended harmonics measurements** to identify the effects of low and high order harmonics on your electrical power system.
- **Conduct guided measurements** for motor-drive input, DC bus, drive output, motor input and shaft measurements (MDA-550) with graphical step-by-step voltage and current connection diagrams.
- **Use simplified measurement setup** with preset measurement profiles to automatically trigger data collection based on the chosen test procedure.
- **Create reports quickly and easily** that are perfect for documenting troubleshooting and collaborative work with others.
- **Measure additional electrical parameters** with full 500 MHz oscilloscope, meter and recording capability for complete range of electrical and electronic measurement on industrial systems.

Specifications

Measurement Function	Specification
DC voltage (V dc)	
Maximum voltage with 10:1 or 100:1 probe	1000 V
Maximum resolution with 10:1 or 100:1 probe	1 mV
Full scale reading	999 counts
Accuracy at 4 s to 10 us/div	± (3 % + 6 counts)
AC voltage (V ac)	
Maximum voltage with 10:1 or 100:1 probe	1000 V
Maximum resolution with 10:1 or 100:1 probe	1 mV
Full scale reading	999 counts
50 Hz	± (3 % + 10 counts) - 0.6 %
60 Hz	± (3 % + 10 counts) - 0.4 %
60 Hz to 20 kHz	± (4 % + 15 counts)
20 kHz to 1 MHz	± (6 % + 20 counts)
1 MHz to 25 MHz	± (10 % + 20 counts)
True-rms voltage (V ac+dc)	
Maximum voltage with 10:1 or 100:1 probe	1000 V
Maximum resolution with 10:1 or 100:1 probe	1 mV
Full scale reading	1100 counts
DC to 60 Hz	± (3 % + 10 counts)
60 Hz to 20 kHz	± (4 % + 15 counts)
20 kHz to 1 MHz	± (6 % + 20 counts)
1 MHz to 25 MHz	± (10 % + 20 counts)
PWM voltage (V pwm)	
Purpose	To measure on pulse width modulated signals, like motor drive inverter outputs
Principle	Readings show the effective voltage based on the average value of samples over a whole number of periods of the fundamental frequency
Accuracy	As Vac+dc for sinewave signals
Peak voltage (V peak)	
Modes	Max peak, min peak, or pk-to-pk
Maximum voltage with 10:1 or 100:1 probe	1000 V
Maximum resolution with 10:1 or 100:1 probe	10 mV
Accuracy	
Max peak, min peak	± 0.2 division
Pk-to-pk	± 0.4 division
Full scale reading	800 counts

Current (AMP) with current clamp	
Ranges	Same as V ac, Vac+dc or V peak
Scale Factors	0.1 mV/A, 1 mV/A, 10 mV/A, 20 mV/A, 50mV/A, 100 mV/A, 200 mV/A, 400 mV/A
Accuracy	Same as Vac, Vac+dc or V peak (add current clamp accuracy)
Frequency (Hz)	
Range	1.000 Hz to 500 MHz
Full scale reading	999 counts
Accuracy	± (0.5 % + 2 counts)
Voltage/Herz ratio (V/Hz)	
Purpose	To show the measured V PWM value (see V PWM) divided by the fundamental frequency on variable ac motor speed drives
Accuracy	% Vrms + % Hz
Voltage unbalance drive input	
Purpose	To show the highest percentage difference of one of the phase vs average of the 3 true-rms voltages
Accuracy	Indicative percentage based on Vac+dc values
Voltage unbalance drive output and motor input	
Purpose	To show the highest percentage difference of one of the phase vs average of the 3 PWM voltages
Accuracy	Indicative percentage based on V PWM values
Current unbalance drive input	
Purpose	To show the highest percentage difference of one of the phase vs average of the 3 AC current values
Accuracy	Indicative percentage based on Aac+dc values
Current unbalance drive output and motor input	
Purpose	To show the highest percentage difference of one of the phase vs average of the 3 AC current values
Accuracy	Indicative percentage based on A ac values
Rise and fall time	
Readings	Voltage difference (dV), time difference (dt), voltage vs time difference (dV/dt), overshoot
Accuracy	As oscilloscope accuracy
Harmonics and spectrum	
Harmonics	DC to 51st
Spectrum ranges	1…9 kHz, 9-150 kHz (20 MHz filter on), up to 500 MHz (voltage modulation)
Shaft voltage	
Events / second	Indicative percentage based on rise and fall time (Impulse discharges) measurements
Report data capture	
Number of screens	Typical 50 screens can be saved in reports (depends on compression ratio)
Transfer to PC	Using 2 GB USB stick or mini-USB to USB cable and FlukeView™ 2 for ScopeMeter™
Probe settings	
Voltage Probe	1:1, 10:1, 100:1, 1000:1, 20:1, 200:1
Current Clamp	0.1 mV/A, 1 mV/A, 10 mV/A, 20 mV/A, 50 mV/A, 100 mV/A, 200 mV/A, 400 mV/A
Shaft Voltage Probe	1:1, 10:1, 100:1

F.7 Fluke current probe Specifications

FLUKE ®

80i-110s
AC/DC Current Probe
Instructions

Introduction

The Fluke 80i-110s (the Probe or Product) is a clamp-on AC/DC Current Probe that reproduces current waveforms found in commercial and industrial power distribution systems. The Probe performance is optimized for accurate reproduction of currents at line frequency and up to the 50th harmonic waveform. The 80i-110s is also compatible with any instrument capable of millivolt measurements.

The Probe provides these benefits:

- Accurate AC, DC, and AC+DC current measurements for Electrical, Electronic, and Automotive applications.
- Shielded for high-noise immunity around electronic motor drives and ignition systems.
- Wide measurement range from 50 mA to 100 A, useful to 10 mA.
- Jaw shaped for easy access to cramped spaces.
- Tactile barrier (see Figure 1, item 1).
- Safety-designed 600 V insulated BNC - compatible with Fluke ScopeMeter® test tools, Power Harmonic analyzers, and oscilloscopes.
- Selectable output of 10 millivolts/1 amp for the 100 A range, and 100 mV/1 A for the 10 A range.

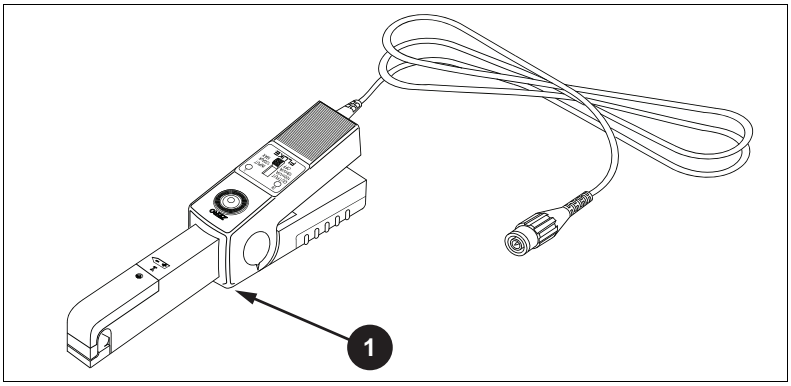

Figure 1. 80i-110s AC/DC Current Probe

PN 4862926 October 2005, Rev. 1, 1/17

482287230777

If the Probe does not perform properly, use these steps to help isolate the problem:

1. Test the battery. Be sure that the green ON-indicator lights when you select the 10 mV/A range or the 100 mV/A range.
2. Inspect the jaw mating surface for cleanliness. If any foreign material is present, the jaws will not close properly and errors will result.
3. Verify that the Probe is zeroed properly. For zeroing be sure that the ScopeMeter test tool or oscilloscope is DC-coupled.
4. Verify that the function selection on the ScopeMeter test tool or oscilloscope is correct, for example, the display vertical resolution is not too low or too high.

Repairs or service not covered in this document must be performed only at a Fluke Service Center. A Probe under warranty will be repaired or replaced (at Fluke's discretion) and returned at no charge.

Cleaning and Storage

Periodically wipe the case with a damp cloth and detergent. Do not use abrasives or solvents. Open the jaws and wipe the magnetic pole pieces with a lightly oiled cloth. Do not allow rust or corrosion to form on the magnetic core ends.

If the Probe is not used for long time periods (>60 days) the battery should be removed and stored separately.

Accessories

An adapter accessory is required to use the Probe with a digital multimeter. The BNC-to-Banana Adapter, Fluke Part PM9081/001, is available to order.

Specifications

Maximum Voltage between any Terminal and Earth Ground	600 V
Dimensions	67 mm x 231 mm x 36 mm (2.6 in x 9.1 in x 1.4 in)
Weight	330 g (11.6 oz), battery included
Output Cable	1.6 m (63 in)
Maximum Conductor Size	11.8 mm (0.46 in)
Maximum Jaw Opening	12.5 mm (0.49 in)
Temperature	
Operating	0 °C to 50 °C (32 °F to 122 °F)
Storage	-30 °C to +70 °C (-22 °F to +158 °F)
Relative Humidity (Operating)	
0 % to 85 %	0 °C to 35 °C (32 °F to 95 °F)
0 % to 45 %	35 °C to 50 °C (95 °F to 122 °F)
Altitude	
Operating	<2000 m (<6560 ft)
Storage	<12 000 m (<40 000 ft)
Demagnetize Probe	Open and close Probe jaws several times

Battery

Type ..... 9 volt, IEC 6LR61

Consumption ..... 8.6 mA typical
12 mA maximum

Service life with Alkaline IEC 6LR61 battery

Typical..... 55 hours

Minimum..... 40 hours

Battery indicator (ON)..... Green LED dims when battery voltage is <6.5 V

Safety

General..... IEC 61010-1: Pollution Degree 2

Measurement ..... IEC 61010-2-032: CAT III 600 V

Electromagnetic Compatibility (EMC)

International..... IEC 61326-1: Portable Electromagnetic Environment
CISPR 11: Group 1, Class A

Group 1: Equipment has intentionally generated and/or use conductively coupled radio-frequency energy which is necessary for the internal functioning of the equipment itself.

Class A: Equipment is suitable for use in all establishments other than domestic and those directly connected to a low voltage power supply network which supplies buildings used for domestic purposes. There may be potential difficulties in ensuring electromagnetic compatibility in other environments, due to conducted and radiated disturbances.

Caution: This equipment is not intended for use in residential environments and may not provide adequate protection to radio reception in such environments.

Emissions that exceed the levels required by CISPR 11 can occur when the equipment is connected to a test object.

USA (FCC) ..... 47 CFR 15 subpart B. This product is considered an exempt device per clause 15.103.

Electrical Specifications

Valid temperature ..... 23 °C ±3 °C (73 °F ±5 °F).

Current Ranges ..... 0 A dc to 10 A dc or ac peak
0 A dc to 100 A dc or ac peak

Output Signals..... 10 A range: 100 mV/A
100 A range: 10 mV/A

Basic Accuracy (DC to 1kHz):

Input Current (DC or AC peak)	Error (after zero check)	
	Range 100 mV/A	Range 10 mV/A
0 A to 10 A	<3 % of reading +50 mA	-
0 A to 40 A	-	<4 % of reading +50 mA
40 A to 80 A	-	<12 % of reading +50 mA
80 A to 100 A	-	<15 % of reading

Extended Accuracy:

For other frequencies, refer to the appropriate input current range and add the error listed below to the "Basic Accuracy" error.

Frequency	Additional Error	
	Range 100 mV/A	Range 10 mV/A
1 kHz to 5 kHz	3 %	3 %
5 kHz to 20 kHz	12 %	12 %
>20 kHz	not specified	not specified

Input Load Impedance
(of host instrument) ..... >1 MΩ in parallel with up to 100 pF

Useful Bandwidth (-3 dB) ..... 0 kHz to 100 kHz

Rise or Fall Time ..... <4 µsec

Output noise level

Range 10 mV/A typical..... 480 µV pk-pk
Range 100 mV/A typical..... 3 mV pk-pk

Max. nondestructive current..... 0 kHz to 2 kHz 140 A peak
2 kHz to 10 kHz 110 A peak
10 kHz to 20 kHz 70 A peak
20 kHz to 50 kHz 30 A peak
50 kHz to 100 kHz 20 A peak

Temperature coefficient..... 2000 ppm/°C max. for temperature from 0 °C to 50 °C (32 °F to 132 °F)

Performance Verification

Verify Probe accuracy with the test setup shown in Figure 5. Required test equipment is defined in Table 1. Toroid coil construction is illustrated in Table 2.

To verify the Probe accuracy:

1. Set up connection.
2. Make the checks called for in Table 3 (100 mV/A).
3. Make the checks called for in Table 4 (10 mV/A).

Table 1. Required Test Equipment

Required	Recommended
AD/DC Calibrator	Fluke 5520A
Digital Multimeter (DMM)	Fluke 45
Small insulated screwdriver	Spectrol
Banana-to-BNC Adapter	Fluke PM9081/001
10-turn Toroid Coil	See Figure 6

Pulse Valves

Ultra Low Leak Extreme Performance Valve

Pulse Valves solenoid valves offer outstanding potential for precision control of Laser Spectroscopy Gas Analysis. Combining high speed, ultra low leak rate, high flow, and high temperature capability in a small size; this rugged valve operates with extreme repeatability and is constructed of non-corroding, passivated stainless steel. Pulse Valves coils are rated for continuous duty and are potted to exclude the environment.

Features

- Smallest footprint in its class
- High speed response times of less than 2 ms
- 100% tested to leak-tight 1 x 10^{-7} cc/sec/atm Helium
- 100% duty cycle in environmental temperatures of up to 221°F (105°C)
- Pressures up to 1250 PSI (86.2 bar)
- Available with a variety of orifices, seals, and voltages to match your application
- RoHS compliant

Typical Applications

- Gas pulse generation for Laser Spectroscopy

Product Specifications

Physical Properties

Valve Type:
Inert Non Isolation
Valve Configuration:
2-Way Normally Closed
Media:
Gases
Operating Environment:
40 to 221°F (4 to 105°C)
Dimensions:
See Dimensions Page
Weight:
2.8 oz (79.4 g)
Porting:
A-LOK®, Flange
Internal Volume:
(Contact factory for details)

Electrical

Voltage (VDC):	20	28
Power (Watts):	12.1	11.2
Current (mA):	606	400
Resistance (Ohm):	33	70
(Ω±5% @ 70°F, 21°C)		
Connection		
12" Lead Wires Standard		

Wetted Materials

Poppet Materials*:
Vespel®**
PTFE
O-Ring:
FFKM (Kalrez®**)

**NOTE: Vespel and Kalrez are trademarks of Dupont.

* See accessories table under ordering information for additional poppet materials.

Performance Characteristics

Operating Pressures / Orifice Diameters:
1x10^{-5} Torr -1250 psi (86.2 bar)/ 0.004" (.10 mm)
0.020" (.51 mm)
0.031" (.79 mm)
1x10^{-5} Torr -750 psi (51.7 bar)/ 0.039" (99 mm)
Proof Pressure:
1.5X rated pressure
Response Time:
<2 ms cycling Down to 160µs with the Parker IOTA ONE Valve Driver. (See Accessories)
Leak Rate:
1 x 10^{-7} cc/sec/atm Helium
Recommended Filtration:
40 µm max
Orifice Shape:
Cone, No Cone (Cone improves exit stream uniformity)

Pulse Valves Ultra Low Leak Extreme Performance Valve

Mechanical Integration

Dimensions

1/4" [6.35 mm] A-LOK® CROSS-SECTION

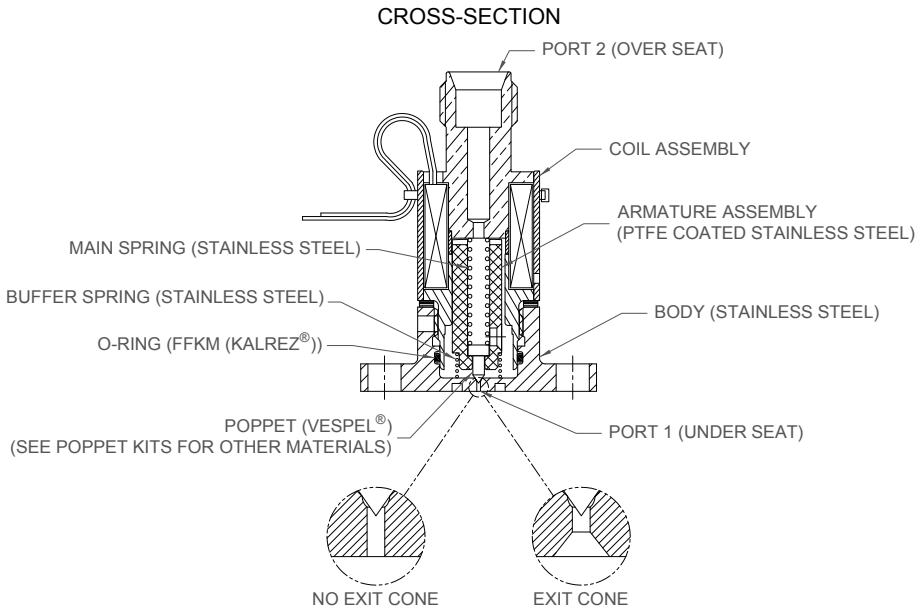

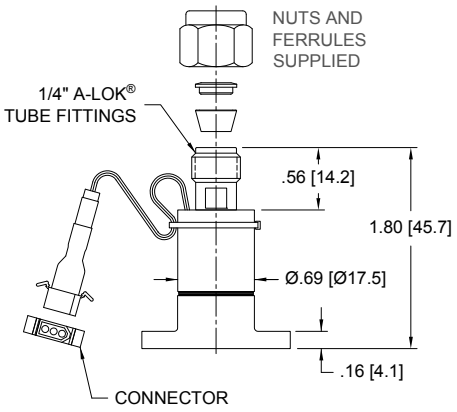

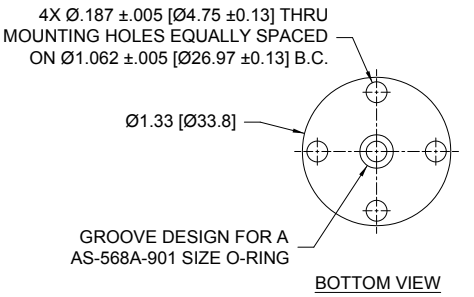

UNITS
IN. [mm.]

Dimensions of Solenoid Pulse Valve Orifice

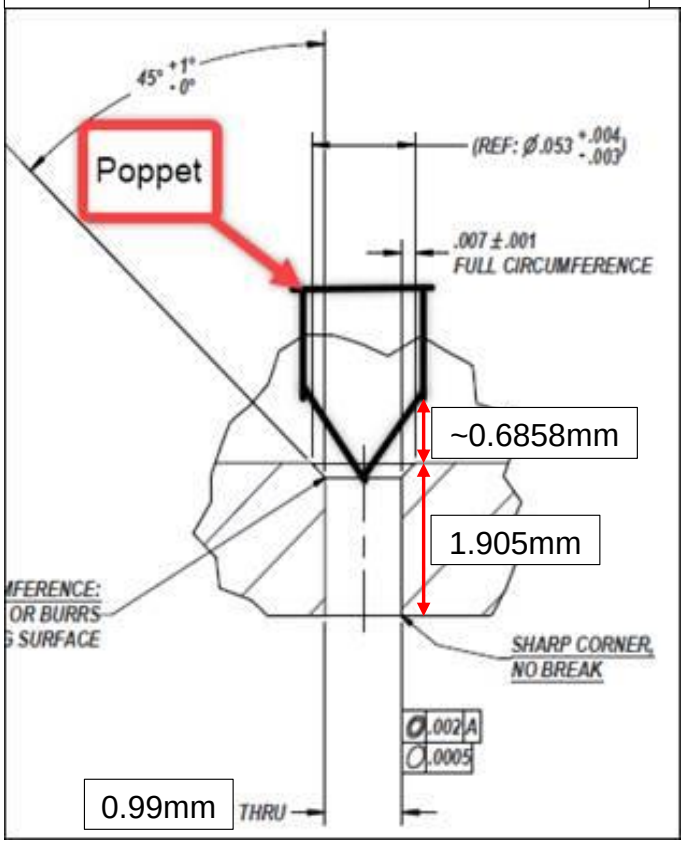

F.9 Hydraulic Atomising Nozzle Specifications

FINE SPRAY

HYDRAULIC ATOMIZING NOZZLES

S STANDARD ANGLE SPRAY | W WIDE ANGLE SPRAY

OVERVIEW: HYDRAULIC ATOMIZING

- Finely atomized, hollow cone spray without compressed air
- Very small drops often achieving misting performance
- Ideal for use in dust control and humidification applications
- Wall-mount options for installation on room walls, vessel bulkheads or pipeline
- Orifice inserts, cores and strainers are easily removed for inspection or cleaning
- Most models can be supplied with an internal strainer
- Spray angles: Standard – 43° to 94°, Wide – 112° to 120°
- Uniform spray distribution from .82 to 130 gph (3.1 to 492 lph)
- Operating pressures from 20 to 1000 psi (1.5 to 69 bar)

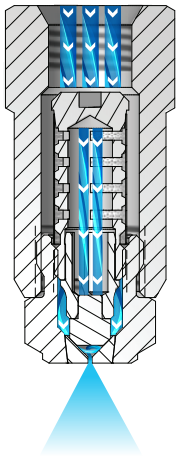

Hydraulic Atomizing Nozzles
The liquid passes through slots in the core component. The slots make the liquid spin in a circle at a very high speed. The energy from the spinning action causes the liquid to break up into very small droplets and form a hollow cone pattern as it exits the orifice.

HYDRAULIC ATOMIZING OPTIONS

LN
1/4" female conn.
Integral strainer

LNN
1/4" male conn.
Integral strainer

LND
1/4" female conn. with 1/2" male wall-mounting threads
Wall-mount
Integral strainer

LNND
1/4" male conn. with 1/2" male wall-mounting threads
Wall-mount
Integral strainer

N
1/4" female conn.

NN
1/4" male conn.

M
1/4" male conn.
Two-piece design

RELATIVE DROP SIZE IN MICRONS

10 to 100	100 to 500	500 to 1000	1000 to 5000

Drop size will vary based on flow rate and pressure.

ORDERING INFORMATION

HYDRAULIC ATOMIZING LN, LND, N AND M

Inlet Conn.	Nozzle Type	–	Material Code	Capacity Size

Example: 1/4 LN – SS 8

BSPT connections require the addition of a "B" prior to the inlet connection.
To order M with strainer, use ML as Nozzle Type.

HYDRAULIC ATOMIZING LN AND N

Inlet Conn.	Nozzle Type	–	Material Code	Capacity Size

Example: 1/4 LN – SS 8W

BSPT connections require the addition of a "B" prior to the inlet connection.

QUICK REFERENCE GUIDE

Model	Connection/Type	Connection Size (in.)	Materials	Page Number	
				Performance Data	Dimensions and Weights
LN	F	1/4	Brass, 303 stainless steel (SS), 316 stainless steel (316SS)	E6	E7
LNN	M	1/4			
LND	F, Wall-mount	1/4	Brass, 303 stainless steel (SS)		
LNND	M, Wall-mount	1/4			
N	F	1/4	Brass, 303 stainless steel (SS), 316 stainless steel (316SS), Polyvinyl chloride (PVC)		
NN	M	1/4	Brass, 303 stainless steel (SS), 316 stainless steel (316SS)		
M	M	1/4	Brass, 303 stainless steel (SS), 316 stainless steel (316SS), Polyvinyl chloride (PVC)		
LN-W	F	1/4	Brass, 303 stainless steel (SS), 316 stainless steel (316SS)	E7	
LNN-W	M	1/4			
N-W	F	1/4			
NN-W	M	1/4			

F = female thread; M = male thread. There is no material code for brass. Leave material code blank when ordering. Other materials available upon request.
For more dimensions and sizes, contact your sales engineer.

S PERFORMANCE DATA: STANDARD ANGLE SPRAY

Inlet Conn. (in.)	Nozzle Type							Capacity Size	Orifice Dia. Nom. (in.)	Core No.	Flow Rate Capacity (gallons per hour)									Spray Angle (°)		
	LN	LNN	LND	LNND	N	NN	M				30 psi	40 psi	60 psi	100 psi	200 psi	300 psi	500 psi	700 psi	1000 psi	40 psi	80 psi	300 psi
1/4	●	●						.30	.016	106	–	–	–	–	–	.82	1.1	1.3	1.5	–	–	51
	●	●						.40	.016	108	–	–	–	–	–	1.1	1.4	1.7	2.0	–	–	58
	●							.50	.016	109	–	–	–	–	1.1	1.4	1.8	2.1	2.5	–	–	63
	●	●	●	●	●	●	●	.60	.016	206	–	–	–	.95	1.3	1.6	2.1	2.5	3.0	–	35	65
	●	●	●	●	●	●	●	1	.020	210	–	1.0	1.2	1.6	2.2	2.7	3.5	4.2	5.0	45	62	72
	●	●	●	●	●	●	●	1.5	.020	216	1.3	1.5	1.8	2.4	3.4	4.1	5.3	6.3	7.5	65	70	72
	●	●	●	●	●	●	●	2	.028	216	1.7	2.0	2.4	3.2	4.5	5.5	7.1	8.4	10.0	70	75	77
	●	●	●	●	●	●	●	3	.028	220	2.6	3.0	3.7	4.7	6.7	8.2	10.6	12.5	15.0	65	70	73
	●	●	●	●	●	●	●	4	.042	220	3.5	4.0	4.9	6.3	8.9	11.0	14.1	16.7	20	72	81	84
	●	●	●	●	●	●	●	6	.042	225	5.2	6.0	7.3	9.5	13.4	16.4	21	25	30	73	79	81
	●	●	●	●	●	●	●	8	.060	225	6.9	8.0	9.8	12.6	17.9	22	28	33	40	85	89	91
	●	●	●	●	●	●	●	10	.064	420	8.7	10.0	12.2	15.8	22	27	35	42	50	82	84	86
	●	●	●	●	●	●	●	12	.076	420	10.4	12.0	14.7	19.0	27	33	42	50	60	78	82	85
	●	●	●	●	●	●	●	14	.076	421	12.1	14.0	17.1	22	31	38	49	59	70	85	88	90
					●	●		16	.086	421	13.9	16.0	19.6	25	36	44	57	67	80	83	86	88
	●	●	●	●	●	●	●	18	.076	422	15.6	18.0	22	28	40	49	64	75	90	81	84	86
	●						●	20	.081	422	17.3	20	24	32	45	55	71	84	100	75	78	80
	●	●	●	●	●	●	●	22	.076	625	19.1	22	27	35	49	60	78	92	110	70	72	75
	●	●	●	●	●	●	●	26	.086	625	23	26	32	41	58	71	92	109	130	73	74	77

Maximum operating pressure depends on material and application. Contact your sales engineer for details.

Highlighted column shows the rated pressure.

F.10 Magnetic Ring Specifications

Magnetic ring MR200
Incrementally coded ring with permanently connected flange, pole length 2 mm

1

Profile

- Easy hollow-shaft mounting
- Rotary encoder system with IP67 protection category (in combination with MSK210)
- Up to 2000 pulses/revolution (8000 increments)
- With reference point as an option

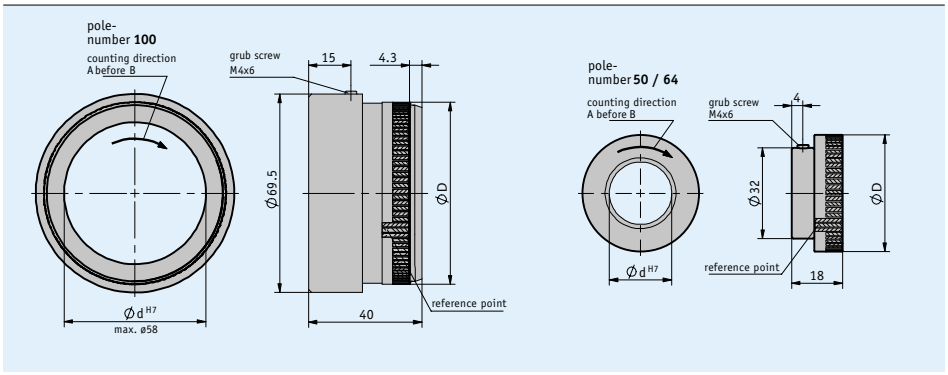

Mechanical data

Feature	Technical data	Additional information
Flange	aluminum	

- **Table of dimensions**

Poles	50	64	100
Diameter D [mm]	32.3	41.2	64.14
Circumference [mm]	100	130	200
Speed [min^{-1}]	≤15000	≤11500	≤7500

System data

Feature	Technical data	Additional information
Pole length	2 mm	
System accuracy	±0.1°	
Measuring range	360°	

Pulses/revolution

Pole number		50	64	100
Sensor scaling factor	20	1000	1280	2000
	16	800	1024	1600
	10	500	640	1000
	8	400	512	800
	5	250	320	500
	4	200	256	400
	1	50	64	100

The table applies to the combination of MR200 with MSK210

Ambient conditions

Feature	Technical data	Additional information
Ambient temperature	0 ... 60 °C	50, 64 pole number
	-20 ... 70 °C	100 pole number
Storage temperature	-20 ... 70 °C	
Relative humidity	100 %	condensation admissible
Protection category	IP67	EN 60529

Order

Ordering table

Feature	Ordering data		Specification	Additional information
Pole number	50	A	50 poles	hard ferrite
	64		64 poles	hard ferrite
	100		100 poles	flexible magnetic tape
			others on request	
Bore/diameter	20	B	ø20 mm	
			others on request	
Type of fastening	MNG	C	hub thread	
	ONG		without hub thread	
Reference point	0	D	without	
	M		with	

Order key

MR200 - [A] - [B] - [C] - [D]

Scope of delivery: MR200

F.11 Magnetic Sensor Specifications

Magnetic sensor MSK210 rotativ
Compact sensor, incremental, digital interface, scaling factor 64

Profile

- max. resolution 0.045° with MR200 and MBR200 (100 poles)
- Repeat accuracy of ±1 increment
- Works with MR200 magnetic ring, MBR200 magnetic tape ring
- Reading distance ≤0.8 mm
- Max. 4600 pulses/revolution with MBR200 (230 poles)

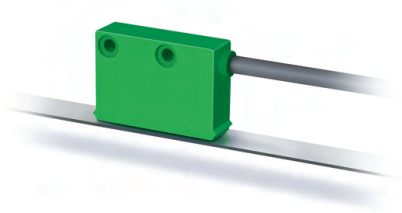

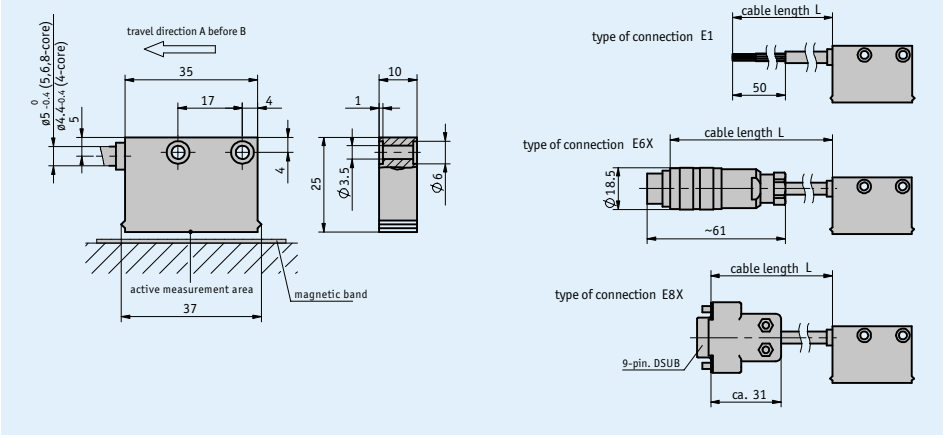

Mechanical data

Feature	Technical data	Additional information
Housing	green plastic	
Sensor/ring reading distance	0.1 ... 0.8 mm	0, I reference signals
	0.1 ... 0.4 mm	R reference signal
Cable sheath	PUR suitable for drag-chain use	4-wire ø4.4 $_{-0.4}$ mm; 5, 6, 8-wire ø5 $_{-0.4}$ mm

Electrical data

Feature	Technical data	Additional information
Operating voltage	24 V DC±20 %	reverse polarity protected
	5 V DC ±5 %	no reverse polarity protection
Current consumption	<20 mA	at 24 V DC, off-load
	<75 mA	loaded
Output circuit	PP, LD (RS422), TTL	PP only with 24 V
Output signals	A, A/, B, B/, I, I/, R, R/	quadrature signal
Output signal level high	>UB - 2.5 V	PP
	>2.5 V	LD
	>2.4 V	TTL
Output signal level low	<0.8 V	PP
	<0.5 V	LD
	<0.4 V	TTL
Jitter	<15 %	0.5 mm reading distance
Pulse width of reference signal	1 increment(s)	
Real-time requirement	speed-proportional signal output	
Type of connection	open cable end	
	plug connector	7/8-pole
	D-Sub	9-pole

Signal pattern

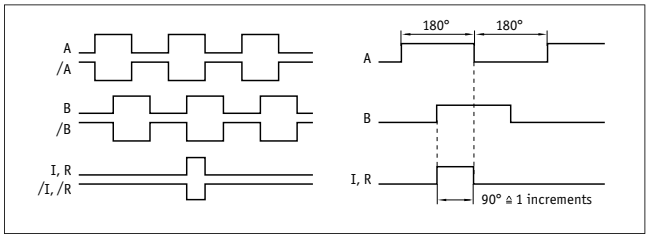

The logical condition of signals A and B is not defined in reference to the index signal I or the reference signal R. It can deviate from the signal form.

System data

Feature	Technical data	Additional information
Scaling factor	1, 5, 10, 20, 64	
System accuracy	±0.1°	
Repeat accuracy	±1 increment(s)	
Measuring range	∞	
Circumferential speed	≤25 m/s	≤2 m/s referencing speed

Ambient conditions

Feature	Technical data	Additional information
Ambient temperature	-10 ... 70 °C	
Storage temperature	-30 ... 80 °C	
Relative humidity	100 %	condensation admissible
EMC	EN 61000-6-2	interference resistance / immission
	EN 61000-6-4	emitted interference / emission
Protection category	IP67	EN 60529
Shock resistance	500 m/s^2, 11 ms	EN 60068-2-27
Vibration resistance	100 m/s^2, 5 ... 150 Hz	EN 60068-2-6

Pin assignment

Not inverted without reference signal

Signal	E1	E6X	E8X
GND	black	1	1
+UB	brownn	2	2
A	red	3	3
B	orange	4	4
nc		5	5
nc		6	6
nc		7	7
nc			8
nc			9

Inverted with reference signal

Signal	E1	E6X	E8X
A	red	1	1
B	orange	2	2
I	blue	3	3
+UB	brown	4	4
GND	black	5	5
A/	yellow	6	6
B/	gren	7	7
I/	violet	8	8
nc			9

Inverted without reference signal

Signal	E1	E6X	E8X
A	red	1	1
B	orange	2	2
nc		3	3
+UB	brown	4	4
GND	black	5	5
A/	yellow	6	6
B/	green	7	7
nc			8
nc			9

Hint for mounting

For systems with reference points on the magnetic ring please take care that sensor and ring are aligned correctly (see picture).

Reference signal	0, I	R
A, Sensor/ring reading distance	≤0.8 mm	≤0.4 mm
B, Lateral offset	±2 mm	±0.5 mm
C, Alignment error	±1°	±1°
D, Longitudinal inclination	±1°	±1°
E, Lateral inclination	±3°	±3°

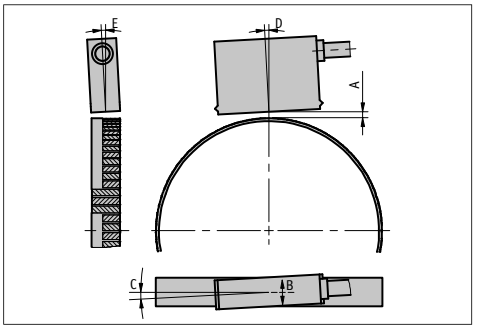

(symbolic sensor representation)

F.12 Relay Switch Specifications

Miniature SSOP
C×R10: 30 V/40 V load voltage
C×R5: 25 V load voltage

PhotoMOS®
RF SSOP 1 Form A C×R10/C×R5
(AQY22○○○V)

mm inch

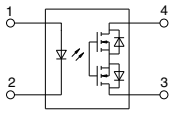

RoHS compliant

FEATURES

1. Miniature package (SSOP) using a new flat lead terminal shape
Compared to previous models (SOP 4-pin), mounting area can be reduced by approximately 53%*. This contributes to improved output signal transit characteristics.

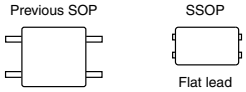

*Comparison of area of SSOP and SOP 4-pin (including leads).

2. Both low on-resistance (R type) and low capacitance (C type) available at excellent characteristics of C×R10

		On resistance (Typical)	Output capacitance (Typical)
C×R10 R type	AQY221R6V	0.18Ω	37.5pF
	AQY221R4V	0.55Ω	24pF
	AQY221R2V	0.75Ω	12.5pF
C×R10 C type	AQY221N2V	9.5Ω	1.0pF
C×R5	AQY221N3V	5.5Ω	1.0pF

TYPICAL APPLICATIONS

1. Measuring and testing equipment
Semiconductor testing equipment, Probe cards, Datalogger, Board tester and other testing equipment
2. Telecommunication and broadcasting equipment
3. Medical equipment
4. Multi-point recorder
Data logger, Warping and Thermocouple, etc.

TYPES

Type			Output rating*1 Load voltage	Output rating*1 Load current	Package	Tape and reel packing style*2 Picked from the 1 and 4-pin side	Tape and reel packing style*2 Picked from the 2 and 3-pin side	Packing quantity in tape and reel
AC/DC dual use	C×R10	Low on-resistance (R type)	30 V	1,000 mA	SSOP	AQY221R6VY	AQY221R6VW	3,500 pcs.
			40 V	500 mA		AQY221R4VY	AQY221R4VW	
			40 V	250 mA		AQY221R2VY	AQY221R2VW	
		Low capacitance (C type)	40 V	120 mA		AQY221N2VY	AQY221N2VW	
	C×R5		25 V	150 mA		AQY221N3VY	AQY221N3VW	

Notes: *1. Indicate the peak AC and DC values.
*2. Tape and reel is the standard packing style for SSOP. Packing quantity of 1,000 pieces is possible. Please consult us.
For space reasons, the three initial letters of the part number "AQY", the package (SSOP) indication "V", and the packaging style "Y" or "W" are not marked on the device. (Ex. the label for product number AQY221R4VY is 221R4)

RATING

1. Absolute maximum ratings (Ambient temperature: 25°C 77°F)

Item		Symbol	C×R10 R type			C×R10 C type	C×R5	Remarks
			AQY221R6V	AQY221R4V	AQY221R2V	AQY221N2V	AQY221N3V	
Input	LED forward current	I_F	50mA					
	LED reverse voltage	V_R	5V					
	Peak forward current	I_{FP}	1A					f=100 Hz, Duty factor=0.1%
	Power dissipation	P_{in}	75mW					
Output	Load voltage (peak AC)	V_L	30V	40V			25V	
	Continuous load current	I_L	1A	0.5A	0.25A	0.12A	0.15A	Peak AC, DC
	Peak load current	I_{peak}	1.5A	1A	0.75A	0.3A	0.4A	100ms (1shot), V_L=DC
	Power dissipation	P_{out}	250mW					
Total power dissipation		P_T	300mW					
I/O isolation voltage		V_{iso}	1,500Vrms					
Ambient temperature	Operating	T_{opr}	–40 to +85°C –40 to +185°F					(Non-icing at low temperatures)
	Storage	T_{stg}	–40 to +100°C –40 to +212°F					

2. Electrical characteristics (Ambient temperature: 25°C 77°F)

Item			Symbol	C×R10 R type			C×R10 C type	C×R5	Condition
				AQY221R6V	AQY221R4V	AQY221R2V	AQY221N2V	AQY221N3V	
Input	LED operate current	Typical	I_{Fon}	0.7 mA	0.9 mA		1.0 mA		AQY221R6V: I_L = 100 mA AQY221R4V: I_L = 500 mA AQY221R2V: I_L = 250 mA AQY221N2V: I_L = 80 mA AQY221N3V: I_L = 80 mA
		Maximum		3.0 mA					
	LED turn off current	Minimum	I_{Foff}	0.1 mA			0.2 mA		
		Typical		0.6 mA	0.8 mA		0.9 mA		
	LED dropout voltage	Typical	V_F	1.35 V (1.14 V at I_F = 5 mA)					I_F = 50 mA
		Maximum		1.5 V					
Output	On resistance	Typical	R_{on}	0.18Ω	0.55Ω	0.75Ω	9.5Ω	5.5Ω	AQY221R6V: I_F = 5 mA, I_L = 1000 mA AQY221R4V: I_F = 5 mA, I_L = 500 mA AQY221R2V: I_F = 5 mA, I_L = 250 mA AQY221N2V: I_F = 5 mA, I_L = 80 mA AQY221N3V: I_F = 5 mA, I_L = 80 mA Within 1 s
		Maximum		0.35Ω	1Ω	1.25Ω	12.5Ω	7.5Ω	
	Output capacitance	Typical	C_{out}	37.5 pF	24 pF	12.5 pF	1.0 pF		I_F = 0 mA, V_B = 0 V, f = 1 MHz
		Maximum		100 pF	30 pF	18 pF	1.5 pF		
	Off state leakage current	Typical	I_{Leak}	—	0.02 nA		0.01 nA		I_F = 0 mA, V_L = Max.
		Maximum		*10 nA					
Transfer character-istics	Turn on time**	Typical	T_{on}	0.2 ms	0.25 ms	0.10 ms	0.02 ms		AQY221R6V: I_F = 5 mA, V_L = 10 V, R_L = 100Ω AQY221R4V: I_F = 5 mA, V_L = 10 V, R_L = 20Ω AQY221R2V: I_F = 5 mA, V_L = 10 V, R_L = 40Ω AQY221N2V: I_F = 5 mA, V_L = 10 V, R_L = 125Ω AQY221N3V: I_F = 5 mA, V_L = 10 V, R_L = 125Ω
		Maximum		0.5 ms	0.75 ms	0.5 ms		0.2 ms	
	Turn off time**	Typical	T_{off}	0.07 ms	0.08 ms		0.02 ms		
		Maximum		0.2 ms					
	I/O capacitance	Typical	C_{iso}	0.8 pF					f = 1 MHz, V_B = 0 V
		Maximum		1.5 pF					
	Initial I/O isolation resistance	Minimum	R_{iso}	1,000 MΩ					500 V DC

Note: Variation possible through combinations of output capacitance and on resistance. For more information, please contact our sales office in your area.

*Available as custom orders (1 nA or less)

**Turn on/Turn off time

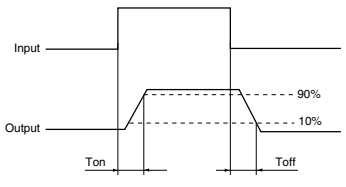

3. Recommended operating conditions (Ambient temperature: 25°C 77°F)
Please use under recommended operating conditions to obtain expected characteristics.

Item		Symbol	Min.	Max.	Unit
LED current		I_F	5	30	mA
AQY221R6V	Load voltage (Peak AC)	V_L	—	15	V
	Continuous load current	I_L	—	1	A
AQY221R4V	Load voltage (Peak AC)	V_L	—	15	V
	Continuous load current	I_L	—	0.5	A
AQY221R2V	Load voltage (Peak AC)	V_L	—	15	V
	Continuous load current	I_L	—	0.25	A
AQY221N2V	Load voltage (Peak AC)	V_L	—	15	V
	Continuous load current	I_L	—	0.12	A
AQY221N3V	Load voltage (Peak AC)	V_L	—	15	V
	Continuous load current	I_L	—	0.15	A

■ **These products are not designed for automotive use.**
If you are considering to use these products for automotive applications, please contact your local Panasonic Corporation technical representative.

REFERENCE DATA

1. Load current vs. ambient temperature characteristics
Allowable ambient temperature: –40 to +85°C
–40 to +185°F

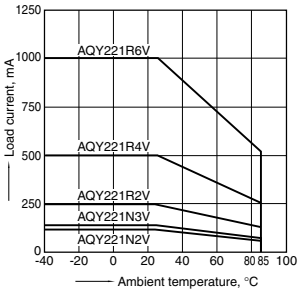

2. Load current vs. Load voltage characteristics
Ambient temperature: 25°C 77°F

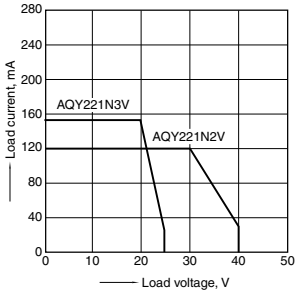

3. On resistance vs. ambient temperature characteristics
Measured portion: between terminals 3 and 4
LED current: 5 mA; Load voltage: 10V (DC)
Continuous load current: 1000mA (DC) AQY221R6V, 500mA (DC) AQY221R4V, 250mA (DC) AQY221R2V, 80mA (DC) AQY221N2V, AQY221N3V

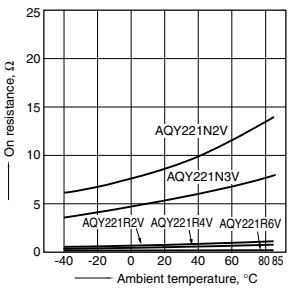

4. Turn on time vs. ambient temperature characteristics
Measured portion: between terminals 3 and 4
LED current: 5 mA; Load voltage: 10V (DC)
Continuous load current: 100mA (DC) AQY221R6V, 500mA (DC) AQY221R4V, 250mA (DC) AQY221R2V, 80mA (DC) AQY221N2V, AQY221N3V

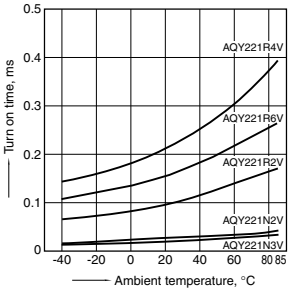

5. Turn off time vs. ambient temperature characteristics
Measured portion: between terminals 3 and 4
LED current: 5 mA; Load voltage: 10V (DC)
Continuous load current: 100mA (DC) AQY221R6V, 500mA (DC) AQY221R4V, 250mA (DC) AQY221R2V, 80mA (DC) AQY221N2V, AQY221N3V

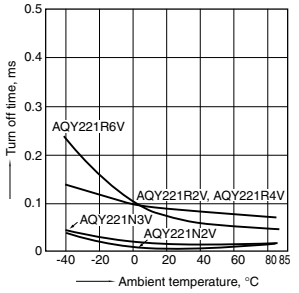

6. LED operate current vs. ambient temperature characteristics
Measured portion: between terminals 3 and 4
Load voltage: 10V (DC)
Continuous load current: 100mA (DC) AQY221R6V, 500mA (DC) AQY221R4V, 250mA (DC) AQY221R2V, 80mA (DC) AQY221N2V, AQY221N3V

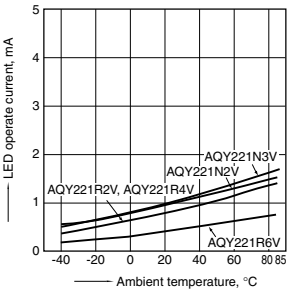

7. LED turn off current vs. ambient temperature characteristics

Measured portion: between terminals 3 and 4
Load voltage: 10V (DC)
Continuous load current: 100mA (DC) AQY221R6V, 500mA (DC) AQY221R4V, 250mA (DC) AQY221R2V, 80mA (DC) AQY221N2V, AQY221N3V

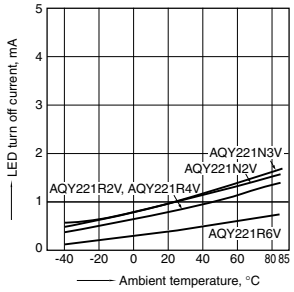

8. LED dropout voltage vs. ambient temperature characteristics

LED current: 5 to 50 mA

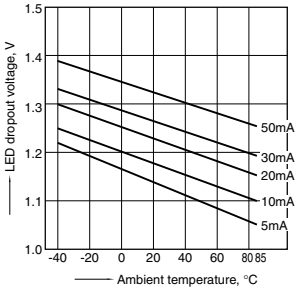

9. Current vs. voltage characteristics of output at MOS portion

Measured portion: between terminals 3 and 4
Ambient temperature: 25°C 77°F

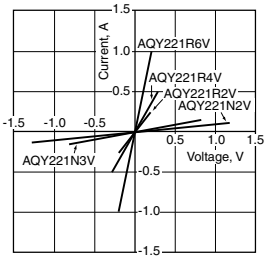

10. Off state leakage current vs. load voltage characteristics

Measured portion: between terminals 3 and 4
Ambient temperature: 25°C 77°F

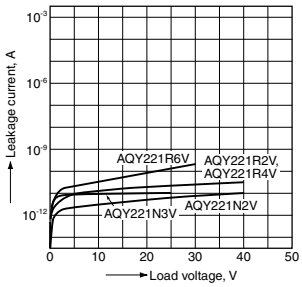

11. Turn on time vs. LED forward current characteristics

Measured portion: between terminals 3 and 4
Load voltage: 10V (DC)
Continuous load current: 100mA (DC) AQY221R6V, 500mA (DC) AQY221R4V, 250mA (DC) AQY221R2V, 80mA (DC) AQY221N2V, AQY221N3V
Ambient temperature: 25°C 77°F

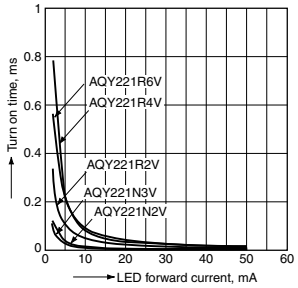

12. Turn off time vs. LED forward current characteristics

Measured portion: between terminals 3 and 4
Load voltage: 10V (DC)
Continuous load current: 100mA (DC) AQY221R6V, 500mA (DC) AQY221R4V, 250mA (DC) AQY221R2V, 80mA (DC) AQY221N2V, AQY221N3V
Ambient temperature: 25°C 77°F

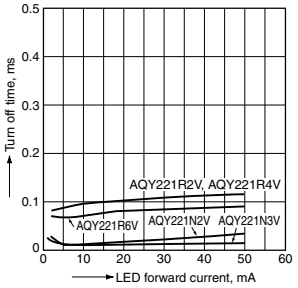

13. Output capacitance vs. applied voltage characteristics

Measured portion: between terminals 3 and 4
Frequency: 1 MHz, 30mVrms
Ambient temperature: 25°C 77°F

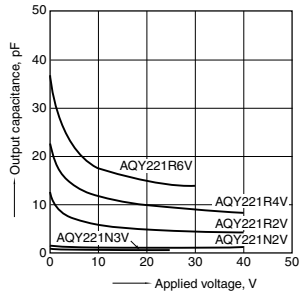

14. Isolation vs. frequency characteristics (50Ω impedance)

Measured portion: between terminals 3 and 4
Ambient temperature: 25°C 77°F

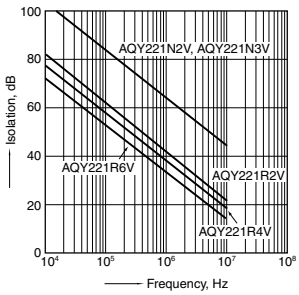

15. Insertion loss vs. frequency characteristics (50Ω impedance)

Measured portion: between terminals 3 and 4
Ambient temperature: 25°C 77°F

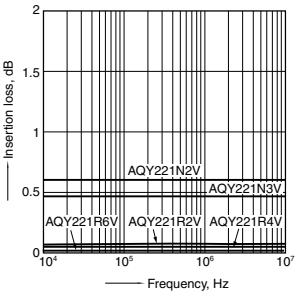

F.13 Shaft Lip Seal Specifications

AS182

AVSLD
avsld.com

Advanced Sealing Devices Pte Ltd

Material: AS182 (Moly Lubricated TFE Polymeric Proprietary Formulation)

Features

- Outstanding resistant to chemicals.
- Exceptionally high level of creep resistance, wear resistance, compressive strength and low coefficient of friction
- Compatible with HFA, HFB and HFC fluids and almost all solvents
- Good initial wear and rubbing or sliding characteristics in both dry and water application
- Frequently used in piston rings to reduce cylinder wall wear

Material Specification

Properties		Value	Unit
Hardness	ASTM D2240	62 ± 5	Shore D
Tensile Strength	ASTM D412	24.8	MPa
Elongation at break	ASTM D412	330	%
Specific Gravity	ISO 1183	2210	kg/m^3
Modulus	ASTM D412	1320	MPa
Coefficient of Friction (dry)		0.15	μ
Coefficient of Friction (oil)		0.01	μ
Minimum Operating Temperature		-200	^oC
Maximum Operating Temperature		260	^oC

Applications

- marine
- aerospace
- oil and gas
- military
- chemical
- medical

69F Tuas South Avenue 1, Singapore 637497
T: (65) 6792 6818 F: (65) 6296 1583
Email: asd@avsld.com Web: www.avsld.com

Bearing data – general

Dimensions

The boundary dimensions of metric stainless steel deep groove ball bearings conform to ISO 15-1998, except for bearings with a WBB1 prefix or an X suffix. Inch series stainless steel deep groove ball bearings conform to ANSI/AFBMA Std. 12.2-1992.

Tolerances

All stainless steel deep groove ball bearings are manufactured as standard to Normal tolerances corresponding to ISO 492-2002.

Internal clearance

SKF stainless steel deep groove ball bearings are manufactured as standard with Normal radial internal clearance to ISO 5753-1991, except for bore diameters < 10 mm (→ **table 2**). Other classes are available upon request. The values for radial internal clearance given in **table 2** are valid for unmounted bearings under zero measuring load.

Misalignment

SKF stainless steel deep groove ball bearings have only a limited ability to accomodate misalignment. The permissible angular misalignment between inner and outer rings which will not produce inadmissibly high additonal stresses in the bearing depends on the radial internal clearance of the bearing in operation, bearing size, the internal design and the forces and moments acting on the bearing. In other words, depending on the various influencing factors, the permissible angular misalignment lies between 2 and 10 minutes of arc. Any misalignment will increase bearing noise and reduce bearing service life. For additional information, contact the SKF application engineering service.

Table 2

Radial internal clearance

Bore diameter d		Radial internal clearance C2		Normal		C3		C4	
over	incl.	min	max	min	max	min	max	min	max
mm		µm							
–	**9,525**	3	8	5	10	8	13	13	20
10	**10**	0	7	2	13	8	23	14	29
10	**18**	0	9	3	18	11	25	18	33
18	**24**	1	10	5	20	13	28	20	36
24	**30**	1	11	5	20	13	28	23	41
30	**40**	1	11	6	20	15	33	28	46
40	**50**	1	11	6	23	18	36	30	51
50	**65**	1	15	8	28	23	43	38	61
65	**80**	1	15	10	30	25	51	46	71

Minimum load

For satisfactory operation, SKF stainless steel deep groove ball bearings must always be subjected to a given minimum load.

The requisite minimum radial load to be applied to SKF stainless steel deep groove ball bearings can be estimated using

$$F_{rm} = k_r \left(\frac{\nu n}{1\,000}\right)^{2/3} \left(\frac{d_m}{100}\right)^2$$

where

F_{rm} = minimum radial load [kN]
k_r = minimum load factor
ν = oil viscosity at operating temperature [mm²/s]
n = rotational speed [r/min]
d_m = bearing mean diameter = 0,5 (d + D) [mm]

When starting up at low temperatures or when the lubricant is highly viscous, even greater minimum loads may be required. The weight of the compoments supported by the bearing, together with external forces, generally exceeds the requisite minimum load. If this is not the case, the bearing must be subjected to an additional radial load.

For applications where stainless steel deep groove ball bearings are used, an axial preload can be applied by adjusing the inner and outer rings against each other or by using springs.

Axial load carrying capacity

SKF stainless steel deep groove ball bearings have the same axial load carrying capacity as standard SKF deep groove ball bearings. If they are subjected to purely axial loads, this load should generally not exceed the value of 0,25 C_0. Excessive axial load can lead to a reduction in bearing service life.

Equivalent bearing loads

Equivalent bearing loads for SKF stainless steel deep groove ball bearings can be calculated the same way as for standard SKF deep groove ball bearings. For additional information, contact the SKF application engineering service.

Designations

The designations for SKF stainless steel deep groove ball bearings follow the basic SKF designation system except for inch types. However, the prefix "W" has been implemented to indicate that the material is stainless steel.

Supplementary designations

In addition to the designation suffixes that are listed in the *SKF General Catalogue*, the following designation suffixes are relevant for SKF stainlees steel deep groove ball bearings:

W	Stainless steel deep groove ball bearing metric series
D/W	Stainless steel deep groove ball bearing inch series
X	One boundary dimension deviates from ISO standard
BB1	Two or more boundary dimensions deviate from ISO standard
2TS	PTFE seal for stainless steel deep groove ball bearing
2ZS	Shield of pressed sheet steel on both sides of the bearing with retaining ring
R	Flanged outer ring
RZ	Non-contact seal for stainless steel deep groove ball bearing
R-2Z	Shield of pressed sheet steel on both sides of the bearing and flanged outer ring
VT378	Food grade grease with aluminium thickener of consistency 2 to the NLGI Scale for a temperature range –25 to +120 °C (normal fill grade)

For additional information, refer to the *SKF General Catalogue* or the *SKF Interactive Engineering Catalogue* available online at www.skf.com.

Metric capped stainless steel deep groove ball bearings
d **20 – 50** mm

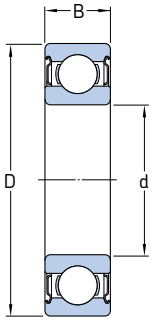

2Z

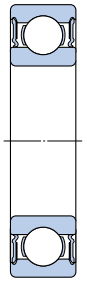

2RS1

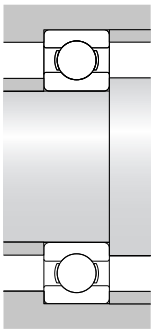

Principal dimensions			Basic load ratings		Fatigue load limit	Speed ratings		Mass	Designation
			dynamic	static		Reference speed	Limiting speed		
d	D	B	C	C_0	P_u				
mm			N		N	r/min		kg	–
20	25	4	572	365	16	53 000	26 000	0,0035	**WBB1-8714-2ZS**
	27	4	585	390	17	–	14 000	0,0059	**W 61704-2RS1**
	27	4	585	390	17	50 000	26 000	0,0057	**W 61704-2ZS**
	32	7	3 120	2 080	90	–	13 000	0,0178	**W 61804-2RS1**
	32	7	3 120	2 080	90	48 000	24 000	0,0173	**W 61804-2Z**
	32	10	3 120	2 080	90	–	13 000	0,0246	**W 63804-2RS1**
	32	10	3 120	2 080	90	48 000	24 000	0,0244	**W 63804-2Z**
	37	9	5 530	3 650	156	–	12 000	0,0354	**W 61904-2RS1**
	37	9	5 530	3 650	156	43 000	20 000	0,0353	**W 61904-2Z**
	42	12	8 060	5 000	212	–	11 000	0,0657	**W 6004-2RS1**
	42	12	8 060	5 000	212	38 000	19 000	0,0651	**W 6004-2Z**
	47	14	10 800	6 550	280	–	10 000	0,1047	**W 6204-2RS1**
	47	14	10 800	6 550	280	34 000	17 000	0,106	**W 6204-2Z**
	52	15	13 800	7 800	335	–	9 500	0,1452	**W 6304-2RS1**
	52	15	13 800	7 800	335	34 000	17 000	0,146	**W 6304-2Z**
25	32	4	618	465	20	–	12 000	0,0073	**W 61705-2RS1**
	37	7	3 380	2 500	108	–	11 000	0,0213	**W 61805-2RS1**
	37	7	3 380	2 500	108	38 000	19 000	0,021	**W 61805-2Z**
	37	10	3 380	2 500	108	–	11 000	0,0297	**W 63805-2RS1**
	37	10	3 380	2 500	108	38 000	19 000	0,0294	**W 63805-2Z**
	42	9	6 050	4 500	193	–	10 000	0,0422	**W 61905-2RS1**
	42	9	6 050	4 500	193	34 000	17 000	0,0423	**W 61905-2Z**
	47	12	8 710	5 850	250	–	9 500	0,077	**W 6005-2RS1**
	47	12	8 710	5 850	250	32 000	16 000	0,0782	**W 6005-2Z**
	52	15	11 700	7 650	335	–	8 500	0,1291	**W 6205-2RS1**
	52	15	11 700	7 650	335	30 000	15 000	0,1299	**W 6205-2Z**
	62	17	17 800	11 200	480	–	7 500	0,2348	**W 6305-2RS1**
	62	17	17 800	11 200	480	26 000	13 000	0,2356	**W 6305-2Z**
30	42	7	3 580	2 900	125	–	9 500	0,0244	**W 61806-2RS1**
	42	7	3 580	2 900	125	34 000	17 000	0,0241	**W 61806-2Z**
	42	10	3 580	2 900	125	–	9 500	0,036	**W 63806-2RS1**
	42	10	3 580	2 900	125	34 000	17 000	0,036	**W 63806-2Z**
	47	9	6 240	5 000	212	–	8 500	0,0477	**W 61906-2RS1**
	47	9	6 240	5 000	212	30 000	15 000	0,0485	**W 61906-2Z**
	55	13	11 400	8 150	355	–	8 000	0,113	**W 6006-2RS1**
	55	13	11 400	8 150	355	28 000	14 000	0,1141	**W 6006-2Z**
	62	16	16 500	11 200	480	–	7 000	0,1958	**W 6206-2RS1**
	62	16	16 500	11 200	480	26 000	13 000	0,1951	**W 6206-2Z**
	72	19	22 900	15 000	640	–	6 300	0,3512	**W 6306-2RS1**
	72	19	22 900	15 000	640	22 000	11 000	0,3496	**W 6306-2Z**

Principal dimensions			Basic load ratings		Fatigue load limit	Speed ratings		Mass	Designation
			dynamic	static		Reference speed	Limiting speed		
d	D	B	C	C_0	P_u				
mm			N		N	r/min		kg	–
35	44	5	1 060	915	39	–	8 500	0,0153	**W 61707-2RS1**
	47	7	3 710	3 350	140	–	8 500	0,0292	**W 61807-2RS1**
	47	7	3 710	3 350	140	30 000	15 000	0,0282	**W 61807-2Z**
	55	10	9 360	7 650	325	–	7 500	0,0743	**W 61907-2RS1**
	55	10	9 360	7 650	325	26 000	13 000	0,0742	**W 61907-2Z**
	62	14	13 800	10 200	440	–	6 700	0,1475	**W 6007-2RS1**
	62	14	13 800	10 200	440	24 000	12 000	0,1489	**W 6007-2Z**
	72	17	22 100	15 300	655	–	6 000	0,2792	**W 6207-2RS1**
	72	17	22 100	15 300	655	22 000	11 000	0,2788	**W 6207-2Z**
	80	21	28 600	19 000	815	–	5 600	0,459	**W 6307-2RS1**
	80	21	28 600	19 000	815	20 000	10 000	0,457	**W 6307-2Z**
40	50	6	1 430	1 270	54	–	7 500	0,0235	**W 61708-2RS1**
	52	7	3 900	3 750	160	–	7 500	0,0322	**W 61808-2RS1**
	52	7	3 900	3 750	160	26 000	13 000	0,0308	**W 61808-2Z**
	62	12	11 900	9 800	425	–	6 700	0,1102	**W 61908-2RS1**
	62	12	11 900	9 800	425	24 000	12 000	0,1113	**W 61908-2Z**
	68	15	14 600	11 400	490	–	6 300	0,1856	**W 6008-2RS1**
	68	15	14 600	11 400	490	22 000	11 000	0,1859	**W 6008-2Z**
	80	18	25 100	17 600	750	–	5 600	0,3578	**W 6208-2RS1**
	80	18	25 100	17 600	750	20 000	10 000	0,3568	**W 6208-2Z**
45	55	6	1 460	1 370	60	–	6 700	0,0262	**W 61709-2RS1**
	58	7	4 940	5 000	212	–	6 700	0,0373	**W 61809-2RS1**
	58	7	4 940	5 000	212	24 000	12 000	0,0363	**W 61809-2Z**
	68	12	12 100	10 800	465	–	6 000	0,1245	**W 61909-2RS1**
	68	12	12 100	10 800	465	20 000	10 000	0,1247	**W 61909-2Z**
	75	16	18 200	15 000	640	–	5 600	0,2388	**W 6009-2RS1**
	75	16	18 200	15 000	640	20 000	10 000	0,238	**W 6009-2Z**
	85	19	28 100	20 400	865	–	5 000	0,3937	**W 6209-2RS1**
	85	19	28 100	20 400	865	18 000	9 000	0,3915	**W 6209-2Z**
50	62	6	1 530	1 530	67	–	6 000	0,0377	**W 61710-2RS1**
	65	7	5 070	5 500	236	–	6 000	0,0503	**W 61810-2RS1**
	65	7	5 070	5 500	236	20 000	10 000	0,0501	**W 61810-2Z**
	72	12	12 500	11 600	500	–	5 600	0,1388	**W 61910-2RS1**
	72	12	12 500	11 600	500	19 000	9 500	0,1393	**W 61910-2Z**
	80	16	19 000	16 600	710	–	5 000	0,2575	**W 6010-2RS1**
	80	16	19 000	16 600	710	18 000	9 000	0,2572	**W 6010-2Z**
	90	20	30 200	23 200	980	–	4 800	0,4436	**W 6210-2RS1**
	90	20	30 200	23 200	980	17 000	8 500	0,4476	**W 6210-2Z**

The SKF model for calculating the frictional moment

Bearing friction is not constant and depends on certain tribological phenomena that occur in the lubricant film between the rolling elements, raceways and cages.

Diagram 1 shows how friction changes, as a function of speed, in a bearing with a given lubricant. Four zones are distinguishable:

- **Zone 1** – Boundary layer lubrication condition, in which only the asperities carry the load, and so friction between the moving surfaces is high.
- **Zone 2** – Mixed lubrication condition, in which a separating oil film carries part of the load, with fewer asperities in contact, and so friction decreases.
- **Zone 3** – Full film lubrication condition, in which the lubricant film carries the load, but with increased viscous losses, and so friction increases.
- **Zone 4** – Full film lubrication with thermal and starvation effects, in which the inlet shear heating and kinematic replenishment reduction factors compensate partially for the viscous losses, and so friction evens off.

To calculate the total frictional moment in a rolling bearing, the following sources and their

Diagram 1

Bearing frictional moment as a function of speed or viscosity

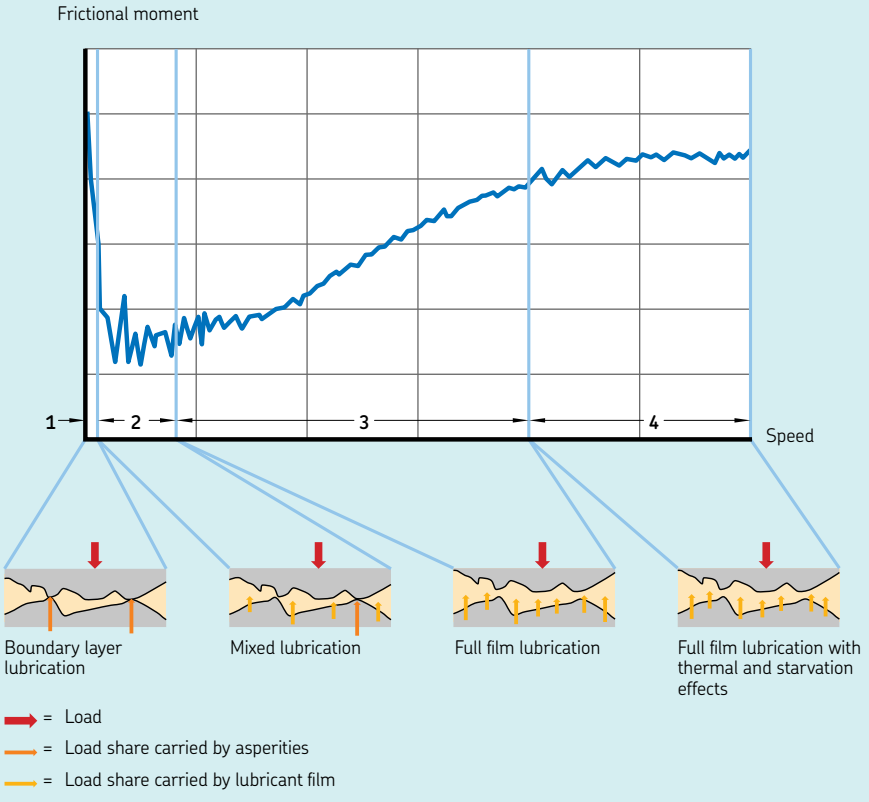

tribological effects must be taken into account:

- the rolling frictional moment and eventual effects of high-speed starvation and inlet shear heating
- the sliding frictional moment and its effect on the quality of the lubrication
- the frictional moment from seal(s)
- the frictional moment from drag losses, churning, splashing etc.

The SKF model for calculating the frictional moment closely follows the real behaviour of the bearing as it considers all contact areas and design changes and improvements made to SKF bearings, including internal and external influences.

The SKF model for calculating the frictional moment uses

$$M = M_{rr} + M_{sl} + M_{seal} + M_{drag}$$

where
M = total frictional moment
M_{rr} = rolling frictional moment
M_{sl} = sliding frictional moment (→ **page 5**)
M_{seal} = frictional moment of seals (→ **page 11**)
M_{drag} = frictional moment of drag losses, churning, splashing etc. (→ **page 12**)

The SKF model is derived from more advanced computational models developed by SKF. It is valid for grease or oil lubricated bearings and is designed to provide approximate reference values under the following application conditions:

- grease lubrication:
  - only steady state conditions (after several hours of operation)
  - lithium soap grease with mineral oil
  - bearing free volume filled approximately 30%
  - ambient temperature 20 °C *(70 °F)* or higher
- oil lubrication:
  - oil bath, oil-air or oil jet
  - viscosity range from 2 to 500 mm^2/s
- loads equal to or larger than the recommended minimum load
- constant loads in magnitude and direction
- normal operating clearance
- constant speed, below the speed ratings
- bearing does not exceed the limits of misalignment

For paired bearings, the frictional moment can be calculated separately for each bearing and the results added together. The radial load is divided equally over the two bearings; the axial load is shared according to the bearing arrangement.

NOTE: The formulae provided in this section lead to rather complex calculations. Therefore, SKF strongly recommends calculating the frictional moment using the tools available online at skf.com/bearingcalculator.

Rolling frictional moment

The rolling frictional moment can be calculated using

$$M_{rr} = \Phi_{ish}\, \Phi_{rs}\, G_{rr}\, (\nu\, n)^{0,6}$$

where
M_{rr} = rolling frictional moment [Nmm]
Φ_{ish} = inlet shear heating reduction factor
Φ_{rs} = kinematic replenishment/starvation reduction factor (→ **page 4**)
G_{rr} = variable (→ **table 1**, **page 6**), depending on:
  - the bearing type
  - the bearing mean diameter d_m [mm] = 0,5 (d + D)
  - the radial load F_r [N]
  - the axial load F_a [N]

n = rotational speed [r/min]
ν = actual operating viscosity of the oil or the base oil of the grease [mm^2/s]

Inlet shear heating reduction factor

A fraction of the overall quantity of oil within a bearing passes through the contact area; only a tiny amount is required to form a hydrodynamic film. Therefore, some of the oil close to the contact area is repelled and produces a reverse flow (→ **fig. 1**). This reverse flow shears the lubricant and generates heat, which lowers the oil viscosity and reduces the film thickness and rolling friction.

For the effect described above, the inlet shear heating reduction factor can be estimated using

$$\Phi_{ish} = \frac{1}{1 + 1{,}84 \times 10^{-9} (n\, d_m)^{1{,}28}\, \nu^{0{,}64}}$$

where

Φ_{ish} = inlet shear heating reduction factor (→ **diagram 2**)
n = rotational speed [r/min]
d_m = bearing mean diameter [mm] = 0,5 (d + D)
ν = actual operating viscosity of the oil or the base oil of the grease [mm²/s]

Fig. 1

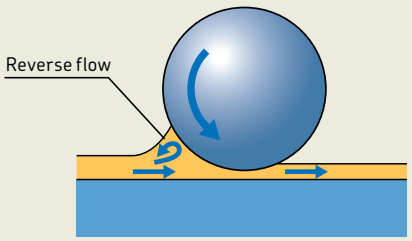

Diagram 2

Inlet shear heating reduction factor Φ_{ish}

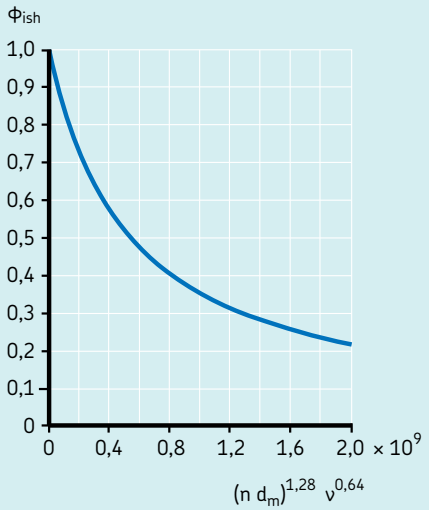

Kinematic replenishment/starvation reduction factor

For oil-air, oil jet, low level oil bath lubrication (i.e. oil level H lower than the centre of the lowest rolling element) and grease lubrication methods, continuous over-rolling displaces excess lubricant from the raceways. In applications where viscosity or speeds are high, the lubricant may not have sufficient time to replenish the raceways, causing a "kinematic starvation" effect. Kinematic starvation reduces the thickness of the hydrodynamic film (decreasing κ value) and rolling friction.

For the type of lubrication methods described above, the kinematic replenishment/starvation reduction factor can be estimated using

$$\Phi_{rs} = \frac{1}{e^{\left[K_{rs}\, \nu\, n\, (d + D) \sqrt{\frac{K_z}{2\,(D - d)}}\right]}}$$

where

Φ_{rs} = kinematic replenishment/starvation reduction factor
e = base of natural logarithm ≈ 2,718
K_{rs} = replenishment/starvation constant:
= 3×10^{-8} low level oil bath and oil jet lubrication
= 6×10^{-8} grease and oil-air lubrication
K_Z = bearing type related geometric constant (**→ table 4, page 14**)
ν = actual operating viscosity of the oil or the base oil of the grease [mm^2/s]
n = rotational speed [r/min]
d = bearing bore diameter [mm]
D = bearing outside diameter [mm]

Sliding frictional moment

The sliding frictional moment can be calculated using

$$M_{sl} = G_{sl}\,\mu_{sl}$$

where
M_{sl} = sliding frictional moment [Nmm]
G_{sl} = variable (→ **table 1**, **page 6**), depending on:
- the bearing type
- the bearing mean diameter d_m [mm] = 0,5 (d + D)
- the radial load F_r [N]
- the axial load F_a [N]

μ_{sl} = sliding friction coefficient

Effect of lubrication on sliding friction

The sliding friction coefficient for full-film and mixed lubrication conditions can be estimated using

$$\mu_{sl} = \Phi_{bl}\,\mu_{bl} + (1 - \Phi_{bl})\,\mu_{EHL}$$

where
μ_{sl} = sliding friction coefficient
Φ_{bl} = weighting factor for the sliding friction coefficient

$$= \frac{1}{e^{2,6 \times 10^{-8}\,(n\,\nu)^{1,4}\,d_m}}$$

(→ **diagram 3**)
e = base of natural logarithm ≈ 2,718
n = rotational speed [r/min]
ν = actual operating viscosity of the oil or the base oil of the grease [mm^2/s]
d_m = bearing mean diameter [mm] = 0,5 (d + D)
μ_{bl} = constant depending on movement:
= 0,12 for n ≠ 0
= 0,15 for n = 0 (starting torque calculation)

μ_{EHL} = sliding friction coefficient in full-film conditions
Values for μ_{EHL} are:
- 0,02 for cylindrical roller bearings
- 0,002 for tapered roller bearings

Other bearings
- 0,05 for lubrication with mineral oils
- 0,04 for lubrication with synthetic oils
- 0,1 for lubrication with transmission fluids

Diagram 3 shows the influence of lubrication conditions on the weighting factor for the sliding friction coefficient:

- For full-film lubrication (corresponding to large values of κ), the value of Φ_{bl} tends to zero.
- For mixed lubrication, which can occur when lubricant viscosity or the bearing speed is low, the value of Φ_{bl} tends to 1, as contact between asperities occurs and friction increases.

Diagram 3

Weighting factor Φ_{bl} for the sliding friction coefficient

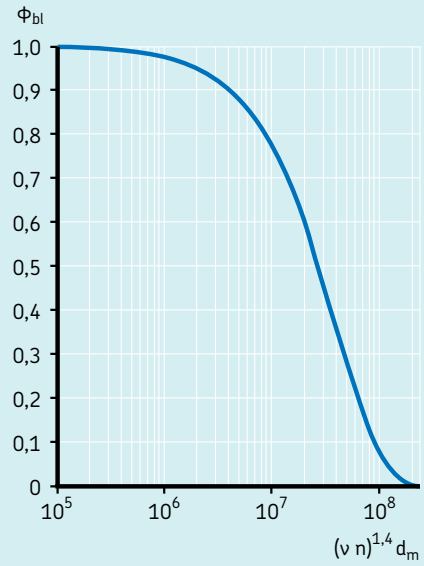

Table 1a

Geometric and load dependent variables for rolling and sliding frictional moments – radial bearings

Bearing type	Rolling frictional variable G_{rr}	Sliding frictional variable G_{sl}
Deep groove ball bearings	when $F_a = 0$	when $F_a = 0$
	$G_{rr} = R_1 d_m^{1,96} F_r^{0,54}$	$G_{sl} = S_1 d_m^{-0,26} F_r^{5/3}$
	when $F_a > 0$	when $F_a > 0$
	$G_{rr} = R_1 d_m^{1,96} \left(F_r + \frac{R_2}{\sin \alpha_F} F_a\right)^{0,54}$	$G_{sl} = S_1 d_m^{-0,145} \left(F_r^5 + \frac{S_2 d_m^{1,5}}{\sin \alpha_F} F_a^4\right)^{1/3}$
	$\alpha_F = 24,6 (F_a/C_0)^{0,24}$ [°]	
Angular contact ball bearings[1]	$G_{rr} = R_1 d_m^{1,97} [F_r + F_g + R_2 F_a]^{0,54}$	$G_{sl} = S_1 d_m^{0,26} [(F_r + F_g)^{4/3} + S_2 F_a^{4/3}]$
	$F_g = R_3 d_m^4 n^2$	$F_g = S_3 d_m^4 n^2$
Four-point contact ball bearings	$G_{rr} = R_1 d_m^{1,97} [F_r + F_g + R_2 F_a]^{0,54}$	$G_{sl} = S_1 d_m^{0,26} [(F_r + F_g)^{4/3} + S_2 F_a^{4/3}]$
	$F_g = R_3 d_m^4 n^2$	$F_g = S_3 d_m^4 n^2$
Self-aligning ball bearings	$G_{rr} = R_1 d_m^2 [F_r + F_g + R_2 F_a]^{0,54}$	$G_{sl} = S_1 d_m^{-0,12} [(F_r + F_g)^{4/3} + S_2 F_a^{4/3}]$
	$F_g = R_3 d_m^{3,5} n^2$	$F_g = S_3 d_m^{3,5} n^2$
Cylindrical roller bearings	$G_{rr} = R_1 d_m^{2,41} F_r^{0,31}$	$G_{sl} = S_1 d_m^{0,9} F_a + S_2 d_m F_r$
Tapered roller bearings[1]	$G_{rr} = R_1 d_m^{2,38} (F_r + R_2 Y F_a)^{0,31}$	$G_{sl} = S_1 d_m^{0,82} (F_r + S_2 Y F_a)$
For the axial load factor Y for single row bearings → **product tables**		
Spherical roller bearings	$G_{rr.e} = R_1 d_m^{1,85} (F_r + R_2 F_a)^{0,54}$	$G_{sl.e} = S_1 d_m^{0,25} (F_r^4 + S_2 F_a^4)^{1/3}$
	$G_{rr.l} = R_3 d_m^{2,3} (F_r + R_4 F_a)^{0,31}$	$G_{sl.l} = S_3 d_m^{0,94} (F_r^3 + S_4 F_a^3)^{1/3}$
	when $G_{rr.e} < G_{rr.l}$	when $G_{sl.e} < G_{sl.l}$
	$G_{rr} = G_{rr.e}$	$G_{sl} = G_{sl.e}$
	otherwise	otherwise
	$G_{rr} = G_{rr.l}$	$G_{sl} = G_{sl.l}$
CARB toroidal roller bearings	when $F_r < (R_2^{1,85} d_m^{0,78}/R_1^{1,85})^{2,35}$	when $F_r < (S_2 d_m^{1,24}/S_1)^{1,5}$
	$G_{rr} = R_1 d_m^{1,97} F_r^{0,54}$	$G_{sl} = S_1 d_m^{-0,19} F_r^{5/3}$
	otherwise	otherwise
	$G_{rr} = R_2 d_m^{2,37} F_r^{0,31}$	$G_{sl} = S_2 d_m^{1,05} F_r$

The geometry constants R and S are listed in **table 2**, starting on **page 8**.
Both loads, F_r and F_a are always considered as positive.
[1] The value to be used for F_a is the external axial load.

Table 1b

Geometric and load dependent variables for rolling and sliding frictional moments – thrust bearings

Bearing type	Rolling frictional variable G_{rr}	Sliding frictional variable G_{sl}
Thrust ball bearings	$G_{rr} = R_1\, d_m^{1,83}\, F_a^{0,54}$	$G_{sl} = S_1\, d_m^{0,05}\, F_a^{4/3}$
Cylindrical roller thrust bearings	$G_{rr} = R_1\, d_m^{2,38}\, F_a^{0,31}$	$G_{sl} = S_1\, d_m^{0,62}\, F_a$
Spherical roller thrust bearings	$G_{rr.e} = R_1\, d_m^{1,96}\, (F_r + R_2\, F_a)^{0,54}$	$G_{sl.e} = S_1\, d_m^{-0,35}\, (F_r^{5/3} + S_2\, F_a^{5/3})$
	$G_{rr.l} = R_3\, d_m^{2,39}\, (F_r + R_4\, F_a)^{0,31}$	$G_{sl.l} = S_3\, d_m^{0,89}\, (F_r + F_a)$
	when $G_{rr.e} < G_{rr.l}$	when $G_{sl.e} < G_{sl.l}$
	$G_{rr} = G_{rr.e}$	$G_{sr} = G_{sl.e}$
	otherwise	otherwise
	$G_{rr} = G_{rr.l}$	$G_{sr} = G_{sl.l}$
		$G_f = S_4\, d_m^{0,76}\, (F_r + S_5\, F_a)$
		$G_{sl} = G_{sr} + \frac{G_f}{e^{10^{-6}\,(n\,\nu)^{1,4}\,d_m}}$

Table 2

Geometric constants for rolling and sliding frictional moments

Bearing type	Geometric constants for rolling frictional moments			sliding frictional moments		
	R_1	R_2	R_3	S_1	S_2	S_3
Deep groove ball bearings	(→ **table 2a**)			(→ **table 2a**)		
Angular contact ball bearings						
– Single row 40°						
72xx BECBP	$4{,}33 \times 10^{-7}$	2,02	$2{,}44 \times 10^{-12}$	$1{,}82 \times 10^{-2}$	0,71	$2{,}44 \times 10^{-12}$
73xx BECBP	$4{,}54 \times 10^{-7}$	2,02	$1{,}84 \times 10^{-12}$	$1{,}64 \times 10^{-2}$	0,71	$1{,}84 \times 10^{-12}$
– Single row 25°						
72xx ACCBM	$3{,}58 \times 10^{-7}$	3,64	$3{,}55 \times 10^{-12}$	$1{,}14 \times 10^{-2}$	1,55	$3{,}55 \times 10^{-12}$
73xx ACCBM	$3{,}48 \times 10^{-7}$	3,64	$1{,}66 \times 10^{-12}$	$9{,}85 \times 10^{-3}$	1,55	$1{,}66 \times 10^{-12}$
– Double row 30°						
32xx A	$5{,}18 \times 10^{-7}$	1,63	$4{,}18 \times 10^{-12}$	$1{,}08 \times 10^{-2}$	1,47	$4{,}18 \times 10^{-12}$
33xx A	$5{,}31 \times 10^{-7}$	1,63	$8{,}83 \times 10^{-13}$	$5{,}48 \times 10^{-3}$	1,47	$8{,}83 \times 10^{-13}$
– four-point contact	$4{,}78 \times 10^{-7}$	2,42	$1{,}40 \times 10^{-12}$	$1{,}20 \times 10^{-2}$	0,9	$1{,}40 \times 10^{-12}$
Self-aligning ball bearings	(→ **table 2b**)			(→ **table 2b**)		
Cylindrical roller bearings	(→ **table 2c**)			(→ **table 2c**)		
Tapered roller bearings	(→ **table 2d**)			(→ **table 2d**)		
Spherical roller bearings	(→ **table 2e**)			(→ **table 2e**)		
CARB toroidal roller bearings	(→ **table 2f**)			(→ **table 2f**)		
Thrust ball bearings	$1{,}03 \times 10^{-6}$			$1{,}6 \times 10^{-2}$		
Cylindrical roller thrust bearings	$2{,}25 \times 10^{-6}$			0,154		
Spherical roller thrust bearings	(→ **table 2g**)			(→ **table 2g**)		

Table 2a

Geometric constants for rolling and sliding frictional moments of deep groove ball bearings

Bearing series	Geometric constants for rolling frictional moments		sliding frictional moments	
	R_1	R_2	S_1	S_2
2, 3	$4{,}4 \times 10^{-7}$	1,7	$2{,}00 \times 10^{-3}$	100
42, 43	$5{,}4 \times 10^{-7}$	0,96	$3{,}00 \times 10^{-3}$	40
60, 630	$4{,}1 \times 10^{-7}$	1,7	$3{,}73 \times 10^{-3}$	14,6
62, 622	$3{,}9 \times 10^{-7}$	1,7	$3{,}23 \times 10^{-3}$	36,5
63, 623	$3{,}7 \times 10^{-7}$	1,7	$2{,}84 \times 10^{-3}$	92,8
64	$3{,}6 \times 10^{-7}$	1,7	$2{,}43 \times 10^{-3}$	198
160, 161	$4{,}3 \times 10^{-7}$	1,7	$4{,}63 \times 10^{-3}$	4,25
617, 618, 628, 637, 638	$4{,}7 \times 10^{-7}$	1,7	$6{,}50 \times 10^{-3}$	0,78
619, 639	$4{,}3 \times 10^{-7}$	1,7	$4{,}75 \times 10^{-3}$	3,6

Table 2b

Geometric constants for rolling and sliding frictional moments of self-aligning ball bearings

Bearing series	Geometric constants for rolling frictional moments			sliding frictional moments		
	R_1	R_2	R_3	S_1	S_2	S_3
12	$3{,}25 \times 10^{-7}$	6,51	$2{,}43 \times 10^{-12}$	$4{,}36 \times 10^{-3}$	9,33	$2{,}43 \times 10^{-12}$
13	$3{,}11 \times 10^{-7}$	5,76	$3{,}52 \times 10^{-12}$	$5{,}76 \times 10^{-3}$	8,03	$3{,}52 \times 10^{-12}$
22	$3{,}13 \times 10^{-7}$	5,54	$3{,}12 \times 10^{-12}$	$5{,}84 \times 10^{-3}$	6,60	$3{,}12 \times 10^{-12}$
23	$3{,}11 \times 10^{-7}$	3,87	$5{,}41 \times 10^{-12}$	0,01	4,35	$5{,}41 \times 10^{-12}$
112	$3{,}25 \times 10^{-7}$	6,16	$2{,}48 \times 10^{-12}$	$4{,}33 \times 10^{-3}$	8,44	$2{,}48 \times 10^{-12}$
130	$2{,}39 \times 10^{-7}$	5,81	$1{,}10 \times 10^{-12}$	$7{,}25 \times 10^{-3}$	7,98	$1{,}10 \times 10^{-12}$
139	$2{,}44 \times 10^{-7}$	7,96	$5{,}63 \times 10^{-13}$	$4{,}51 \times 10^{-3}$	12,11	$5{,}63 \times 10^{-13}$

Table 2c

Geometric constants for rolling and sliding frictional moments of cylindrical roller bearings

Bearing series	Geometric constants for rolling frictional moments	sliding frictional moments	
	R_1	S_1	S_2
Bearing with cage of the N, NU, NJ or NUP design			
2, 3	$1{,}09 \times 10^{-6}$	0,16	0,0015
4	$1{,}00 \times 10^{-6}$	0,16	0,0015
10	$1{,}12 \times 10^{-6}$	0,17	0,0015
12, 20	$1{,}23 \times 10^{-6}$	0,16	0,0015
22	$1{,}40 \times 10^{-6}$	0,16	0,0015
23	$1{,}48 \times 10^{-6}$	0,16	0,0015
High capacity bearings with cage of the NCF .. ECJB, RN .. ECJB, NJF .. ECJA, RNU .. ECJA or NUH .. ECMH design			
22	$1{,}54 \times 10^{-6}$	0,16	0,0015
23	$1{,}63 \times 10^{-6}$	0,16	0,0015
Full complement bearings of the NCF, NJG, NNCL, NNCF, NNC or NNF design			
All series	$2{,}13 \times 10^{-6}$	0,16	0,0015

Table 2d

Geometric constants for rolling and sliding frictional moments of tapered roller bearings

Bearing series	Geometric constants for rolling frictional moments		sliding frictional moments	
	R_1	R_2	S_1	S_2
302	$1{,}76 \times 10^{-6}$	10,9	0,017	2
303	$1{,}69 \times 10^{-6}$	10,9	0,017	2
313 (X)	$1{,}84 \times 10^{-6}$	10,9	0,048	2
320 X	$2{,}38 \times 10^{-6}$	10,9	0,014	2
322	$2{,}27 \times 10^{-6}$	10,9	0,018	2
322 B	$2{,}38 \times 10^{-6}$	10,9	0,026	2
323	$2{,}38 \times 10^{-6}$	10,9	0,019	2
323 B	$2{,}79 \times 10^{-6}$	10,9	0,030	2
329	$2{,}31 \times 10^{-6}$	10,9	0,009	2
330	$2{,}71 \times 10^{-6}$	11,3	0,010	2
331	$2{,}71 \times 10^{-6}$	10,9	0,015	2
332	$2{,}71 \times 10^{-6}$	10,9	0,018	2
LL	$1{,}72 \times 10^{-6}$	10,9	0,0057	2
L	$2{,}19 \times 10^{-6}$	10,9	0,0093	2
LM	$2{,}25 \times 10^{-6}$	10,9	0,011	2
M	$2{,}48 \times 10^{-6}$	10,9	0,015	2
HM	$2{,}60 \times 10^{-6}$	10,9	0,020	2
H	$2{,}66 \times 10^{-6}$	10,9	0,025	2
HH	$2{,}51 \times 10^{-6}$	10,9	0,027	2
All other	$2{,}31 \times 10^{-6}$	10,9	0,019	2

Table 2e

Geometric constants for rolling and sliding frictional moments of spherical roller bearings

Bearing series	Geometric constants for rolling frictional moments				sliding frictional moments			
	R_1	R_2	R_3	R_4	S_1	S_2	S_3	S_4
213 E, 222 E	$1,6 \times 10^{-6}$	5,84	$2,81 \times 10^{-6}$	5,8	$3,62 \times 10^{-3}$	508	$8,8 \times 10^{-3}$	117
222	$2,0 \times 10^{-6}$	5,54	$2,92 \times 10^{-6}$	5,5	$5,10 \times 10^{-3}$	414	$9,7 \times 10^{-3}$	100
223	$1,7 \times 10^{-6}$	4,1	$3,13 \times 10^{-6}$	4,05	$6,92 \times 10^{-3}$	124	$1,7 \times 10^{-2}$	41
223 E	$1,6 \times 10^{-6}$	4,1	$3,14 \times 10^{-6}$	4,05	$6,23 \times 10^{-3}$	124	$1,7 \times 10^{-2}$	41
230	$2,4 \times 10^{-6}$	6,44	$3,76 \times 10^{-6}$	6,4	$4,13 \times 10^{-3}$	755	$1,1 \times 10^{-2}$	160
231	$2,4 \times 10^{-6}$	4,7	$4,04 \times 10^{-6}$	4,72	$6,70 \times 10^{-3}$	231	$1,7 \times 10^{-2}$	65
232	$2,3 \times 10^{-6}$	4,1	$4,00 \times 10^{-6}$	4,05	$8,66 \times 10^{-3}$	126	$2,1 \times 10^{-2}$	41
238	$3,1 \times 10^{-6}$	12,1	$3,82 \times 10^{-6}$	12	$1,74 \times 10^{-3}$	9 495	$5,9 \times 10^{-3}$	1 057
239	$2,7 \times 10^{-6}$	8,53	$3,87 \times 10^{-6}$	8,47	$2,77 \times 10^{-3}$	2 330	$8,5 \times 10^{-3}$	371
240	$2,9 \times 10^{-6}$	4,87	$4,78 \times 10^{-6}$	4,84	$6,95 \times 10^{-3}$	240	$2,1 \times 10^{-2}$	68
241	$2,6 \times 10^{-6}$	3,8	$4,79 \times 10^{-6}$	3,7	$1,00 \times 10^{-2}$	86,7	$2,9 \times 10^{-2}$	31
248	$3,8 \times 10^{-6}$	9,4	$5,09 \times 10^{-6}$	9,3	$2,80 \times 10^{-3}$	3 415	$1,2 \times 10^{-2}$	486
249	$3,0 \times 10^{-6}$	6,67	$5,09 \times 10^{-6}$	6,62	$3,90 \times 10^{-3}$	887	$1,7 \times 10^{-2}$	180

Table 2f

Geometric constants for rolling and sliding frictional moments of CARB toroidal roller bearings with a cage

Bearing series	Geometric constants for rolling frictional moments		sliding frictional moments	
	R_1	R_2	S_1	S_2
C 22	$1,17 \times 10^{-6}$	$2,08 \times 10^{-6}$	$1,32 \times 10^{-3}$	$0,8 \times 10^{-2}$
C 23	$1,20 \times 10^{-6}$	$2,28 \times 10^{-6}$	$1,24 \times 10^{-3}$	$0,9 \times 10^{-2}$
C 30	$1,40 \times 10^{-6}$	$2,59 \times 10^{-6}$	$1,58 \times 10^{-3}$	$1,0 \times 10^{-2}$
C 31	$1,37 \times 10^{-6}$	$2,77 \times 10^{-6}$	$1,30 \times 10^{-3}$	$1,1 \times 10^{-2}$
C 32	$1,33 \times 10^{-6}$	$2,63 \times 10^{-6}$	$1,31 \times 10^{-3}$	$1,1 \times 10^{-2}$
C 39	$1,45 \times 10^{-6}$	$2,55 \times 10^{-6}$	$1,84 \times 10^{-3}$	$1,0 \times 10^{-2}$
C 40	$1,53 \times 10^{-6}$	$3,15 \times 10^{-6}$	$1,50 \times 10^{-3}$	$1,3 \times 10^{-2}$
C 41	$1,49 \times 10^{-6}$	$3,11 \times 10^{-6}$	$1,32 \times 10^{-3}$	$1,3 \times 10^{-2}$
C 49	$1,49 \times 10^{-6}$	$3,24 \times 10^{-6}$	$1,39 \times 10^{-3}$	$1,5 \times 10^{-2}$
C 59	$1,77 \times 10^{-6}$	$3,81 \times 10^{-6}$	$1,80 \times 10^{-3}$	$1,8 \times 10^{-2}$
C 60	$1,83 \times 10^{-6}$	$5,22 \times 10^{-6}$	$1,17 \times 10^{-3}$	$2,8 \times 10^{-2}$
C 69	$1,85 \times 10^{-6}$	$4,53 \times 10^{-6}$	$1,61 \times 10^{-3}$	$2,3 \times 10^{-2}$

Table 2g

Geometric constants for rolling and sliding frictional moments of spherical roller thrust bearings

Bearing series	Geometric constants for rolling frictional moments				sliding frictional moments				
	R_1	R_2	R_3	R_4	S_1	S_2	S_3	S_4	S_5
292	$1,32 \times 10^{-6}$	1,57	$1,97 \times 10^{-6}$	3,21	$4,53 \times 10^{-3}$	0,26	0,02	0,1	0,6
292 E	$1,32 \times 10^{-6}$	1,65	$2,09 \times 10^{-6}$	2,92	$5,98 \times 10^{-3}$	0,23	0,03	0,17	0,56
293	$1,39 \times 10^{-6}$	1,66	$1,96 \times 10^{-6}$	3,23	$5,52 \times 10^{-3}$	0,25	0,02	0,1	0,6
293 E	$1,16 \times 10^{-6}$	1,64	$2,00 \times 10^{-6}$	3,04	$4,26 \times 10^{-3}$	0,23	0,025	0,15	0,58
294 E	$1,25 \times 10^{-6}$	1,67	$2,15 \times 10^{-6}$	2,86	$6,42 \times 10^{-3}$	0,21	0,04	0,2	0,54

Frictional moment of seals

Where bearings are fitted with contact seals, the frictional losses from the seals may exceed those generated by the bearing. The frictional moment of seals for bearings that are sealed on both sides can be estimated using

$$M_{seal} = K_{S1}\, d_s^{\beta} + K_{S2}$$

where
M_{seal} = frictional moment of seals [Nmm]
K_{S1} = constant (→ **table 3**), depending on:
- the seal type
- the bearing type and size

d_s = seal counterface diameter [mm] (→ **table 3**)
β = exponent (→ **table 3**), depending on:
- the seal type
- the bearing type

K_{S2} = constant (→ **table 3**), depending on:
- the seal type
- the bearing type and size

In cases where there is only one seal, the friction generated is 0,5 M_{seal}.

For deep groove ball bearings with RSL seals and D > 25 mm, use the calculated value of M_{seal}, irrespective whether there is one or two seals.

Table 3

Seal frictional moment: Exponent and constants

Seal type Bearing type	Bearing outside diameter [mm] D over	 incl.	Exponent and constants β	 K_{S1}	 K_{S2}	Seal counterface diameter d_s [1]
RSL seals						
Deep groove ball bearings	–	25	0	0	0	d_2
	25	52	2,25	0,0018	0	d_2
RSH seals						
Deep groove ball bearings	–	52	2,25	0,028	2	d_2
RS1 seals						
Deep groove ball bearings	–	62	2,25	0,023	2	d_1, d_2
	62	80	2,25	0,018	20	d_1, d_2
	80	100	2,25	0,018	15	d_1, d_2
	100		2,25	0,018	0	d_1, d_2
Angular contact ball bearings	30	120	2	0,014	10	d_1
Self-aligning ball bearings	30	125	2	0,014	10	d_2
LS seals						
Cylindrical roller bearings	42	360	2	0,032	50	E
CS, CS2 and CS5 seals						
Spherical roller bearings	62	300	2	0,057	50	d_2
CARB toroidal roller bearings	42	340	2	0,057	50	d_2

[1] Designation of the dimension listed in the product tables

Drag losses

Bearings lubricated by the oil bath method are partially submerged or, in special situations, completely submerged. The drag losses that occur when the bearing is rotating in an oil bath contribute to the total frictional moment and should not be ignored. Drag losses are not only influenced by bearing speed, oil viscosity and oil level, but also by the size and geometry of the oil reservoir. External oil agitation, which can originate from mechanical elements, such as gears or cams, in close proximity to the bearing should also be taken into consideration.

Drag losses in oil bath lubrication

The SKF model for calculating drag losses in oil bath lubrication considers the resistance of the rolling elements moving through the oil and includes the effects of the oil viscosity. It provides results with sufficient accuracy under the following conditions:

- The oil reservoir is large. Effects from reservoir size and geometry or external oil agitation are negligible.
- The shaft is horizontal.
- The inner ring rotates at a constant speed. The speed does not exceed the permissible speed.
- The oil viscosity is within the limits:
  - ≤ 500 mm^2/s when the bearing is submerged up to, and including, half of its outside diameter (oil level H ≤ D/2)
  - ≤ 250 mm^2/s when the bearing is submerged more than half of its outside diameter (oil level H > D/2)

The oil level H is measured from the lowest contact point between the outer ring raceway and the rolling element (→ **fig. 2**, **page 14**). The postion of the lowest contact point can be estimated with sufficient accuracy using:

- for tapered roller bearings: outside diameter D [mm]
- for all other radial rolling bearings: outer ring mean diameter [mm] = 0,5 (D + D_1)

The frictional moment of drag losses for ball bearings can be estimated using

$$M_{drag} = 0{,}4\, V_M\, K_{ball}\, d_m^5\, n^2 + 1{,}093 \times 10^{-7}\, n^2\, d_m^3 \left(\frac{n\, d_m^2\, f_t}{\nu}\right)^{-1{,}379} R_s$$

The frictional moment of drag losses for roller bearings can be estimated using

$$M_{drag} = 4\, V_M\, K_{roll}\, C_w\, B\, d_m^4\, n^2 + 1{,}093 \times 10^{-7}\, n^2\, d_m^3 \left(\frac{n\, d_m^2\, f_t}{\nu}\right)^{-1{,}379} R_s$$

The rolling element related constants are:

$$K_{ball} = \frac{i_{rw}\, K_z\, (d + D)}{D - d}\, 10^{-12}$$

$$K_{roll} = \frac{K_L\, K_Z\, (d + D)}{D - d}\, 10^{-12}$$

The variables and functions used in the equations for the frictional moment of drag losses are:

$$C_w = 2{,}789 \times 10^{-10}\, l_D^3 - 2{,}786 \times 10^{-4}\, l_D^2 + 0{,}0195\, l_D + 0{,}6439$$

$$l_D = 5\,\frac{K_L\, B}{d_m}$$

$$f_t = \begin{cases} \sin(0{,}5\ t), & \text{when } 0 \le t \le \pi \\ 1, & \text{when } \pi < t < 2\,\pi \end{cases}$$

$$R_s = 0{,}36\, d_m^2\, (t - \sin t)\, f_A$$

$$t = 2\cos^{-1}\left(\frac{0{,}6\, d_m - H}{0{,}6\, d_m}\right) \qquad \text{When } H \ge 1{,}2\, d_m, \text{ use } H = 1{,}2\, d_m$$

$$f_A = 0{,}05\ \frac{K_z\,(D + d)}{D - d}$$

where
M_{drag} = frictional moment of drag losses [Nmm]
V_M = drag loss factor (→ **diagram 4**, **page 14**)
B = bearing width [mm]
- for tapered roller bearings → width T
- for thrust bearings → height H

d_m = bearing mean diameter [mm]
= 0,5 (d + D)
d = bearing bore diameter [mm]
D = bearing outside diameter [mm]
H = oil level (→ **fig. 2**, **page 14**) [mm]
i_{rw} = number of ball rows
K_Z = bearing type related geometric constant (→ **table 4**, **page 14**)
K_L = roller bearing type related geometric constant (→ **table 4**, **page 14**)
n = rotational speed [r/min]
ν = actual operating viscosity of the lubricant [mm^2/s]

Drag losses for vertical shafts

The model for fully submerged bearings can be used to calculate an approximate value of the drag losses for vertical shaft arrangements. The value obtained for M_{drag} should be multiplied by a factor equal to the width (height) that is submerged relative to the total bearing width (height).

Drag losses for oil jet lubrication

To calculate drag losses for the oil jet lubrication method, use the oil bath model, with the oil level H at half the diameter of the lowest rolling element. The value obtained for M_{drag} should be multiplied by a factor of two. Certainly, this approximation can vary depending on the rate and direction of oil flow. However, if the oil level H is known when oil is flowing and the bearing is at a stand-still, this value can be used directly in the drag loss calculation to obtain a more accurate estimate.

Fig. 2

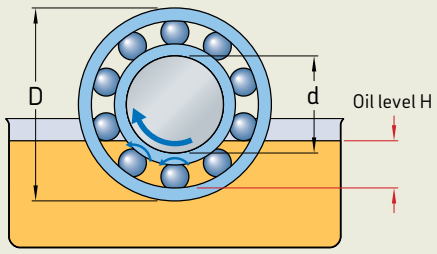

Table 4

Geometric constants K_Z and K_L

Bearing type	Geometric constants K_Z	K_L
Deep groove ball bearings		
– single and double row	3,1	–
Angular contact ball bearings		
– single row	4,4	–
– double row	3,1	–
– four-point contact	3,1	–
Self-aligning ball bearings	4,8	–
Cylindrical roller bearings		
– with a cage	5,1	0,65
– full complement	6,2	0,7
Tapered roller bearings	6	0,7
Spherical roller bearings	5,5	0,8
CARB toroidal roller bearings		
– with a cage	5,3	0,8
– full complement	6	0,75
Thrust ball bearings	3,8	–
Cylindrical roller thrust bearings	4,4	0,43
Spherical roller thrust bearings	5,6	0,58[1)]

[1)] Only for single mounted bearings

Diagram 4

Drag loss factor V_M

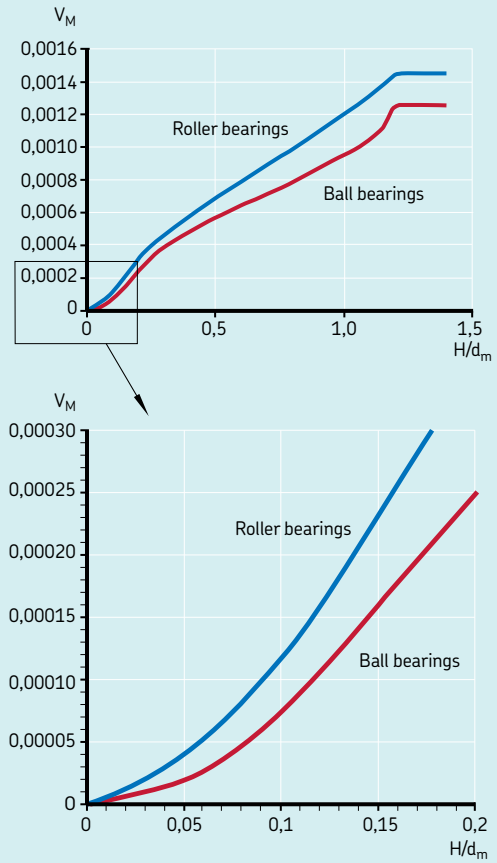

Additional effects on the frictional moment

Effects of clearance and misalignment on friction

Changes in clearance or misalignment in bearings influence the frictional moment. The model considers normal internal operating clearance and an aligned bearing. However, high bearing operating temperatures or speeds might reduce internal bearing clearance, which can increase friction. Misalignment generally increases friction. However, for self-aligning ball bearings, spherical roller bearings, CARB toroidal roller bearings and spherical roller thrust bearings, the corresponding increase of friction is negligible.

Effects of grease fill on friction

When a bearing has just been lubricated or relubricated with the recommended amount of grease, the frictional values realized in the bearing can be much higher than those originally calculated. The effect can be seen as an increase in operating temperature. The time it takes for friction to decrease depends on the speed of the application and the time it takes for the grease to distribute itself within the free space in the bearing.

This effect can be estimated by multiplying the rolling frictional moment by a factor of 2 to 4, where 2 applies for light series bearings (narrow width series) and 4 for heavy series bearings.

However, after the running-in period, the frictional moment in the bearing is similar to, or even lower than, that for oil lubricated bearings. Bearings filled with an excessive amount of grease may show higher frictional values.

Additional information for specific bearing types and performance classes

Hybrid bearings

The higher values for the modulus of elasticity of rolling elements made of silicon nitride decreases the contact area in the raceways to significantly reduce rolling and sliding friction. Additionally, the lower density of ceramic rolling elements, when compared with steel, reduces the centrifugal forces, which also may reduce friction at high speeds.

Standard hybrid ball bearings

Using the above equations, the frictional moment for hybrid angular contact ball bearings can be calculated by multiplying the geometric constants R_3 and S_3 of the bearings with steel rolling elements by a factor 0,41, i.e. 0,41 R_3 and 0,41 S_3, respectively.

Hybrid deep groove ball bearings in high-speed applications are usually preloaded axially. Under these conditions, hybrid deep groove ball bearings behave like angular contact ball bearings with a similar reduced frictional moment.

Appendix G

Calibration Data of Measuring Devices

G.1 Pressure Transducer

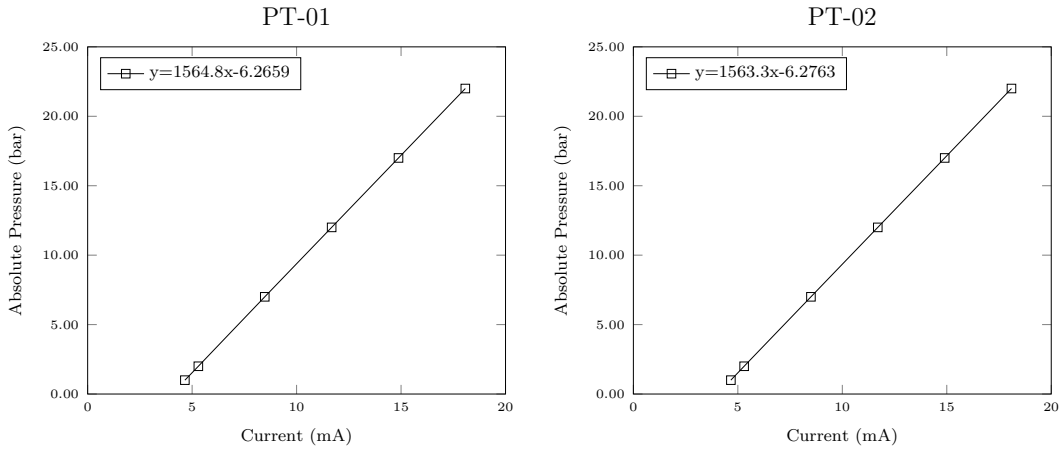

Figure G.1: Calibration data for WIKA A-10 pressure transducers (PT-01 and PT-02).

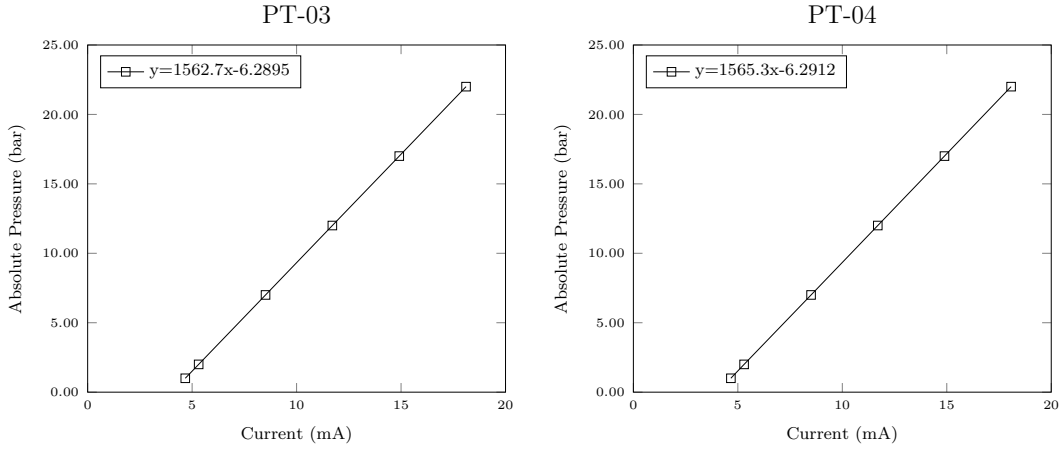

Figure G.2: Calibration data for WIKA A-10 pressure transducers (PT-03 and PT-04).

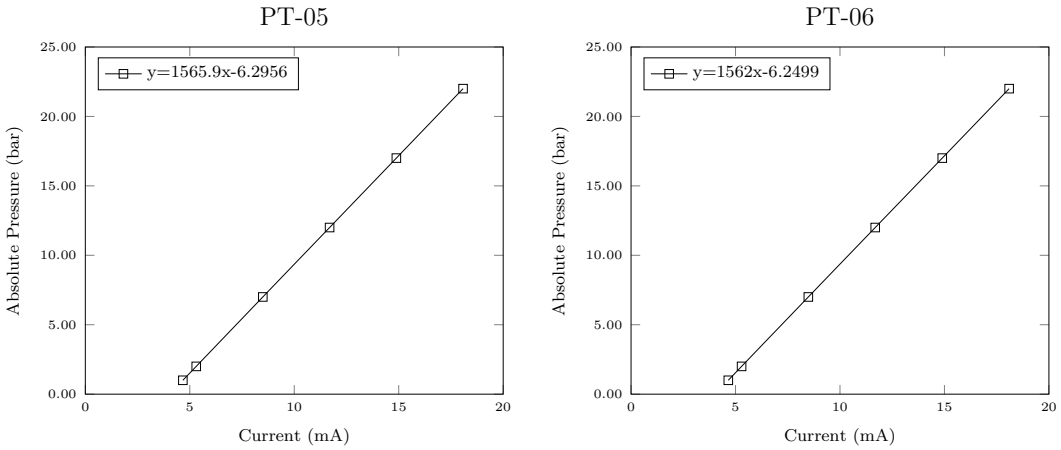

Figure G.3: Calibration data for WIKA A-10 pressure transducers (PT-05 and PT-06).

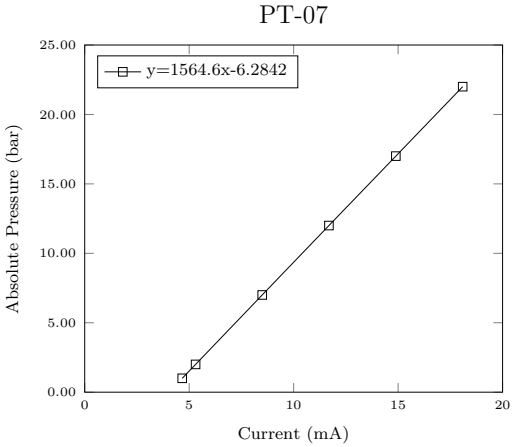

Figure G.4: Calibration data for WIKA A-10 pressure transducers (PT-07).

G.2 Piezoresistive Pressure Transducer

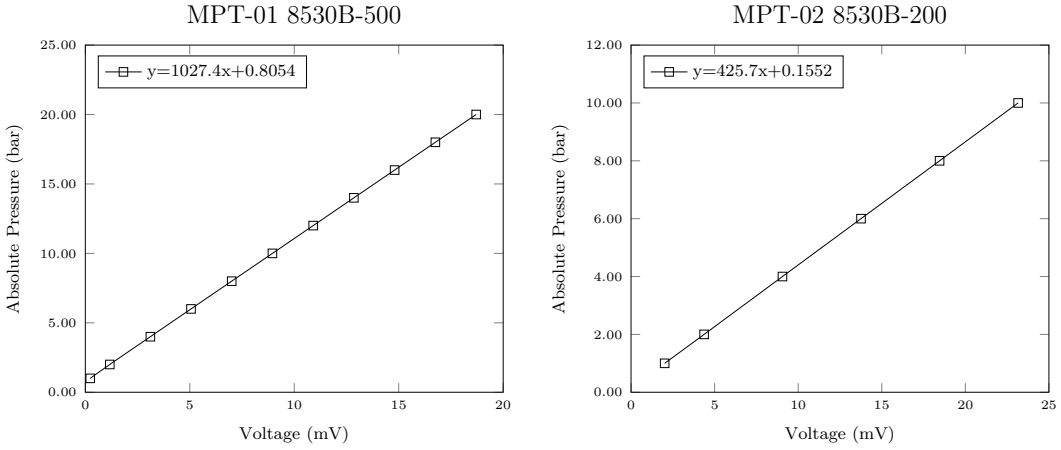

Figure G.5: Calibration data for Endevco pressure transducers (MPT-01 and MPT-02).

G.3 Thermocouple

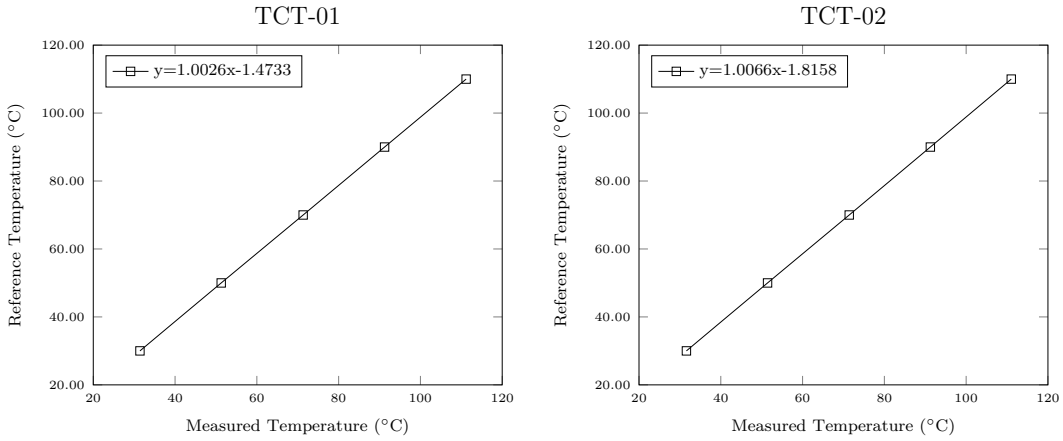

Figure G.6: Calibration data for Type T thermocouple (TCT-01 and TCT-02).

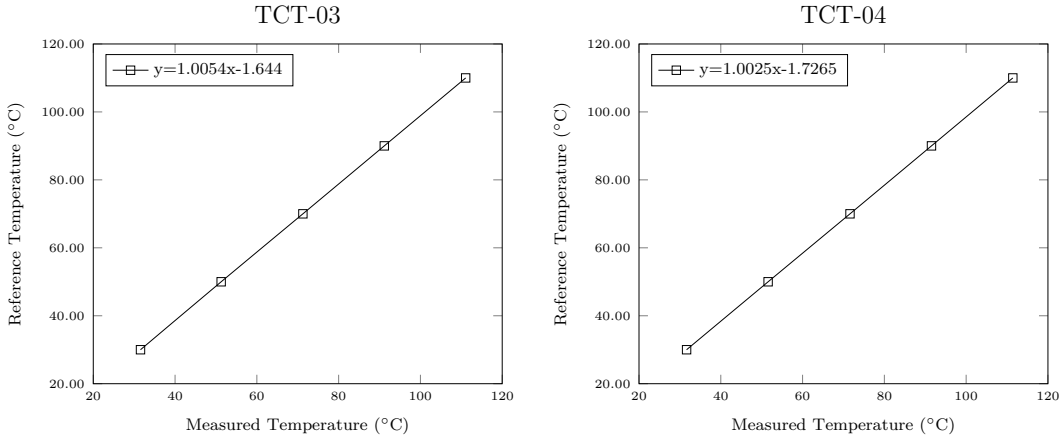

Figure G.7: Calibration data for Type T thermocouple (TCT-03 and TCT-04).

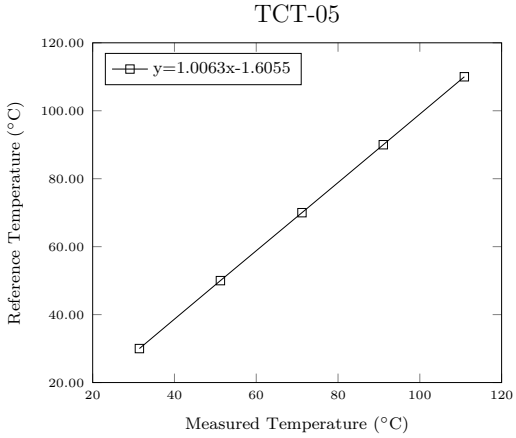

Figure G.8: Calibration data for WIKA A-10 pressure transducers (PT-05).

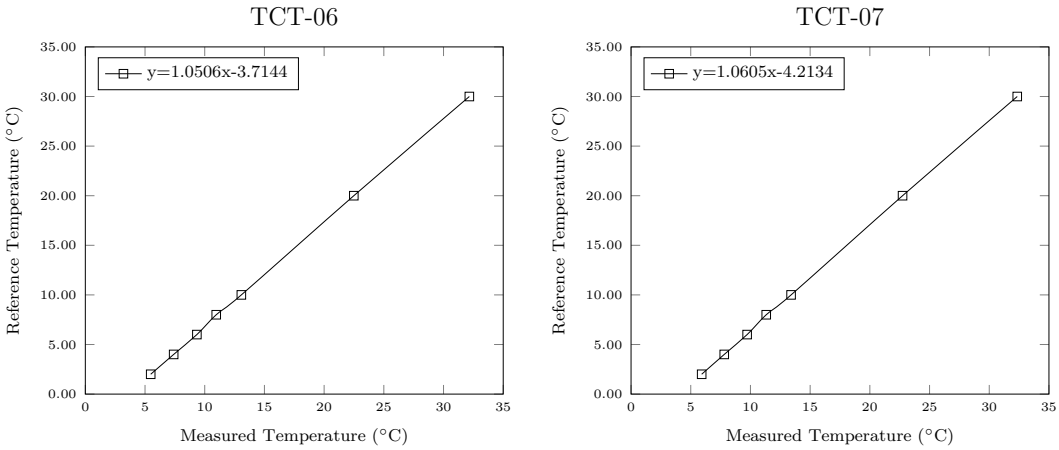

Figure G.9: Calibration data for Type T thermocouple (TCT-06 and TCT-07).

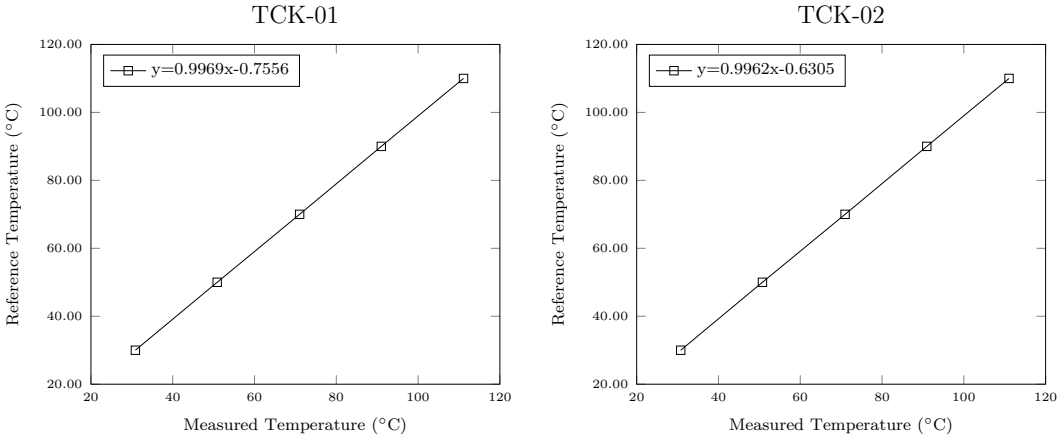

Figure G.10: Calibration data for Type K thermocouple (TCK-01 and TCK-02).

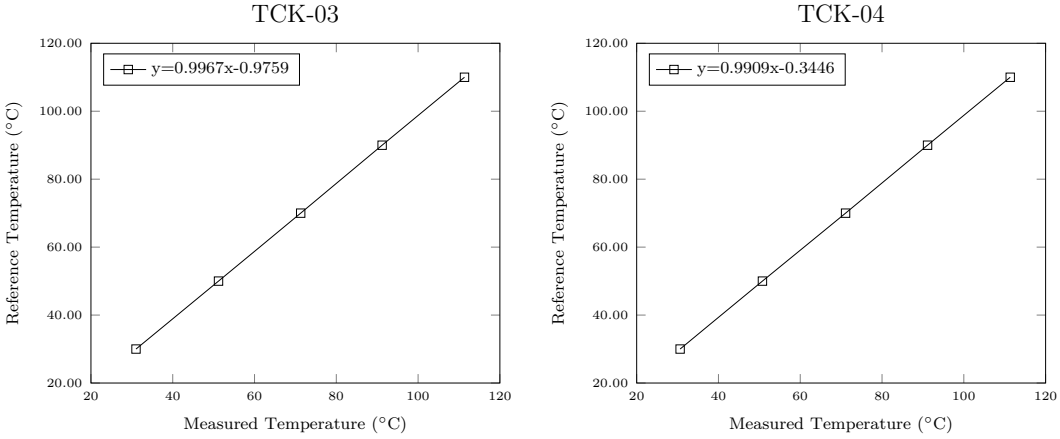

Figure G.11: Calibration data for Type K thermocouple (TCK-03 and TCK-04).